https://doi.org/10.15388/vu.thesis.103
https://orcid.org/0000-0002-4645-3473

VILNIAUS UNIVERSITETAS
FIZINIŲ IR TECHNOLOGIJOS MOKSLŲ CENTRAS

AGNĖ
MIKALAUSKAITĖ

Magnetinių geležies oksido nanodalelių paviršiaus dekoravimo aukso nanokompozitais tyrimas

DAKTARO DISERTACIJA

Gamtos mokslai,
Chemija (N 003)

VILNIUS 2020

Disertacija rengta 2015– 2019 metais Fizinių ir technologijos mokslų centro Elektrocheminės medžiagotyros skyriuje
Mokslinius tyrimus rėmė Lietuvos mokslo taryba ir Italijos užsienio reikalų ministerija.

Mokslinis vadovas:
Dr. Arūnas Jagminas (Fizinių ir technologijos mokslų centras, gamtos mokslai, chemija – N 003).

Gynimo taryba:
Pirmininkas – **prof. dr. Valentinas Snitka** (Kauno technologijos universitetas, gamtos mokslai, chemija – N 003).
Nariai:
doc. habil. dr. Vidmantas Gulbinas (Fizinių ir technologijos mokslų centras, gamtos mokslai, fizika – N 002);
prof. habil. dr. Aivaras Kareiva (Vilniaus universitetas, gamtos mokslai, chemija – N 003);
prof. habil. dr. Rimantas Ramanauskas (Fizinių ir technologijos mokslų centras, gamtos mokslai, chemija – N 003);
prof. habil. dr. Almira Ramanavičienė (Vilniaus universitetas, gamtos mokslai, chemija – N 003).

Disertacija ginama viešame Gynimo tarybos posėdyje 2020 m. lapkričio mėn. 27 d. 11 val. Fizinių ir technologijos mokslų centro D401 auditorijoje.

Adresas: Saulėtekio al. 3, LT-10257 Vilnius, tel. +37052648884; el. paštas office@ftmc.lt

Disertaciją galima peržiūrėti Vilniaus universiteto, Fizinių ir technologijos mokslų centro bibliotekose ir VU interneto svetainėje adresu: *https://www.vu.lt/naujienos/ivykiu-kalendorius*

https://doi.org/10.15388/vu.thesis.103
https://orcid.org/0000-0002-4645-3473

VILNIUS UNIVERSITY
CENTER FOR PHYSICAL SCIENCES AND TECHNOLOGY

Agnė
MIKALAUSKAITĖ

Investigation on the Surface Decoration of Magnetic Iron Oxide Nanoparticles with Gold Nanocomposites

DOCTORAL DISSERTATION

Natural sciences,
Chemistry (N 003)

VILNIUS 2020

This dissertation was written between 2015 and 2019 State research institute Center for Physical Sciences and Technology. The research was supported by Research Council of Lithuania and Ministry of Foreign Affairs and International Cooperation.

Academic supervisor:
Dr. Arūnas, Jagminas (Center for Physical Sciences and Technology, natural sciences, chemistry – N 003).
Dissertation Defence Panel:
Chairman – **prof. dr. Valentinas Snitka** (Kaunas Technology universtity, natural sciences, chemistry – N 003)
Members:
doc. habil. dr. Vidmantas Gulbinas (Center for Physical Sciences and Technology, natural sciences, physical – N 002)
prof. habil. dr. Aivaras Kareiva (Vilnius university, natural sciences, chemistry – N 003)
prof. habil. dr. Rimantas Ramanauskas (Center for Physical Sciences and Technology, natural sciences, chemistry – N 003)
prof. habil. dr. Almira Ramanavičienė (Vilnius university, Natural sciences, chemistry – N 003)

This doctoral dissertation will be defended in a public meeting of the Dissertation Defence Panel at 11 am. on 27th November 2020 in meeting room D401 of the Center for Physical Sciences and Technology

Address: Sauletekio av., 3, D401, Vilnius, Lithuania, Tel. +37052648884; e-mail: office@ftmc.lt

The text of this dissertation can be accessed at the libraries of Center for Physical Sciences and Technology and Vilnius university, as well as on the website of Vilnius University: www.vu.lt/lt/naujienos/ivykiu-kalendorius

TURINYS

SUTARTINIŲ ŽYMĖJIMŲ IR SIMBOLIŲ SĄRAŠAS

ASGPEM	aukštos skiriamosios gebos elektronų transmisijos mikroskopija
AuNd	aukso nanokristalai
AuNkl	aukso nanoklasteriai
ATP	adenozintrifosfatas
$CoFe_2O_4$@AR	kobalto ferito ir skirtingų aminorūgščių kompleksas
CTAB	heksadeciltrimetilamonio bromidas
DOPA	dopamino hidrochloridas
DPA	D-penicilaminas
EDX	rentgeno spindulių energijos dispersinė analizė
EG	etilenglikolis
Erl	„Erlotinib“ komercinis vaistas
Fe_3O_4	magnetitas
Fe_xO_y	geležies oksidų bendra formulė
FTIR	Furje transformacijos infraraudonųjų spindulių spektroskopija
GLT	glutationas
HDD	1,2-heksadekandiolis
HepG2	hepatokarcinomos vėžio ląstelių grupė
γ-Fe_2O_3	maghemitas
JSA	jaučio serumo albuminas
KN	kvantinis našumas
K562	leukemijos ląstelių grupė
LPRP	lokalaus paviršiaus plazmonų rezonanso juosta
MBR	magnetinis branduolinis rezonansas
Met	D,L-metionino aminorūgštis
$MeFe_2O_4$	metalų geležies oksidų bendra formulė
$MeFe_2O_4$@Met	metalų geležies oksidų ir D,L-metionino kompleksas
MIK	mažiausios inhibuojančios koncentracijos vertės
Mnd	magnetinės geležies oksido nanodalelės
Nd	nanodalelės
OLA	oleilaminas
OR	oleino rūgštis
PAA	poliamidoaminas
PAM	paviršiaus aktyvi medžiaga

PAR	poliakrilo rūgštis
PDA	polidopaminas
PEM	peršviečiama elektronų mikroskopija
PMR	polimetakrilorūgštis
PPI	polipropileno iminas
PVP	poli-vinilpirolidonas
~R	paviršiaus funkcinių grupių bendras žymėjimas
ROS	aktyvios deguonies formos
RSD	rentgeno spindulių difrakcinė analizė
SPIONs	superparamagnetinės geležies oksido nanodalelės
STAB	natrio-triacetoksiborohidridas
THPC	tetrakis (hidroksimetil) fosfonio chloridas
TOAB	tetraoktilamonio bromidas

ĮVADAS

Darbo aktualumas

Šiuo metu nanomedicina yra sparčiai besivystanti medicinos mokslo sritis. Tai sietina su naujai atrandamomis ir įvairiose technologijose pritaikomomis, nanometrinio dydžio dalelėmis, kurios pasižymi išskirtinėmis cheminėmis, fizinėmis ir optinėmis savybėmis. Nanomedicinos tikslas – žmogaus biologinių sistemų visapusiškas monitoringas, kontrolė, gydymas, apsauga ir stiprinimas molekuliniame lygmenyje naudojant inžinerinius prietaisus ir nanostruktūras. Šios naujos idėjos apjungia savyje optines, magnetines, elektronines bei struktūrines dalelių savybes.

Teranostika - nauja nanomedicinos sritis, dažniausiai siejama su nanotechnologijomis, kadangi jas pasitelkiant, galima sukurti nanodaleles, kurios patobulintų navikų diagnostiką, užtikrintų tikslesnį ligos eigos stebėjimą bei kartu turėtų terapinį poveikį. Atsižvelgiant į dabartinius diagnostikos ir terapijos metodų trūkumus, ypatingas mokslininkų dėmesys yra skiriamas biologiškai suderintoms bei tikslingai veikiančioms nanometrinio dydžio magnetinėms nanodalelėms ir intensyvia liuminescencija pasižymintiems aukso nanoklasteriams, kurių savybių sujungimas leistų sukurti dvigubo funkcionalumo kompozitus, pasižyminčius ir magnetinėmis ir liuminescencinėmis savybėmis.

Dėl mažo dydžio bei biosuderinamumo $MeFe_2O_4$@Au *Nd* lėčiau šalinamos iš organizmo. Taigi mokslininkai tiki, kad biosuderinamos, mažos, NIR srityje fluorescuojančios, auksu dengtos magnetinės nanodalelės yra daug žadantys kompozitai *in vivo* auglių vaizdinimo ir tikslinės terapijos plėtrai.

Darbo tikslas

Efektyvių magnetinių nanodalelių auksavimo ir aukso klasterių sintezės metodų paieška, gautų produktų charakterizavimas ir taikymas nanomedicinoje.

Darbo uždaviniai

- Optimizuoti magnetinių nanodalelių hidroterminę sintezę jų stabilizavimui pasitelkiant aminorūgštis.
- Ištirti magnetinių *Nd* efektyvaus paviršiaus padengimo auksu galimybes panaudojant aminorūgštis kaip bioreduktorius.
- Ištirti raudonai fluorescuojančių aukso klasterių sintezę naudojant naujus bioreduktorius ir vandenilio tetrachlorauratą ($HAuCl_4$).
- Nustatyti sintezės produktų sudėtį, struktūrą, apsuptį ir susidarymo mechanizmą.
- Ištirti Au^0/Au^+ *Nd* antibankterines savybes
- Ištirti gautų Au klasterių panaudojimo ląstelių vaizdinimui galimybes.

Disertacijos praktinė vertė

- Parinktos ir optimizuotos vandeninių tirpalų sudėtys 2, 5, ir 15 nm dydžio $CoFe_2O_4$ *Nd* sintezei ko-nusodinimo būdu bei kontroliuojamam jų pavišiaus padengimui aukso luobele.
- Pateiktas magnetinių $CoFe_2O_4$@Au *Nd* auksavimo mechanizmas.
- Ištirta dopamino hidrochlorido adsorbcija ant $CoFe_2O_4$ ir $CoFe_2O_4$@Au *Nd* paviršiaus.
- Parinktos ir optimizuotos vandeninių tirpalų sudėtys Fe_3O_4 *Nd* sintezei ir perspektyviam jų pavišiaus padengimui Au^0/Au^+ aukso nanokristalais.
- Pasiūlytas efektyvus Au^0/Au^+ ultra smulkių nanokristalų „nukabinimas“ nuo Fe_3O_4 *Nd* paviršiaus.
- Ištirtos Au^0/Au^+ nanokristalų baktericidinės savybės itin aukšto atsparumo antibiotikams patogenų atžvilgiu.
- Parinktas naujas ir pigus bioreduktorius *AuNkl* sintezei.
- Ištirtos sukurtų aukso klasterių sudėtis, struktūra ir liuminescencinės savybės parodant, kad šie unikalūs klasteriai pasižymi stabilumu ir intensyvia raudonos šviesos emisija.

Disertaciją sudaro 8 skyriai, iš kurių trys tiriamieji: literatūros apžvalga, metodai ir medžiagos bei rezultatai, o likusieji, t.y. įvadas, išvados, literatūros šaltiniai, autorės mokslinių straipsnių sąrašas šio darbo tematika, pranešimai

konferencijose ir dalyvavimas tarptautiniuose mainuose, tikslinių mokslinių įgūdžių plėtimas tarptautinėse mokyklose ir padėka mokslininkams bei visiems prisidėjusiems, apibendrina viso tiriamojo darbo aktualumą, svarbumą bei naujumą.

Įvadiniame skyriuje pateikiamas temos aktualumas, suformuluotas darbo tikslas bei uždaviniai ir gautų rezultatų naujumas. Literatūros apžvalgos pirmoje dalyje apžvelgta geležies oksido magnetinių nanodalelių struktūra ir savybės. Glaustai pristatomi $MeFe_2O_4$ ir *AuNkl Nd* sintezės metodai pateikiant jų trūkumus ir unikalumą. Antroje dalyje aprašyta magnetinių *Nd* paviršiaus auksavimo bei dekoravimo auksu žinomi būdai bei jų trūkumai. Skyriaus pabaigoje pristatomos tiriamųjų objektų panaudojimo galimybės šiuolaikinėje teranostikoje ir antibakteriniuose tyrimuose.

Antrajame skyriuje aprašomi darbe tirti ir naudoti $CoFe_2O_4$, Fe_3O_4 *Nd* ir *AuNkl* sintezės, bei $CoFe_2O_4$ ir Fe_3O_4 *Nd* paviršiaus padengimo auksu metodai, hidroterminių ir terminių sintezių sąlygos ir reagentai. Gautų produktų struktūros, sudėties bei magnetinių ir antimikrobinių tyrimų metodikos ir įranga pateikti skyrelio gale.

Trečiajame skyriuje detaliai pristatomi vykdytų tyrimų rezultatai, jų naujumas ir praktinio taikymo galimybės.

Disertacijos darbo pabaigoje pateiktos išvados, cituojama literatūra ir autoriaus publikuoti darbai šio darbo tema.

Ginamieji teiginiai:

1. D,L-metionino aminorūgšties imobilizavimas magnetinių *Nd* paviršiuje įgalina padengti jų paviršių aukso nanokristalais bei aukso luobele.
2. Au^0/Au^+ nanokristalus galima ,,nukabinti“ nuo $CoFe_2O_4$@Au ir Fe_3O_4@Au *Nd* paviršiaus D,L-metionino pertekliumi.
3. Au^0/Au^+ nanokristalams būdingos baktericidinės savybės prieš antibiotikams itin atsparius patogenus.
4. Raudonai liuminescuojančius aukso klasterius galima susintetinti maisto papildų, turinčių šakotųjų aminorūgščių, pagalba.

1. LITERATŪROS APŽVALGA

1.1. Magnetinių geležies oksido nanodalelių *(MNd)* sintezė, savybių, sudėties ir struktūros valdymas

1.1.1. *MNd* struktūra ir charakteristika

Standartinė magnetitų formulė yra AB_2O_4, kur A Fe(II), o B Fe(III). Frituose Fe(II) keičia Mn, Co, Ni ir kt. metalų katijonai (1.1 pav.).

Maghemitų ir magnetitų kristalinės gardelės yra panašios. Jos turi tankiai supakuotą kubinę struktūrą (deguonies atžvilgiu) (1.1 lentelė). Skiriasi tik Fe^{2+} ir Fe^{3+} jonų padėtys, kurios užima tetraedrines arba oktaedrines tuštumas [1].

Žemoje temperatūroje susintetinti magnetito (Fe_3O_4) kristalai įprastai yra maži (<100 nm) ir turi būti apsaugoti nuo tolimesnės oksidacijos, nes oksiduojantis magnetitui susidaro maghemitas (γ-Fe_2O_3). Maghemitas yra pilnai oksiduotos formos magnetitas. Oksidacija siekia 11% išstumiant Fe^{2+} iš oktaedrinių ir Fe^{3+} – iš tetraedrinių kristalo vietų jas padarant laisvas. Magnetito į maghemitą perėjimo metu medžiagos spalvos gama keičiasi nuo juodos iki raudonai rudos. Magnetito ir maghemito formuojamos struktūros turi kubinę gardelę (1.1 lentelė). Ji vadinama kubine atvirkštine špineline struktūra (1.1 pav.), susidarančia deguoniui formuojant tankiai supakuotą kubinę gardelę, kurioje geležies katijonai užpildo tetraedrines ir oktaedrines tuštumų vietas. Fe (III) katijonai užpildo laisvas tetraedrines, o Fe (II) – oktaedrines struktūrų vietas. Priklausomai nuo geležies užimtų vietų, maghemitas gali turėti skirtingos simetrijos struktūrą. Visiškai užlipdytos struktūros maghemitas yra kubinės formos kristalas. Jį galima charakterizuoti rentgeno spindulių struktūriniais tyrimais [2].

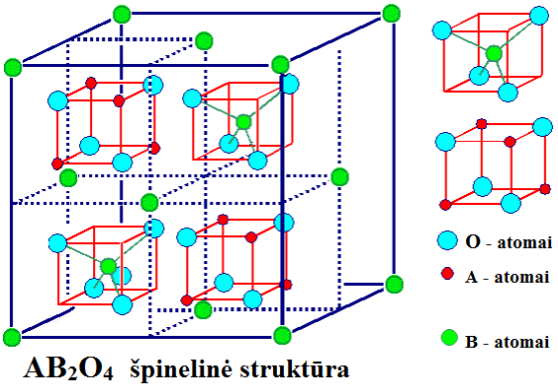

1.1 pav. Kubinė atvirkštinė špinelinė struktūra, kurioje A žymi Fe(II) jonus užimančius 1/4 oktaedrinių tuštumų, o B - Fe(III) jonus lygiomis dalimis pasiskirsčiusius 1/4 oktaedrinėse ir 1/8 tetraedrinėse tuštumose. Redaguota iš [3] literatūros šaltinio.

1 lentelė. *MNd* klasifikacija, struktūra ir charakteristika.

Geležies oksidai	Krist. sistema, nm	Krist. strukt.	Fizikinės charakteristikos		Būdingos smailių charakteristikos	
			Tankis g·cm^{-3}	Tipas	XRD, 2Θ	IR, cm^{-1}
Magnetitas (Fe_3O_4)	Kubinė a=0,8396		5,18	Feromagnetikas	30,12; 35,45; 43,06; 53,44; 56,99; 62,57; 74,04	400; 590
Maghemitas (γ-Fe_2O_3)	Kubinė a=0,8347		4,87	Feromagnetikas	23,86; 26,21; 30,29; 35,72; 43,38; 53,90; 57,45; 63,07; 74,61	400; 450; 570; 590; 630
Hematitas (α-Fe_2O_3)	Heksagoninė a=0,5035 c=1,375		5,3	Antiferomagnetikas	30,26; 35,74; 43,28; 53,95; 57,42; 63,27; 74,68	574-530; 478-456; 352-314

Yra žinoma, jog kobalto ferito ($CoFe_2O_4$) sudėtis stambiakristalinėje būsenoje yra stechiometrinė, tačiau susidarant nanodalelėms yra stebimas nežymus kationų išsimėtymas špinelinėje struktūroje.

1.1.2. *MNd* magnetinės savybės

Geležies oksido nanodalelių svarbiausia savybė yra magnetizmas. Gebėjimas įsimagnetinti ir būti valdomoms išoriniu magnetiniu lauku (H) daro jas patrauklias įvairiems tyrimams. $MeFe_2O_4$ *Nd* turi nuolatinius magnetinius momentus ir pasižymi stipriomis magnetinėmis savybėmis, tad priskiriamos feromagnetikų ($\mu >> 1$), o kai yra mažesnės nei 20 nm - paramagnetikų ($\mu > 1$), medžiagų grupėms. Feromagnetinių medžiagų magnetiniai momentai išoriniame magnetiniame lauke išsidėsto vienas kito atžvilgiu tvarkingai ir lygiagrečiai, o nebeveikiant H, įmagnetėjimas lieka (B_r) (1.2 pav.). Feromagnetikams yra būdingas histerezės kilpos reiškinys: taške 0 domenai yra orientuoti netvarkingai, o medžiaga neįmagnetinta; jos sukeltas vidinis magnetinis laukas $B = 0$. Išorinis magnetinis laukas H, veikdamas feromagnetiką, orientuoja magnetinius momentus savo kryptimi ir magnetinį medžiagos įsisotinimą (M_s).

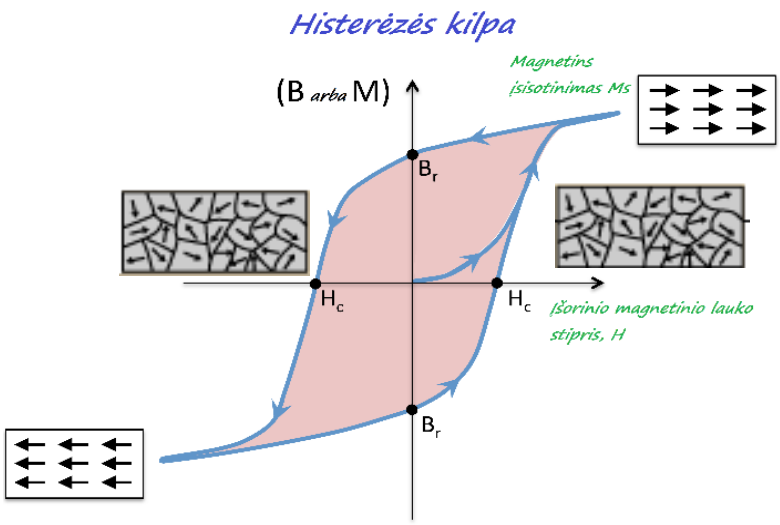

1.2 pav. Histerėzės kilpos schema veikiant feromagnetiką išoriniu magnetiniu lauku (H). Redaguota iš [4] literatūros šaltinio.

Paramagnetinės medžiagos turi mažą, bet teigiamą magnetinį jautrį (χ_m). Tokių medžiagų atomai turi tam tikrą nuolatinį magnetinį momentą. Kai paramagnetikas įnešamas į išorinį magnetinį lauką, jo atomų magnetiniai momentai yra orientuojami to lauko kryptimi. Tačiau šiai orientacijai trukdo šiluminis judėjimas, galintis ją suardyti. Tam tikruose temperatūrų intervaluose paramagnetikų įmagnetėjimas (J) yra proporcingas išorinio magnetinio lauko indukcijai ir atvirkščiai proporcingas absoliutinei temperatūrai. Kai temperatūra žemesnė už T_C, įmagnetėjimas pasiekia įsotinimą, ir tai reiškia, kad atomų magnetiniai momentai yra tvarkingai orientuoti išorinio magnetinio lauko kryptimi. Aukštesnėje negu Kiuri temperatūroje šiluminis judėjimas yra pakankamai intensyvus, kas sąlygoja netvarkingą magnetinių momentų orientaciją - tada feromagnetikai virsta paramagnetikais (5.14 pav.).

Esant aukštai temperatūrai, kuri vadinama blokuojančia temperatūra (T_B), kiekviena nanodalelė tampa atskira magnetine sfera ir pasižymi supermagnetinėmis savybėmis. Šios nanodalelės turi didžiulę magnetinio momento konstantą ir veikia kaip gigantiškas paramagnetinis atomas, greitai reaguojantis į magnetinį lauką. Tokiomis savybėmis pasižyminčios magnetinės nanodalelės yra perspektyvios biomedicinoje, nes aglomeratų susidarymo galimybės kambario temperatūroje yra visiškai nežymios [4].

1.1.3. *MNd* formavimas

Magnetinių nanodalelių formavimasį ir augimą galima aprašyti remiantis *LaMer* ir *Dinegar* suformuota diagrama. Grafiškai ji pavaizduota 1.3 paveiksle. Diagramoje vaizduojamas atomų supakavimas prasideda pirmoje stadijoje persitvarkant reakcijoje dalyvaujančioms prekursorių molekulėms. Pastaroji priklauso nuo aplinkos temperatūros bei mikrobangų, ultragarso ar kitų naudojamų sintezei energijos šaltinių parametrų. Šios fazės metu susiformavusių metalinių atomų koncentracija didėja iki kritinio branduolių kiekio (C_{min}). Pasiekus šią ribą, procesas pereina į kitą fazę, kurios metu pradeda formuotis kristalų užuomazgos. Branduolių augimas vyksta iki įsisotinimo (*super-saturation*) ribos. Laipsniškai sumažėjus atomų koncentracijai, vėliau lėtėja ir kristalų užuomazgų susidarymo bei brandulių augimo procesai. Įdomu tai, jog pasiekus persotinimo būseną, toliau branduolių augimas yra neskatinamas. Tik nuolat tiekiant atomus per

prekursorių skaidymą, branduoliai gali augti vis didesni, kol vėl yra pasiekiama sugeneruotų branduolių paviršiaus atomų ir tirpale esančių atomų pusiausvyra. Nanokristalų augimas ir jų forma priklauso nuo termodinamiškai arba kinetiškai kontroliuojamo režimo. Įvaldžius šį branduolių augimo mechanizmą, atsiranda galimybė kontroliuoti *Nd* formą ir nanokristalų dydį. Paskutinės, III fazės (*Ostwaldo* brandinimas), metu vyksta didesnių nanodalelių brandinimas mažesniųjų sąskaita. Jo metu vidutinis dalelių dydis auga, o esantis tirpale nanodalelių skaičius mažėja.

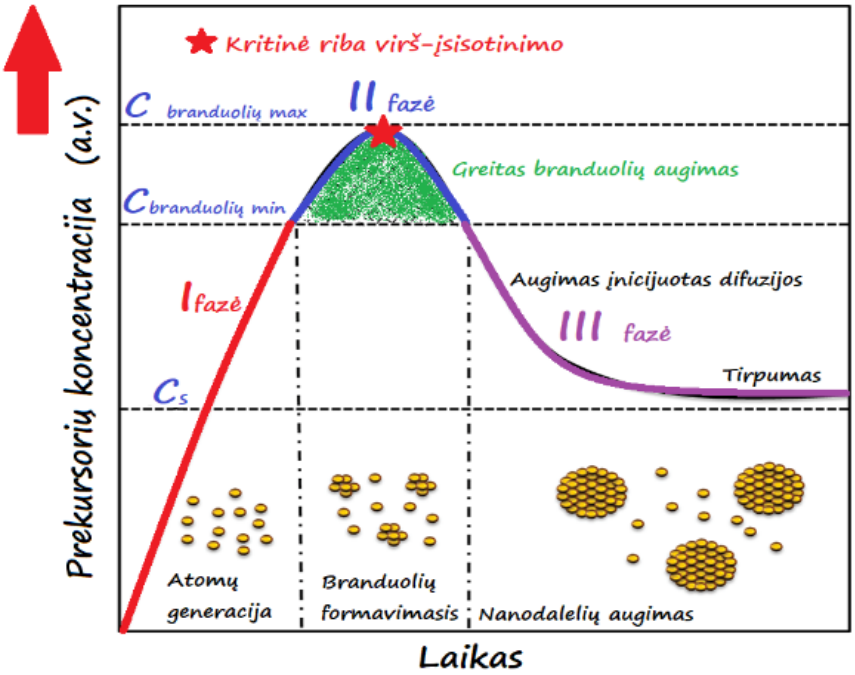

1.3 pav. LaMer diagrama, rodanti atomų koncentracijos kitimą inicijuojant augimą, suformuojant, brandinant bei siekiant tolimesnio augimo remiantis „Ostwald“ principu. Redaguota iš [5] literatūros šaltinio.

1.1.4. *MNd* sintezės metodai

Geležies oksidų nanodalelių sintezės metodas atlieka svarbų vaidmenį jų dydžiui, formai, dydžių dispersijai, paviršiaus energetinei būsenai ir savybėms. Norimo dydžio, sudėties ir magnetinių savybių nanodalelių

sintezei pasiūlyta visa eilė metodų. Trys svarbiausi sintezės metodai parodyti 1.4 pav. Cheminė *Nd* sintezė yra naudojama dažniausiai, todėl beveik 90% paskelbtų mokslinių darbų yra sietini su šiuo sintezės metodu. Populiariausi yra mikroemulsinis, temperatūrinio skaldymo, hydroterminis, solvoterminis, sonocheminis, mikrobangų iniciavimo, ko-nusodinimo, nusodinimo iš garų fazės bei zolio-gelio. Sintezei gali būti naudojami tiek vandeniniai, tiek nevandeniniai tirpalai bei tiek neorganinės, tiek organinės kilmės druskos. Dėl mažesnės kainos ir tvarumo sintezė vandeniniuose tirpaluose laikoma patrauklesne. Tačiau dažniausiai pagrindinė problema ir iššūkis tyrėjams yra monodispersinių *Nd* suformavimas ir aglomeracija dėl jų magnetinės sąveikos.

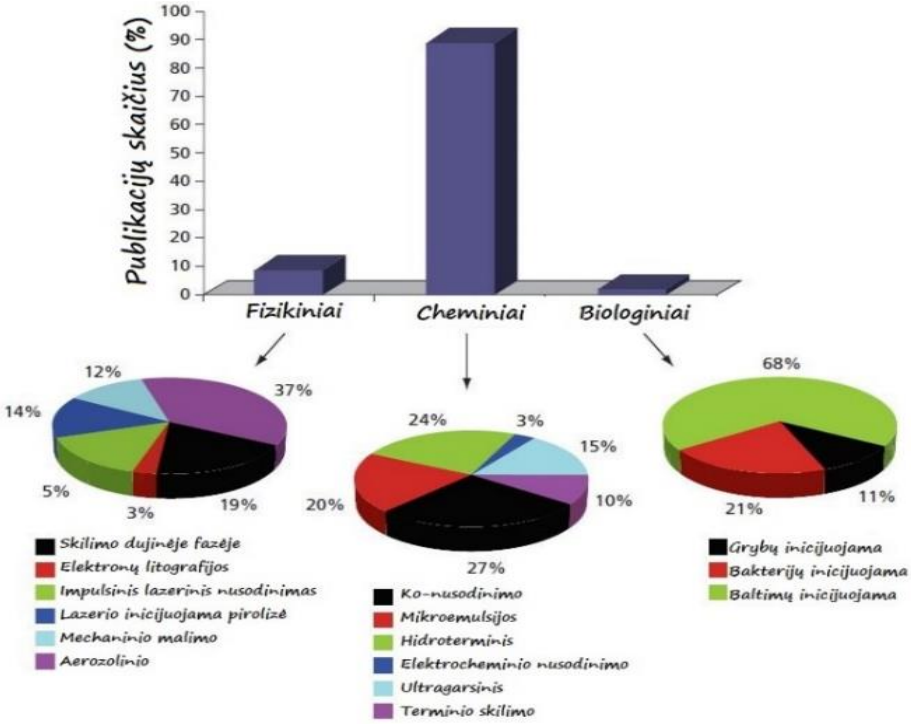

1.4 pav. Magnetinių nanodalelių sintezės metodų, naudotų iki šiol publikuotuose straipsniuose, diagrama. Redaguota iš [6] literatūros šaltinio.

1.1.5. *MNd* sintezė ko-nusodinimo metodu

Šiuo metodu geležies hidroksido branduoliai formuojami ir auginami vandeniniuose tirpaluose. Sintezės metu Me(II) ir Fe(III) su deguonimi junginių nuosėdos susidaro kai į tirpalą, turintį Fe(III) ir Fe(II) ar Me(II) druskų, pridedama šarmo (NH_4OH arba NaOH). Susidariusios drebučių pavidalo geležies oksido nuosėdos yra surenkamos magnetu ar centrifugavimo būdu. Magnetinio skysčio stabilizavimui nuo magnetinės sąveikos papildomai pridedama koncentruoto šarmo, rūgšties, paviršiaus aktyvių medžiagų ar polimerinių darinių [7].

Ko-nusodinimo sintezės cheminė reakcijos lygtis yra:

$$Me^{2+} + 2Fe^{3+} + 8OH^- \rightarrow MeFe_2O_4 + 4H_2O$$

Iki šiol ko-nusodinimo sintezės metodas yra naudojamas tada, kai siekiama suformuoti norimo dydžio ir magnetinių savybių *Nd* [8].

Žinoma, kad Fe_3O_4 bei kitų feritų *Nd* dydis, paviršiaus ir magnetinės savybės priklauso nuo jų sintezei naudotų dvivalenčių metalų ir trivalentės geležies druskų prigimties (chloridų, sulfatų, nitratų, perchloratų ir kt.), tirpalo ruošimo sąlygų, terpės pH, temperatūros, maišymo intensyvumo, trukmės, aplinkos ir tirpalo koncentracijos [9, 10].

Nd branduolių susidarymas ko-nusodinimo reakcijos metu vyksta dviem stadijomis (1.3 pav.) [11, 2]. Pirmosios (staigios ir nekontroliuojamos) metu pradeda formuotis kristalų užuomazgos, o reagentų koncentracija pasiekia kritinę, vadinamą ,,virš įsisotinimo'' (*super-saturation*) būseną. Antroji stadija dėl sulėtėjusios reakcijos komponentų difuzijos užsimezgusios nanodalelės paviršiaus link yra lėta, todėl šioje stadijoje reakciją galima kontroliuoti lengviau [12].

Dar 1980 m. Sugimoto ir Matijevic panaudojo skirtingus oksiduojančius agentus ir pastebėjo, jog kiekvienas jų veikia vis kitaip, susidarant skirtingų dydžių sferinėms dalelėms [13]. Toks pats rezultatas buvo gautas tada, kai geležies ir geležies hidroksido vandeniniai tirpalai buvo brandinami stecheometriškai [14]. Nustačius, kokią įtaką daro skirtingi faktoriai bandoma susintetinti sferines, kubines ir kt. formų vienodesnio dydžio (monodispersines) magnetines *Nd*, nes vienodo dydžio nanodalelės yra itin paklausios tolesniam jų panaudojimui nanomedicinoje bei katalizėje [15]. Be to, kontroliuodami *Nd* dydį mokslininkai gali patikimiau atskleisti nuo nanodalelių dydžio priklausančias fizikines, magnetines ir chemines kristalo struktūrines savybes [16]. Kai geležies oksido *Nd* dydis tampa mažesnis nei

20 nm, jos priskiriamos superparamagnetinėms medžiagoms. Didesniosios po įmagnetėjimo turi savitą išliekamąjį įmagnetėjimą ir yra feri/feromagnetinės medžiagos [17].

Pastebėta, jog geležies oksido magnetinių *Nd* skersmuo mažėja, didėjant sintezės terpės joninei jėgai ir pH vertei. Abu šie parametrai daro įtaką ir susidariusių magnetinių *Nd* paviršiaus elektrostatiniam krūviui. Šios sintezės metu dažniausiai naudojamas tirpalų pH intervalas yra nuo 8 iki 14, nes deguonies aplinkoje ir esant Me^{2+}/Fe^{3+} koncentracijoms santykiu 1:2 tik šiame diapazone yra pilnai pasiekiamas druskų iškritimas į nuosėdas. Keičiant pH vertę buvo nustatyta, jog galima reguliuoti susidarančių sferinių *Nd* dydį nuo 2 iki 15 nm [18, 19]. Taip pat yra atlikta tyrimų, parodančių, kaip magnetito *Nd* vidutinis dydis priklauso nuo nusodinimo terpės rūgštingumo [20, 21]. *Nd* dydis mažėja, kai padidėja reakcijos terpės temperatūra, nes reakcijos temperatūros didinimas sumažina magnetinio branduolio aglomeracijos laipsnį ir tuo pačiu – *Nd* dydį. Tačiau aukštoje temperatūroje dalelių polidispersiškumas išauga, kas grindžiama *Nd* judrumo ir susidūrimo suintensyvėjimu karštuose tirpaluose bei aglomeracija [22, 23]. Tą pačią išvadą padarė ir kiti tyrėjai [11, 24, 25].

Ko-nusodinimo metodu susintetintų geležies oksido *Nd* magnetinės savybės priklausomai nuo jų dydžio bei stabilumo labai skiriasi. Tuo pačiu nepanašios ir jų panaudojimo galimybės. Todėl 2 - 15 nm dydžių *Nd* siekiama atrinkti į ultra-smulkių (0.5 - 2 nm), smulkių (2 - 5 nm) ir 5 - 15 nm dydžių frakcijas. Siekiant sumažinti ir visiškai išvengti *Nd* agregavimo ir padidinti jų stabilumą sintezės metu, buvo pradėti naudoti papildomi augimo reguliatoriai. Naudojantis jais buvo gautos monodispersinės ir stabilesnės *Nd*.

Norint išvengti magnetinių *Nd* agregavimo siekiama, kad reakcijos metu pusiausviroji reakcijos pH vertė nesikeistų. Tai pasiekiama didinant pradinį sintezės tirpalo pH. Be to pusiausviroji pH vertė turi būti artima tirpalo *Nd* nulinio krūvio taškui (pH_{pzc}). Pavyzdžiui, maghemito nanodalelių iškritimas į nuosėdas esant pH=2. Siekiant išsaugoti dalelių monodispersiškumą, šiuo metu naudojami gelių tinklai ar pūslelės. Jos atskiria *Nd* vieną nuo kitos. Stabilumui padidinti, *Nd* dengiamos silicio kserogeliu, elastano, polistireno, poliakrilo ir kitais kopolimerų sluoksniais [25].

Mokslinėje literatūroje sutinkama įvairių pasiūlymų, kaip būtų galima pasigaminti superparamagnetinių feritų nanodalelių (*SPIONs*). Tai nanometrinio dydžio magnetinių geležies oksido, maghemito (γ-Fe_2O_3), magnetito (Fe_3O_4) ir feritų ($MeFe_2O_4$) *Nd*.

1.1.6. *MNd* sintezė terminio skaldymo metodu

Plačiai naudojamas magnetinių bei superparamagnetinių geležies oksidų *Nd* sintezės metodas yra terminis organinių prekursorių, kaip antai $[M^{n+}(acac)_n]$, kur (M = Fe, Mn, Co, Ni, Cr, o n = 2 arba 3, acac=acetylacetonatai) [26], $M_x(cup)_x$ (cup=N-N-nitrozofenylhydroksylaminai) [27, 28], karbonilai ($Fe(CO)_5$) [29] ir kt. skaldymas. Sintezė atliekama aukštos virimo temperatūros tirpikliuose. Naudojami: benzylo eteris, etilendiaminas, oleino rūgštis (OA), oleilaminas (OLA), 1, 2-heksadekandiolis (HDD), 1-oktadecenas, 1-tetradecenas ir kt. [30]. Sintezės metu naudojami karbonilai ir paviršiaus aktyvios medžiagos (PAM) sulėtina branduolių susidarymo procesą ir stipriai daro įtaką adsorbcijai ant branduolių ir nanokristalų, kas slopina magnetinių *Nd* augimo procesą.

Šio metodo pagrindinis principas yra sukontroliuoti organinių prekursorių įpurškimo terminį skilimą į verdančius tirpiklius metu (1.5 pav.). Metalinės geležies *Nd* sintetinamos iš $Fe(CO)_5$, poliizobuteno tirpale N_2 atmosferoje palaikant pastovią 170ºC temperatūrą. Priklausomai nuo $Fe(CO)_5$ ir poliizobuteno santykio, *Nd* dydis gali svyruoti nuo 2 iki 10 nm [31]. $Fe(acac)_3$ atveju, terminis skilimas vyksta katijoniniuose metalo centruose, tiesiogiai susidarant geležies oksido nanodalelėms.

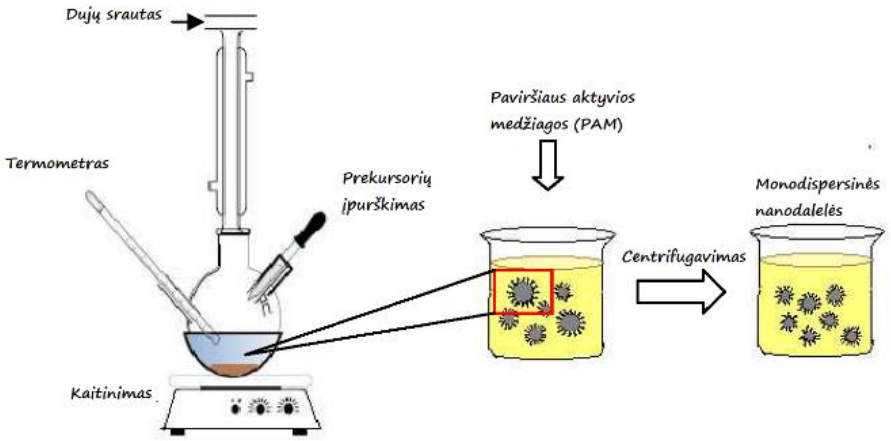

1.5 pav. Nanodalelių sintezės iliustracija organinių prekursorių terminio skaldymo keliu. Redaguota iš [32] literatūros šaltinio.

Hyeon ir kt. ištyrė monodispersinių geležies oksido *Nd* susidarymą iš pigaus ir netoksiško geležies karbonilo ($Fe(CO)_5$). Tuo tikslu buvo ruošiamas Me-oleato kompleksas ištirpinant karbonilą organiniame tirpiklyje ir lėtai kaitinant iki tirpiklio virimo temperatūros, kurioje prasideda monodispersinių geležies oksido kristalitų formavimasis ir *Nd* augimas (1.6 pav.). Vienos sintezės metu buvo gauta per 40g monodispersinių geležies oksido *Nd*, nenaudojant jokių *Nd* augimo stabilizatorių. Taip pat buvo pastebėta, jog šiuo sintezės būdu susintetinamų monodispersinių magnetinių *Nd* dydį galima reguiuoti keičiant jų sintezės terpės temperatūrą ir kt. parametrus. 1.6 paveiksle pavaizduotas susintetintų magnetinių nanodalelių dydžių pasiskirstymas nuo 6 iki 20 nm [33].

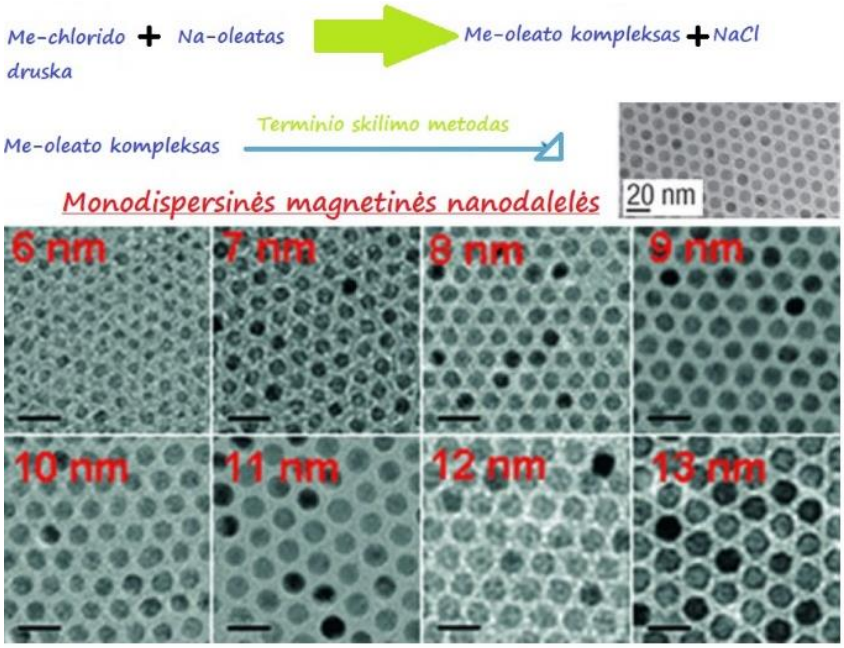

1.6 pav. Terminės sintezės metodu susintetintų magnetinių *Nd* peršvietimo elektroninės mikroskopijos (PEM) vaizdai. *Nd* gautos skaldant metalo-oleatą aukštos virimo temperatūros tirpiklyje. Gauti monodispersiniai 6, 7, 8, 9, 10, 11, 12 ir 13 nm dydžių nanokristalai. Redaguota iš [33] literatūros šaltinio.

Terminio skaldymo metodas naudojamas skirtingos morfologijos geležies oksido magnetinėms *Nd* gauti. Pavyzdžiui, Amara ir kt. susintetino Fe_3O_4 nanokubus ir nanosferas keičiant feroceno ir polivinilpirolidono (PVP) kiekius mišinyje. Aprašytu metodu sintezė vykdoma vienu etapu ir yra paprasta [34]. Demortière kartu su savo grupe taip pat ištyrė monodispersinių geležies oksido nanokristalų morfologiją ir dydžių pasiskirstymą sintetinant *Nd* terminio skilimo metodu. Jų darbo rezultatai įrodė, jog panaudojant skirtingus tirpiklius ir paviršiaus aktyvias medžiagas galima reguliuoti *Nd* dydį nuo 2,5 iki 14 nm (1.7 pav.) [35]. Dėl ženklios paviršiaus energijos geležies oksido nanodalelės įprastai yra energetiškai nestabilios. Taigi, atlikus *Nd* sintezę yra sunku išlaikyti visą sistemą stabilią bei nekeičiančią savybių. Sistemos dispersiškumas lemia dalelių aglomeraciją. Šioje sąveikoje stipriai veikia Van der Valso jėgos. Suspensijose visos dalelės yra linkusios agreguoti, o mažindamos savo paviršiaus energiją jos išauga iki mikrometrinių dydžių.

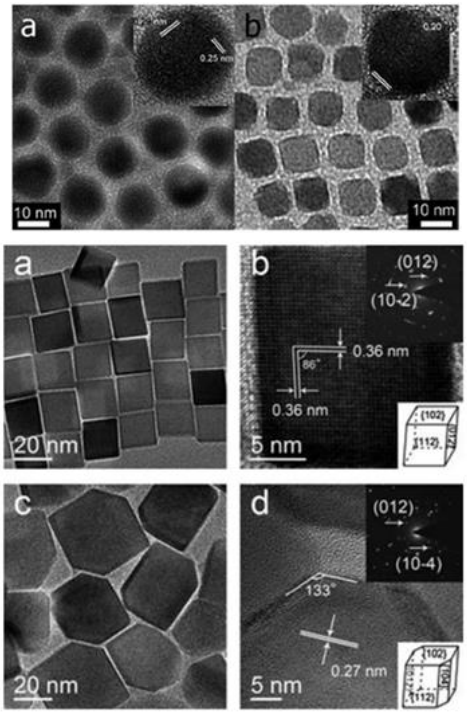

1.7 pav. Skirtingų formų ir dydžių magnetinių *Nd* aukštos skiriamosios gebos PEM vaizdai: a) sferinės, b) kūbinės ir c) šešiakampės. Redaguota iš [35] literatūros šaltinio.

Kuo mažesnis *Nd* dydis, tuo daugiau *Nd* turi laisvosios paviršinės energijos ir mažiau aglomeruoja. Ultragarsu maišant nanodalelių tirpalą, purtant, naudojant paviršiaus aktyviąsias medžiagas, keičiant pH, galima susilpninti ar netgi panaikinti *Nd* aglomeraciją [36].

Siekiant išlaikyti kuo stipresnes *Nd* magnetines savybes, dispersiškumą bei padidinti jų funkcionalumą sintezės metu ar po jos, minėtosios *Nd* dažnai papildomai yra veikiamos mažinančiais agregavimą stabilizatoriais.

1.2. Magnetinių geležies oksido nanodalelių *(MNd)* paviršiaus dekoravimas aukso nanokristalais (*AuNd*)

Fe_3O_4 magnetinių nanodalelių paviršiaus padengimas auksu yra svarbus ne tik dėl jų stabilumo, tačiau ir dėl jų tolesnio tikslinio panaudojimo nanomedicinoje: magnetinio rezonanso vaizdinimui *in vivo,* vaistų pernašai, audinių atstatymui, hipertermijai ir kt. [37, 38]. Auksas ant *Nd* paviršiaus suteikia galimybę patikimai prikabinti prie magnetinės *Nd* paviršiaus įvairias biologines molekules, vaistus ir žymenis. Tai lėmė ženklų magnetinių *Nd* sintezės ir jų paviršiaus funkcionalizavimo auksu tyrimų augimą pastarajame dešimtmetyje.

Tolygiam ir valdomam magnetinių nanodalelių paviršiaus padengimui aukso sluoksniu ar Au nanodalelėmis, didelę reikšmę turi magnetinių nanodalelių prigimtis (sudėtis ir struktūra), sintezės metodas, naudotų *Nd* augimo stabilizatorių sudėtis ir jų savybės. Nepaisant daugybės siūlymų, tolygus padengimas magnetinių *Nd* paviršiaus auksu šiuo metu išlieka problema, kuri itin būdinga didelio paviršiaus ploto SPION nanodalelėms. Todėl magnetinių *Nd* tolesnė panaudojimo specifika kelia griežtus reikalavimus jų savybėms: cheminei sudėčiai, dalelių dydžių dispersijai, magnetinių savybių stabilumui ir adsorbcinėms savybėms.

1.2.1. *MNd* paviršiaus dekoravimas *AuNd* tiesioginės redukcijos metodu

Magnetito ir maghemito *Nd* paviršiaus auksavimui buvo pasiūlyta panaudoti hidroksilaminą [39], natrio borohidridą [40], bei natrio citratą [41]. Tačiau naudojant šiuos reduktorius dažnai po reakcijos susidaro pavieniai aukso kristalai tik tirpale, o *Nd* paviršius nesidengia auksu [42]. 2001 m. Cui‘s mokslininkų grupė paskelbė publikaciją, kurioje siūloma magnetines *Nd* dengti auksu redukuojant $[AuCl_4]^-$ jonus hidroksilaminu. Prieš redukuojant

Au^{3+} jonus 9 nm skersmens maghemito (γ-Fe_2O_3) *Nd* paviršiuje, pasiūlyta maghemitą oksiduoti iki Fe_3O_4 tuo pačiu hidroksilaminu [43, 44]. Šis metodas su įvairiomis modifikacijomis buvo sėkmingai naudojamas smulkių Fe_3O_4 ir γ-Fe_2O_3 *Nd* paviršiaus padengimui. Kitame darbe magnetinių *Nd* paviršių pirmiausia buvo siūlyta apdoroti 0,1 M tetrametilamonio hidroksido tirpalu, o auksą turinčius jonus redukuoti hidroksilaminu [45]. Dar kitu siūlymu iš pradžių magnetinės *Nd* buvo patalpintos į ultragarsinę natrio citrato tirpalo vonelę citrato anijonų adsorbcijai. Aukso redukcija buvo sukeliama į tirpalą įpilant NH_2OH, HCl pertekliaus ir 1% $HAuCl_4$, pakartojant procedūrą kelis kartus per 10 minučių. Teigiama, kad taip galima gauti auksu dengtas magnetito *Nd*, kurių skersmuo siekia 60 nm [46]. Daugiafunkcinių magnetinių geležies oksido *Nd* padengimui auksu pasiūlyta Au^+ jonų redukcija natrio citratu [47].

2011 m. Ren ir kt. pateikė siūlymą teigiamai įkrautas mezoporinės paviršiaus struktūros Fe_3O_4 *Nd* padengti aukso sluoksniu, $HAuCl_4$ redukcijai panaudojant $NaBH_4$ tirpalą (1.8 pav.). Šios Fe_3O_4@Au *Nd* pasižymi NIR šviesos absorbcija, todėl, veikiant jas lazerio spindulių pluošteliu, Fe_3O_4@Au *Nd* gautą energiją konvertuoja į šilumą ir gali būti naudojamos fototerminiam vėžinių ląstelių naikinimui [48].

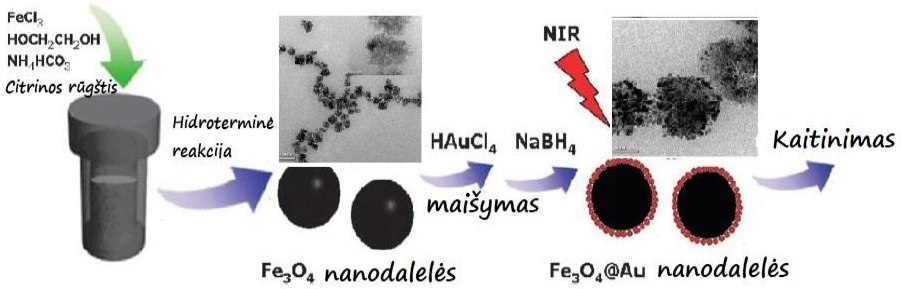

1.8 pav. Fe_3O_4@Au *Nd* sintezės schema. Redaguota iš [48] literatūros šaltinio.

Tiesioginės $HAuCl_4$ redukcijos ant Fe_3O_4 *Nd* paviršiaus metodai yra pigūs ir greiti, tačiau taip vykdant paviršiaus padengimą aukso apvalkalu sunku kontroliuoti Au *Nd* tankį ant Fe_3O_4 *Nd* paviršiaus. Be to, tokiu būdu funkcionalizuojant Fe_3O_4 *Nd* paviršių, neišvengiama *Nd* agregacijos.

1.2.2. *MNd* paviršiaus dekoravimas *auksu* panaudojant organinius reduktorius

Magnetines *Nd*, pagamintas skaldant organinius Fe junginius, pasiūlyta dengti auksu taip pat ir organiniuose tirpaluose. Organinių geležies druskų (karbonilų, oleatų ir acetilacetonatų) pagrindu susintetintas geležies oksido *Nd* siūloma dengti auksu, vykdant acetato jonų redukcija chloroformu, esant oleilaminui. Tankesnio aukso *Nd* apvalkalo suformavimui magnetines *Nd* pasiūlyta apdoroti natrio citrato ir heksadeciltrimetilamonio bromido (CTAB) vandeniniais tirpalais, o po to auksuoti redukuojant aukso jonus aplinkos temperatūros vandeniniame tirpale askorbo rūgštimi ir natrio-triacetoksiborohidridu (STAB). Cho S.J. ir kt. magnetines *Nd* su aktyviomis heksadeciltrimetilamonio bromido (CTAB) paviršiaus funkcinėmis grupėmis pasiūlė dengti auksu redukuojant vandenilio tetrachlorauratą, natrio borohidrido tirpalu. Paviršiaus aukso apvalkalo tankumas buvo reguliuojamas keičiant $HAuCl_4$ koncentraciją tirpale [49]. Wang su bendradarbiais Fe_3O_4 *Nd* paviršiaus padengimui auksu panaudojo aukso acetato druskos tirpalą aukso jonus redukuojant 190 °C temperatūroje oleilaminu [50]. Superparamagnetinėms 10 nm dydžio, gautoms klasikiniu organinės sintezės keliu iš geležies (III) oleato, auksuoti Park ir kt. taip pat siūlo naudoti $HAuCl_4$ redukciją oleilaminu [51]. Tuo tikslu Fe_3O_4@Au *Nd* siūloma prieš dengimą apdoroti ultragarsu 0,1 M CTAB ir 0,1 M natrio citrato tirpale – tokiu būdu pašalinamos nuo jų paviršiaus organinių junginių liekanos, o *Nd* neagreguoja.

Poli-vinilpirolidonas (PVP) yra dar viena polimerinė paviršiaus aktyvioji medžiaga naudojama gauti Fe_3O_4@PVP-Au *Nd*. Rezultatas pasiekiamas dviem etapais. Pirmiausia atliekamas geležies (III) acetilacetonato (Fe_{acac}) terminis skaldymas aukštos virimo temperatūros oktilo eterio, 1,2-heksadekanediolio ir PVP tirpale. Susintetintų Fe_3O_4 *Nd* paviršius auksuojamas redukuojant Au jonus acetato oktilo eterio tirpale tais pačiais reduktoriais. Reakcija vykdoma 2 val. 80 °C ir 2 val. 215 °C temperatūrose [42]. Šis metodas leidžia lengvai kontroliuoti Fe_3O_4 *Nd* dydį, stabilumą bei Au apvalkalo storį. Tačiau vandeniniuose tirpaluose Fe_3O_4@PVP-Au *Nd* yra linkusios agreguoti.

Dėl modifikuotų auksu magnetinių nanodalelių naujų savybių – gero dispersiškumo, pakitusio paviršiaus krūvio bei lengvesnio surinkimo – jos gerai pritaikomos gamyboje, imunologijoje, magnetinio rezonanso tyrimuose, bei optoelektronikoje [52].

Šiame darbe magnetinių nanodalelių paviršiaus dekoravimui auksu bei padengimui aukso luobele buvo sukurti nauji originalūs keliai. Tam sėkmingai buvo ištirtos ir panaudotos tiek magnetinių Nd stabilizavimui, tiek auksavimui įvairios aminorūgštys. Pasiūlytas proceso mechanizmas.

Literatūroje skelbti magnetinių nanodalelių auksavimo būdai, sintezių ypatumai ir *Nd* savybės detaliau aprašytos mūsų apžvalgoje, publikuotoje 2019 m. monografijoje A. Jagminas ir A. Mikalauskaite. *Functionalization of Iron Oxide-Based Magnetic Nanoparticles with Gold Shell. In: Xiao-Yu Yang & Nidhi Chauhan (Eds) Photoenergy and Thin Film Materials* (Chapter 15, p. 617-660) 2019. Scrivener Publishing LLC [53].

1.3. Au klasterių (*AuNkl*) sintezės, savybių ir struktūros valdymas

1.3.1. *AuNkl* sintezės metodai

Aukso nanoklasteriai (*AuNkl*) – tai aukso atomų struktūros, kurių dydis mažesnis nei 2 nm. Jie pasižymi specifine, su jų dydžiu susijusia savybe – fluorescencija – ir yra netoksiški lyginant su kvantiniais taškais. Dėl šios priežasties *AuNkl* yra tinkami ne tik bandymams *in vitro*, bet ir *in vivo,* pavyzdžiui biologinių objektų žymėjimams. Fluorescuojantys aukso klasteriai yra sintetinami cheminės redukcijos būdu, dalyvaujant aukso prekursorius stabilizuojančioms ir redukuojančioms medžiagoms. Įprastai Au jonų šaltinis yra chloro (trifenilfosfino) aukso (I) druska [54], reduktoriai – natrio borhidridas ($NaBH_4$), citratai, hidrazino hidratas, fosfonio chloridas (THPC) askorbo arba folio rūgštys [55]. Iš stabilizuojančių *AuNkl* augimą medžiagų minėtini įvairūs tiolatai, baltymai, peptidai, DNR oligonukleotidai, dendrimerai ir daugybė polimerų.

Seniai žinoma, kad tiolines grupes turintys junginiai dėl formuojamos stiprios sąveikos tarp aukso ir sieros junginių gali būti naudojami kaip stabilizatoriai fluorescuojančių *AuNkl* sintezei cheminės redukcijos keliu. Įprastai šios grupės junginiais stabilizuoti *AuNkl* fluorescuoja nuo mėlynos (400 nm) iki artimosios IR (700 nm) šviesos [56]. Dauguma tiolines (S-S) funkcines grupes turinčių medžiagų, kaip antai glutationas (GLT), kaptoprilas [57], dihidrolipo rūgštis [58], dodekanetiolis [59], D-penicilamino (DPA) [60], lipoinė rūgštis [61], merkaptopropiono rūgštis [62], feniletiltiolatas [63], tiolato α-ciklodekstrinas [64], tioproninas [65] yra plačiai naudojamos Au (III)

jonų surišimui ir stabilizavimui, jų redukavimui panaudojant stiprius ($NaBH_4$) ir kt. reduktorius [66, 67, 68]. Tačiau jų suformuoto monosluoksnio dažnai nepakanka tinkamai aukso nanoklasterių fluorescensijai gauti: ji retai viršija 0,1 % kvantinį našumą [69]. Siekdami pagerinti kvantinį *AuNkl* našumą, Liu ir kt. pasiūlė, tiolinių funkcinių grupių agregacija grįstą emisijos stiprinimą (*aggregation-induced emission AIE*) (1.9. pav.). Šis rezultatas buvo pasiektas trimis stadijomis. Pirmiausia buvo gauti Au(I)-S junginių kompleksai. Vėliau, pakartotinai atliekant redukciją ir pridedant pirminių prekursorių, buvo sudaromi Au(0)-Au(I)-S junginių kompleksai. Jų agregaciją valdant etanolio priedais, gautas fluorescensijos kvantinis našumas (*KN*) siekė iki 15 %. Taip pat pastebėta, jog priklausomai nuo GLT ir $HAuCl_4$ koncentracijų santykio, gautų *AuNkl* fluorescensija gali kisti nuo 600 nm iki 800 nm. Įdomu tai, jog skirtinga emisija pasižymintys *GLT-AuNkl* klasteriai yra vienodo 2,5 nm dydžio. Tai reiškia, jog fluorescencijos bangos ilgį galima reguliuoti didinant arba mažinant Au(0)-Au(I)-S junginių kompleksų santykį [70].

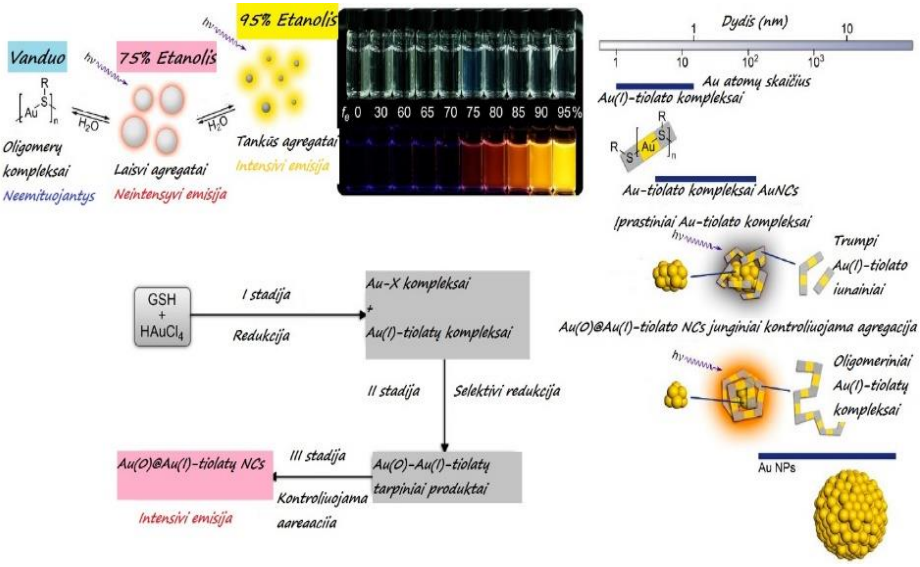

1.9 pav. Aukso nanoklasterių formavimo schema panaudojant trijų stadijų tiolinių funkcinių grupių agregaciją. Redaguota iš [70] literatūros šaltinio.

Fluorescuojančių *AuNkl* paruošimui taip pat naudojamos dendrimerų molekulės: poli-amidoaminas (PAA), polipropileno iminas (PPI) ir kt. Jie

naudojami kaip biokonjugatų kompleksodariai. Naudojant $NaBH_4$ kaip reduktorių, PAA stabilizuoti *AuNkl* pasižymi KN iki 41% 384 ir 450 nm šviesos bangų ilgiuose [71]. Kai PAA/Au molinis santykis keičiamas nuo 1: 1 iki 1:15, gaunami skirtingų Au atomų skaičių turintys *AuNkl*: Au^5, Au^8, Au^{13}, Au^{23} ir Au^{31}. Jų emisija svyruoja nuo UV iki artimosios IR šviesos bangų ilgių, o KN – nuo 10 % iki 70 % [72].

3 lentelė. Aukso nanoklastrių foto-fizikinės savybės (redaguota iš [72] literatūros šaltinio):

AuNCs	Sužadinimo energija (eV)	Emisijos energija (eV)	Kvantinis našumas (%)	Gyvavimo trukmė (ns)
Au_5	0,42	0,45	70	3,5
Au_8	0,54	0,55	42	7,5
Au_{13}	0,38	0,41	25	5,2
Au_{23}	0,21	0,26	15	3,6
Au_{31}	0,20	0,10	10	-

Nustatyta, kad polimerai, turintys daug funkcinių grupių, tokie kaip poli-akrilo rūgštis (PAR) ir poli-metakrilo rūgštis (PMR), gali būti perspektyviais stabilizatoriais fluorescuojančių *AuNkl* sintezėje [73]. Šiais polimerais stabilizuotų *AuNkl* savybės priklauso nuo polimero struktūros, funkcinių grupių įvairovės bei Au ir polimero koncentracijų santykio [74, 75].

Biologiškai aktyvios molekulės, tokios kaip baltymai ir poli-aminorūgštys, taip pat buvo panaudotos fluorescuojančių *AuNkl* gamyboje. Jos pasižymi biosuderinamumu su gyvomis ląstelėmis. 2009 m. Xie su bendradarbiais susintetino fluorescuojančius *AuNkl*, tam panaudodami jaučio serumo albuminą (JSA) kaip redukuojantį ir stabilizuojantį agentą; suspensija buvo laikoma 12 valandų 37 °C temperatūroje [76]. Šis metodas tapo itin patraukliu dėl savo pigumo panaudojus komerciškai prieinamą baltymą ir puikių naujo klasterio savybių. *JSA- AuNkl* talpino 25 Au atomus (Au^{25}), pasižymėjo aukštu KN (~6 %), geru biologiniu suderinamumu ir puikiu fotostabilumu (1.10 pav.). Ši publikacija buvo cituota daugiau nei 1590 kartų. Pasiūlyta sintezė tapo populiariausiu fluorescensinių *AuNkl* sintezės metodu. Be to, ji buvo sėkmingai pritaikyta kitų metalų klasterių sintezei ir tyrimams.

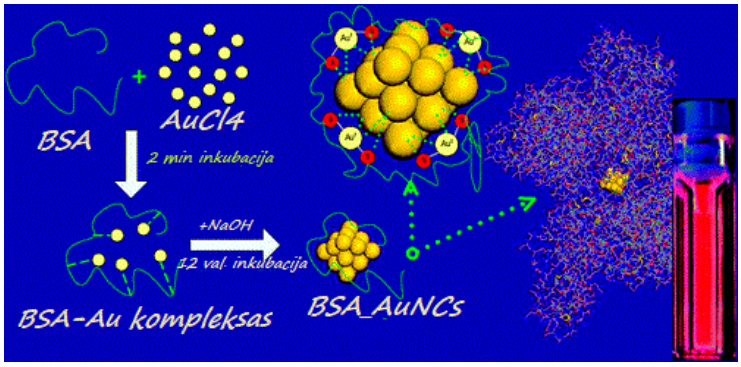

1.10 pav. Raudonai liuminescuojančių aukso klasterių sintezės shema, panaudojant JSA, $HAuCl_4$ redukcijai. Redaguota iš [76] literatūros šaltinio.

Vėliau aukso klasterių sintezei buvo panaudoti ir kiti baltymai: lizocimas [77], DNR-azė I [78], kiaušinių baltymas [79], krienų peroksidazė [80], ovalbuminas [81], insulinas [82], pepsinas [83], ribonuklеazė A [84], transferinų šeimos baltymai [85, 86], tripolis [87] ir denatūruotas jaučio serumo albuminas [88]. Visi susintetinti *AuNkl* pasižymėjo fluorescensija, o jų kvantiniai našumai svyravo nuo 4,3 % iki 56 %. Įdomu tai, kad insulinu stabilizuoti *AuNkl* išlaikė savo biologinį suderinamumą kraujo gliukozės reguliavimo ir *in vivo* tyrimuose.

DNR oligonukleotidai ir nukleotidai taip pat buvo panaudoti vandenilio tetrachloraurato rūgšties reduktoriais *AuNkl* sintezėje. Pavyzdžiui, Liu su bendradarbiais pavyko susintetinti mėlynai fluorescuojančius *AuNkl* su poli-adenino DNR oligonukleotidais esant neutraliam pH ir poli-citozinui, esant rūgštiniam pH reduktoriumi naudojant citratą [89].

Zhangas ir kt. aukso klasterio sintezei stabilizatoriumi panaudojo tioeterio (PMR) polimerą o redukavimui – prekursorių tirpalo ultravioletinį (8W; 365 nm) švitinimą (6 val.). Gauti *AuNkl* pasižymėjo 610 nm šviesos emisija ir 5,3 % kvantiniu našumu (1.11a pav.). Teigiama, kad fotoredukcija, lyginant su chemine, yra pranašesnė, nes sintezei nereikia stiprių reduktorių, tokių kaip natrio borohidridas, o susintetinti *AuNkl* nėra toksiški [90]. Panaudojant PTMP su PtBMA ligandu ir organinių tirpalų su prekursoriais UV švitinimą, buvo gauti ultrasmulkūs Au^5 nanoklasteriai, pasižymintys aukštu KN =20,1 % ir mėlynos šviesos emisija (1.11b pav.). Šių *AuNkl* dydį galima koreguoti keičiant polimero ir Au^+ jonų koncentracijas [91].

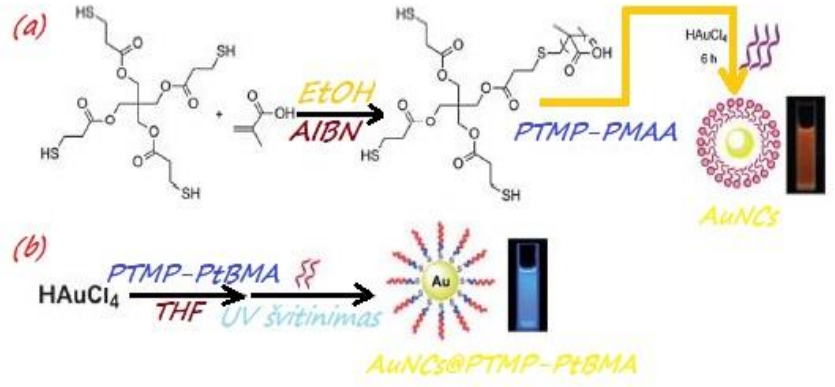

1.11 pav. a) PMR polimero panaudojimo schema raudonai liuminescuojančių *AuNkl* sintezei ir b) ultra smulkių mėlyną šviesą emituojančių *AuNkl* sintezė panaudojant PTMP-PtBMA ligandų ir THF organinių tirpalų prekursorius. Redaguota iš [90] literatūros šaltinio.

Naujausi tyrimai parodė, kad *AuNkl* gali susidaryti bakterijose, grybuose ir augaluose [92]. Metalo klasterių bioredukcija į nanodaleles organizmuose vyksta, jiems siekiant išsivalyti nuo sunkiųjų metalų [93]. Wang ir kt. šį reiškinį pastebėjo vėžio ląstelėse, kuomet navikines ląsteles supantys baltymai redukavo $HAuCl_4$ ir stabilizavo redukcijos produktą [94]. Nustatyta, kad tokios vėžio ląstelių grupės, kaip žmogaus hepatokarcinomos (HepG2) ir leukemijos (K562), spontaniškai gamina fluorescuojančius *AuNkl*, o Au(III) jonų redukcija vyksta ląstelių citoplazmos dalyje. Tačiau *AuNkl* mechanizmą kol kas yra sunku paaiškinti ir tai išlieka perspektyvia tyrimų tema.

Siekiant gauti itin mažų liuminescuojančių aukso nanoklasterių, buvo panaudota ir elektroredukcija. Tokiai *AuNkl* sintezei naudotas homopolimeras, poli (N-vinilpirolidonas) (PVP) [95]. Taip paruošti fluorescuojantys *AuNkl* susideda tik iš dviejų – trijų atomų, todėl laikomi mažiausiais Au klasteriais. Tiriant ultragarsiniu liuminescenciniu metodu nustatyta, jog tokios struktūros yra stabilios ir pasižymi fotoliuminescencija. Jos atveria naujus kelius kuriant naujas nanomedžiagas, aktualias šių dienų nanomedicinos mokslų plėtrai.

Šiame darbe raudonai švytinčių aukso klasterių sintezė tyrinėta naudojant įvairias aminorūgštis ir baltymus. Pirmą kartą aptikta, kad kai kurie maisto papildai gali sėkmingai būti panaudojami raudonai fluorescuojančių klasterių

sintezei. Jų optinės savybės ir kvantinis našumas tik neženkliai nusileidžia Au nanoklasteriams, susintetintiems su JSA ar transferinu.

1.4. Magnetinių geležies oksido *Nd* dekoravimas *AuNkl*

Aukso klasteriai yra itin mažo dydžio nanodariniai, pasižymintys stipria liuminescensija juos žadinant tam tikro ilgio šviesos banga. Ši *AuNkl* savybė yra patraukli siekiant panaudoti teranostikoje. Raudonai liuminescuojantys aukso klasteriai dažniausiai būna stabilizuoti didelės molekulinės masės junginiais: jaučio serumo albuminu [76], laktoferinu [96], žmogaus insulinu [97] ir kt. Jie pasižymi geru fotostabilumu, ilga gyvavimo trukme ir biologiniu suderinamumu su gyvomis organizmų ląstelėmis. Tačiau magnetinių *Nd* konjugacija su fluorescencinėmis aukso nanodalelėmis iki šiol išlieka didele problema dėl *AuNkl* fluorescencijos slopimo ar visiško jos praradimo hibridinėse nanostruktūrose. Sreenivasan tyrėjų grupė pranešė apie novatorišką raudonai liuminescuojančių aukso klasterių prijungimo prie superparamagnetinių *Nd* paviršiaus metodą. Šiam tikslui *AuNkl* buvo susintetinti panaudojus JSA, o superparamagnetinės *Nd* buvo susintetintos hidrotermiškai jas funkcionalizuojant dopaminu [98]. Tyrimų rezultatai apie SPIONs *Nd* ir *AuNkl* konjugaciją ir tikslinę Erlotinib vaisto pernašą į kasos vėžines ląsteles *in vitro* diagnostinuose bei terapiniuose tyrimuose (1.12 pav.) buvo aprašyti 2017 m. Sony su bendraautoriais. *AuNkl* prijungimo prie *SPIONs Nd* paviršiaus ir taikomo vaisto prikabinimo rezultatas buvo pasiektas šiuo keliu:

1) Panaudojus arginino aminorūgštį, kaip sintezės reduktorių bei paviršiaus aktyvų junginį, susintetintos teigiamai įkrautos Fe_3O_4 nanodaleles.

2) Raudonai liuminescuojantys aukso klasteriai buvo susintetinti panaudojant šiek tiek modifikuotą Xie ir kt. metodiką: *AuNkl* sintezei naudotas mikrobangų reaktorius, užtikrinantis jo tolygų bei galingą kaitinimą.

3) *AuNkl* prikabinimas prie SPIONs *Nd* atliekamas ultragarsinėje vonelėje su PBS buferiniu tirpalu, kurio pH=7.

4) Ant neigiamai įkrautų Fe_3O_4@*AuNkl* hibridinių dalelių, jas patapinus ultragarsinėje vonelėje ir nuolat palaikant 25 °C temperatūrą, prikabinant „Erl‘‘ vaisto molekules.

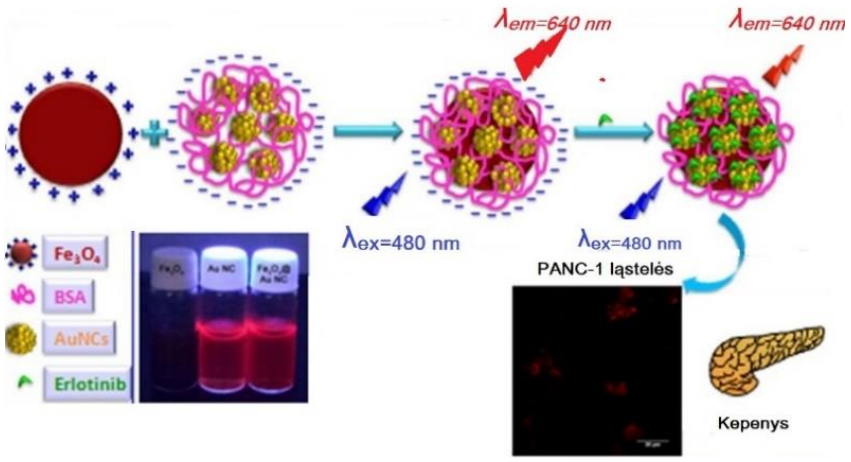

1.12 pav. Fe_3O_4@*AuNkl*@Erl sintezės ir tikslinio panaudojimo PANC-1 kasos navikinių ląstelių diagnostikai ir terapijai schema. Redaguota iš [99] literatūros šaltinio.

Fe_3O_4@*AuNkl*@Erl kompozitų toksiškumo tyrimai su sveikomis kasos ląstelėmis parodė, jog eksperimento metu jų morfologija išlieka nepakitusi, kas patvirtina jų netoksiškumą. Vienok nustatyta, kad infekuotoms vėžinėms PANC-1 ląstelėms (1.12 pav.) jos yra labai toksiškos. Šiais tyrimais dar kartą buvo patvirtinta, kad Fe_3O_4 ir *AuNkl* nanokompozitai gali būti panaudoti teranostikoje [99].

1.5. Magnetinų geležies oksido *Nd* ir *AuNkl* pritaikymas teranostikoje

Mokslininkai nuolatos ieško naujų gydymo būdų, siekdami, kad sukurtų medžiagų veiksmingumas būtų greitas, ekonomiškas ir turėtų kuo mažesnį šalutinį poveikį. Tad pastaruosius 10 metų intensyviai vystoma teranostinės nanomedicinos sritis vadovaujantis idėja kad tinkamas vaistas tinkamam pacientui, tinkamu momentu gali suvaldyti mirtiną vėžį. Todėl teranostikoje kuriamoms medžiagoms šiuo metu yra keliami aukšti selektyvumo reikalavimai. Siekiama panaudoti naujus preparatus infekuotų ląstelių grupių efektyviam aptikimui. Kartu reikalaujama, kad jos pasižymėtų biosuderinamumu su sveikų ląstelių aplinka ir būtų biologiškai suskaidomos į netoksiškus šalutinius produktus [100].

Magnetinių *Nd* ir *AuNkl* moksliniai tyrimai ir pritaikymas daro didelę įtaką teranostikos tyrimų plėtrai bei pažangai. Šiuo metu jau naudojami keli komerciniai preparatai, vienas jų yra ferumoksitolis (Feraheme®). Tai vaistas, skirtas sunkios stadijos mažakraujystės gydymui bei magnetinio rezonanso vaizdinimui. Feraheme® yra nestechiometrinis magnetitas (superparamagnetinis geležies oksidas), padengtas poligliukozės sorbitolio karboksimetileteriu. Bendras koloidinių sferinės formos dalelių dydis yra 17–31 nm. Jo formulė yra $Fe_{5874}O_{8752}C_{11719}H_{18682}O_{9933}Na_{414}$, o molekulinė masė – 750 g/mol [101]. Be to, šiuo metu susperparamagnetinių nanodalelių preparatai ferumoksidas (Endorem®) ir ferukarbotranas (Resovist®) (60 nm dydžio) yra tikslingai naudojami kepenų pažeidimams diagnozuoti [6].

Nors pastarojo dešimtmečio tyrimai rodo geras magnetinių nanodalelių panaudojimo galimybes baltymų atskyrimui ir gryninimui, dar nėra sukurta tikslių ir pigių sistemų šių metodų taikymui praktikoje.

1.5.1. Auksu dekoruotų *MNd* ir *AuNkl* panaudojimas diagnotisniuose tyrimuose

Auksu dekoruotos ir tikslingai funkcionalizuotos geležies oksido *Nd* gali laisvai patekti į ląstelių vidų difuzijos, pinocitozės ar kitais medžiagų transporto per membraną keliais. Dėl šio judėjimo netoksiški nanodalelių hibridai yra plačiai taikomi genų terapijai[102]. Esant galimybei *Nd* valdyti išoriniu magnetiniu lauku, jos pritaikomos tikslinėje vaistų pernašoje į pažeistų ląstelių vietas [103]. Magnetinės *Nd* sėkmingai panaudojamos kontrasto pagerinimui magnetinio rezonanso vaizdinimo (MRV) *in vivo* tyrimuose ir vėžinių ląstelių šalinimo hipertermijoje [104, 105, 106, 107]. Šioje srityje auksu dekoruotos magnetinės *Nd* yra pranašesnės už nedekoruotas Fe_2O_3 *Nd* dėl 4–5 kartus greičiau pasiekiamos 42 °C temperatūros, procedūrai naudojant tas pačias *Nd* koncentracijas. Šis efektas siejamas su aukso sluoksniu, esančiu ant *Nd* paviršiaus, – jame greičiau ir tolygiau akumuliuojama šiluma, išskiriama branduolio kintamo magnetinio lauko aplinkoje. Nustatyta, kad maghemito *Nd* yra citotoksiškesnės tirtoms ląstelių rūšims. Auksu dengtų *Nd* biosuderinamumas yra siejamas su Au apvalkalu, – dėl jo tiesioginio ląstelių membranos ir dalelių šerdies (Fe_2O_3) sąlyčio nėra ir ląstelių viduje nesukeliamas deguonies laisvojo radikalo ($O_2^{\bullet-}$) oksidacinis stresas. Paminėtina, kad auksu dengtos superpamagnetinės *Nd* yra

priskiriamos naujos kartos daugiafunkcinėms hibridinėms *Nd* vėžinių ląstelių teranostikai [108, 109].

Magnetinio rezonanso vaizdinime (MRV) vienodo dydžio aukso apvalkalą turinčios superparamagnetinės *Nd* yra sėkmingai naudojamos kaip neigiamą T2 kontrastą gerinančios medžiagos. Aukso sluoksnį, esantį ant Fe_3O_4 *Nd* paviršiaus, galima funkcionalizuoti prikabinant aptamerus [110], organines molekules [111], padengiant silicio apvalkalu [112], polimeriniais junginiais [113] ir t.t. Dėl jų nanodalelės tampa potencialiomis hibridinėmis kontrastinėmis molekulėmis. Li su bendradarbiais ištyrė Fe_3O_4@Au *Nd* daromą įtaką pelių HeLa navikinių ląstelių *in vivo* vaizdavime. Po tikslinės Fe_3O_4@Au *Nd* injekcijos per 10 minučių HeLa navikinių ląstelių sritys tapo 34,61 kartų tamsesnėmis, taip žymiai padidindamos kontrastą sveikų ląstelių atžvilgiu. Dėl geros rentgeno spindulių absorbcijos šios magnetinės *Nd* gali būti naudojamos ir kaip kompiuterinės tomografijos kontrastinės medžiagos, turinčios dvigubą modalumą [114, 115]. Cai mokslinė grupė sukūrė Fe_3O_4@Au *Nd* biosuderinamus poli-g-glutamo (PGA) ir poli-L-lizino (PLL) rūgščių apvalkalus. Magnetinio rezonanso (MR) ir kompiuterinės tomografijos (KT) tyrimai parodė, jog ši Fe_3O_4@Au@PGA/ PLL *Nd* sistema pasižymi ne tik geresniu T2 kontrastu *in vivo* vėžinėse ląstelėse, bet ir stipresniu MR tiriant poodinius audinius ir kepenis *in vivo* (1.13 pav.) [116].

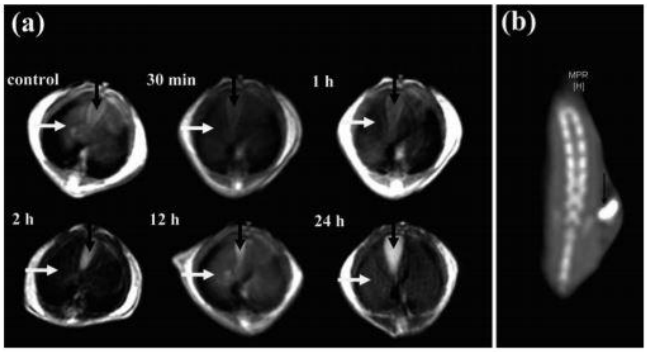

1.13 pav. Pelių kepenų audinio T2 kontrasto MR vaizdai prieš ir po 30 min., 1, 2, 12 ir 24 val. Fe_3O_4@Au@PGA/ PLL *Nd* injekcijos į pelės veną (a). (b) KT poodinio audinio vaizdas po Fe_3O_4@Au@PGA/ PLL *Nd* injekcijos į pelės nugarinę sritį. Redaguota iš [116] literatūros šaltinio.

1.5.2. Auksu dekoruotų *MNd* ir *AuNkl* aktyvumo tyrimai

Dėl mikroorganizmų sparčių mutacijų ir gerėjančio jų atsparumo natūraliems ir sintetiniams antibiotikams, antimikrobinių medžiagų kūrimas šiuo metu yra ypač aktualus. Antimikrobinių medžiagų veikimas įprastai yra klasifikuojamas pagal bakterijų augimo slopinimą priskiriant bakteriostatinei arba baktericidinei veiklai.

Koloidinis auksas nuo seno yra žinomas kaip medžiaga, turinti antibakterinių savybių ir naudojama išorinėms žaizdoms ir infekcijoms gydyti. Jo hibridinės struktūros su magnetinėmis nanodalelėmis mokslininkams atveria naujas galimybes kuriant antimikrobinius agentus skirtingoms bakterijų rūšims. Harush-Frenkel su bendradarbiais išnagrinėjo baktericidinį *Nd* veikimą ir pastebėjo, kad neigiamą krūvį turinčių nanodalelių endocitozė yra ne tokia efektyvi, kaip turinčių teigiamą. Teigiamą krūvį turinčios nanodalelės lengvai patenka į ląstelių įlinkius kuriuos formuoja membranos išorėje esantys receptoriai. Jos yra gimininingesnės membranai, todėl lengviau patenka į ląstelių vidų [117]. Siekiant išsiaiskinti įvairių nanokompozitų antimikrobinį mechanizmo veikimą su tam tikros prigimties mikroorganizmais, labai svarbu įvertinti Fe_3O_4@Au *Nd* savybes ir jų specifiškumą, kurie daro didžiausią įtaką ląstelių citotoksiškumui. Šios savybės priklauso nuo *Nd* dydžio, morfologijos, sintezės būdo, funkcinių grupių apsupties ir stabilumo.

Pastebėta, jog Fe_3O_4@Au *Nd* veikia baktericidiškai tiek gramteigiamas, tiek gramneigiamas bakterijas, visiškai sunaikindamos jų augimo bei dauginimosi sistemas. Nanodalelių patekimas į ląstelę ir toksiškumas taip pat priklauso nuo apvalkalo krūvio ir elektrostatinės nanodalelės, ir bakterijos sąveikos. Išskiriami trys keliai, kuriais nanodalelės patenka į ląsteles: 1) mechaniškai pažeisdamos ląstelės membraną, 2) endocitozės ir fagocitozės metu ir 3) difuzijos per bakterijų membraną keliu, kur patekusios jas veikia toksiškai (1.14 pav.) Nustatyta, kad nanodalelės poveikio efektyvumas priklauso nuo jos cheminės sudėties ir bakterijos tipo [118].

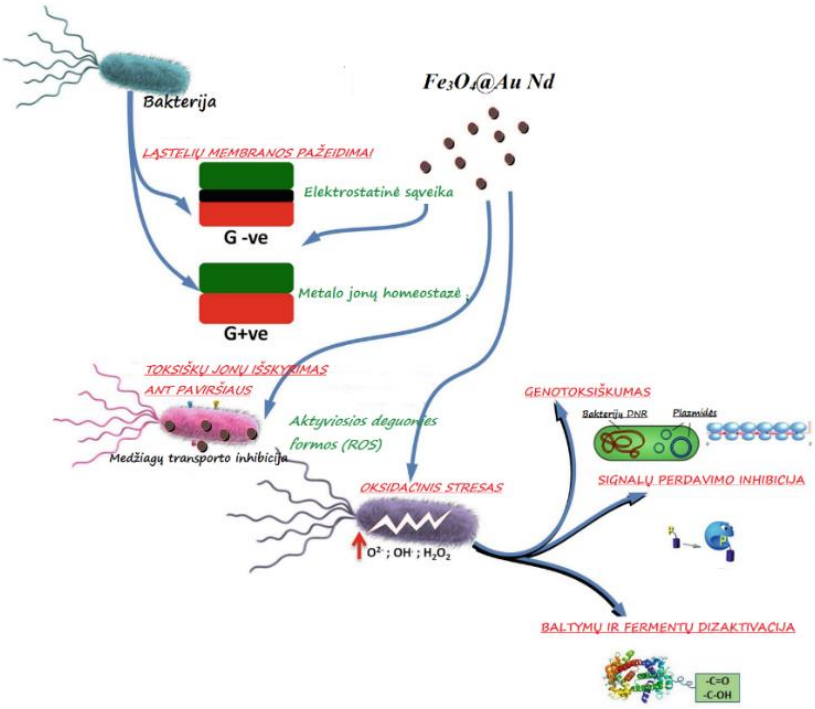

1.14 pav. Fe_3O_4@Au *Nd* baktericidinio poveikio iliustracija. Redaguota iš [119] literatūros šaltinio.

Yra žinoma, jog magnetinės *Nd* padengtos sidabru bei auksu gali būti baktericidinės [120, 121]. Pavyzdžiui, Ahmed ir bendradarbiai sukūrė Fe_3O_4@Au ir Fe_3O_4@Ag *Nd* kompozitus, kurie pasižymėjo baktericidiniu poveikiu ypač aukštu patogeniškumu pasižyminčioms bakterijų rūšims. Šios bakterijos yra aptinkamomis vandens ir nuotekų telkiniuose. Baktericidinės Fe_3O_4@Au ir Fe_3O_4@Ag *Nd* buvo susintetintos hidroterminės sintezės keliu, ant jų paviršiaus prikabinant tiokarbamido ir formaldehido funkcines grupes ir vėliau jas panaudojant Ag (I) ir Au (III) redukcijai. Fe_3O_4@Au ir Fe_3O_4@Ag *Nd* antimikrobinis aktyvumas buvo tirtas prieš ir po Ag(I) arba Au(II) ekspozicijos su *Escherichia coli*, *Salmonella typhimurium* ir *Pseudomonas aeruginosa* gramneigiamomis bei gramteigiamomis *Listeria monocytogenes*, *Staphylococcus aureus*, *Enterococcus faecalis* ir *Bacillus subtilis* bakterijų bei *Candida albicans* grybeliniu patogenais. Tyrimo metu nustatyta, jog abi *Nd* grupės yra toksiškos tirtoms mikroorganizmų rūšims, skiriasi tik tirtų nanodalelių mažiausios inhibuojančios koncentracijos (MIK) vertės.

Nustatyta MIK Fe_3O_4@Ag *Nd*: 1,5, 2,0, 1,5, 1,0 ir 2,5 mg/ml, o Fe_3O_4@Au *Nd*: 6,0, 4,0, 4,0, 4,0 ir 6 mg/ml atitinkamai po 40 min. kontaktavimo su *Escherichia coli*, *Salmonella typhimurium*, *Listeria monocytogenes*, *Staphylococcus aureus* ir *Candida albicans* patogenais. *Staphylococcus aureus* Xen 30 ir *Pseudomonas aeruginosa* Xen 5 žinomos kaip antibiotikui – Meticilenui – atsparios bakterijų atmainos. Jų sunaikinimui Burki ir kt. sukūrė Fe_3O_4@Au *Nd* ir vantomicino (VAN), kolistino (COL) ir kationinių antibakterinių receptorių (CAPs) kompozitus (1.15 pav.) [122].

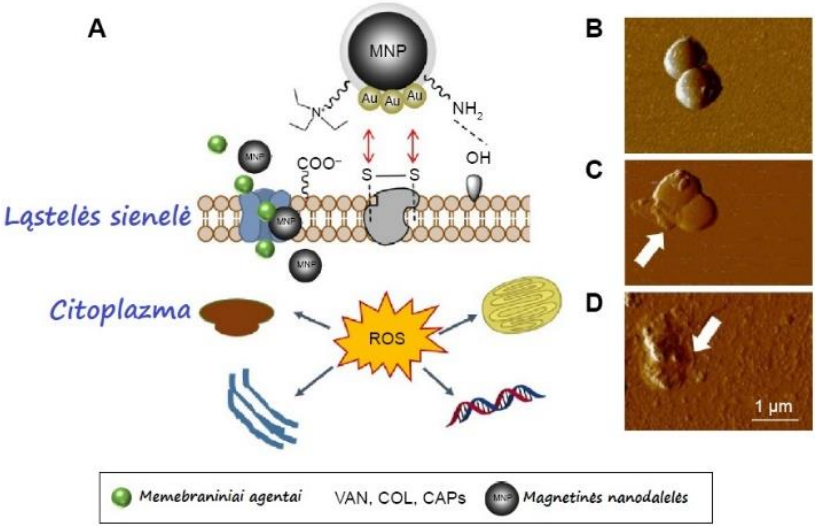

1.15 pav. A) Fe_3O_4@Au *Nd*, padengtų vantomicino (VAN), kolistino (COL) ir kationinių antibakterinių receptorių (CAPs) kompozitais, sinergetinio mechanizmo schema ir atominės jėgos miksokopijos vaizdai (AJM) B) *Staphylococcus aureus* Xen 30, C) vaizdas po 10 µg/ml Fe_3O_4@Au@CAPs *Nd* injekcijos ir D) *Staphylococcus aureus* Xen 30 membranos destrukcijos schema ir vaizdas pradėjus veikti Fe_3O_4@Au@CAPs *Nd*. Redaguota iš [122] literatūros šaltinio.

Žinia, kad auksu padengtos magnetinės *Nd* taip pat gali būti naudojamos bakterijoms identifikuoti, jas sukoncentruoti ir pašalinti veikiant išoriniu magnetiniu lauku. Pavyzdžiui, Wang ir kt. susintetino $MnFe_2O_4$@Au *Nd* su paviršiuje prikabintais specifiniais antikūnais prieš *Staphylococcus aureus*. Jų pagalba mikroorganizmų aptikimo riba siekė iki 10 ląstelių/ml [118].

Antimikrobinės mūsų susintetintų magnetinių nanodalelių ir aukso ultra smulkių nanodalelių savybės buvo ištirtos kelių antibiotikams itin atsparių

patogenų atžvilgiu. Gauti nauji rezultatai publikuoti 2019 metais prestižiniame *Journal of Material Science and Engineering žurnale C.*

Darbe susintetintų auksuotų magnetinių *Nd* tyrimai vėžinių ląstelių diagnostikai buvo vykdomi Nacionaliniame vėžio institute, tačiau šiame darbe jie nepateikiami.

2. METODAI IR MEDŽIAGOS

2.1. Geležies oksido magnetinių *Nd* sintezė ir paviršiaus dekoravimas auksu

Nanodarinių sintezei buvo naudojami chemiškai grynos $CoCl_2$, $Fe_2(SO_4)_3 \cdot 5H_2O$, $HAuCl_4 \cdot 3H_2O$ medžiagos. Magnetinių nanodalelių augimo reguliatoriais ir stabilizatoriais naudotos švarios diglikolio ir citrinos rūgštys, dauguma aminorūgščių ir dopamino hidrochloridas. Reakcijos tirpalų pH buvo reguliuojamas dedant pačių išvalytą NaOH tirpalą. Sintezė buvo vykdoma argono dujų aplinkoje. Tirpalų ruošimui naudotas distiliuotas / dejonizuotas vanduo. *Nd* buvo ištirpinamos HCl rūgšties tirpaluose, o Co ir Fe kiekiai vėliau buvo analizuojami induktyviai susietos plazmos optine emisine spektroskopija.

2.1.1. 2 ir 5 nm $CoFe_2O_4$ *Nd* sintezė

Kobalto ferito *Nd* buvo gaminamos termostatuojamame 80 °C temperatūros stiklo reaktoriuje tradiciniu ko-nusodinimo metodu. Sintezės metu tirpalas 3 val. nuolat buvo maišomas argono dujomis. Tirpalų ruošimui naudotos $CoCl_2$ ir $Fe_2(SO_4)_3$ druskos ir 75 $mmol \cdot L^{-1}$ diglikolio rūgšties tirpalas; bendra metalų druskų koncentracija – 100 $mmol \cdot L^{-1}$. Siekiant gauti stechiometrinę *Nd* sudėtį, pradinės $CoCl_2$ ir $Fe_2(SO_4)_3$ druskų koncentracijos parinktos 1,1:1 santykiu [123]. Pridedant 5 $mmol \cdot L^{-1}$ NaOH tirpalą ir maišant buvo pasiekiamas pH 12,1 – 12,5. Gautos $CoFe_2O_4$ *Nd* buvo centrifuguojamos 10867 x g, 3 min. ir kruopščiai praplaunamos 5 kartus po 10 mL dejonizuotu vandeniu. Susidarę supernatantų tirpalai buvo sujungiami į vieną. Juose esančios ultra smulkios ir smulkios *Nd* frakcijos buvo džiovinamos 60 °C temperatūroje ir charakterizuojamos.

2.1.2. 15 nm $CoFe_2O_4$ *Nd* sintezė

15 nm $CoFe_2O_4$ *Nd* sintezė vykdyta 25 ml talpos nerūdijančio plieno – teflono autoklave, pagal 2.1. lentelės I dalyje aprašytą receptūrą. Sintezė truko 10 val. 130 °C temperatūroje keliant 10 °C/min greičiu. $CoFe_2O_4$ *Nd* buvo plaunamos dejonizuotu vandeniu ir nusodinamos naudojant magnetą.

Itin smulkios frakcijos produktai buvo surinkti panaudojant etanolio tirpalą ir ilgesnį laiką centrifuguojant. Sintezės produktai džiovinti 60 °C temperatūroje (2.1 lentelė I dalis).

2.1 lentelė. $CoFe_2O_4$ *Nd* sintezės bei jų dekoravimo *AuNd* reagentai ir sąlygos.

I Sintezės sąlygos	**2,0 nm***	**~ 5,0 nm****	**~15 nm****
Druskos		$CoCl_2$ ir $Fe_2(SO_4)_3$	
Druskų santykis, mmol·L^{-1}		50:50	
Augimo reguliatorius,		Diglikolio rūgštis	
mmol·L^{-1}		75	
Reakcijos pH		12,2	
Temperatūra, °C	80		130
Laikas, val.	3		10
Reaktorius	Ar, stiklo		Teflono
pH po praplovimo	7		7
II Padengimo auksu sąlygos			
D, L-metionino kiekis, mmol·L^{-1}		15	
$HAuCl_4$ konc., mmol·L^{-1}		30	
Temperatūra, °C		37	
Reakcijos pH		12	
Laikas, val.		20	

*Ultra smulkios *nd* surinktos iš trijų paskutinio plovimo supernatantų frakcijų, jas sujungus.
** *Nd* gautos po plovimo surenkant supernatanto likutį.

2.1.3. $CoFe_2O_4$ Nd produktų dekoravimas auksu

D,L-metioninas panaudotas $HAuCl_4$ redukcijai ant skirtingų dydžių ≤ 2; ~5 ir ~15 nm $CoFe_2O_4$ *Nd* paviršiaus (2.1 pav.). Sintezė atlikta kambario temperatūroje, sumaišius $CoFe_2O_4$ *Nd* su 15 mmol·L^{-1} D,L-metionino ir 30 mmol L^{-1} $HAuCl_4$ vandeniniais tirpalais. Tirpalų pH buvo koreguojamas 1 mol L^{-1} NaOH tirpalu iki pH 12, o sintezių metu termostatuojamas esant 37 °C temperatūrai, 20 val. (2.1 lentelė, II dalis).

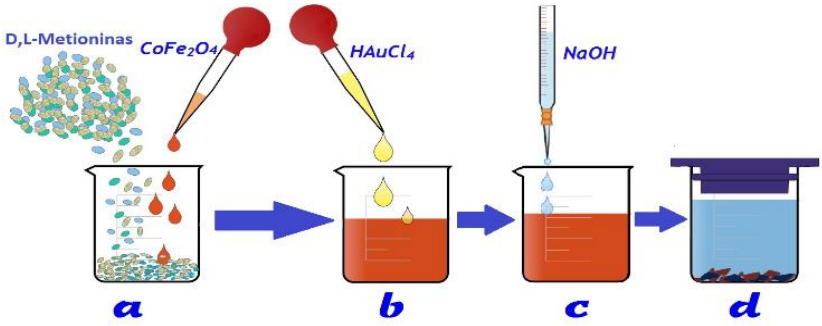

2.1 pav. $CoFe_2O_4$ *Nd* paviršiaus padengimo auksu schema, demonstruojanti eksperimento su D, L-metionino reduktoriumi etapus.

2.1.4. $CoFe_2O_4$@Met *Nd* sintezė, dekoravimas Au^0/Au^+nanokristalais

Atliekant $CoFe_2O_4$@Met *Nd* sintezę, pirminis prekursorių mišinys buvo gautas kruopšiai sumaišant 25 mmol·L^{-1} $CoCl_2$, 50 mmol·L^{-1} $FeCl_3$ ir 0.2 mmol·L^{-1} D,L-metionino vandeninius tirpalus. Po to jis buvo šarminamas iki pH 12,4 lašinant 5 mmol·L^{-1} NaOH ir galiausiai praskiedžiamas dejonizuotu vandeniu iki 12,5 mL tūrio. Paruoštas mišinys iš stiklinėlės buvo perpilamas į 25 mL talpos nerūdijančio plieno – teflono autoklavą ir patalpinamas į programuojamą mufelinę krosnelę 10 val. 130 °C temperatūroje. Gautas produktas buvo centrifuguojamas 3 min. 10867 x g, plaunamas dejonizuotu vandeniu iki neutralaus pH ir džiovinamas iki sausų $CoFe_2O_4$@Met *Nd* (2.2. lentelė, I dalis).

Au^0/Au^+ nanokristalų augimui ant magnetinių nanodalelių paviršiaus, buvo pasiūlytas būdas į $CoFe_2O_4$@Met *Nd* vandeninį tirpalą įpilti 10 mmol·L^{-1} D,L-metionino ir 10 mmol·L^{-1} $HAuCl_4$ tirpalo. Šis mišinys pašarminus 1 mol·L^{-1} NaOH tirpalu buvo maišomas apie 10 min ir supilamas į stiklo reaktorių 4 val., vėliau palaikant pastovią 37 °C temperatūrą vis pamaišant. Gautos $CoFe_2O_4$@Met@Au nanodalelės buvo plautos dejonizuotu vandeniu, jas surenkant ant stiklinėlės dugno išoriniu magnetu (2.2 lentelė, II dalis).

Au^0/Au^+ nanokristalų desorbcijai nuo magnetinių *Nd* paviršiaus buvo sukurtas naujas būdas: pagaminami 20 ml švarių $CoFe_2O_4$@Met@Au *Nd* ir sotaus D,L-metionino vandeniniai tirpalai. Jų mišinys patalpinamas į ultragarsinę vonelę ir veikiamas apie 20 min., kol tirpalas įgauna skaidriai rožinę spalvą.

2.2 lentelė. $CoFe_2O_4$@Met *Nd* sintezės bei jų dekoravimo Au^0/Au^+ nanokristalais reagentai ir sąlygos.

I Sintezės sąlygos	**$CoFe_2O_4$@Met (3.0 – 8.5 nm)**
Druskos	$CoCl_2$ ir $FeCl_3$
Druskų santykis, mmol·L^{-1}	25:50
Augimo reguliatorius, mmol·L^{-1}	D,L-metioninas 0.2
Reakcijos pH	12,4
Temperatūra, °C	130
Laikas, val.	10
Reaktorius	Teflono
pH po praplovimo	7
II Padengimo aukso Au^0/Au^+ nanokristalais sąlygos	
D, L-metionino kiekis, mmol·L^{-1}	10
$HAuCl_4$ koncentracija, mmol·L^{-1}	10
Temperatūra, °C	37
Reakcijos pH	12,2
Laikas, val.	4
III Au^0/Au^+ nanokristalų atskyrimas nuo CoFe@Met@Au nanodalelių paviršiaus	
CoFe@Met@Au	
D, L-metionino kiekis, mol	0,3
Veikimas ultragarsu, min	7

2.1.5. Fe_3O_4@Met *Nd* sintezė ir dekoravimas Au^0/Au^+nanokristalais

Fe_3O_4@Met *Nd* sintezės tirpalas buvo ruošiamas iš 15 mmol·L^{-1} $FeSO_4$, 30 mmol·L^{-1} $FeCl_3$ ir 0.2 mmol·L^{-1} D,L-metionino vandeninių tirpalų. Jo pH 12,3 vertė buvo pasiekiama lašinant 5 mmol·L^{-1} NaOH tirpalą. Fe_3O_4@Met *Nd* sintezė, plovimas ir džiovinimas buvo vykdomi kaip ir CoFe@Met *Nd* atveju, aprašytu 2.2.4. skyriuje (2.3 lentelė, I dalis).

Smulkių Au^0/Au^+ nanokristalų sintezei augimas vyko į Fe_3O_4@Met *Nd* vandeninį tirpalą įpilant 10 mmol·L^{-1} D,L-metionino ir 4 mmol·L^{-1} $HAuCl_4$ tirpalų. Šis mišinys buvo maišomas apie 10 min., pašarminamas iki pH 12,2 2.0 mol·L^{-1} koncentracijos NaOH tirpalu ir supilamas į reaktorių. Sintezė truko 4 val, palaikant 37 °C temperatūrą ir kaskart pamaištant. Gautos $CoFe_2O_4$@Met@Au nanodalelės buvo plaunamos dejonizuotu vandeniu, jas po to nusodinant magnetu (2.3 lentelė, II dalis).

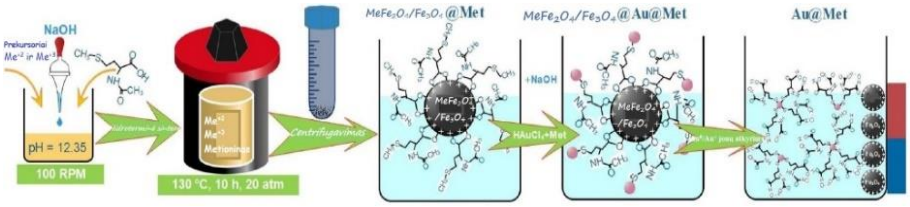

2.2 pav. Fe_3O_4 *Nd* paviršiaus funkcionalizavimo auksu schema demonstruojanti eksperimento su D,L-metionino reduktoriumi etapus.

2.3 lentelė. Fe_3O_4@Met *Nd* sintezės bei jų dekoravimo Au^0/Au^+ nanokristalais reagentai ir sąlygos

I Sintezės sąlygos	**Fe_3O_4@Met (3.0 – 8.5 nm)**
Druskos	$FeSO_4$ ir $FeCl_3$
Druskų santykis, mmol·L^{-1}	15:30
Augimo reguliatorius, mmol·L^{-1}	D, L-metioninas 0,2
Reakcijos pH	12,35
Temperatūra, °C	130
Laikas, val.	10
Reaktorius	Teflono
pH po praplovimo	7
II Padengimo aukso Au^0/Au^+ nanokristalais sąlygos	
Fe_3O_4@Met, mg	3,5
D,L-metionino kiekis, mmol·L^{-1}	10
$HAuCl_4$ koncentracija, mmol·L^{-1}	4
Temperatūra, °C	37
Reakcijos pH	12,4
Laikas, val.	4
III Au^0/Au^+ nanokristalų atskyrimas nuo Fe_3O_4@Met@Au nanodalelių paviršiaus	
Fe_3O_4@Met@Au, mg	
D,L-metionino kiekis, mol·L^{-1}	0,3
Veikimas ultragarsu, min	7

Au^0/Au^+ nanokristalų desorbcijai nuo magnetinių *Nd* paviršiaus buvo pagaminamas švarių Fe_3O_4@Met@Au *Nd* ir sotaus D,L-metionino vandeninio tirpalo 20 ml tūrio mišinys ir 20 min patalpinamas į ultragarsinę vonelę, kol tirpalo spalva tampa silpnai rožine.

2.1.6. Antibakteriniai Au^0/Au^+ nanokristalų tyrimai

Antibakteriniai Fe_3O_4@Au@Met *Nd* ir Au^0/Au^+ nanokristalų tyrimai buvo atlikti patalpinant *Nd* mėginius kartu su užaugintomis bakterijų kolonijomis į maistinę agaro terpę. Tyrimai atlikti 24 val. bėgyje palaikant 37 ± 1 °C temperatūrą. Siekiant gauti 6,4-8 × 10^8 kolonijas formuojančių vienetų (CFU) mililitre šviežios kultūros buvo praskiedžiamos sterilioje M9 augimo terpėje. Optinis terpės tankis buvo nustatomas spektrofotometriškai ties 600 nm šviesos ilgio banga. Nadojantis formule OD_{600} 1= $8 \cdot 10^8$ (ląst.sk./ml) buvo nustatytas ląstelių skaičius (nuo 0,08 iki 0,1). Logaritminio augimo stadijoje ląstelių buvo sėjama po 100 µL suspensijos į 96 šulinėlių ląstelių kultūrų plokštelę. Į paruoštas terpes su skirtingais kiekiais Fe_3O_4@Au@Met *Nd* arba Au^0/Au^+ *Nd* buvo pridedama po 100 µl vandens. Nanodalelių koncentracija buvo 70 arba 30 $mg \cdot L^{-1}$. Mėginiai buvo inkubuoti 24 val. maišant 150 aps/min greičiu. Neigiamiems kontroliniams tyrimams buvo panaudotas švarus D,L-metioninas ir Fe_3O_4 *Nd*. Ląstelių augimo metu iš kiekvieno šulinėlio buvo paimama po 100 µl suspensijos. Ji buvo praskiedžiama mėgintuvėlyje ir užsėjama ant Petri lėkštelėje esančios agar-agaro augimo terpės. Po vienos dienos inkubacijos 37 ± 1 °C temperatūroje mikroorganizmų augimas buvo ištiriamas skaičiuojant užaugusių kolonijų skaičių. Kiekvienas tyrimas kartotas po tris kartus.

2.1.7. Au nanoklasterių sintezė

Raudonai liuminescuojantiems aukso nanoklasteriams (*AuNkl*) susintetinti $HAuCl_4$ redukcijai pirmą kartą buvo panaudotas šakotųjų aminorūgščių maisto papildas, kurio prekinis ženklas ,,AAFS“. AAFS ir kt. naudotų maisto papildų sudėtis pateikta 2.4 lentelėje. Sintezė optimizuota šarminei (pH 12.2) terpei stiklo reaktoriuje 20 val. palaikant nuolatinę 37 °C temperatūrą. Sintezės schema ir tirpalo sudėtis pateikta 2.3 paveiksle ir 2.5 lentelėje.

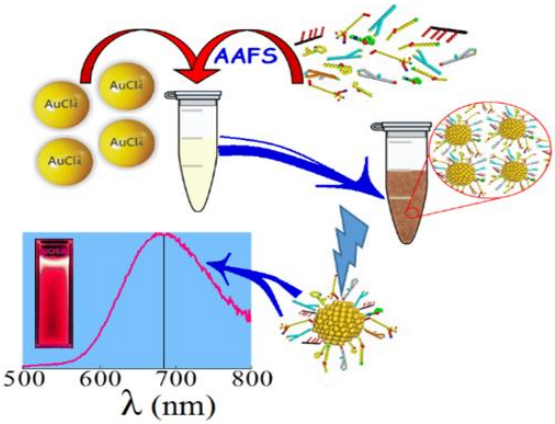

2.3 pav. Aukso nanoklasterių sintezės schema, panaudojant šakotųjų aminorūgščių maisto papildą (AAFS).

2.4 lentelė. Nurodytų aminorūgščių kiekis 100 g išbandytuose komerciniuose maisto papilduose.

	Maisto papildas	***AAFS, g***	***100% pieno miltelių kompleksas, g***	***100% išrūgų milteliai, g***
Aminorūgštys	Alaninas	3.99	3.34	3.37
	Argininas	0.39	1.47	1.78
	Asparaginas	2.1	7.63	7.6
	Cisteinas	0.49	1.54	2.06
	Glutamo r.	3.4	-	-
	Glutaminas	-	12.67	14.7
	Glicinas	0.3	0.98	1.28
	Histidinas	0.7	1.19	1.24
	Izoleucinas	1.34	4.48	4.7
	Leucinas	3.96	7.42	8.28
	Lizinas	2.97	6.72	7.46
	Metioninas	0.38	1.54	1.6
	Fenilalaninas	0.58	2.17	2.23
	Prolinas	1.21	3.92	4.23
	Serinas	0.96	3.22	3.73
	Treoninas	1.36	4.62	4.8
	Triptofanas	0.42	0.98	1.27
	Tirozinas	0.52	1.86	2.36
	Valinas	3.08	4.13	4.34

2.5 lentelė. Susintetintų aukso nanoklasterių sintezės sąlygos ir reagentai

Sintezės sąlygos	*AuNkl*
$HAuCl_4$ koncentracija, $\mu mol \cdot L^{-1}$	3
Aminorūgščių maisto papildą (AAFS), mg/ml	5
Reakcijos pH	10÷13,5
Temperatūra, °C	37
Laikas	20 val.

2.2. Suformuotų struktūrų tyrimai

Auksuotų nanodalelių koncentracija (N_i) buvo nustatoma iš bendros $CoFe_2O_4$ feritų masės, esančios magnetiniame skystyje (m_n) ir vienos *Nd* masės (m_i) santykio.

$$N_i = m_n/m_i$$

Analizė buvo atliekama susietos plazmos optinės emisijos spektrometrijos (ICP-OES) metodu naudojant induktyviai susietos plazmos optinį emisinį spektrometrą *OPTIMA 7000 DV (Perkin Elmer)*. Skaičiavimuose $CoFe_2O_4$ feritų tankis buvo laikomas 5,2 $g \cdot cm^{-3}$. $CoFe_2O_4$. *Nd* stechiometrija buvo nustatoma išanalizavus kobalto ir geležies kiekius, mėginį prieš tai ištirpinus HCl (1:1). Matavimai buvo atliekami atsižvelgiant į emisijos smailes, esančias kobalto 228,6 nm ir geležies 239,5 nm bangų ilgiuose. Kalibracijos kreivės buvo gautos iš standartinio tirpalo pagaminus nuo 1 iki 50 ppm koncentracijų tirpalus. Standartinis elementų kiekio aptikimo ribos nuokrypis, analizuojant mažiausiai 4 kartus, buvo ± 2,6 %.

Furje transformacijos infraraudonieji spektrai buvo registruojami kambario temperatūroje *ALPHA FTIR* (Bruker, Inc., Germany) spektrometru su *DLATGS* detektoriumi. Spektrinė skiriamoji geba buvo 4 cm^{-1}. Spektrai buvo registruojami atliekant 100 skenavimų. Nanodalelių dariniai buvo supresuojami į KBr tabletes. Ekspermentinių smailių atpažinimui buvo naudota *GRAMS/A1 8.0* (Thermo Scientific) programinė įranga.

Nanodalelių morfologija buvo tirta peršvietimo elektroniniu mikroskopu *MORGAGNI 268*. Mėginiai buvo ruošiami išplovus nanodaleles spiritu. Lašas gauto koloidinio tirpalo mikropipete buvo užnešamas ant angline plėvele *(EP 300 Å)* padengto varinio tinklelio. Išdžiuvus mėginiui, jo 3 mm diametro apskritimo iškarpa buvo patalpinama į peršvietimo elektroninio mikroskopo talpiklį. Mėginio peršvietimui naudota 72 kV greitinanti įtampa. Peršviečiamo objekto vaizdai buvo stebimi *CCD* kamera. Vidutinis nanodalelių dydis buvo

apskaičiuojamas išmatavus mažiausiai 200 dalelių. Ultra smulkios kobalto ferito nanodalelės buvo tiriamos didelės raiškos peršvietimo mikroskopu *LIBRA 200 FE*; naudota 200 kV greitinanti įtampa. Be to, dalis jų buvo užneštos ant žėručio ir ištirtos atomo jėgos *Veeco AFM diInnova* modelio skenuojančiu mikroskopu. AJM vaizdai gauti su ant lankstaus laikiklio pritvirtinta silicio adatėle esant pastoviems T = 3,5 – 4,5 μm, f_o = 297 – 347 kHz, L = 110 – 140 μm, k = 20-80 N m^{-1}, W = 25 – 35 μm parametrams ir naudojant virpančio zondo režimą.

Nanodalelių kristališkumui, fazinei sudėčiai ir kristalitų dydžiams įvertinti buvo užrašytos ir analizuotos gautų produktų rentgenodifraktogramos. Tuo tikslu naudotas rentgenodifraktometras *D8 (Bruker AXS*, Germany), kuriame Göbel veidrodis buvo naudotas CuKα radiacijos spindulių monochromatoriumi. Spektrai užrašyti 2Θ kampų geometrijoje, [18–55]^o intervale, 0,02^o žingsniu, kaupinant 8 s.

Au^0/Au^+ nanokristalų, nusodintų ant kobalto ferito *Nd* paviršiaus, būsena buvo tiriama rentgeno fotoelektronų spektrometru *ESCALAB MKII*.

Mesbauerio spektrai 9-390 K temperatūrose buvo išmatuoti Mesbauerio spektrometru panaudojant krosnelę (WissEl), uždaro ciklo helio kriostatą (Advance Research Systems) ir ^{57}Co šaltinį. Tuo tikslu $CoFe_2O_4$ nanodalelės buvo nusodintos ant popieriaus filtro, kuris buvo peršviečiamas γ-spinduliuote (sugerties geometrija). Spektrų išreiškimui pospektriais naudotas programinis paketas Normos (*Site ir Dist*). Paminėtina, kad Normos Site programa spektrai yra aprašomi nedideliu skaičiumi pospektrių šeštukų ar dubletų paprastai atspindinčių tam tikras Fe atomo padėtis ar būsenas. Kai tai buvo neįmanoma, t.y. kai spektrai išplitę dėl superparamagnetinės relaksacijos, naudota Normos Dist programa. Šiuo atveju mėginio spektras buvo aprašomas rinkiniais šeštukų, kurių hipersmulkus laukas B kinta fiksuotu žingsniu pasirinktame intervale. Superparamagnetinės nanodalelių relaksacijos įtakos Mesbauerio spektro formai įvertinti buvo naudotas vidutinis hipersmulkus laukas $\langle B \rangle = \sum_i P_i B_i$, kur P_i yra Mesbauerio spektrų pospektrio su hipersmulkiu lauku B_i santykinis plotas. Nustatyta perėjimo temperatūra nuo superparamagnetinės iki magnetinės būsenos, kada $\langle B \rangle \approx 0{,}5\ B_0$, kur B_0 yra maksimumas hipersmulkaus lauko, pastebėto žemiausioje temperatūroje, vertė.

Sausų kobalto ferito *Nd* magnetinio stiprumo matavimai kambario temperatūroje buvo atliekami vibruojančio mėginio magnetometru *FH 54*

veikiant mėginį nuolatiniu 4.4 kOe stiprio magnetiniu lauku. Dalis magnetinių tyrimų buvo atlikti Fizikinių savybių matavimo sistema „*Quantum Design Physical Properties*“ (QD-PPMS), esančia prof. Marco Affronte vadovaujamoje QD-PPMS laboratorijoje (Italija). Ši sistema leidžia automatizuotus matavimus atlikti kintamos temperatūros intervale (1,9 ÷ 400 K) ir kintančiame magnetiniame lauke iki 7 Teslų (2.4 pav.) [124].

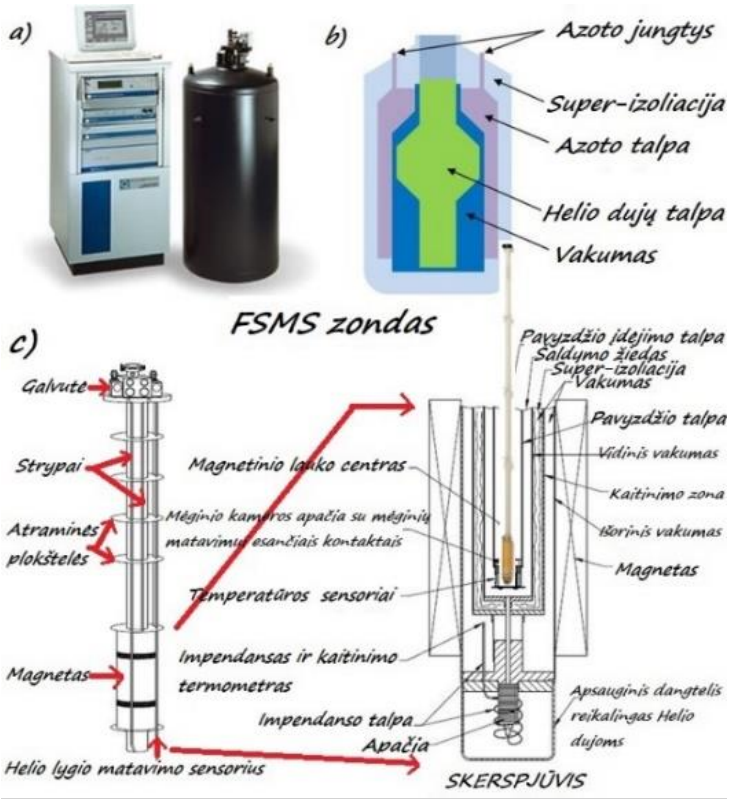

2.4 pav. Fizikinių savybių matavimo sistemos „Quantum Design Physical Properties“ (QD-PPMS) schema.

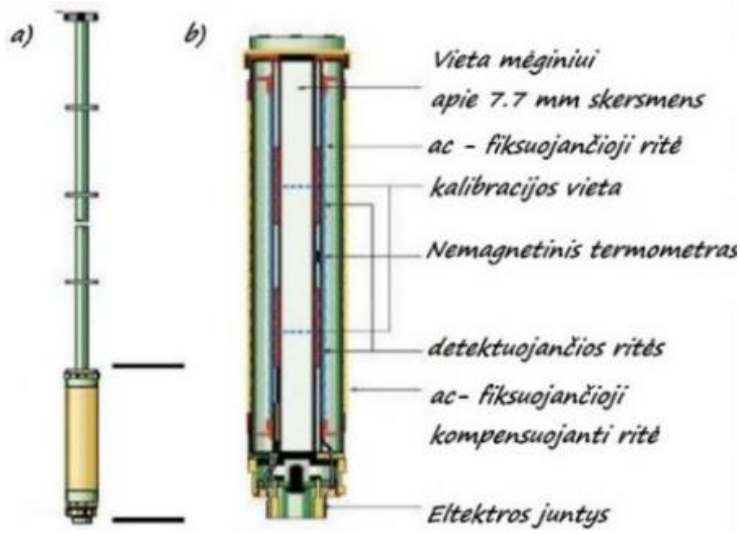

2.5 pav. Mėginio miltelių patalpinimo ritės schema QD-PPMS sistemos prietaise.

Sausi magnetinių nanodalelių mėginio milteliai buvo patalpinami į ritėje skirtą mėginio vietą (2.5 pav.) ir kartu su rite įstatomi į QD-PPMS sistemos pagridinę talpą, kurioje vėliau magnetinės *Nd* buvo veikiamos norimu magnetiniu lauku ir temperatūra. Visi matavimai buvo atliekami palaikant nuolatines 300; 200 arba 4 K mėginių temperatūras ir veikiant kintančiu išoriniu magnetiniu lauku nuo 0 iki 3 T. Gauti duomenys buvo išreikšti magnetinio jautrio χ (emu) vienetais, kurie *OriginLab 8* kompiuterine programa buvo perskaičiuojami į χ (emu·mol^{-1}) ar M(DC)(*μB/f.u.*) naudojant (2) ir (3) formules:

$$\chi(\text{emu}\cdot\text{mol}^{-1}) = \chi\cdot(M/m\cdot 10), \qquad (2)$$

kur: M – mėginio molinė masė (g·mol^{-1}); m – matuojamo mėginio masė (g); χ – magnetinis jautris gautas QD-PPMS matavimų metu (emu); sistemoje nustatytas pastovus dydis 10 (Oe)

$$M(DC)(\mu_B/f.u.) = \chi\cdot(M/m\cdot\mu_B\cdot N_A), \qquad (3)$$

kur: M – mėginio molinė masė (g·mol^{-1}); m – matuojamo mėginio masė (g); χ – magnetinis jautris, gautas QD-PPMS matavimų metu (emu) o μ_B ir N_A vienetai atitinkamai apibrėžiami kaip 9,274 · 10^{-21} (erg·G^{-1}) ir 6,022 · 10^{23} (mol^{-1}) (dydis erg·G^{-1} yra lygus emu).

UV-vis spektrofotometrijos matavimai buvo atlikti naudojant spektrofotometrą *Jasco V – 670* (JAV). Tyrimams naudotos plastikinės UV mikrokiuvetės. Optinio kelio ilgis jose 1 cm. Duomenys buvo apdorojami naudojant UV Winlab v.2.85.04 programinę įrangą. Visiems optiniams matavimams atlikti buvo naudojama „Hellma Optik“ (Jena, Vokietija) kvarco kivetė su 1 cm ilgio optiniu keliu. Dejonizuotas vanduo buvo naudojamas kaip palyginamasis tirpalas. Registruojami šviesos sugerties spektrai 300 – 800 nm srityje. Spektrofotometriniai matavimai atlikti kambario temperatūroje.

Tirtų *AuNCs* tirpalų absorbcijos spektrai buvo matuojami naudojant Jasco V670 spektrofotometrą. Fluorescencijos spektrai 400 – 750 nm diapazone buvo matuojami naudojant fluorescencijos spektrometrą Edinburgh–F900 (Edinburgo prietaisai, Jungtinė Karalystė). Fluorescencijai sužadinti buvo naudojamas pikosekundinis impulsinis diodinis lazeris EPL-375, skleidžiantis apie 70 ps trukmės impulsus esant 375 nm bangos ilgiui. Vidutinė impulso galia buvo 0,15 mW / mm^2. Visi fluorescencijos spektrai buvo pakoreguoti atsižvelgiant į prietaiso jautrumą. Visų mėginių 10 mm kiuvetės optinis tankis buvo apie 0,1 esant 375 nm. Fluorescencijos skilimo kinetika nanosekundžių laiko intervale buvo matuojama naudojant laiko koreliacijos pavienių fotonų skaičiavimo (TCSPC) metodą, naudojant tą patį Edinburgo F900 spektrometrą. Pulso (375 nm) pasikartojimo dažnis buvo 2 MHz, o nustatymo laiko skiriamoji geba buvo apie 100 ps. Visų kinetinių matavimų lazerio spinduliuotės intensyvumas, diafragmos tarpas, matavimo laikas buvo vienodi.

3. REZULTATAI

Siekiant rasti patikimą magnetinių nanodalelių dekoravimo auksu kelią, šiame darbe atlikti tyrimai $HAuCl_4$ redukcijai panaudojant įvairias aminorūgštis pasižyminčias biosuderinamumu ir funkcinių grupių įvairove. Natūraliai organizme sintetinama 20 pagrindinių aminorūgščių, iš kurių yra sudaryti įvairias funkcijas atliekantys baltymai. Aminorūgštys skirstomos pagal turimas funkcines grupes ir erdvinę struktūrą. Be karboksilo funkcinės grupės, aminorūgštys turi merkapto (-SH), sulfido (=S), hidroksilo (-OH) ir kt. funkcines grupes [125].

Šiame tyrime vandenilio tetrachloraurato redukcijai ant magnetinių *Nd* paviršiaus buvo išbandyta 19 aminorūgščių. Tirtos dvi galimybės: panaudoti aminorūgštis magnetinių *Nd* sintezėje jų stabilizavimui, aktyvių funkcinių grupių prikabinimui bei tiesioginiam $HAuCl_4$ redukavimui. Padengti švarių neigiamai įkrautų magnetinių nanodalelių paviršių panaudojant $HAuCl_4$ tirpalus ir aminorūgštis.

Nustatyta, kad vien tik karboksilo funkcines grupes ir amino grupes turinčios aminorūgštys neturi pastebimos įtakos magnetinių *Nd* sintezei, jų paviršiaus savybėms ar padengimui auksu. Tačiau pastebėta, kad metionino (Met), lizino (Lyz), cisteino (Cys), arginino (Arg) ir histidino (His) aminorūgščių elgsena su magnetinėmis *Nd* skiriasi nuo kitų aminorūgščių. Ji buvo ištirta detaliau.

3.1. $CoFe_2O_4$ ir $CoFe_2O_4$@Au *Nd* sudėtis ir struktūra

Šiame tyrime naudotos ultra smulkios (≤ 2,0 nm) ir smulkios (~ 5,0 nm) kobalto ferito nanodalelės. Susintetintos naudojant citrinos arba diglikolio rūgštis, priklausomai nuo vėliau auksavimui naudojamo bioreduktoriaus, vitamino C, ar D,L-Metionino rūgščių. Supernatantuose likusių plūduriuojančių nanodalelių PEM analizė parodė, jog susintetintos $CoFe_2O_4$ *Nd* yra sferinės ir ultra smulkaus 1,6 ± 0,5 nm dydžio (3.1a pav.), o likučio dalelių dydis yra apie 5 nm (3.1.b pav.).

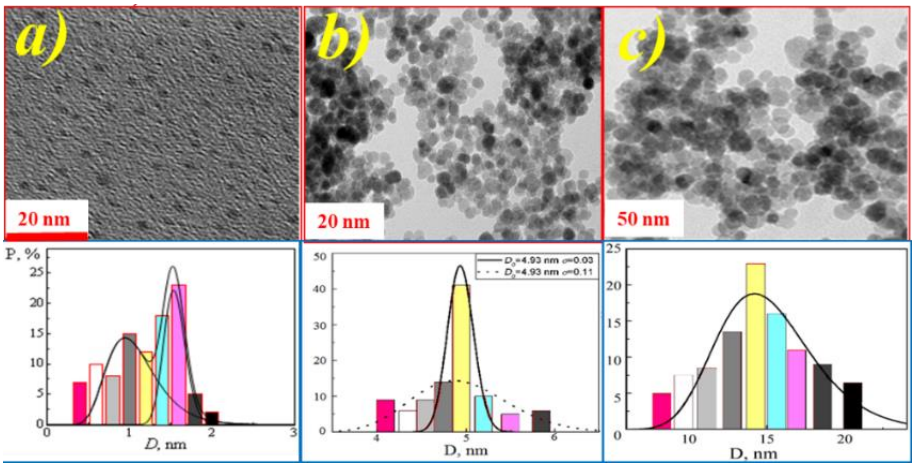

3.1 pav. Susintetintų $CoFe_2O_4$ feritų *Nd*: a) ultra-smulkių 2 nm, b) smulkių 5 nm ir c) 15 nm PEM vaizdai ir jų dydžių pasiskirstymo histogramos.

15 nm vidutinio dydžio $CoFe_2O_4$ ferito *Nd* buvo susintetintos hidroterminės sintezės būdu naudojant tos pačios, kaip ir smulkių *Nd* sintezei, sudėties tirpalus (žr. 2.1.2). Optimaliomis sąlygomis (130 °C, $\partial T/\partial t$ 10 °C/min) sintezės trukmė buvo 10 val. *Nd* frakciją, surinktą po sintezės centrifugavimo būdu (trečias centrifugatas praplaunant), sudarė sferinės, 15 nm vidutinio dydžio dalelės (3.1c pav.). Šios sintezės metu smulkių supernatanto frakcijų nesusidarė. Iš peršvietimo elektroninės mikroskopijos vaizdų aiškiai matyti, jog ir mažesnės $CoFe_2O_4$ *Nd* yra taisyklingos sferinės formos. 5 ir 15 nm vaizduose pastebimas nežymus magnetinių nanodalelių dydžio persiklojimas, kurį galėjo lemti nepakankamas mėginio praskiedimas paruošimo metu. Tirtų $CoFe_2O_4$ *Nd* dydžio pasiskirstymo stulpelinės dydžių pasiskirstymo diagramos pateiktos 3.1 pav.

$CoFe_2O_4$ *Nd* 1–3 nm rentgenogramos smailės pateiktos 3.2 paveiksle a) nėra intensyviai išreikštos; jų išplitimas rodo tiriamo objekto itin smulkią, kristalinę struktūrą. Šių *Nd* cheminės analizės metu buvo gauta sudėties variacija $Co_{0,91}Fe_{2,09}O_4$-$Co_{0,98}Fe_{2,02}O_4$ ribose. Šie ir RSD rezultatai leidžia tikėtis, kad ir ultra smulki sintezės frakcija turi artimą tiek stechiometrinę, tiek kristalinę $CoFe_2O_4$ *Nd* struktūrą.

Lyginant gautų $CoFe_2O_4$ *Nd* rentgenodifraktogramas su kristalinio $CoFe_2O_4$ etalonu (PDF 04-007-8945) nustatyta, jog gautos kobalto ferito *Nd*

turi atvirkštinę špinelinę polikristalinę struktūrą, nepriklausomai nuo jų dydžio, sintezės sąlygų bei naudoto stabilizuojančio agento prigimties.

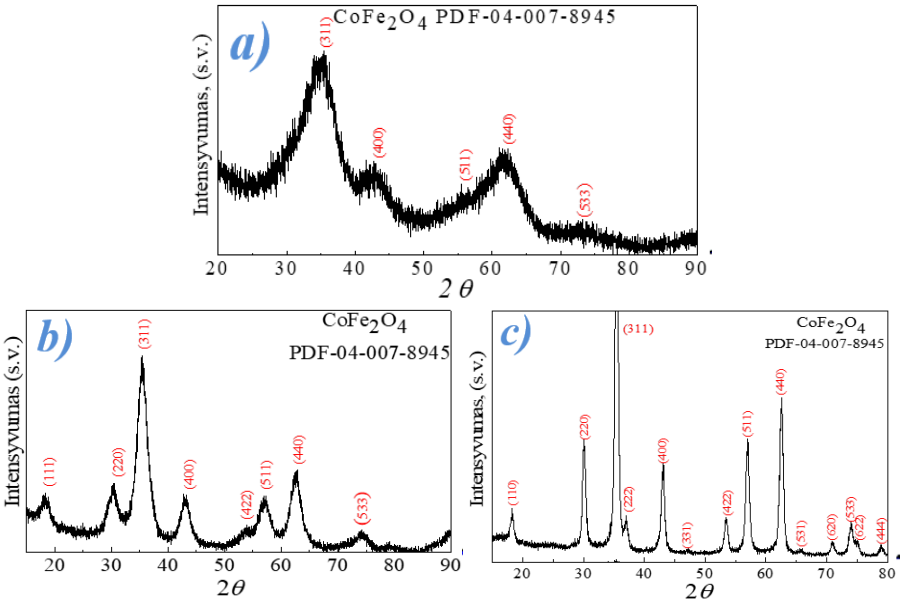

3.2 pav. a) Ultra smulkių (1–3 nm), b) smulkių (5 nm) ir c) 15 nm $CoFe_2O_4$ *Nd* rentgenodifraktogramos.

Gauti skirtingų dydžių $CoFe_2O_4$@Au *Nd*, ARPEM ir PEM vaizdai pateikti 3.3 ir 3.4 paveiksluose. Iš pateiktų PEM vaizdų matyti, jog $CoFe_2O_4$ *Nd* po auksavimo padidėja. Ištyrus mažiausia du šimtus $CoFe_2O_4$ *Nd* PEM vaizdų nustatyta, kad ultra smulkios kobalto ferito nanodalelės po paviršiaus auksavimo, redukuojant $HAuCl_4$ D,L-metioninu padidėja nuo ~1,6 nm iki ~2,5 nm. Metalinio aukso buvimas ant $CoFe_2O_4$ *Nd* paviršiaus papildomai ištirtas aukštos skiriamosios gebos peršvietimo elektronų mikroskopija (ARPEM) bei išmatuoti tarplokštuminiai aukso atomų, esančių $CoFe_2O_4$@Au *Nd* paviršiuje, atstumai. Šiuo būdu nustatyta, jog ultra smulkių kobalto ferito nanodalelių paviršius padengtas auksu. Jo struktūra artima fcc metalinio aukso atomų supakavimo 0,24 nm (111) atstumu plokštumai.

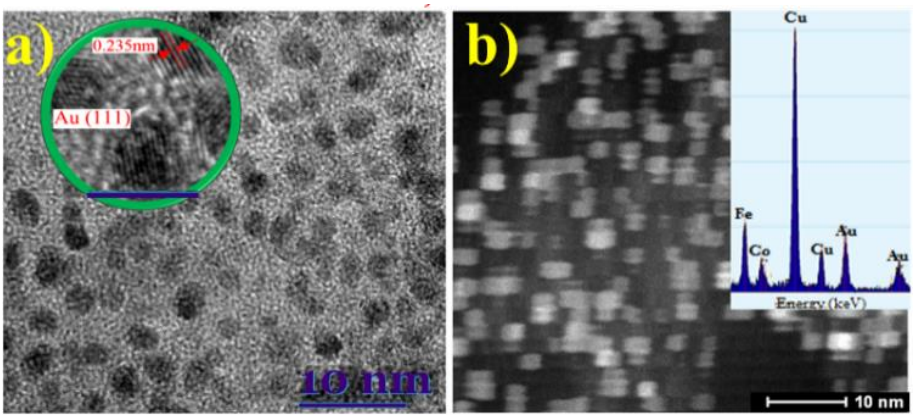

3.3 pav. a) Ultra smulkių 1,6 nm $CoFe_2O_4$@Au *Nd* PEM vaizdas. Intarpinime apskritime pateiktas ARPEM vaizdas demonstruoja ant $CoFe_2O_4$ *Nd* paviršiaus esančio Au tarplokštuminius atstumus, kurie yra 0,24 nm (5 nm skalėje). B) $CoFe_2O_4$@Au *Nd* STM vaizdas, o EDX spektras rodo elementinę $CoFe_2O_4$@Au *Nd* sudėtį.

Taip pat panašūs rezultatai gauti su smulkiomis ir didesnėmis $CoFe_2O_4$ *Nd*. Redukuojant $HAuCl_4$ D,L-metioninu ant 5 ir 15 nm $CoFe_2O_4$ *Nd* paviršiaus gauta, jog nuo pradinio kobalto ferito *Nd* skersmens jos atitinkamai išaugo iki 6,6 nm (3.4 a pav.) ir 16,5 nm (3.4 b pav.). Taip pat pastebėta, jog įprastai stabilios $CoFe_2O_4$ *Nd* po paviršiaus padengimo auksu tampa nestabilios ir nusėda ant dugno (3.4 intarpas pav.) nenaudojant išorinio magneto.

Iš apskaičiuotų dydžių pasiskirstymo stulpelinių diagramų (3.4 a, b, c, pav.) pastebimas *Nd* polidispersiškumo išaugimas, kurį nesunku įžiūrėti ir PEM vaizduose. Mūsų nuomone, šis pokytis sietinas su daliniu ir netolygiu *Nd* paviršiaus padengimu auksu ar aukso nanodalelių susiformavimu ant $CoFe_2O_4$ *Nd* paviršiaus. Dėl didesnio paviršiaus ploto stipriausiai išaugęs dydžių pasiskirstymo intervalas matomas ant didesnių 15 nm $CoFe_2O_4$ *Nd* lyginant su mažesnėmis *Nd.*

Chemine analize siekta nustatyti suredukuoto Au kiekį ant $CoFe_2O_4$ *Nd* paviršiaus D,L-metioninu. Nustatyta, jog po 4 val. $HAuCl_4$ redukcijos visų dydžių, t.y. 1,6; 5 ir 15 nm $CoFe_2O_4$ *Nd* likutiniame terpės tirpale nesuredukuoto aukso buvo likę mažiau nei 2 % (3.1 lentelė).

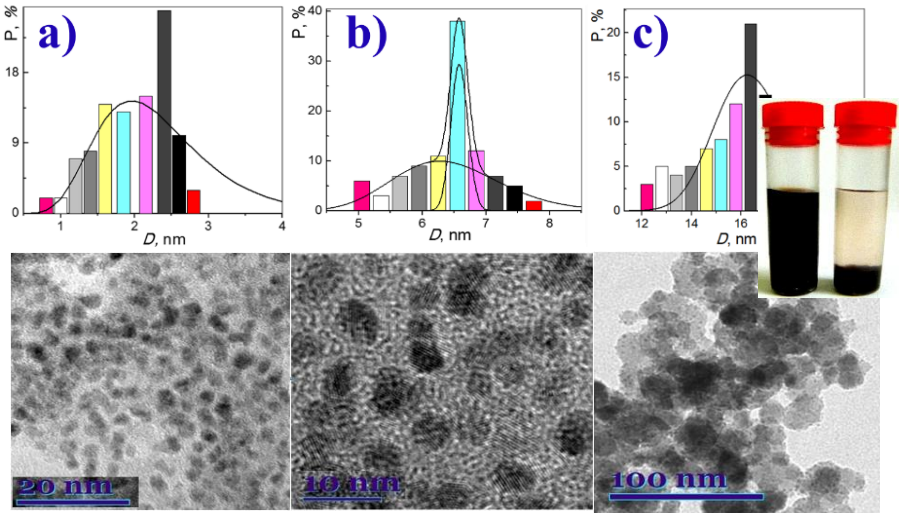

3.4 pav. Ultra-smulkių (~1,6 nm) (a), smulkių (~5) (b) ir didesnių (~15 nm) (c) $CoFe_2O_4$ *nd* dydžių pasiskirstymo histogramos po 4 val. auksavimo redukuojant $HAuCl_4$ metioninu. T=37 °C. Apačioje jų PEM vaizdai

3.1 lentelė Nesuredukuotos $HAuCl_4$ kiekis (%) po 4 val. redukcijos D,L- metioninu ant nurodyto dydžio $CoFe_2O_4$ *Nd* paviršiaus. T= 37 °C.

Ø, $CoFe_2O_4$ *nd*, nm	Likusio Au^0 kiekis, %
1,6	1,7
5	0,38
15	0,14

Iš pateiktos 3.1 lentelės duomenų pastebima, jog neredukuotas vandenilio tetrachloraurato kiekis mažai priklauso nuo $CoFe_2O_4$ nanodalelių dydžio. Tačiau patikimesnei išvadai formuluoti reiktų įvertinti padengto auksu $CoFe_2O_4$@Au *Nd* realų paviršiaus plotą ir susidariusio sluoksnio tankumą.

Siekiant tiksliau įvertinti ant $CoFe_2O_4$@Au nanodalelių suformuoto metalinio aukso sluoksnio vientisumą ir tankumą buvo pasitelkti ir kiti tyrimų metodai. Pirmiausia, siekta nustatyti ar tolygiai ant sferinių $CoFe_2O_4$ *Nd* paviršiaus D,L-metioninas redukuoja $HAuCl_4$ esančius Au jonus. Tam išsiaiškinti buvo ištirpintas kobalto ferito *Nd* branduolys per naktį 1:1 HCl

tirpale. Tirtos 16,5 nm vidutinio dydžio $CoFe_2O_4$@Au nanodalelės. Likę aukso lukštai buvo išplauti vandeniu ir tirti PEM (3.5 pav.).

$CoFe_2O_4$ šerdies tirpinimo druskos rūgštyje metodu nustatyta, jog redukuojant $HAuCl_4$ D,L-metioninu ant 15 nm $CoFe_2O_4$ *Nd* paviršiaus susidariusi aukso danga yra gan tolygi ir sferinė. Taip pat nustatyta, jog keičiant redukcijos laiką $CoFe_2O_4$ *Nd* paviršių galima dekoruoti nuo dalinio aukso nanodalelėmis paviršiaus padengimo iki tolygaus viso paviršiaus ploto užpildymo aukso sluoksniu.

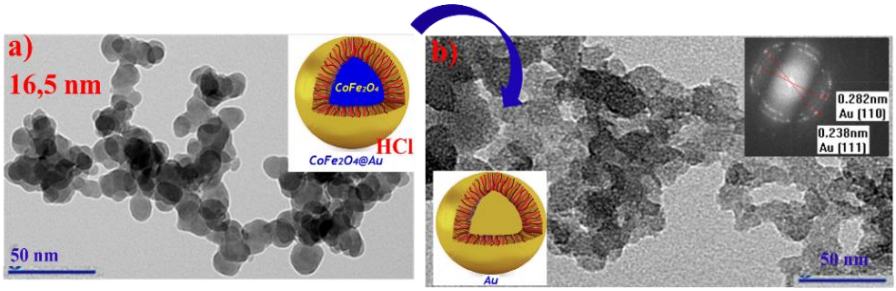

3.5 pav. A) 16,5 nm vidutinio dydžio $CoFe_2O_4$@Au *Nd* PEM vaizdas. (b) Tų pačių $CoFe_2O_4$@Au *Nd* po vienos naties laikymo 1:1 HCl tirpale likusių Au apvalkalo lukštų PEM vaizdas. Intarpinis b) dalyje EDX spektras nuo $CoFe_2O_4$@Au *Nd* paviršiaus liudija difrakciją nuo (111) ir (110) Au^0 kristalo plokštumų.

Chemine analize nustatyta, jog naudojant 25 $mg \cdot L^{-1}$ D,L-metionino aminorūgšties kiekį po redukcijos ant $CoFe_2O_4$ *Nd,* redukuojasi visa panaudota 30 $mmol \cdot L^{-1}$ $HAuCl_4$. Pakartotinai atliekant jau 16,5 nm vidutinio dydžio $CoFe_2O_4$@Au nanodalelių paviršiaus dengimą, į reakcijos tirpalą įpilta papildomai 30 $mmol \cdot L^{-1}$ $HAuCl_4$, o jos redukcija 37 °C temperatūroje tęsta dar 4 valandas. Po sintezės tirpale liko 79 % nesuredukuoto vandenilio tetrachloraurato. Surinkus ir išplovus $CoFe_2O_4$@Au *Nd,* padaryti PEM mėginiai ir atlikta jų sudėties analizė. *Nd* morfologija pateikta 3.6 pav.

Nustatyta, jog $CoFe_2O_4$ *Nd* aukso paviršiaus sluoksnis tapo tankesnis bei tolygesnis. Šio tyrimo metu $CoFe_2O_4$@Au *Nd* įgavo taisyklingą sferinę formą. Tačiau po pakartotinos $HAuCl_4$ redukcijos, $CoFe_2O_4$@Au *Nd* skersmuo ženkliai padidėjo iki 16,5 nm. Dėl to, kaip minėta ir literatūroje, susilpnėja ir net visiškai yra prarandamos magnetinės *Nd* savybės.

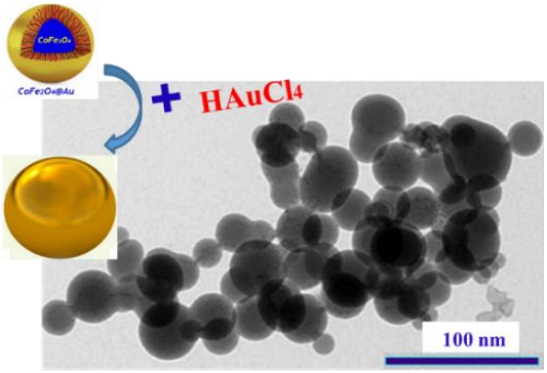

3.6 pav. $CoFe_2O_4$ nanodalelių, du kartus dengtų auksu, PEM vaizdas.

3.1.1. Furje transformacijos IR spektroskopinės analizės tyrimai

Siekiant nustatyti, ar D,L-metioninas yra ne tik tinkamas $HAuCl_4$ ant $CoFe_2O_4$ nanodalelių paviršiaus bioreduktorius, bet ir nanodaleles tirpale stabilizuojantis agentas, atlikta $CoFe_2O_4$ ir $CoFe_2O_4$@Au *Nd* Furje transformacijos infraraudonųjų spindulių spektroskopijos (FTIR) analizė. Ištirtos $CoFe_2O_4$ ir $CoFe_2O_4$@Au *Nd* prieš ir po dopamino hidrochlorido ($C_8H_{12}ClNO_2$) (DOPA) adsorbcijos išlaikant *Nd* ~15 val. 13 mmol·L^{-1} koncentracijos tirpale, kambario temperatūroje. Žinia, kad Fe_3O_4 ir Co_3O_4 medžiagoms yra būdingi Fe-O ir Co-O ryšių IR vibraciniai virpesiai: Fe-O ryšį charakterizuoja 570 – 580 cm^{-1} [126, 127, 128], o Co-O ryšį dubletinės smailės, stebimos 570/670 cm^{-1} [129, 130, 131] bangų ilgių intevaluose. Švaraus DOPA ($C_8H_{12}ClNO_2$) spektras pateiktas (3.7a pav.). Jį charakterizuoja vibracinės smailės IR srityje ties: 814, 876, 1115, 1190, 1260, 1286, 1320, 1341, 1499 ir 1614 cm^{-1} bangos ilgiais. $CoFe_2O_4$@Au nanodalelių FTIR spektras yra pateiktas 3.7.b paveiksle. Šių *Nd* spektrui charakteringi virpesiai, priskirtini Fe-O ir Co-O ryšių virpesiams. Mažesnio intensyvumo, matomos smailės 1380 ir 1570 cm^{-1} IR bangų ilgiuose gali būti būdingos karboksilinių/amidinių funkcinių grupių virpesiams. Pastarosios galėjo atsirasti po $CoFe_2O_4$ *Nd* paviršiaus dengimo auksavimo tirpale su metioninu. Labiausia tikėtina, jog $CoFe_2O_4$@Au nanodalelių FTIR spektre atsiradę ryšių virpesius ties 1380 ir 1570 cm^{-1} duoda redukcijos metu susidaręs metionino sulfoksidas [132]. Dopamino adsorbcijos tyrimui ant auksuotų ir neauksuotų kobalto ferito *Nd* pasirinktos 15 nm vidutinio dydžio $CoFe_2O_4$ nanodalelės.

$CoFe_2O_4$ *Nd* ir dopamino mišinys vandeniniame tirpale buvo laikyti vieną naktį kambario temperatūroje. Po inkubacijos dalelės buvo išplautos kelis kartus vandeniu ir paruošiami mėginiai FTIR analizei. $CoFe_2O_4$@DOPA (3.7c pav.) ir $CoFe_2O_4$@Au_DOPA (3.7d pav.) dalelių charakteringuose spektruose matomos Fe-O ir Co-O ryšiams charakteringos smailės ties 580 – 587 cm^{-1} bangos ilgiais. Be to iš FTIR spektrų matyti, kad atlikus magnetinių nanodalelių inkubaciją DOPA tirpale, atsiranda papildomų smailių, būdingų dopaminui. $CoFe_2O_4$@Au_DOPA atveju fiksuojamos papildomos smailės: 815, 875, 1122, 1272, 1291, 1338, 1496 ir 1496 cm^{-1} dažniuose (3.7d pav.), o $CoFe_2O_4$@DOPA spektre – 1125, 1273, 1297, 1486, ir 1621 cm^{-1} dažniuose. (3.7.c pav.). Lyginant šiuos spektrus su gryno dopamino IR virpesiais aiškiai matyti, jog tiek $CoFe_2O_4$, tiek $CoFe_2O_4$@Au nanodalelių paviršius yra padengtas dopaminu.

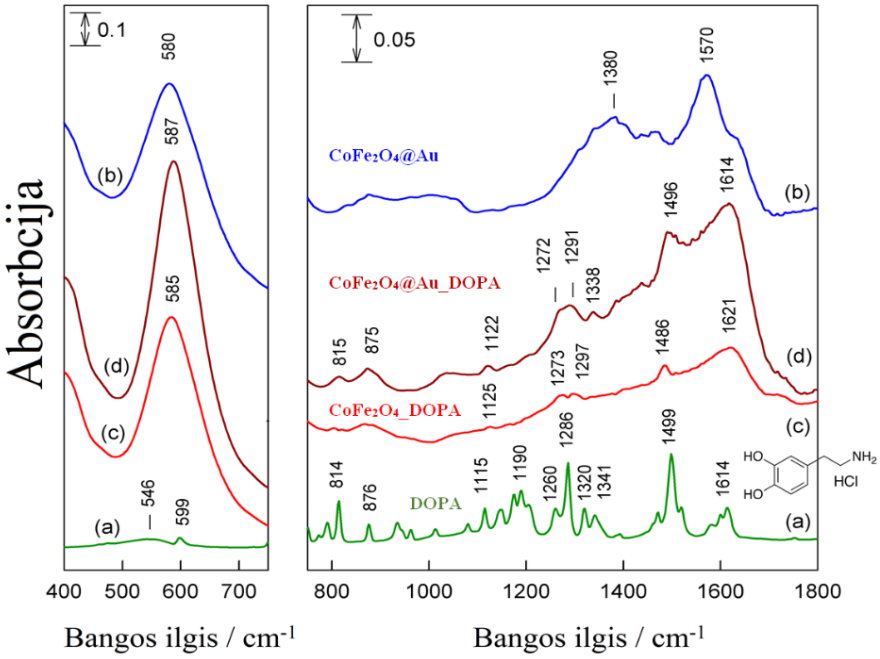

3.7 pav. FTIR absorbcijos spektrai: a) dopamino hidrochlorido ($C_8H_{12}ClNO_2$), b) $CoFe_2O_4$@Au *Nd*, c) $CoFe_2O_4$ *Nd* ir d) $CoFe_2O_4$@Au *Nd* po inkubacijos 13 $mmol \cdot L^{-1}$ DOPA tirpale kambario temperatūroje per naktį ir praplovimo vandeniu.

Intensyviausiai sutampantys dopamino ir $CoFe_2O_4$@Au_DOPA FTIR virpesiai yra 814, 1286 ir 1499 cm^{-1} dažniuose. 1499 cm^{-1} priskirtinas

aromatinio žiedo C-C, o 814 cm^{-1} ir 1286 cm^{-1} – simetriško C-O-H ryšių vibracijai. $CoFe_2O_4$@Au_DOPA spektro smailės, esančios 1496 cm^{-1} bangos ilgyje, poslinkis atspindi N-C ryšio deformaciją (tempimą) [133, 134, 135, 136]. Stebima ir dopamino adsorbcija ant $CoFe_2O_4$ *Nd*. Ją charakterizuoja 1486 cm^{-1} FTIR spektro smailė. Nustatyta, kad padengus auksu $CoFe_2O_4$ *Nd*, adsorbuoto dopamino aromatinio žiedo C-C jungties vibracinis virpesys pasislinko nuo 1486 cm^{-1} iki 1496 cm^{-1}, t.y. per 10 cm^{-1}. Šį pokytį, matyt, reikėtų sieti su skirtingai orientuotų dopamino molekulių adsorbcija ant $CoFe_2O_4$ ir $CoFe_2O_4$@Au nanodalelių.

Ištyrus $HAuCl_4$ redukcijos D,L-metioninu ant $CoFe_2O_4$ *Nd* paviršiaus ypatumus, buvo suformuota padengimo principinė schema. Ji pateikta 3.8 pav. ir atspindi D,L-metioninu stabilizuotų kobalto ferito nanodalelių paviršiaus padengimą auksu bei auksuotų *Nd* paviršiaus stabilizaciją metionino sulfoksidu.

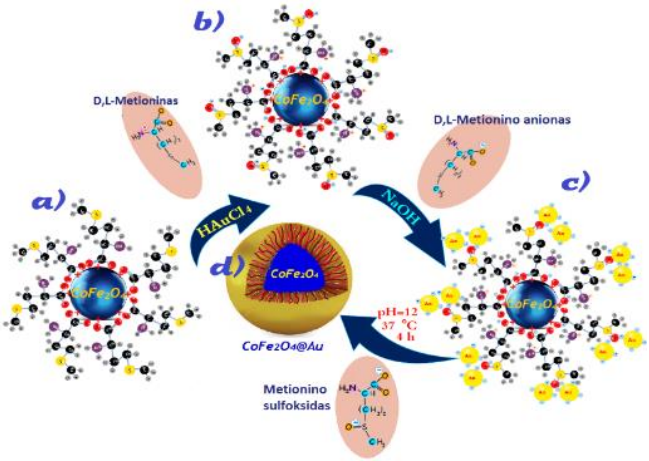

3.8 pav. Virsmų schema, atspindinti $HAuCl_4$ redukciją ant $CoFe_2O_4$ paviršiaus D,L-metionino aminorūgštimi.

Tyrimų rezultatai apibendrinti moksliniame straipsnyje: Mikalauskaitė, A.; Kondrotas, R.; Niaura, G. ir Jagminas A., *Gold Coated Cobalt Ferrite Nanoparticles via Methionine-Induced Reduction.* DOI: jp-2015-03528u. Journal of Physical Chemistry C, 2015.

3.2. $CoFe_2O_4$@AR *Nd* sudėtis ir struktūra

Siekiant ištirti aminorūgščių daromą įtaką kobalto ferito nanodalelių struktūrai, stabilumui ir magnetinėms savybėms, tirta $CoFe_2O_4$ *Nd* sąveika su įvairiomis aminorūgštimis: metioninu (Met), lizinu (Lys), cisteinu (Cys), argininu (Arg) ir histidinu (His). $CoFe_2O_4$@AA *Nd* sintetintos indentiškomis 2.1.4. skyriuje aprašytomis sąlygomis ir charakterizuotos PEM bei QD-PPMS metodais.

Skirtingų aminorūgščių daroma įtaka kobalto feritų nanodalelių dydžiui tirta PEM metodu. Iš gautų vaizdų nustatyta, jog kiekviena aminorūgštis turi skirtingą poveikį galutiniam produktui. Didesnio skersmens 11 ir 25 nm yra $CoFe_2O_4$@Arg ir $CoFe_2O_4$@Lys *Nd* (3.9 a ir b pav.). Be to, naudojant argininą, gautos $CoFe_2O_4$@Arg *Nd* yra netaisyklingos sferinės formos su būdingu plačiu dydžių pasiskirstymo intervalu (3.9 pav., a intarpas). Tuo tarpu 25 nm dydžio $CoFe_2O_4$@Lys *Nd* yra apvalios sferinės formos (3.9 pav., b intarpas). Beje, smulkių (6 nm) ir ultra smulkių (2,5 nm) dydžių *Nd* buvo gautos sintezei panaudojus histidino ir cisteino aminorūgštis (3.10 a ir b pav.).

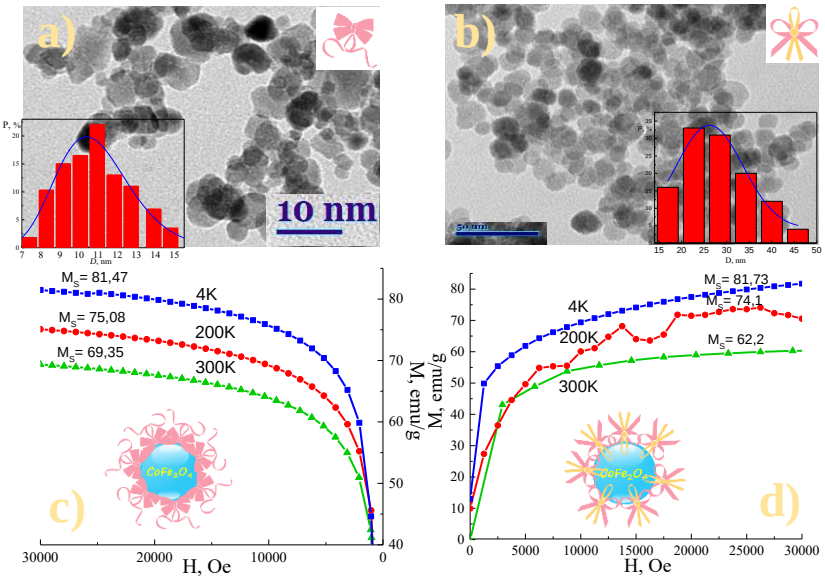

3.9 pav. a) $CoFe_2O_4$@Arg *Nd* ir b) $CoFe_2O_4$@Lys *Nd* PEM vaizdai su jų dydžių pasiskirstymo histograma. c) ir d) grafikuose pateikiamos atitinkamai $CoFe_2O_4$@Arg ir $CoFe_2O_4$@Lys *Nd* magnetinio įsistotinimo kreivės 4 K, 200 K ir 300 K temperatūrose.

Įvairių $CoFe_2O_4$@AA *Nd* magnetinio įsitotinimo (M_s) vertės buvo nustatytos pasitelkus fizikinių savybių matavimo analizės metodą *(Physical Property Measurement System*, QD-PPMS*)*. Tuo tikslu mėginiai buvo patalpinami į išorinį H_{max} = 3 Teslos stiprumo magnetinį lauką ir šaldomi 300 K, 200 K ir 4 K temperatūrose. Nustatyta, kad veikiant išoriniu magnetu smulkesnes $CoFe_2O_4$@Hys ir $CoFe_2O_4$@Cys *Nd* yra sukuriamas neigiamas magnetinis laukas. Tad grafiškai pavaizdavus gautus duomenis matomos abiejų tirtų mėginių superparamagnetinės būsenos.

Tuo tarpu didesnių $CoFe_2O_4$@Arg (3.10c pav.) ir $CoFe_2O_4$@Lys *Nd* (3.9d pav.) dydžių magnetinio įsitotinimo vertės yra aukštesnės nei ultra smulkių $CoFe_2O_4$@His (3.10c pav.) ir smulkių $CoFe_2O_4$@Cys (3.10d pav.) *Nd*.

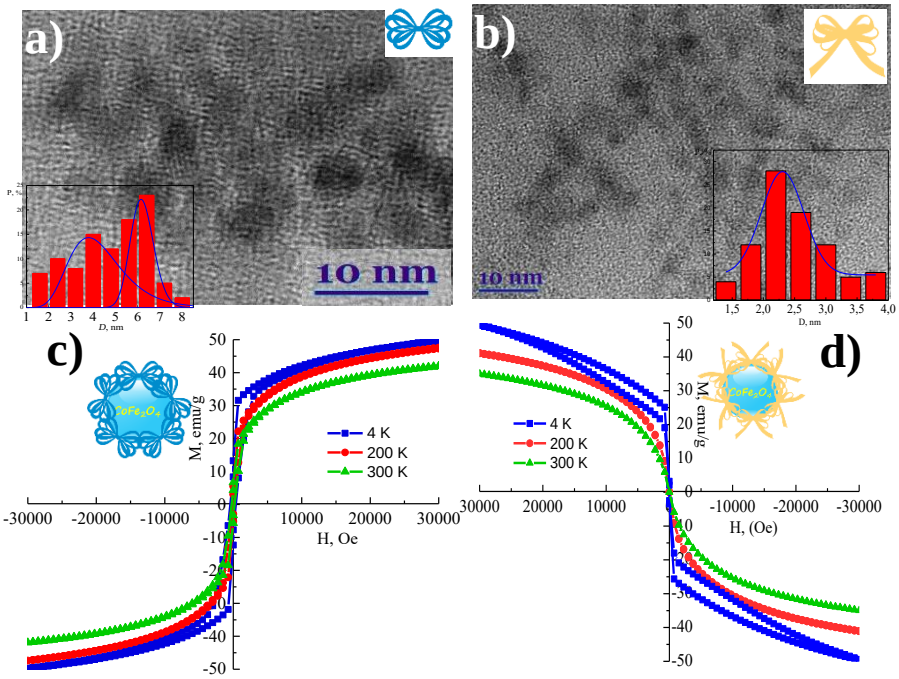

3.10 pav. a) $CoFe_2O_4$@Hys *Nd* ir b) $CoFe_2O_4$@Cys *Nd* PEM vaizdai su dydžių pasiskirstymo histograma. c) ir d) grafikai iliustruoja atitinkamai $CoFe_2O_4$@Hys ir $CoFe_2O_4$@Cys *Nd* magnetinio įsistotinimo kreives 4 K, 200 K ir 300 K temperatūrose, suteikiant kintamą ±3 Teslų dydžio išorinį magnetinį lauką.

Tai sietina su domenų dydžiais, charakteringais stambesnėms *Nd*: kad visi magnetiniai momentai būtų tvarkingai orientuoti išorinio magnetinio lauko kryptimi, jiems reikia suteikti daugiau energijos. Aukštesnėje 300 ir 200 K temperatūroje visų tirtų mėginių M_s yra žemesnė; tai sąlygoja pakankamai didelis magnetinių domenų šiluminis judėjimas, nes sukuria netvarkingą magnetinių momentų orientaciją. 3.2 lentelėje pateikiami gauti duomenys apie ištirtų $CoFe_2O_4$@AA *Nd* struktūrą, dydį ir jų skirtingas magnetines savybes.

3.2 lentelė $CoFe_2O_4$@AA *Nd* dydžiai ir magnetinio įsisotinimo vertės.

$CoFe_2O_4$@AA *Nd*	Amino r. struktūrinė formulė	Ø, dydis, nm	Įsisotinimas M_s, emu g^{-1}		
			300 K	200 K	4 K
$CoFe_2O_4$@Arg	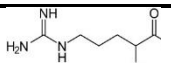	11	69,35	75,08	81,47
$CoFe_2O_4$@Lys		25	62,2	62,2	81,73
$CoFe_2O_4$@His	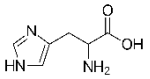	6	41,9	47,57	49,5
$CoFe_2O_4$@Cys	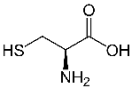	2,25	35,09	41,08	48,57

3.3. $CoFe_2O_4$@Met dekoruotų Au^0/Au^+ *Nd* sudėtis ir struktūra

Šiame darbe sferinės ~6 nm dydžio $CoFe_2O_4$@Met nanodalelės buvo susintetintos šarminiame tirpale panaudojus prekursoriais $CoCl_2$, $FeCl_3$ ir pirmą kartą – D,L-metioniną. Sintezė optimizuota hidroterminėmis sąlygomis: 130 °C, 10 val. (3. 11 pav.), parenkant prekursorių koncentracijas eksperimentiniu keliu stechiometrinės sudėties ferito *Nd* formavimui. Panaudotas D,L-metioninas stabilizavo galutinio produkto feroskystį ir ženkliai sumažino $CoFe_2O_4$@Met *Nd* tarpusavio agregaciją.

Ištyrus optimaliomis sąlygomis susintetintas $CoFe_2O_4$@Met *Nd* rentgeno spindulių difrakcija (RSD), patvirtinta jų polikristalinė špinelinė struktūra. Gautos rentgenodifraktogramos smailės 2θ pozicijose: 18.29 (111), 30.08 (220), 35.44 (311), 43.06 (400), 53.45 (422), 56.97 (511) 62.59 (440) ir 74.01 (533) gerai sutampa su $CoFe_2O_4$ (PDF kortelė 00-022-1086) etalono smailių vertėmis. Šererio formule [137] apskaičiuotas vidutinis *Nd* dydis (~6 nm)

apytikriai sutampa su peršvietimo elektroninės mikroskopijos analizės metodu gautu rezultatu, t.y. 5,8 nm (3.11 a pav).

$CoFe_2O_4$@Met *Nd* magnetinės savybės buvo ištirtos prieš ir po jų padengimo auksu. Tyrimai atlikti kambario temperatūroje mėginius veikiant išoriniu magnetiniu lauku ir užrašant jų liekamojo įmagnetėjimo reikšmes. Kaip ir tikėtasi, gauti rezultatai patvirtino spėjimus, jog $CoFe_2O_4$@Met@Au *Nd,* pasižymi silpnesnėmis magnetinėmis savybėmis (3.11 d pav.). Kaip matyti, $CoFe_2O_4$ *Nd*, pasiekta magnetizacijos soties būsena vandenilio tetrachloraurato tirpale išorinio magnetinio lauko H_{max} = 4,4 kOe zonoje sumažėja nuo pradinės 27 emu g^{-1} iki 21 emu g^{-1}. Pažymėtina, kad uždara histerezės kilpa rodo superparamagnetinę $CoFe_2O_4$@Met *Nd* būseną tiek prieš, tiek po dekoravimo auksu, būdingą smulkioms (iki 10 nm skersmens) *Nd* (3.11 d pav.).

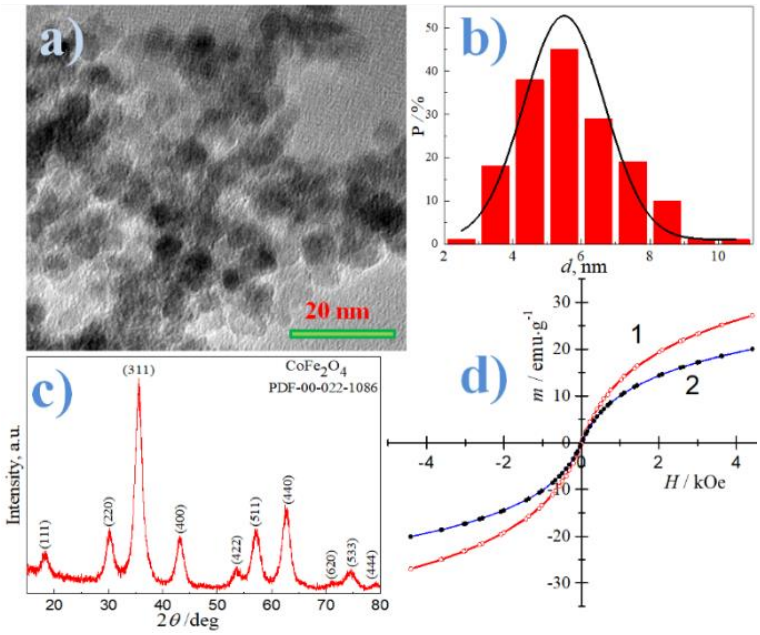

3.11 pav. a) $CoFe_2O_4$@Met *Nd* PEM vaizdas, b) suformuotų *Nd* dydžių pasiskirstymo histograma, c) $CoFe_2O_4$@Met *Nd* rentgenodifraktograma ir d) magnetinės kreivės $CoFe_2O_4$@Met *Nd* prieš (1) ir po (2) dekoravimo aukso nanodalelėmis.

Au nanokristalų susiformavusių ant $CoFe_2O_4$@Met *Nd* paviršiaus struktūra buvo ištirta ARPEM metodu ji pateikta 3.12 paveiksle. Dalelių

paviršiuje galima įžiūrėti sferinius ~2 nm skersmens iškilimus, o EDX spektras rodo, kad tai – auksas. Beje, EDX spektre matoma intensyvi Ni smailė sietina su PEM mikroskopijai naudotu profesionalaus mėginių laikikliu.

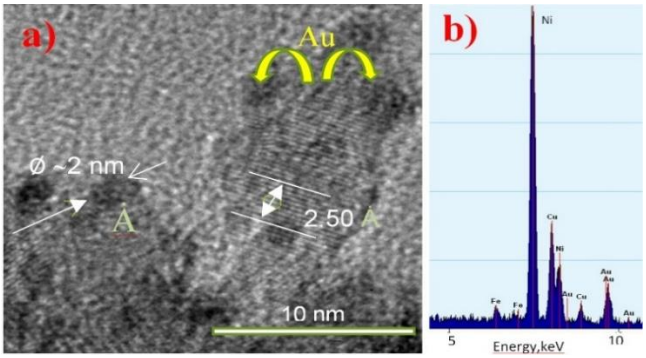

3.12 pav. a) $CoFe_2O_4$@Met@Au *Nd* ASPEM vaizdas ir b) pasirinkto ploto EDX spektras.

Siekiant nustatyti sunaudoto Au kiekį $CoFe_2O_4$@Met *Nd* ,,dekoravimui“, buvo atlikta tirpalo ICP-MS analizė prieš ir po $HAuCl_4$ redukcijos. Gauti rezultatai džiugino, nes po aukso jonų redukcijos tirpale jų sumažėjo ~99,3 %.

Tiksliau įvertinti susidariusių *Nd* paviršiuje Au nanodarinių prigimtį ir dydį, Au nanokristalus bandyta atskirti nuo $CoFe_2O_4$@Met *Nd* paviršiaus. Nustatyta, kad tai galima padaryti į 10 mmol·L^{-1} metionino vandeninį tirpalą įdėjus 10 mg išdžiovintų $CoFe_2O_4$@Met@Au *Nd* ir veikiant ultragarsu ~20 min sulaukti tirpalo spalvos nusidažymo rausvai rožine (3.13 pav.). Šis tirpalas buvo analizuojamas UV-vis spektrometru matuojant tirpalų šviesos absorbciją. Kontroliniais tirpalais naudoti D,L-metionino ir $HAuCl_4$ tirpalai. D,L-metionino tirple (3.13 paveikslas, 1 kreivė) šviesos sugerties nebuvo nustatyta; $HAuCl_4$ absorbcijos smailė nustatyta ties 291 nm (3.13 pav., 2 kreivė), kaip ir būdinga auksui, o rožinio tirpalo absorbcijos spektro intensyviausios smailės nustatytos 377 ir 522 nm ilgio bangose (3.13. pav., 3’ ir 3’’ kreivės). Remiantis literatūros šaltiniais galima teigti, jog šių smailių padėtis daugiausia priklauso nuo Au *Nd* rūšies bei dydžio [138], 377 nm smailė atitinka metalinių Au nanodalelių lokalaus paviršiaus plazmonų rezonanso juostą [139, 140]. Taigi Au nanodalelių, ,,nukeltų“ nuo $CoFe_2O_4$@Met *Nd* paviršiaus, t.y. rausvojo tirpalo LPRP maksimumo vietų

spektre padėtys rodo, kad D,L-metioninu stabilizuotų aukso *Nd* dydis yra labai mažas. Ši prielaida dar kartą patvirtinta atlikus AJM tyrimus, kuriais tiriamojo mėginio tirpalą užlašinus ant laidaus žėručio substrato paviršiaus, buvo nustatytas Au *Nd* dydis ~1-2 nm (3.14. pav.).

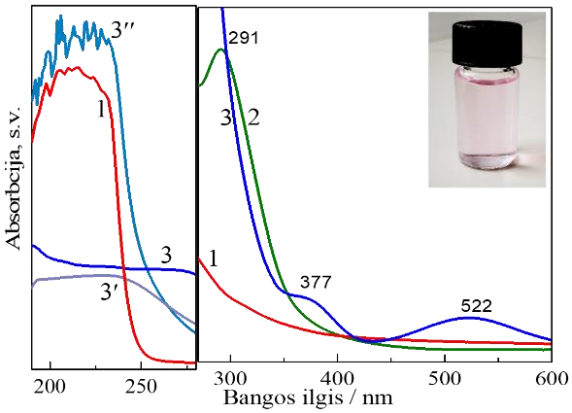

3.13 pav. UV-vis šviesos sugerties spektrai: D,L-Metionino 1), $HAuCl_4$ 2), 3) neskiesto Au nanokristalų tirpalo, gauto desorbuojant nuo $CoFe_2O_4$@Met *Nd* paviršiaus. 3′ du ir 3″ keturis kartus skiestų tų pačių tirpalų spektrai.

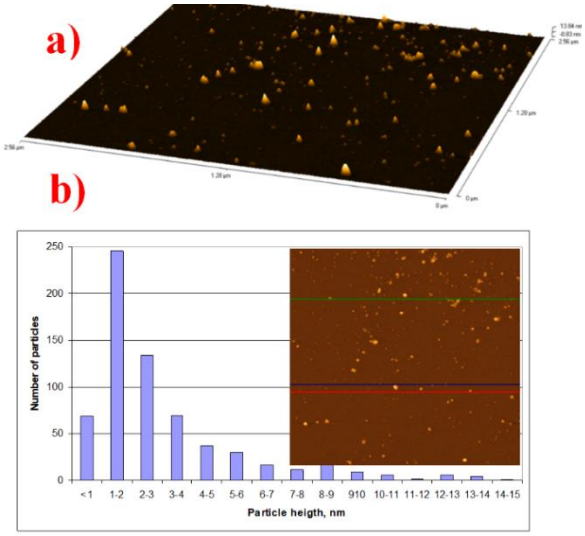

3.14 pav. Au nanokristalų, desorbuotų nuo $CoFe_2O_4$@Met *Nd* paviršiaus a) AJM 3D vaizdas ir dydžių pasiskirstymo histograma b).

Aukso nanokristalų elemetinės prigimties tyrimai buvo atlikti rentgeno fotoelektronų spektroskopijos (RFS) analizės metodu. 3.15 paveiksle pavaizduotas susintetintoms $CoFe_2O_4$@Met-Au nanodalelėms būdingas fotoelektronų spektras. Matavimai atlikti 80÷95 eV energijų diapozone identifikuojant tik Au jonų ryšių energijų spektrus. Nustatyta, kad aukso smailę sudaro dvi Au $4f_{7/2}$ ir Au $4f_{5/2}$ dedamosios su 83,94 eV ir 85,74 eV ryšio energijomis. Šios fotonų energijos priklauso skirtingų būsenų Au jonams: pirmoji 83,94 eV būdinga metaliniam Au^0 [141], o 85,74 eV yra priskirtina Au^+ [141, 142] buvimui. Nustatyta, kad Au^0 ir Au^+ jonų bendrai yra 13,7 % skaičiuojant visą mėginyje identifikuotą auksą; jame Au^+ sudaro 1,39 % (1 %). Šie rezultatai gauti pirmą kartą. Iki šiol, literatūroje nėra jokios informacijos apie magnetinių nanodalelių paviršiaus padengimą Au^0/Au^+ nanokristalų hibridiniais dariniais ir tokių apvalkalų savybes.

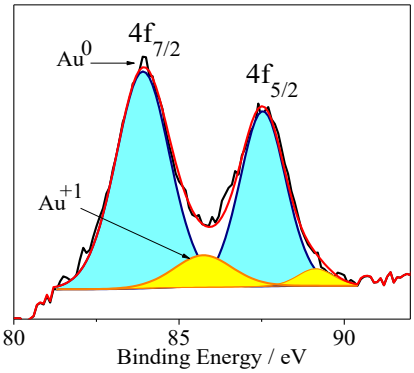

3.15 pav. Au 4f dekonvuliuotas rentgeno fotoelektroninis spektras (XPS).

3.3 lentelė $CoFe_2O_4$@Met-Au *nd* elementų ryšio energijos ir koncentracija XPS duomenimis.

Elementai	Smailės *BE*	*FWHM*, eV	Plotas (*P*), CPS	Atomų, %
Au4f	83.94	1.96	12435.07	1.39
C1s	284.87	2.88	18041.56	36.02
N1s	399.98	2.24	2647.25	3.02
O1s	530.21	3.03	55974.26	40.37
Fe2p3	710.75	3.70	63210.72	12.68
Co2p3	780.67	3.29	36815.35	6.47

Taigi šiais tyrimais nustatyta, jog kobalto ferito *Nd* sintezei panaudojant metionino aminorūgštį galime kontroliuoti ne tik magnetinių *Nd* augimą, jų stabilumą, bet ir paviršiaus padengimą Au^0/Au^+ nanodalelėmis [141].

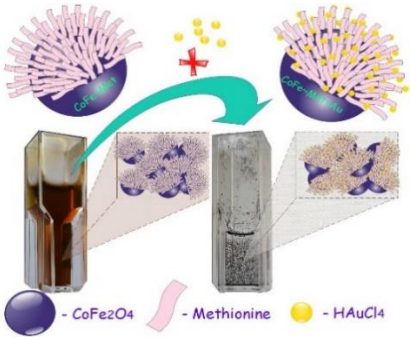

3.16 pav. $CoFe_2O_4$ *Nd* paviršiaus padengimo Au^0/Au^+ nanokristalais schema.

Mūsų pasiūlytas $CoFe_2O_4$@Met *Nd* paviršiaus padengimo Au^0/Au^+ nanokristalais metodas imobilizuojant *Nd* paviršiuje metionino aminorūgštį buvo publikuotas 2017 m. *Belstein Journal of Nanaotechnology*.

3.4. Au^0/Au^+ *Nd* sudėtis ir struktūra

Šiame tyrime Au^0/Au^+ nanokristalais buvo padengtos susintetinto laboratorijoje magnetito Fe_3O_4@Met nanodalelės; jų dekoravimo auksu receptūros pateiktos 2.2.5. skyriuje. Gautų Fe_3O_4@Met *Nd* PEM vaizdas pateiktas 3.17 a) paveiksle, o b) dalyje pateiktas šių *Nd* aukštos skiriamos gebos peršvietimo elektronų mikroskopijos vaizdas. Pastarąja nustatyta, kad susintetintos *Nd* yra magnetitas su jam būdingu atomų 2,5 Å tarpplokštuminiu atstumu.

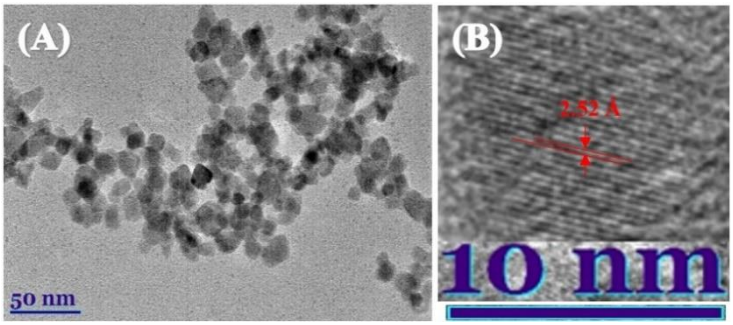

3.17 pav. Fe_3O_4@Met *Nd* PEM vaizdas (A) ir *Nd* smulkioji struktūra ASGPEM vaizde (B).

Užrašyta Fe_3O_4@Met *Nd* rentgenodifraktograma pateikta 3.18 pav. Jos pagrindinės smailės *2θ* pozicijose: 18.28, 30.08, 35.43, 43.06, 53.42, 56.94, 62.53, 70.94, 73.97, 74.97 ir 78.93 atitinka polikristalinę Fe_3O_4 struktūrą lyginant su etalonine magnetito rentgenodifraktograma (PDF kortelė 04-005-4319) ir gerai dera su jo (111), (220), (311), (400), (422), (511), (440), (620), (533), (622) ir (444) plokštumų vertėmis (3.18 a pav.). Fe_3O_4@Met *Nd* dydis buvo įvertintas pasitelkiant Halder–Wagner skaičiavimus ir gautas dydžių pasiskirstymas su maksimumu ~11,9 nm apytiksliai sutampa su peršvietimo elektronų mikroskopijos gautu rezultatu (11 nm) (3.18 b) pav.).

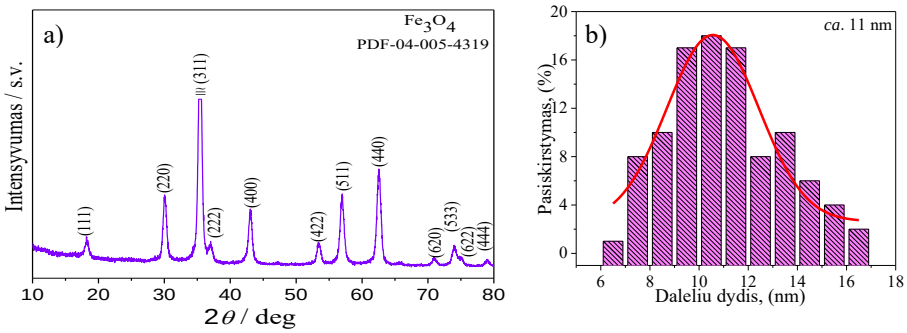

3.18 pav. a) Fe_3O_4@Met *Nd* rentgenodifraktograma ir b) *Nd* dydžių pasiskirstymo stupelinė diagrama.

Fe_3O_4@Met-Au *Nd* buvo tiriamos tiek PEM, tiek aukštos skiriamosios gebos peršviečiamąja elektronų mikroskopija (ASGPEM). PEM vaizdai, pateikti 3.19 paveikse, rodo gausybę tamsių taškelių, nusėdusių ant *Nd* paviršiaus (A) dalis. Jų smulkios struktūros tyrimai ASGPEM (3.19 pav., B) parodė, kad taškeliai priskirtini auksui.

Tyrimų duomenys, pateikti 3.20 paveiklse, yra ,,nukabinti“ nuo auksuotų magnetito *Nd* aukso dariniai. Jie buvo tiriami PEM ir skenuojančia 3D atomo jėgos mikroskopija. Ištyrus ,,nukabintų“ *Nd* PEM ir AJM vaizdus (3.20 A ir B paveikslai) nustatyta, kad Au^0/Au^+ *Nd* dydis nėra vienodas ir varijuoja 1 – 5 nm ribose. Nanodalelių dydžių pasiskirstymo diagrama (3.20 pav.,C) parodė, kad didžiausias jų kiekis yra 1 – 2 nm skersmens.

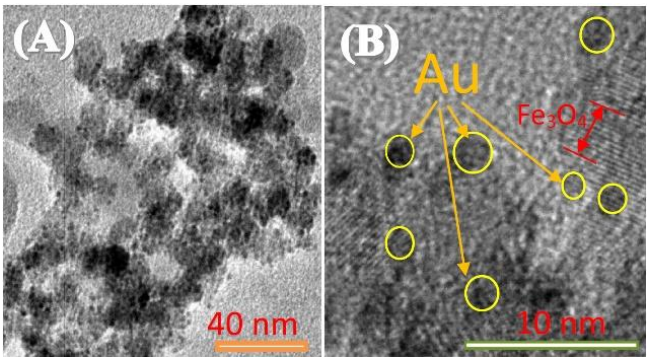

3.19 pav. a) Fe_3O_4@Met *Nd* PEM ir b) ASGPEM vaizdai.

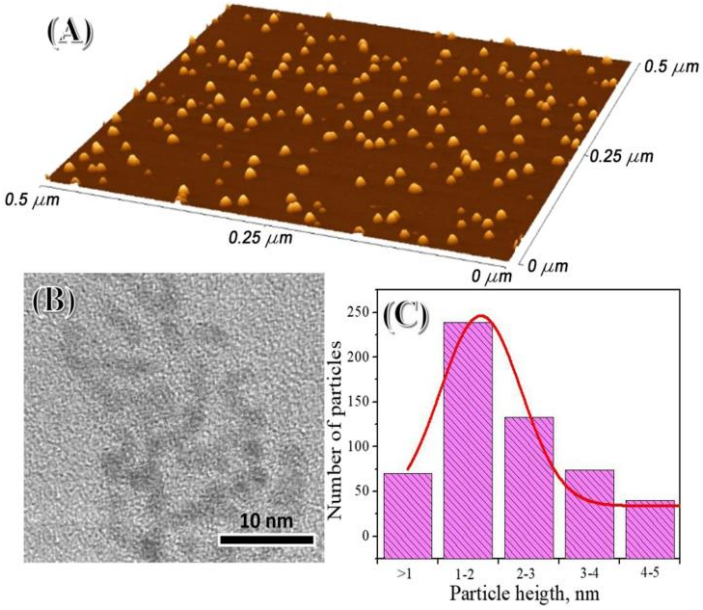

3.20 pav. a) Au^0/Au^+ *Nd* 3D AJM, b) PEM vaizdai ir c) dydžių pasiskirstymo diagrama.

3.5. Au^0/Au^+ *Nd* antibakteriniai tyrimai

Žinia, kad Cis-platina yra vienas efektyviausių priešvėžinių preparatų [143]. Šio vaisto efektyvumas yra grindžiamas vėžinių ląstelių ,,nužudymu“ Pt^+ jonais, esančiais Pt^0/Pt^+ kombinacijoje. Vedami šios idėjos mes ištyrėme ultra smulkių Au^0/Au^+ Nd, sukurtų 3.3. skyriuje aprašytu keliu, antimikrobinę

elgseną. Tyrimai buvo atlikti su daugumai antibiotikų atspariomis gram-teigiamomis: *Staphylococcus aureus (MRSA*) (ATCC 433300), *Micrococcus luteus* (GTC-BTL, B-30S) ir gram-neigiamomis: *Acinetobacter baumannii* (ATCC BAA-747) bei *Salmonella enterica* (GTCBTL, B-25) bakterijomis. Šio tyrimo metu mikroorganizmai buvo inkubuojami M9 skystoje terpėje kartu su 70 arba 30 mg·L^{-1} Au^0/Au$^+$ *Nd* arba atitinkamai su Fe_3O_4@Au@Met *Nd* ir suskaičiuojami po 24 val. jų maišymo palaikant nuolatinę 37°±1°C temperatūrą. Neigiamai kontrolei įvertinti tirta 100 mg·L^{-1} švarios D,L-metionino aminorūgšties ir 1 g·L^{-1} Fe_3O_4@Met *Nd* įtaka mikroorganizmų kolonijų augimui.

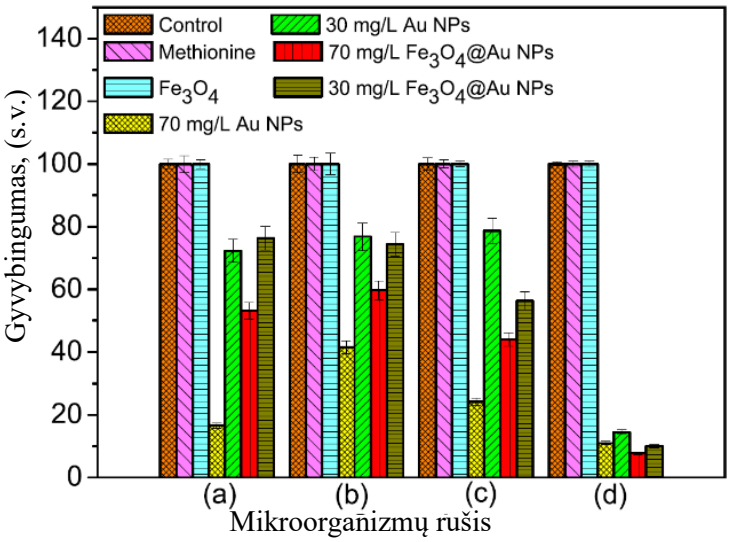

3.21 pav. Au^0/Au$^+$ *Nd* ir Fe_3O_4@Au *Nd* antibakterinio aktyvumo diagramos po 24 val. jų inkubacijos su gram-neigiamomis A. baumannii (a), S. enterica (b) ir gram-teigiamomis S. aureus (MRSA) (c) bei M. luteus (d) bakterijomis. Palyginimui pateiktos kolonijų gyvibingumo histogramos su švaria D,L-metionino aminorūgštimi ir magnetitu.

Pateiktose stulpelinėse diagramose (3.21 pav.) lengvai matyti, kad Au^0/Au$^+$ *Nd* ir Fe_3O_4@Au@Met *Nd* rodo intensyviausias baktericidines savybes prieš *M. luteus* bakterijų šeimą. Šie rezultatai taip pat patvirtina teiginį, jog žmogui patogeniniai mikroorganizmai, tokie kaip *M. luteus*, yra virulentiški ir atsparūs antibiotikams [144]. Taip pat nustatyta, jog didinant Au *Nd* koncentraciją, mažėja bakterijų kolonijų skaičius. Lyginant su

kontrole, 70 mg·L^{-1} Au^0/Au$^+$ *Nd* mėginių baktericidinis efektyvumas siekia 84,4–58,5 % gram-neigiamoms bakterijoms ir net 89,1–75,7 % gram-teigiamoms. 3.22 paveiksle pavaizduotos petri lėkštelės su maistinių medžiagų agarinėje terpėje augintomis gram-neigiamomis ir gram-teigiamomis bakterijomis. Ženklus mikroorganizmų, pabuvojusių kartu su Au^0/Au$^+$ *Nd,* skaičiaus sumažėjimas yra akivaizdus. Be to, pastebėta, jog sumažinus Au^0/Au$^+$ *Nd* koncentraciją iki 2,3 kartų, jų įtaka tirtų mikrooganizmų kolonijų augimui nėra vienoda: *A. baumannii* atveju kolonijų išaugimas padidėjo 3,05, *S. enterica* – 2,52, *S. (MRSA)* – 1,35 ir *M. luteus* – 1,04 kartų. Šie rezultatai patvirtina ir įrodo, jog pasirinkti mikroorganizmai yra tikrai specifiški ir unikalūs savo patogeniškumu tiek tirtoms Au^0/Au$^+$ *Nd,* tiek ir gyviems organizmams.

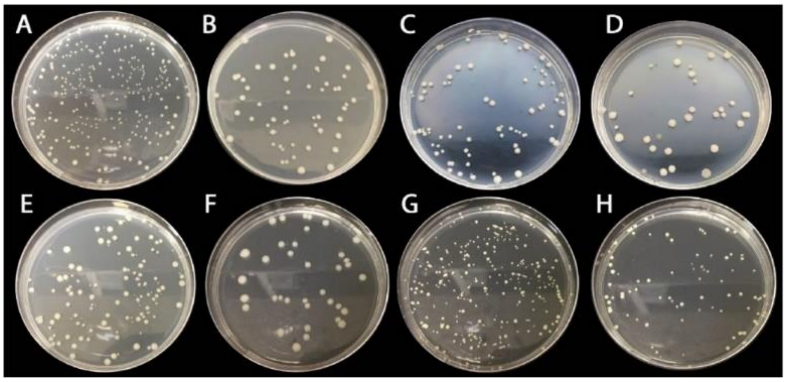

3.22 pav. Au^0/Au$^+$ *Nd* antimikrobinis aktyvumas gram-neigiamų (A–B) *A. baumannii*, (C–D) *S. enterica* ir gram-teigiamų (E–F) meticilinui-atsparių *S. aureus*, bei (G–H) *M. luteus* mikroorganizmų atžvilgiu. Visi mirkoorganizmai buvo auginami 24 val. skystoje M9 terpėje be (a, c, e, g) ir su (b, d, f, h) 70 mg·L^{-1} Au^0/Au$^+$ *Nd*.

Lyginant gautus rezultatus su pateikta medžiaga literatūroje, galima teigti, jog jie taip pat patvirtina K. Zheng grupės gautus rezultatus, jog Au^0 *Nd,* kurių dydis yra apie 6 nm, neturi antibakterinių savybių prieš *B. subtilis* ir *E. coli* mikroorganizmus [145]. Didžiausią atsparumą tiek ultra smulkioms aukso, tiek Fe_3O_4@Au@Met nanodalelėms turėjo *S. enterica* tirtos rūšies mikrooganizmai. Taip pat, pažymėtina, jog Fe_3O_4@Met *Nd* ir D,L-metionino aminorūgšties atvejais buvo gauti tokie pat kolonijas formuojančių vienetų kiekiai, kaip ir kontroliniame mėginyje. Remiantis metionino antimikrobiniais aktyvumo tyrimais, šis aukso kristalų ir magnetito stabilizuojantis agentas yra

netoksiškas, biosuderinamas ir gali būti lengvai metabolizuojamas bakterijų [146].

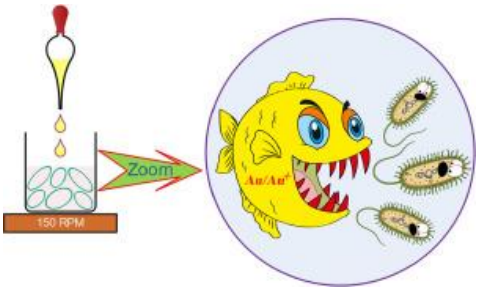

3.23 pav. Au^0/Au^+ *Nd* baktericidiškumo schema.

Šių tyrimų rezultatai buvo publikuoti 2019 metais prestižiniame *Materials Science & Engineering C* mokslo žurnale.

3.6. Aukso nanoklasterių sintezės tyrimai

Magnetinių *Nd* paviršiaus dekoravimo auksu $HAuCl_4$ tirpaluose ypatumai buvo ištirti nustatant susintetintų itin smulkių aukso *Nd*, priskirtinų klasteriams, liuminescenciją. Klasteriams priskiriamos nanodalelės mažesnės nei 5 nm. Jų valentinės elektronų juostos plotis (energijų lygmenų tarpai) įprastai yra didesni lyginant su *Nd* dydžiu.

Literatūros apžvalgos 1.3.1. skyriuje yra aprašytas Xie ir bendradarbių 2009 m. sukurtas raudonai liuminescuojančių aukso klasterių sintezės metodas $HAuCl_4$ redukavimui panaudojant jaučio serumo albuminą (JSA) [76]. Šis klasteris pasižymėjo stipria raudonos šviesos liuminescencija ir veikė 7 % kvantiniu našumu. Ieškodami pigesnių pakaitalų JSA, mes atlikome aukso klasterių sintezę su įvairiais sportininkų naudojamais maisto papildais. Siekta susintetinti 1 nm ir 3 nm dydžių aukso klasterius ir palyginti jų liuminescencines savybes. Sintezės atliktos stiklo reaktoriuje palaikant nuolatinę 37 °C temperatūrą 20 val. Naudoti vandeniniai šarminiai $HAuCl_4$ tirpalai (pH 12.2) aukso jonų redukcijai papildomai ištirpinant įvairius maisto papildus.

3.6.1. Aukso klasterių fotoliuminescenciniai tyrimai

Siekiant rasti maisto papildą raudonai liuminescuojančio klasterio sintezei, buvo išbandyti šakotųjų aminorūgščių ‚AAFS‘, 100 % pieno miltelių ir 100 % išrūgų miltelių priedai. Susintetintų aukso klasterių liuminescenciniai spektrai yra pateikti 3.24 pav. Visi šie papildų kompleksai yra vartojami sportininkų raumenų masės padidinimui. Aukso nanoklasteriai, susintetinti su šakotų aminorūgščių papildu po sužadinimo lazeriu 470 nm ilgio šviesa, pasižymėjo itin intensyvia raudonos šviesos (690 nm) emisija. Ištyrus jų emisijos stabilumą per kelias paras pastebėtas tik nežymus jos intensyvumo sumažėjimas (3.24 b pav.).

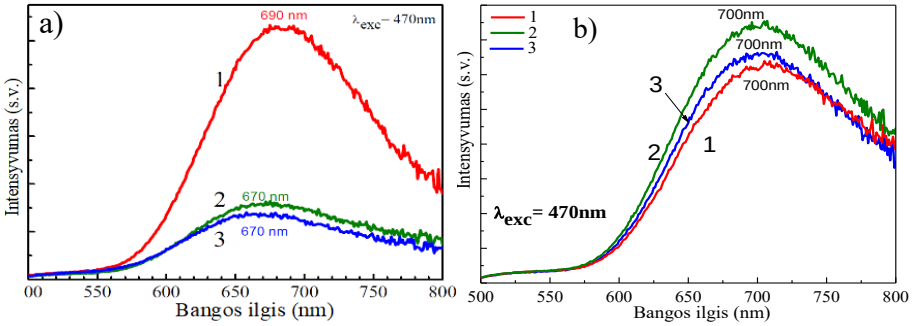

3.24 pav. Liuminescenciniai Au klasterių spektrai, gauti: a) panaudojant skirtingus maisto papildus: 1) ‚AAFS’; 2) 100% pieno miltelių kompleksą ir 3) 100% išrūgų miltelius. B) ‚AAFS’ Au klasterio spektrai: 1 pradinis, 2 po paros, 3 po dviejų parų.

Siekiant optimizuoti *AuNkl* sintezę buvo ištirta susintetintos medžiagos liuminescencijos intensyvumo priklausomybė nuo sintezei panaudoto ‚AAFS‘ koncentracijos. Gauti rezultatai su skirtingomis papildo koncentracijomis ir tirpalų pH vertėmis pateikti atitinkamai 3.25 paveikslo a) ir b) dalyse. Iš gautų liuminescencijos intensyvumo kreivių buvo nustatyta, jog susintetinti *AuNkl* pasižymi intensyviausia liuminescencija 670 – 690 nm srityje kai sintezei panaudota 16 – 20 mg/ml AAFS (3.24 a pav., kreivės 3 ir 4), o reakcijos tirpalo pH ~ 12,0 (2.24 b pav., 3 kreivė).

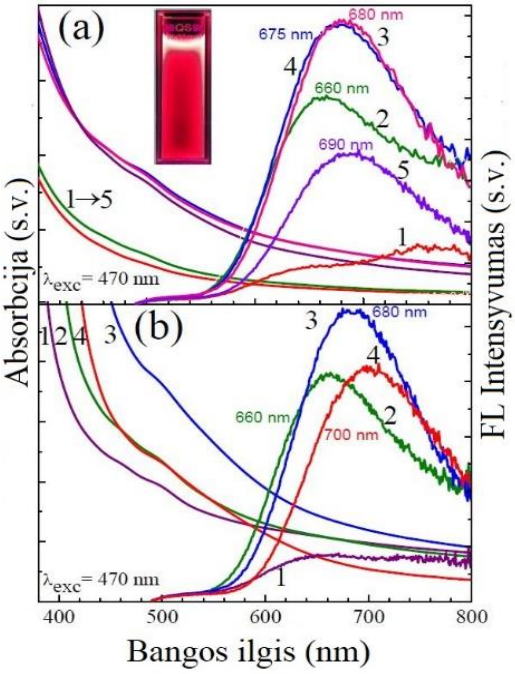

3.25 pav. Laboratorijoje susintetintų Au klasterių absorbcijos ir liuminescencijos spektrai. *AuNkl* sintezė atlikta (a): 3.0 μM/mL $HAuCl_4$ tirpale redukcijai panaudojant: (1) 8; (2) 12; (3) 16; (4) 20 ir (5) 24 mg/mL ‚AAFS'. (b) dalyje pateikti produktų, susintetintų su 20 mg/mL ‚AAFS' priklausomai nuo reakcijos tirpalo pH: (1) 11.0; (2) 11.5; (3) 12.0 ir (4) 12.5 spektrai. Visais atvejais sintezė buvo vykdyta 37 ºC temperatūroje. Jos trukmė – 20 val. Spektrai gauti žadinant produktus 470 nm ilgio šviesos banga.

Nustatyta, jog sintezei naudoto maisto papildo koncentracija viršija 20 mg/ml, o pH – 12,5, produkto liuminescencija ima slopti, o liuminescencijos smailė pasislenka per 10 – 20 nm didesnės bangos ilgių srities link (2.25 a pav., 5 ir 2.25 b pav., 4 kreivės). Papildo koncentracijai esant mažiau 8 mg/ml, o tirpalo pH – mažiau 11, liuminescencija pasižyminčių *AuNkl* formavimosi nebevyksta.

3.26 a) paveiksle pavaizduotas susintetintų optimaliomis sintezės sąlygomis aukso klasterio, naudojant ‚AAFS', fotoemisijos spektrai kintant sužadinimo šviesai (a) ir emisijos gesimo kreivė po sužadinimo 690 nm šviesa (b). Akivaizdu, kad *AuNkl* liuminescencijos intensyvumas priklauso ir nuo juos sužadinamos šviesos intensyvumo. Stipriausiai liuminescencuoja aukso klasteriai, sužadinti 405 nm ilgios šviesos banga (3.26 a pav. 1 kreivė).

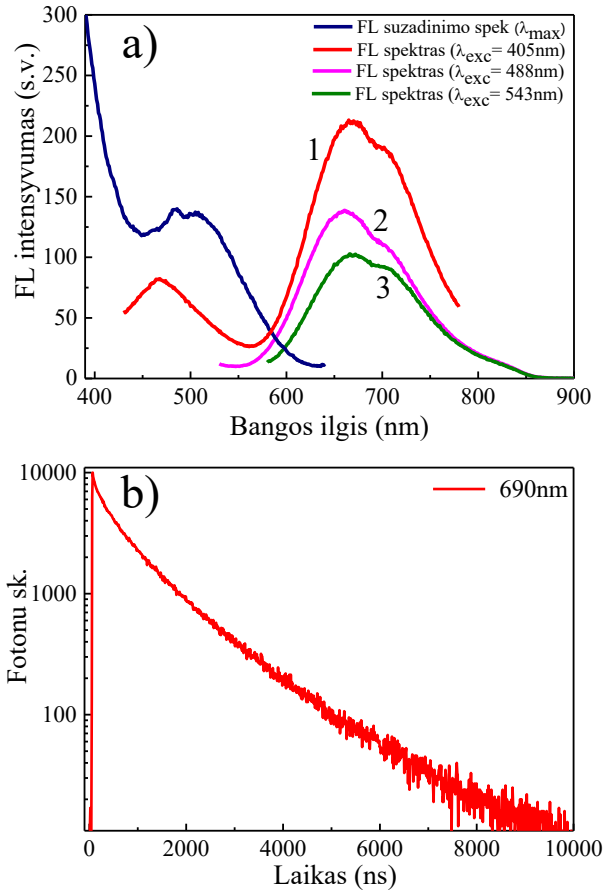

3.26 pav. a) Liuminescenciniai Au klasterių spektrai juos sužadinus 405 nm (1), 488 nm (2) ir 543 nm (3) ilgio šviesa. Paveikslo b) dalyje pateikta Au klasterio, sužadinto 690 nm šviesa (liuminescensijos maksimumas), emisijos gesimo kinetinė kreivė.

3.26 b paveiksle pavaizduota tirtų *AuNkl* gyvavimo trukmė juos sužadinus 690 nm ilgio šviesa. Nustatyta, jog *AuNkl* susintetinti panaudojant ‚AAFS‘ maisto papildą $HAuCl_4$ redukcijai pasižymi ~2 μs gyvavimo trukme ir neeksponentiniu jos slopimu. *AuNkl* kvantinio našumo įvertinimui buvo pasinaudota Jellium metodu panaudojant etaloninį 2-[2-[2-(4-dimetilaminofenil)-vinil]-6-izopropil-piran-4-ilidene]-malononitrilas (DCM) metanolio mišinį. Jo kvantinis našumas yra 33 – 34 % [72]. Nustatyta, jog sintezei panaudojus ‚AAFS‘ raudonai liuminescuojančių *AuNkl* kvantinis našumas siekia kaip ir JSA atveju – 7.0 %.

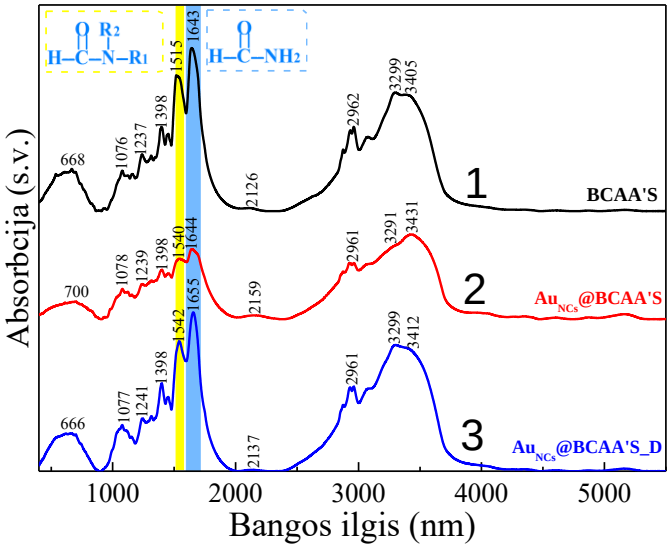

3.27 pav. Medžiagų infraraudonieji spektrai: AAFS maisto papildo (1) ir susintetintų aukso klasterių prieš (2) ir po jų (3) dializės.

AuNkl paviršių supančių funkcinių grupių įvertinimui buvo užrašyti FTIR spektrai. Jie pateikti 3.27 paveiksle. Nesunku pastebėti, kad ‚AAFS' spektro (1 kreivė) pagrindinius virpesius demonstruoja ir susintetinti produktai. Tai rodo, kad ‚AAFS' maisto papildas ne tik redukuoja $HAuCl_4$, bet ir stabilizuoja susidariusius *AuNkl*. Identifikuotos dominuojančio paviršiaus grupės atitinka amidą I (CO ruožas) 1658-1643 cm^{-1} ir amido II (CN ir NH) juosta 1515-1544 cm^{-1} (3.27 pav.) [147].

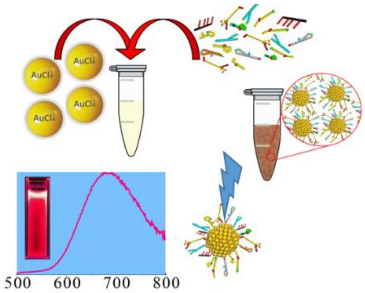

3.28 pav. Raudonai liuminescuojančių *AuNkl* sintezės schema.

Šių tyrimų rezultatai buvo publikuoti 2016 metais *Biointerface Research in Applied Chemistry* mokslo žurnale.

4. IŠVADOS

1. Nustatyta kobato ferito *Nd* auksavimo procedūrų, neutralizuojant jų paviršių vitaminu C ir vėliau redukuojant mažos koncentracijos vandenilio tetrachlorauratą, seka.

2. Sukurtas įvairaus dydžio kobalto ferito *Nd* paviršiaus padengimo auksu procesas, panaudojant $HAuCl_4$ redukcijai D,L-metionino aminorūgštį.

3. $CoFe_2O_4$@Au *Nd* suformavimas patvirtintas RSD, PEM, EDX, aukštos skiriamosios gebos PEM tyrimais, Mesbauerio spektrų kaita, *Nd* vidutinio dydžio padidėjimu bei FTIR spektrais.

4. FTIR spektrų analize įrodyta skirtinga dopamino hidrochlorido adsorbcija ant $CoFe_2O_4$ ir $CoFe_2O_4$@Au *Nd* paviršiaus.

5. Optimizuota aukso klasterių sintezė pirmą kartą panaudojant šakotųjų aminorūgščių maisto papildą.

6. Gauti aukso klasteriai pasižymi raudona liuminescencija 670-710 nm šviesos bangų srityje ir ~7 % kvantiniu našumu, artimu klasteriams, susintetintiems su jaučio serumo albuminu.

5. SUMMARY

Introduction

Curently, nanomedicine is a rapidly developing area of nanotechnology medical science. It is imputable to the newly discovered and applied in nanoelectronic biosensors, molecular nanotechnology and etc., nanometer-sized particles, which have exceptional chemical, physical and optical properties. The goal of nanomedicine is the comprehensive monitoring, control, treatment, protection, and enhancement of human biological systems at the molecular level using engineering devices and nanostructures. These novel ideas combine the optical, magnetic, electronic, and structural properties of particles.

Theranostics is a new area of nanomedicine, mostly associated with nanotechnologies. It is applied for the production and to developing of nanoparticles that might improve the diagnosis of tumours, ensure more accurate monitoring of the diseases and, at the same time, induces a theranostic effect. Regarding the current shortcomings of diagnostic and therapeutic methods, scientists paid much attention to biologically compatible and targeted nanometer-size magnetic nanoparticles and gold nanoclusters (*AuNCs*) with intense luminescence, which combination of properties might allow for the creation of dual-function composites.

$MeFe_2O_4$@Au *NPs,* due to their small size and biocompatibility, are eliminated more slowly from the body. Therefore, researchers believe that biocompatible, small, NIR-fluorescent, gold covering magnetic nanoparticles are promising composites for the development of in vivo tumour imaging and targeted therapy.

Major goal

Search for reliable methods of coating magnetic *NPs* with gold in order to synthesize the gold clusters, characterization them and show possible application areas of the obtained products in nanomedicine.

Objectives

✓ Optimize the hydrothermal synthesis of magnetic nanoparticles for their stabilization using amino acids.

✓ Investigate the possibilities of magnetic *NPs* efficient surface covering with gold using amino acids as reducers.

✓ Investigate the synthesis of red luminescent gold clusters using new bioreducers and Hydrogen tetrachloroaurate ($HAuCl_4$).

✓ Determine the composition, structure, enclosure, and the formation mechanism of synthesized products.

✓ Investigate the antibacterial properties of Au^0/Au^+ *NPs*

✓ Investigate the possibilities of using the obtained Au clusters for cell imaging.

Statements of defence

1. Immobilization of D,L-methionine amino acid on the surface of magnetic *NPs* in order to cover their surface with gold nanocrystals (*NCs*) and shell.
2. Au^0/Au^+ nanocrystals can be "detached" from the surface of $CoFe_2O_4$@Au and Fe_3O_4@Au *NPs* with an excess of D,L-methionine.
3. Au^0/Au^+nanocrystals have bactericidal properties against antibiotic-resistant pathogens.
4. Gold nanoclusters demonstrating red luminescence can be synthesized in the environment of low-cost branched amino acid food supplements.

The practical value of dissertation

✓ Established and optimized compositions of aqueous solutions for 2, 5, and 15 nm size $CoFe_2O_4$ *NPs* synthesis by co-precipitation and controlled covering of their surface with gold nanocrystals and shell.

✓ Introduced the gold deposition mechanism on magnetic $CoFe_2O_4$@Au *NPs*.

✓ Investigated the adsorption of dopamine hydrochloride on the surface of $CoFe_2O_4$ and $CoFe_2O_4$@Au *NPs*.

✓ Established and optimized compositions of aqueous solutions for Fe_3O_4 *NPs* synthesis and their surface covered by the Au^0/Au^+ gold nanocrystals.

✓ Efficient Au^0/Au^+ ultrafine nanocrystals have been proposed "detached" from the Fe_3O_4 *NPs* surface.

✓ Investigated the bactericidal properties of Au^0/Au^+ nanocrystals against extremely high antibiotic resistance pathogens.

✓ Established a new and cheap bioreductor for *AuNkl* synthesis.

✓ Investigated the composition, structure, and luminescence properties of the synthesized gold clusters.

Among various functional nanostructures, gold-coated and decorated magnetic nanoparticles (*NPs*) have attracted a lot of attention because of their biological compatibility and recently demonstrated potential applications in nanomedicine, biosensing, drug delivery, cells separation, etc.

The coprecipitation process in aqueous solution is perhaps the simplest and the most efficient chemical way to synthesize iron oxide nanoparticles (*SPIONs*) The method is based on the chemical reactions taken place in an aqueous monophasic liquid medium, allowing the control of both the nucleation and growth of iron hydroxide nuclei. The synthesis procedure consists of the precipitation of ferric and ferrous hydroxides by addition of a base(e.g., NH_4OH or NaOH) to a solutions of Fe(III) and Fe(II) salts (eq 1). Then, the gelatinous iron hydroxide precipitate is isolated by magnetic decantation or centrifugation and treated with the concentrated base or acid solutions to electrostatically stabilize the ferrofluid. Alternatively, the iron hydroxide precipitate can be sterically stabilized to the resulting Fe_3O_4 or other ferrites by heating in the presence of a suitable surfactant, namely, oleic acid (OA) [7]. According to Sugimoto and Matijevic [13], magnetite *NPs* can be also formed by oxidation of ferrous hydroxide suspensions [14]. It is commonly accepted that using these co-precipitation ways, it is possible to fabricate *NPs* in predetermined shapes and size by adjusting the solution pH, concentration of precursors, as well as the nature and concentration of the capping agents [15].

The syntheses of iron oxide-based *NPs* under hydrothermal treatment conditions can be also attributed to a separate co-precipitation approach. In the case of Fe(II) and Fe(III) salts, a high pressure induced hydrolysis of these ions proceeded by the reaction:

$$Fe^{2+} + Fe^{3+} + 8OH^- = Fe_3O_4 + 4H_2O \qquad (1)$$

results in the facile one-pot formation of magnetite *NPs*.

High efficiency, crystallinity, and in situ functionalization of magnetite *NPs* with the desired linkers are typical advantages of these *NPs*. In many cases, however, these *NPs* are not monodisperse and prone agglomerate in aqueous solutions and physiological fluids. To prevent agglomeration, their surfaces are covered with positively charged polymers [7]. As a matter of fact, the attached molecules changed the surface charge and chemical properties of

the magnetic core. Moreover, these capping layers might affect the capability to coat them with gold.

Gold shells can be formed on the surface of magnetite nanoparticles using separately prepared the gold seeds that can be further attached to the surface of magnetic *Nps* by coprecipitation together with or after formation of a polymeric shell. The direct deposition methods are suitable for the covering or decoration of magnetic iron oxide nanoparticles by perchloric acid [9, 10], sodium citrate [41], hydroxylamine [39], followed by interactive additions of chloroauric acid and a reducing agent to pre-treated *NPs* suspension have been proposed.

Recently, fluorescent gold clusters exhibiting low toxicity have received significant attention for bioimaging. Consequently, several methods have been proposed for the synthesis of blue and red-fluorescent gold clusters and their application in nanomedicine. Among them, protein directed synthesis of red-luminescent gold clusters have been considered as more prospective.

The synthesis of biocompatible, red-luminescent *AuNCs* with emission peak at 640 nm and QY ≈6% has been first reported by Ying et al. [76]. The authors used encapsulation of Au (III) ions by thiol groups, present in cysteine residues, in alkaline solution of bovine serum albumin (BSA) and the subsequent reduction. Similarly, for cells bio imagining, Liu et al. [82] successfully prepared water-soluble fluorescent *AuNCs* capped with dihidrolipoic acid and modified with polyethylene glycol, BSA and streptavidin, demonstrating that these proteins are advantageous as reducing and stabilizing agents. During past several years, *AuNCs* have been also successfully synthesized using other proteins such as lysozyme [77], trypsin [87], pepsin [83], bovine [79], human insulin [82], and horseradish peroxidase [80]. The formation of fluorescent *AuNCs* in protein-containing solutions was attributed to complexation of $AuCl_4^-$ ions to Au (I) and the subsequent reduction to Au^0 by tyrosine or tryptophan residues [89] and stabilization with cysteine residues, although exact formation and stabilization mechanisms are still an open question.

Methods

The morphology of as-grown products was investigated by a transmission electron microscope (TEM, model MORGAGNI 268) operated at an accelerating voltage of 72 keV. The average size of nanoparticles was

estimated from at least 200 species observed in their TEM images. High-resolution transmission electron microscopy (HRTEM) studies of as-synthesized products were performed using a LIBRA 200 FE at an accelerating voltage of 200 keV.

X-ray powder diffraction experiments were performed on a D8 diffractometer (Bruker AXS, Germany), equipped with a Gobel mirror as a primary beam monochromator for Cu Kα radiation.

X-ray photoelectron spectroscopy (XPS) measurements were carried out to obtain information about the elemental chemical states and surface composition of the $CoFe_2O_4$ and $CoFe_2O_4$@Au nanoparticles. Upgraded Vacuum Generator ESCALAB MKII spectrometer fitted with a new XR4 twin anode was used. The nonmonochromatized Mg K_α X-ray source was operated at $h\nu$ = 1253.6 eV with 300 W power (20 mA/15 kV), and the pressure in the analysis chamber was lower than 5 × 10−7 Pa during spectral acquisition. The spectra were acquired with an electron analyzer pass energy of 20 eV for narrow scans and resolution of 0.05 eV and with a pass energy of 100 eV for survey spectra. All spectra were recorded at a 90° take off angle and calibrated using the C 1s peak at 284.6 eV. The spectra calibration, processing, and fitting routines were done using Avantage software (5.918) provided by Thermo VG Scientific. Core level peaks of Fe 2p, Co 2p, Au 4f, C 1s, and O 1s were analyzed using a nonlinear Shirley-type background, and the calculation of the elemental composition was performed on the basis of Scofield's relative sensitivity factors.

The FTIR spectra were recorded in transmission mode with a Bruker Vertex 70v vacuum FTIR spectrometer over the wavenumber range of 4000–400 cm^{-1}. A 7 mm thick KBr discs were prepared under high pressure by mixing the powdered samples with KBr powder. Samples for AFM measurements were prepared by casting a drop (20 μL) of gold *NPs* solution on freshly cleaved V^{-1} grade muscovite mica (SPI supplies, USA). The drop of solution was removed after 60 s by spinning the sample at 1000 rpm. The commercially available atomic force microscope microscope (AFM) diInnova (Veeco instruments inc., USA) was used to take three-dimensional (3D) images of gold nanoparticles. Magnetization measurements were accomplished using a vibrating-sample magnetometer calibrated by a Ni sample of similar dimensions as the studied sample. The magnetometer was composed of the vibrator, the lock-in amplifier, and the electromagnet. The

magnetic field was measured by a testameter FH 54 (Magnet-Physics Dr. Steingrover GmbH).

Absorption spectra of investigated *AuNCs* solutions were measured using the Jasco V670 spectrophotometer. Hellma Optik (Jena, Germany) quartz cuvette with 1 cm length optical path was used for all optical measurements. Fluorescence spectra in the 400–750 nm range were measured with Edinburgh-F900 fluorescence spectrometer (Edinburgh instruments, United Kingdom). A picosecond pulsed diode laser EPL-375 that emits about 70–ps duration pulses at 375 nm was used to excite fluorescence. The average pulse power was 0.15 mW/mm^2. All fluorescence spectra were corrected for the instrument sensitivity. The optical density in the 10-mm cuvette of all samples was about 0.1 at 375 nm. Time-resolved fluorescence measurements. Fluorescence decay kinetics in the nanosecond time range were measured using Time-Correlated Single Photon Counting (TCSPC) method by utilizing the same Edinburgh F900 spectrometer. The pulse (375 nm) repetition rate was 2 MHz and the time resolution of the setup was about 100 ps. The laser radiation intensity, the aperture gap, measurement time for the all kinetics measurements were the same.

Gold-Coated Cobalt Ferrite Nanoparticles via Methionine-Induced Reduction

Functionalized superparamagnetic nanoparticles (*Nps*) recently are one of the most investigated research topics. In this study, we present an efficient protocol for gold deposition onto the surface of cobalt ferrite ($CoFe_2O_4$) *Nps* by a simple one-pot reduction of $AuCl_4^-$ ions with methionine amino acid, that in turn produce the biocompatible *Nps* stabilizing shell. In contrast to the reported gold deposition recipes, the adopted herein is distinguished by the simplicity and evade of mono-gold crystallites nucleation and growth in the deposition solution bulk. This work was based on our observations that in contrast to other amino acids methionine is prone to reduce $AuCl_4^-$ species at the walls of glass vessel instead of nucleation the Au^0 particles in the solution bulk. In the presence of $CoFe_2O_4$ *Nps*, however, the covering of magnetic *Nps* was observed not of glass vessel walls. The advantage of our functionalization method lies in it's high yield, simplicity and avoidance of gold crystals formation.

In this study, we have synthesized three groups of $CoFe_2O_4$ *NPs* of different sizes. In **figure 5.1.** are shown TEM images of nanoparticulated products synthesized in the deoxygenated solution containing 50 $CoCl_2$ + 50 $Fe_2(SO_4)_3$ + 75 mmol L^{-1} diglycolic acid + NaOH up to pH = 12.4 at 80 °C for 3 h (a, b) and by hydrothermal treatment at 130 °C for 10 h (c). The size distribution histograms of corresponding *NPs* are shown in the bottom. The deposition of gold was conducted later through sonication of $CoFe_2O_4$ *NPs* in the solution containing 0.9 mg mL^{-1} *NPs*, 0.3 $HAuCl_4$, 0.3 mmol L^{-1} methionine and NaOH (to adjust the pH to 12.0) at physiological temperature of 37 °C and stirring conditions for 4 h.

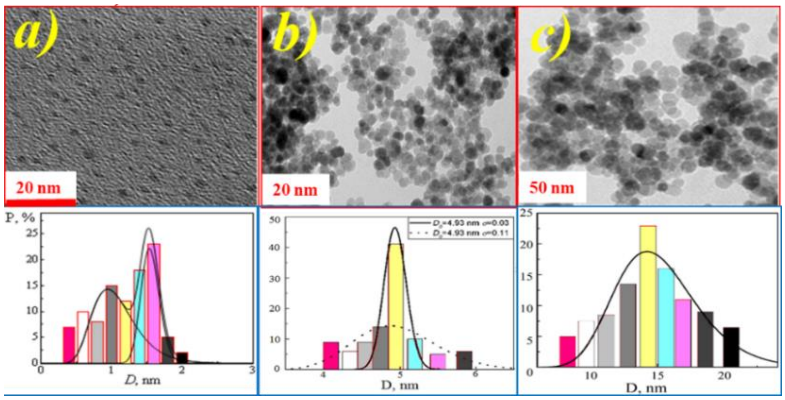

Fig. 5.1. The synthesized $CoFe_2O_4$ *Nd*: a) ultra-fine 2 nm, b) fine and (c) 15 nm PEM images and histograms of their size distribution.

Figure 5.2. shows the TEM (a) and STEM (b) images of $CoFe_2O_4$@Au *NPs* fabricated by methionine-directed gold deposition. Insert EDX spectrum of gold-plated nanoparticles. In the green circled inset, HRTEM image of the products demonstrating the Au lattice spacing at about 0.24 nm (scale bar 5 nm). Upon the plating the average size of $CoFe_2O_4$ *NPs* increased from 2 to 2.5 nm. Similar results were also obtained in the case of sonication $CoFe_2O_4$ *NPs* with average size of 5 nm **(Fig. 5.1. b)** and 15 nm **(Fig. 5.1. c)**. In these cases, the average size of ferrite *NPs* increased to 6.5 and 16.5 nm, respectively **(Fig. 5.3. a, b, c)**.

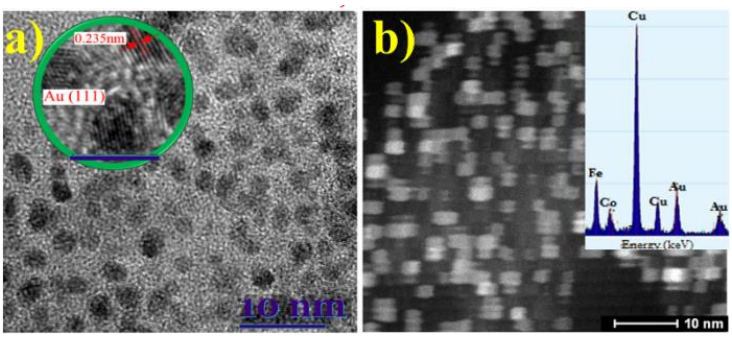

Fig. 5.2. TEM (a) and STEM (b) images of $CoFe_2O_4$@Au *NPs*. In the green circled Inset, HRTEM image of the products, demonstrating the Au lattice spacing, is shown. EDX spectrum of final product is presented in the (b) part inset.

The principle scheme of $HAuCl_4$ reduction with D, L-methionine on the surface of $CoFe_2O_4$ *NPs* is presented in **Figure 5.4.** We established that apart reduction of gold ions D, L-methionine stabilized cobalt ferrite nanoparticles. These data indicate the possible mechanism but are not sufficient to explain the exact picture of reactions resulting in the core–shell structure formation.

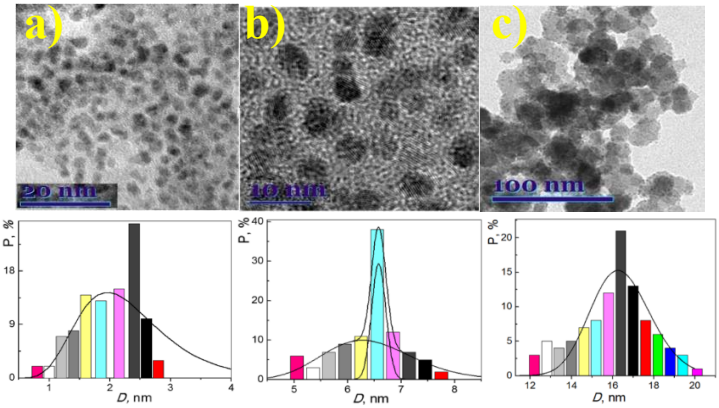

Fig. 5.3. TEM images for a) 2.5, b) 6.5 and c) 16.5 nm sized $CoFe_2O_4$@Au *NPs* after gold deposition. In the bottom panels, their size distribution histograms.

To investigate variation of the surface chemical properties of $CoFe_2O_4$ *NPs* upon the covering with a gold shell, the bare as well as gold-coated *NPs* were dispersed ultrasonically in the solution of 13 $mmol \cdot L^{-1}$ dopamine hydrochloride (DOPA) and kept at ambient temperature overnight. Following careful rinsing and drying they were further investigated by FTIR spectroscopy.

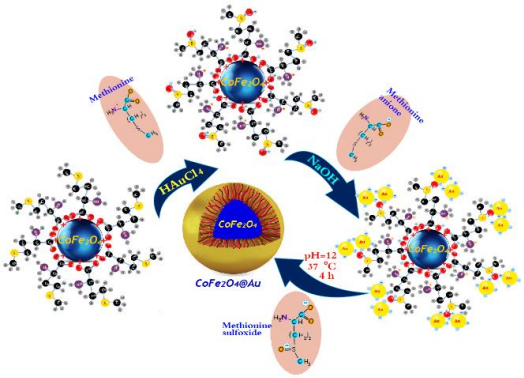

Fig. 5.4. Scheme of Methionine-mediated synthesis of magnetic nanoparticles.

Figure 5.5. compares the infrared spectra of (d) crystalline dopamine, (a) $CoFe_2O_4$@Au nanoparticles, (c) dopamine modified $CoFe_2O_4$ nanoparticles, and (a) dopamine-modified $CoFe_2O_4$@Au nanoparticles in the spectral regions of 400 − 750 (left panel) and 750 − 1800 cm^{-1} (right panel). The spectrum of pure DOPA is shown in **Figure 5.5. curve d.** It is characterized by vibrational peaks in the IR region at: 814, 876, 1115, 1190, 1260, 1286, 1320, 1341, 1499, and 1614 cm^{-1} wavelengths. Comparison in dopamine modified $CoFe_2O_4$ **(Fig. 5.5. curve c)** and dopamine-modified $CoFe_2O_4$@Au **(Fig. 5.5. curve b)** *NPs* with dopamine FTIR spectrum (**Fig. 5.5. curve d**) immediately confirms the presence of adsorbed dopamine on the surface of nanoparticles. The most intense dopamine bands at 814, 1286, and 1499 cm^{-1} had equivalent features at 815, 1284, and 1496 cm^{-1} in the infrared spectrum of modified nanoparticles. The band near 1499 cm^{-1} was assigned to aromatic ring CC stretching vibration, while the bands near 1286 and 814 cm^{-1} belongs to C-O-H symmetric bending and ring deformation/N-C stretching vibrational modes, respectively [133, 134, 135, 136]. However, in this case the characteristic band near 1499 cm^{-1} of dopamine downshifts to 1486 cm^{-1} because of interaction with nanoparticles. We note that this band may serve as a marker band for discrimination between the $CoFe_2O_4$ and $CoFe_2O_4$@Au *NPs* because peak frequency differs by as much as 10 cm^{-1}. Presented FTIR spectra suggest that $CoFe_2O_4$ *Nps* are covered completely by Au shell.

The innovative gold deposition method is expected open new horizons for the design of biocompatible water dispersible gold/methionine-functionalized ferrite nanoparticles by a simply controllable way.

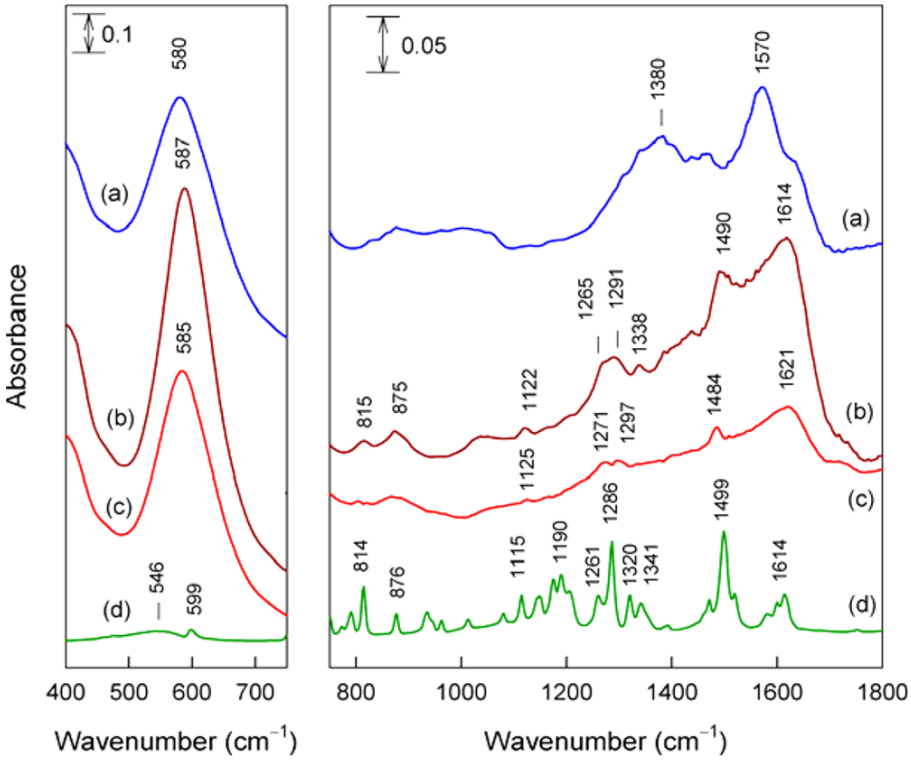

Fig. 5.5. FTIR absorbance spectra of (a) $CoFe_2O_4$@Au nanoparticles, (b) dopamine-modified $CoFe_2O_4$@Au *NPs*, (c) dopamine modified $CoFe_2O_4$ *NPs*, and (d) crystalline dopamine in the spectral regions of 400−750 (left panel) and 750−1800 cm^{-1} (right panel).

Methionine-mediated synthesis of $CoFe_2O_4$@Met *NPs* and functionalization with gold nanocrystals

In this investigation, we created a novel synthesis method for $CoFe_2O_4$ *NPs* capped with a biocompatible methionine shell ($CoFe_2O_4$@Met), which in turn is capable to reduce and attach the gold species. In this way, iron oxide-based *NPs* decorated with Au^0/Au^+ *NCs* were formed for the first time. Obtained products confirmed by HRTEM, AFM, FTIR, XPS and chemical analysis.

A hydrothermal approach was applied to synthesize the superparamagnetic $CoFe_2O_4$@Met *NPs* stabilized with methionine. In **Figure 5.6. a),** TEM image of $CoFe_2O_4$@Met *NPs* synthesized hydrothermally in a solution containing

25.0 mmol·L^{-1} $CoCl_2$, 50 mmol·L^{-1} $FeCl_3$, 0.2 mol·L^{-1} methionine, and NaOH to pH 12.4 at 130 °C for 10 h is shown. The size distribution histogram and XRD pattern of the as-formed *NPs* are shown in panels **b)** and **c)**, respectively. Panel **d)** shows the room temperature magnetization plots for $CoFe_2O_4$@Met *NPs* probe as a function of applied magnetic field before (1) and following their sonication in the hydrogen tetrachloroaurate solution (2) revealing the saturation magnetization value decrease from an initial 27 emu g^{-1} to 21 emu g^{-1} at H_{max} = 4.4 kOe confirmed the claim that gold species deposited onto the magnetic core remain superparamagnetic.

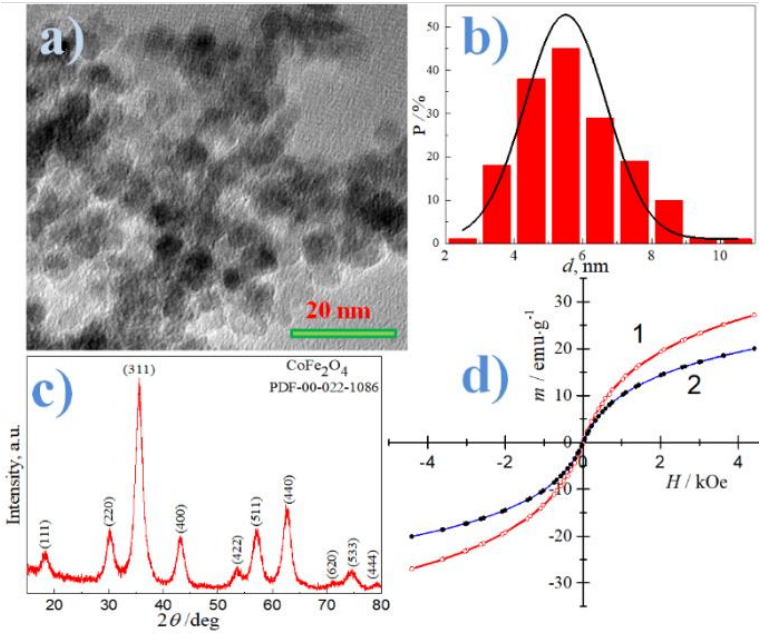

Fig. 5.6. a) TEM image of $CoFe_2O_4$@Met *NPs* synthesized hydrothermally. The size distribution histogram and XRD pattern of the as-formed *NPs* are shown in panels b) and c), respectively. In panel d), the magnetic responses of $CoFe_2O_4$@Met *NPs* before (1) and after (2) gold *NCs* deposition.

The deposition of gold *NCs* at the surface of magnetite *NPs* was confirmed also by HRTEM image of $CoFe_2O_4$@Met *NPs* after the gold deposition and EDX investigations (**Fig. 5.7**). From these, the formation of numerous gold species at the surface of $CoFe_2O_4$@Met *NPs* is obvious. The ICP-MS analysis of the gold plating shows that methionine molecules are capable to reduce the gold ions at the *NPs* surface with more than 99 % yield.

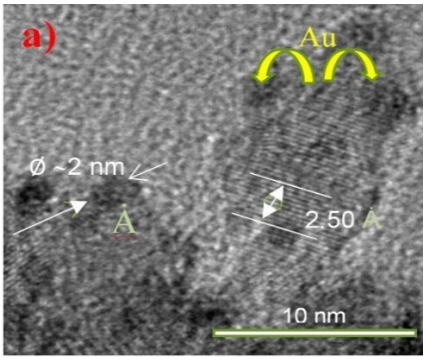

Fig. 5.7. TEM images of $CoFe_2O_4$@Met *NPs* formed as in Figure 5.6. after gold *NCs* deposition.

To determine the size of gold nanocrystals it was detached from the $CoFe_2O_4$@Met/Au *NPs* surface by ultrasonic agitation of 10 mg probe in the solution containing 10 mmol·L^{-1} methionine. As a result, a reddish-pink solution (**Fig. 5.8**) was obtained after 20 min processing. **Figure 5.8** shows the peak locations of the localized surface plasmon resonance (LSPR) 1st curve of methionine, 2nd of hydrogen tetrachloroaurate soliution, 3th of reddish-pink colored solution of gold species (inset) collected from the $CoFe_2O_4$@Met–Au *NCs* initially exhibits two locations peaks at 522 and 377 nm that indicates that the size of the methionine-stabilized gold species is extremely small. As it was determined by AFM the vast majority of gold species tethered to $CoFe_2O_4$@Met *NPs* surface was 2 nm size (**Fig. 5.9**).

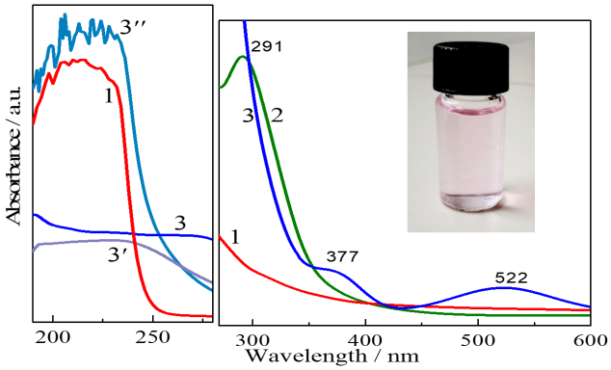

Fig. 5.8. Absorption spectra of methionine (1), tetrachlorauric acid (2) and reddish-pink colored solution of gold species (Inset) collected from the

$CoFe_2O_4$@Met Au nanoparticles before (3) and following two-times (3') and four-times (3'') dilution.

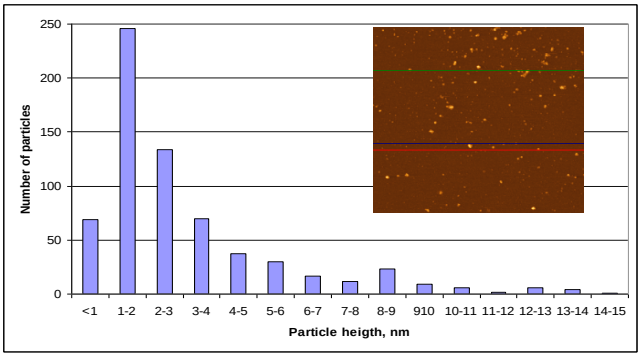

Fig. 5.9. Typical AFM images and size distribution histogram of Au species removed from the surface of $CoFe_2O_4$@Met-Au *Nps*.

XPS investigations were further conducted. **Figure 5.10** depicts the characteristic XP spectrum of as-grown $CoFe_2O_4$@Au-Met *NPs*. The analysis of the Au $4f_{7/2}$ core-level spectrum revealed the binding energy (BE) value of 83.94 eV typical for metallic Au^0 [141]. The fitting of the Au 4f core-level spectrum by using two spin-orbit split Au $4f_{7/2}$ and Au $4f_{5/2}$ components, however, shows an additional shoulder peaked at 85.74 eV which could be ascribed to Au^+ ions [141, 142]. To our best knowledge, there is only one Au^0/Au^+ anchoring method recently reported in our work [141] which used the methionine and proved the presence of the Au^+ ions by the additional peak at 85.74 eV.

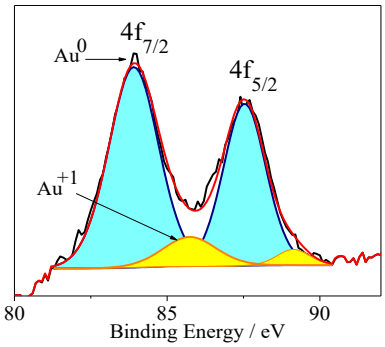

Fig. 5.10. Deconvoluted X-ray photoelectron spectrum (XPS) of Au 4f.

This investigation has shown that by adding the methionine to the solutiong during synthesis of $CoFe_2O_4$@Met *NPs* one can control the growth of magnetic *NPs*, namely, their stability and coverage with Au^0/Au^+ *NCs*. The elaborated functionalization of magnetic *NPs* with gold *NCs* represents a promising multi-task platform for linking magnetic *NPs* with specific targeting ligands, such as aptamers and antibodies.

In conclusion, this study describes a novel and efficient pathway for covering of various cobalt ferrite nanoparticles with gold shell without nucleation and growth of the separate gold crystals using amino acid methionine as a reducer of gold species and stabilizing agent for *Nps*. It is supposed that upon initial dispersion of ferrite *Nps* in the methionine solution amino acid interacts with the surface of cobalt ferrite *Nps* through the carboxyl bond.

Ultra-small methionine-capped Au^0/Au^+ *NCs* as efficient drug against the antibiotic-resistant bacteria

In this study, we synthesized and tested ultra-small gold and gold-functionalized magnetite *NPs* comprised of Au^0/Au^+ for possible inactivation of multi-drug resistant bacteria. To the best of our knowledge, the antimicrobial behavior of ultra-small gold *NCs* stabilized with the amino acid has not been investigated against the most dangerous microorganism, such as methicillin-resistant *Staphylococcus aureus*, *Acinetobacter baumannii*, and *Salmonella enterica*.

In this study, gold *NCs*, ultra-small, quite uniform in size, and containing zero-valent gold were synthesized on the surface of magnetite *NPs* by reducing the hydrogen tetrachloroaurate with methionine molecules capped at the surface of Fe_3O_4 *NPs*. **Figure 5.11 a** shows TEM image of Fe_3O_4@Met *NPs*, synthesized in the hydrothermally adapted concentration of iron salts (45 $mmol \cdot L^{-1}$) and methionine (0.2 $mol \cdot L^{-1}$), at 130 °C for 10 h is shown. In addition in part b) HRTEM image of these *NPs* is depicted.

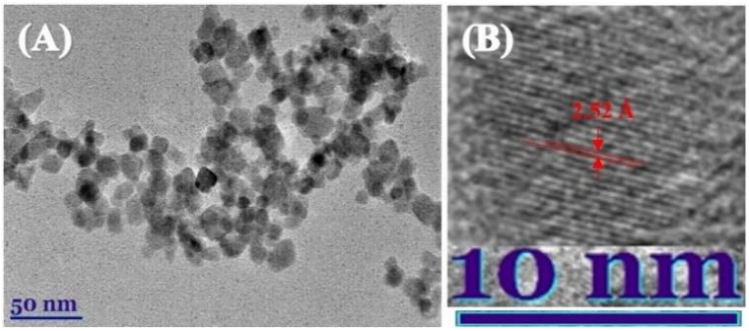

Fig. 5.11. a) TEM and b) HRTEM images of Fe_3O_4@Met *NPs*

The formation of numerous gold species on the surface of methionine-stabilized Fe_3O_4 *NPs* after their sonication in the $HAuCl_4$ solution under adapted herein conditions. From the TEM inspection, however, it was difficult to determine the size distribution of attached gold species, although most of them seem to be spherical and les than ≤ 2.0 nm in size (**Fig. 5.12.**).

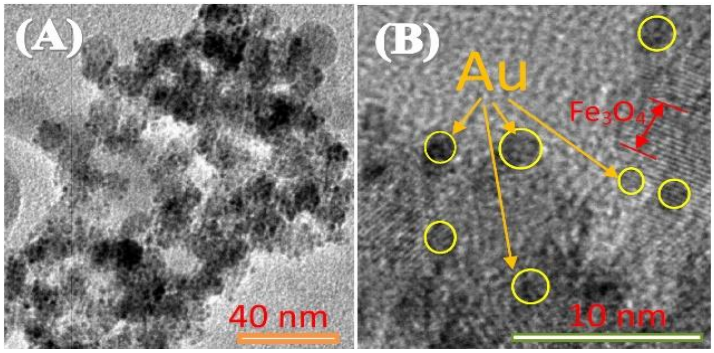

Fig. 5.12. TEM (A) and HRTEM (B) images of magnetite *NPs* after decoration with gold nanocrystals via methionine-induced $HAuCl_4$ reduction.

To remove ultra-small gold *NCs* from the surface of Fe_3O_4 *NPs* for the first time we have used the same methionine amino acid as a detaching agent. This procedure was conducted *via* ultrasound agitation of gold coated magnetite *NPs* in methionine solution attributing the detachment effect to the stronger interaction of the amino acid with gold nanocrystals compared to that in Au-Fe_3O_4 bond. The obtained light-pink solution due to dispersion of ultra-small gold *NCs* was further investigated by sampling on the Lacey grid

followed by AFM and TEM observations for the particle size inspection. As seen from **Figure 5.13.** the detached ultra-small gold nanocrystals exhibit mainly the spherical particle morphology with an average diameter of about 2 nm and a quite narrow size distribution. It is note worthy, that they seem to be aggregated.

It is commonly accepted that gold *NPs* are nontoxic and biocompatible. Currently, Xie and co-workers [143] reported that small-sized gold *NPs* possess cytotoxity against several cancer cells. To check this effect, we performed a set of antimicrobial tests with ultra small Au^0/Au^+ *NPs* attached to the surface of magnetite *Nps via* Methionine-templated growth and gold deposition way [132].

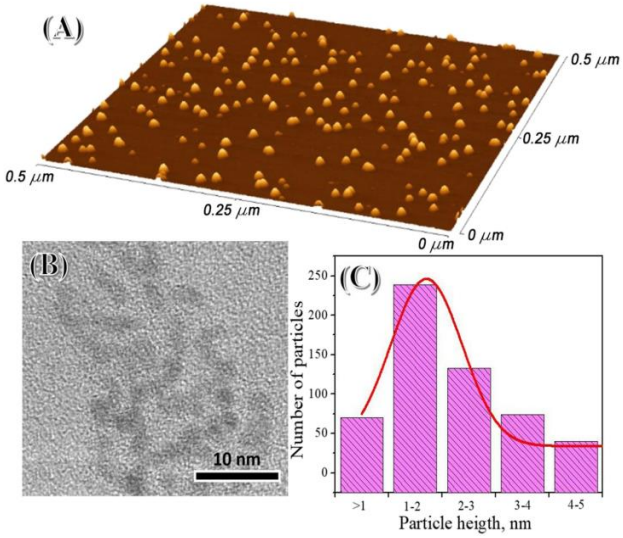

Fig. 5.13. AFM 3D view of magnetite *NPs* (A), whereas TEM image and size distribution histogram of gold *NPs* detached from magnetite nanoparticles are shown in the (B) and (C) parts, respectively.

In these experiments, two multidrug resistant gram-negative microorganisms (*A. baumanni* and *S. enterica*) and two gram-positive ones (*S. aureus* and *M. luteus*) were tested. Bacterium survival data after 24 h incubation with bare Fe_3O_4 and gold-decorated Fe_3O_4@Au *NPs* are shown in figure 5.14.

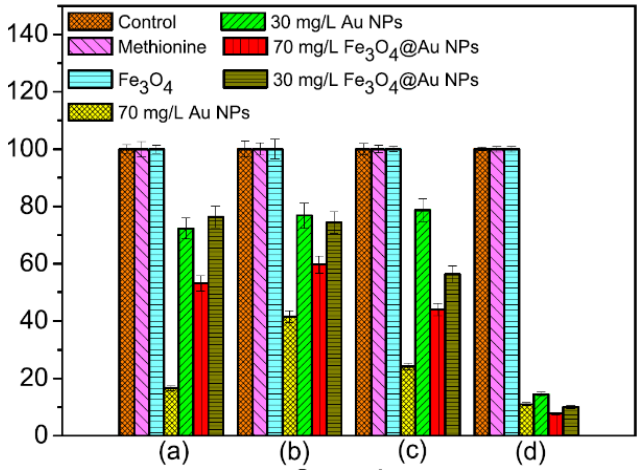

Fig. 5.14. Antimicrobial activities of the synthesized Au@Met and Fe_3O_4@Au *NPs* after 24 h incubation with gram-negative A. baumannii (a), S. enterica (b), and gram-positive S. aureus (MRSA) (c), M. luteus (d). For comparison, the behavior of pure D,L-methionine and magnetite *NPs* is presented.

For comparison, the survival results of all tested bacteria sonicated with methionine alone are also presented. As seen, any antimicrobial effects can be viewed for the nude Fe_3O_4 *NPs* and D,L-Methionine amino acid. Contrary, the incubation of Fe_3O_4@Au *NPs* with all bacteria tested in this study demonstrated more or less antimicrobial efficiency. Most significant, e.g. about 90 %, reduce was obtained for *M. luteus* population whereas in the cases of *A. baumannii, S. enterica,* and *S. aureus* incubation with a same content of Fe_3O_4@Au *NPs* result in reduction of bacteria population survival by to 55, 60 and 43 %, respectively.

Synthesis of red-fluorescent gold nanoclusters and characterization

This work first time shows the cost-effective synthesis of *AuNCs* by reduction of hydrogen tetrachloroaurate with amino acid food supplement (AAFS) resulting in the formation of stable and biocompatible *NCs*, with characteristic intense red photoluminescence (PL), peaked from 660 to 705 nm, and average lifetime of several mikroseconds. We note that application of cheap amino acid cocktails, instead of earlier proposed pure and

significantly expensive BSA [76], insulin, pepsin and others [77-87], makes this synthesis very attractive.

In the first setup, several currently popular amino acid food supplements, were tested as reducers of hydrogen tetrachloroaurate in an alkaline medium and physiological temperature (37 ºC). **Figure 5.15 a)** shows the PL spectra of *AuNCs* formed in the alkaline (pH=12.0) solutions containing 3 μmol·ml^{-1} $HAuCl_4$ and 20 mg·mL^{-1} food supplements: BCAA'S **1st**, 100% Milk complex **2nd** and 100% Whey protein professional **3th curve**. *AuNCs* synthesized with a branched amino acid supplement after excitation at 470 nm in length exhibited extremely intense red light (690 nm) emission. By examination the stability of as-synthesized *AuNCs* emission over a few days, only a slight decrease in its intensity was observed (**Fig. 5.15 b**).

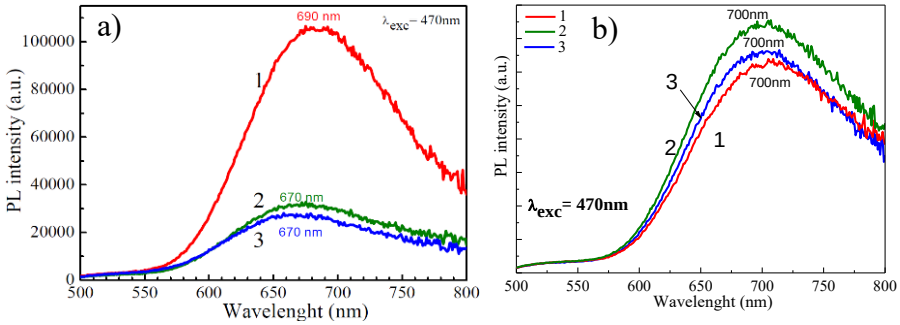

Fig. 5.15. Fluorescence spectra of formed *AuNCs* from different food supplements: (1) BCAA'S, (2) 100% Milk complex and (3) 100% Whey protein professional after 20 h synthesis at 37 ºC. B) *AuNCs* formed via BCAA'S stability spectras: 1 initial, 2 after day, 3 after two days.

To find the optimal conditions for the synthesis of *AuNCs* with BCAA'S food supplement, the influence of solution concentration on the pH value was investigated. **Figure 5.16 a)** shows the localized surface plasmon resonance and PL spectra of *AuNCs* formed *via* BCAA'S food supplement-mediated synthesis in the solution containing 8, 12, 16, 20 and 24 mg·mL^{-1} BCAA'S. Judging from the intensity of red PL spectra, *AuNCs* with the maximum PL emission in the range between 670 and 690 nm are formed in the solution containing 16-20 mg·mL^{-1} of BCAA'S at the optimal pH = 12 (**Fig. 5.16 b**).

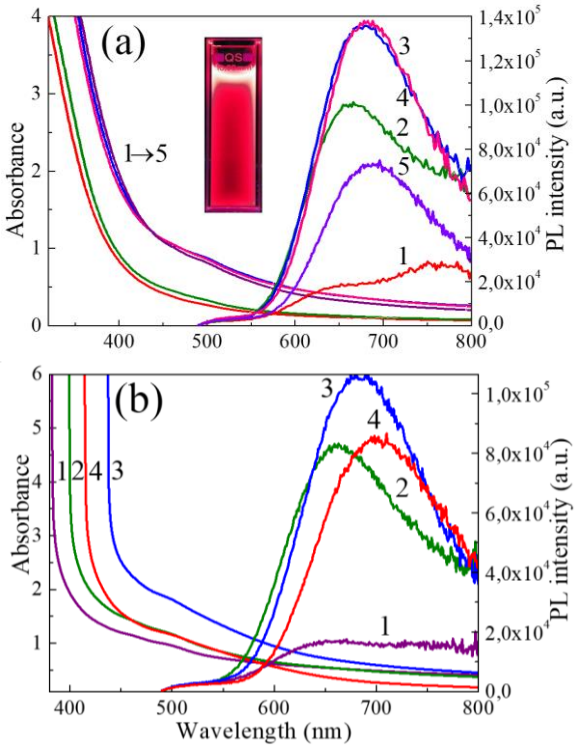

Fig. 5.16. (a) Absorption and PL spectra of *AuNCs* formed *via* BCAA'S food supplement-mediated synthesis in the 3.0 μM/mL $HAuCl_4$ solution containing: 8 (1); 12 (2); 16 (3); 20 (4) and 24 (5) mg/mL BCAA'S; all kept at a pH = 12.2 and 37 °C for 20 h. In (b) panel, the absorption and PL spectra of *AuNCs* fabricated in 3.0 μM/mL $HAuCl_4$ solution containing 20 mg/mL BCAA'S at pH: 11.0 (1); 11.5 (2) 12.0 (3) and 12.5 (4) at 37 ºC for 20 h. λ_{exc}= 470 nm. In the Inset, the colour of fabricated *AuNCs* under UV irradiation is shown.

The PL intensity of the obtained Au@BCAA'S *NCs* and emission light peak position strongly depend on the excitation wavelength decreasing with λ_{exc} (**Fig. 5.17 a**). The strongest photoluminescence is in gold clusters at λ_{exc} = 405 nm (**Fig. 5.17 a, 1st curve**). The lifetime of red PL of Au@BCAA'S *NCs* with non-exponential decay typically exceeds several μs (**Fig. 5.17 b**). Such long lifetimes are not typical for *AuNCs* fabricated *via* templating with earlier reported proteins such as BSA [76] and others [77-87].

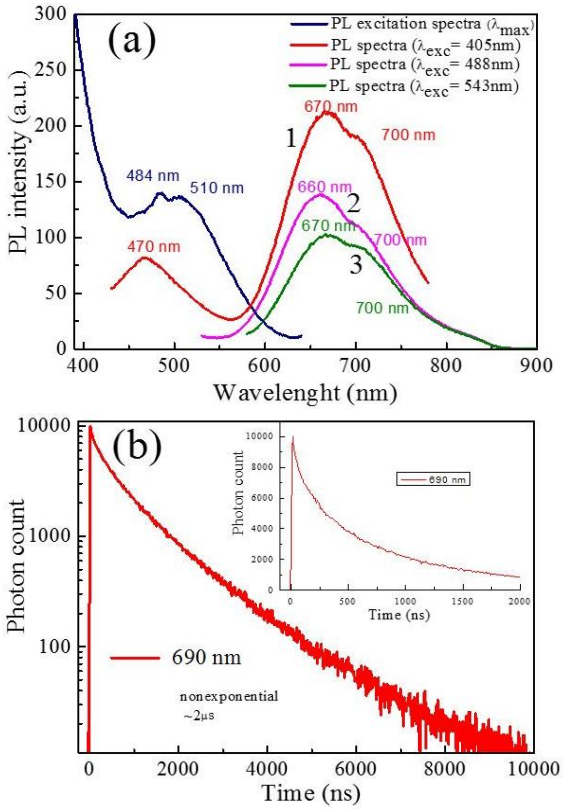

Fig. 5.17. (a): Variation of PL spectra of BCAA'S-mediated *AuNCs* with the excitation light wavelength (nm): 405 (1); 488 (2) and 543 (3). In (b): Typical photoluminescence intensity decay for BCAA'S-mediated *AuNCs* at PL band peak position 690 nm.

The quantum yield (QY) of ~7.0% was obtained for red-luminescent Au@BCAA'S *NCs* fabricated under the optimized conditions. Note, that such QY is higher than reported for red-luminescent *AuNCs* synthesized using even BSA protein-directed reduction of chloroauric acid [21]. Furthermore, the obtained in this study Au@BCAA'S *NCs* typically have photoemission peak position from 670 to 705 nm, indicating on the inclusion of Au_{27}-Au_{29} atoms in each nanocluster, based on the spherical Jellium model.

We suspect that this study opens a new directions of research in the green synthesis of biocompatible *AuNCs* using low-cost amino acid food supplements instead of pure proteins and can be useful for future fluorescent nanocluster technologies.

Conclusions

1. A simple method for coating the surface of magnetic *Nps* with gold using vitamin C as a reducing agent capable of to binding with cobalt ferrite was developed.

2. This study describes a novel and efficient way for covering of various cobalt ferrite nanoparticles with gold shell without nucleation and growth of the separate gold crystals using methionine as a reducer of gold species and stabilizing agent of *Nps*.

3. Formation of $CoFe_2O_4$@Au *NPs* was confirmed by XRD, TEM, EDX, high-resolution TEM studies, variation of *NPs* size, and FTIR spectra.

4. FTIR spectral analysis showed different adsorption behavior of dopamine hydrochloride on the surface of $CoFe_2O_4$ and $CoFe_2O_4$ @ Au *NPs*.

5. Gold cluster synthesis for the first time using a branched-chain amino acid food supplement was optimized.

6. The obtained gold clusters characterized by intense red photoluminescence, peaked in a vicinity of 670–710 nm, a relatively long lifetime of several microseconds, and high quantum yield of approximately 7%, similar to ones synthesized with bovine serum albumin.

6. LITERATŪROS SĄRAŠAS

1. Zhou, J.; Ralston, J.; Sedev, R.; Beattie, D. A., *Functionalized gold nanoparticles: synthesis, structure and colloid stability*. Journal of Colloid and Interface Science, 2009, nr. 331 (2), p. 251-262.

2. Cornell, P.M. and Schwertmann, U. (1996) *The Iron Oxides: Structure, Properties, Reactions, Occurrence and Uses.* 2nd Edition, Wiley-VCH, Weinheim, 703.

3. De PR Moreira, I.; Roldán, A.; Illas, F., Electronic and magnetic structure of bulk cobalt: *The α, β, and ε-phases from density functional theory calculations.* The Journal of chemical physics, 2010, nr. 133 (2), p. 024701.

4. Rinkevičius V. *Elektra ir Magnetizmas.* Vilniaus universiteto leidykla; 2004.

5. Lamer, V. K.; Dinegar, R. H. Theory, *Production and Mechanism of Formation of Monodispersed Hydrosols.* J. Am. Chem. Soc. 1950, 72 (11), 4847−4854.

6. Mahmoudi, M.; Sant, S.; Wang, B.; Laurent, S.; Sen, T. Superparamagnetic iron oxide nanoparticles (SPIONs): development, surface modification and applications in chemotherapy. Advanced Drug Delivery Reviews 2011, 63, 24–46.

7. Bensebaa F., Zavaliche F., L'Ecuyr P., Cochrane R.W., Veres T., *Microwave synthesis and characterization of co-ferrite nanoparticles.* J. Coll. Interface Sci. 277, 104-110, 2004.

8. Sandeep Kumar, V. Magnetic nanoparticles-based biomedical and bioanalytical applications. J Nanomed Nanotechol 4 (2013): e130.

9. Pereira, C., Pereira, A. M., Fernandes, C., Rocha, M., Mendes, R., Fernández-García, M. P., & Freire, C. Superparamagnetic MFe_2O_4 (M= Fe, Co, Mn) nanoparticles: tuning the particle size and magnetic properties through a novel one-step coprecipitation route. Chemistry of Materials, (2012), 24(8), 1496-1504.

10. Arias, Jose L., L. Harivardhan Reddy, and Patrick Couvreur. *Fe_3O_4/chitosan nanocomposite for magnetic drug targeting to cancer.* Journal of Materials Chemistry 22.15 (2012): 7622-7632.

11. Gribanov, N. M., Bibik, E. E., Buzunov, O. V., & Naumov, V. N. *Physico-chemical regularities of obtaining highly dispersed magnetite by the method of chemical condensation.* Journal of Magnetism and Magnetic Materials, 1990, 85(1-3), 7-10.

12. Tartaj P, Morales MP, Veintemillas-Verdaguer S, et al. 2006. *Synthesis, properties and biomedical applications of magnetic nanoparticles.* In: Buschow KHJ, ed. Handbook of magnetic materials, Vol. 16. Elsevier, p 403–82

13. Sugimoto T., Matijevic E., Formation of uniform spherical magnetite particles by crystallization from ferrous hydroxide gels. J. Colloid Interface Sci. 1980, 74, 227–243.

14. Indira, T. K., and P. K. Lakshmi. *Magnetic nanoparticles–a review.* Int. J. Pharm. Sci. Nanotechnol 3.3 (2010): 1035-1042.

15. Langer, Stephen A., Raymond E. Goldstein, and David P. Jackson. *Dynamics of labyrinthine pattern formation in magnetic fluids.* Physical Review A 46.8 (1992): 4894.

16. Steigerwald, Michael L., and Louis E. Brus. *Semiconductor crystallites: a class of large molecules.* Accounts of Chemical Research 23.6 (1990): 183-188.

17. Baumgartner, Jens, et al. *Nucleation and growth of magnetite from solution.* Nature materials 12.4 (2013): 310.

18. Faraji M, Yamini Y , Rezaee M . 2010. Magnetic nanoparticles: synthesis, stabilization, functionalization, characterization, and applications. J Iran Chem Soc. 7: 1– 37.

19. Iida H, Takayanagi K , Nakanishi T , Osaka T . 2007. Synthesis of Fe_3O_4 nanoparticles with various sizes and magnetic properties by controlled hydrolysis. J Colloid Interface Sci . 314 : 274 – 280 .

20. Vayssieres, Lionel, et al. Size tailoring of magnetite particles formed by aqueous precipitation: an example of thermodynamic stability of nanometric oxide particles. Journal of colloid and interface science 205.2 (1998): 205-212.

21. Lian, Suoyuan, et al. *Synthesis of magnetite nanorods and porous hematite nanorods.* Solid State Communications 129.8 (2004): 485-490.

22. Ziolo RF , Giannelis EP , Weinstein BA , O'horo MP , Ganguly BN , Mehrotra V , et al. *Matrix-mediated synthesis of nanocrystalline g 3 -Fe_2O_3: a new optically transparent magnetic material.* Science. 1992, 257 : 219 – 223 .

23. Govan J, Gun'ko YK. Recent Advances in the Application of Magnetic Nanoparticles as a Support for Homogeneous Catalysts. Nanomaterials 2014, 4: 222 – 241.

24. Babes, L., Denizot, B., Tanguy, G., Le Jeune, J. J., & Jallet, P. *Synthesis of iron oxide nanoparticles used as MRI contrast agents: a parametric study.* Journal of colloid and interface science, 1999, 212(2), 474-482.

25. Sun, Shouheng, et al. *Monodisperse $MeFe_2O_4$ (Me= Fe, Co, Mn) nanoparticles*. Journal of the American Chemical Society 126.1 (2004): 273-279.

26. Wang, Yuanfeng, et al. One-pot reaction to synthesize superparamagnetic iron oxide nanoparticles by adding phenol as reducing agent and stabilizer. Journal of Nanoparticle Research 14.4 (2012): 755.

27. Rockenberger, Jörg, Erik C. Scher, and A. Paul Alivisatos. *A new nonhydrolytic single-precursor approach to surfactant-capped nanocrystals of transition metal oxides.* Journal of the American Chemical Society 121.49 (1999): 11595-11596.

28. Liang, Xin, et al. *Synthesis of nearly monodisperse iron oxide and oxyhydroxide nanocrystals.* Advanced Functional Materials 16.14 (2006): 1805-1813.

29. Woo, Kyoungja, et al. *Easy synthesis and magnetic properties of iron oxide nanoparticles.* Chemistry of Materials 16.14 (2004): 2814-2818.

30. Nakaya, Masafumi, Ryo Nishida, and Atsushi Muramatsu. Size control of magnetite nanoparticles in excess ligands as a function of reaction temperature and time. Molecules 19.8 (2014): 11395-11403.

31. Farrell, Dorothy, Sara A. Majetich, and Jess P. Wilcoxon. *Preparation and characterization of monodisperse Fe nanoparticles.* The Journal of Physical Chemistry B 107.40, 2003: 11022-11030.

32. Chen, J. P., Lee, K. M., Sorensen, M., Klabunde, K. J., Hadjipanayis, G. C., *Magnetic Propertie of Microemulsion Synthesized Cobalt Fine Particles,* Journal of Applied Physics, 1994, 75 (10), pp. 5876-5878

33. Park, Jongnam, et al. *Ultra-large-scale syntheses of monodisperse nanocrystals.* Nature materials 3.12 (2004): 891.

34. Amara, Daniel, Judith Grinblat, and Shlomo Margel. Solventless thermal decomposition of ferrocene as a new approach for one-step synthesis of magnetite nanocubes and nanospheres. Journal of Materials Chemistry 22.5 (2012): 2188-2195.

35. Demortiere A, Panissod P, Pichon B P, Pourroy G, Guillon D, Donnio B and Begin-Colin S. *Size-dependent properties of magnetic iron oxide nanocrystals*. Nanoscale 2011, 3, 225.

36. Li, Z.; Sun, Q.; Gao, M. Preparation of water-soluble magnetite nanocrystals from hydrated ferric salts in 2-pyrrolidone: mechanism leading to Fe_3O_4. Angewandte Chemie International Edition 2004, 44, 123.

37. Corot, Claire, et al. *Recent advances in iron oxide nanocrystal technology for medical imaging.* Advanced drug delivery reviews 58.14 (2006): 1471-1504.

38. Wu, Wei, et al. Sonochemical synthesis, structure and magnetic properties of air-stable Fe_3O_4/Au nanoparticles. Nanotechnology 18.14 (2007): 145609.

39. Wu, A.; Ou, P.; Zeng, L. *Biomedical applications of magnetic nanoparticles.* NANO, 2010, vol. 5, nr. 5, p. 245-270.

40. Fan, Z.; Skelton, M.; Singh, A. K.; Senapati, D.; Khan, S. A.; Ray, P. C. Multifunctional Plasmonic Shell–Magnetic Core Nanoparticles for Targeted Diagnostics, Isolation, and Photothermal Destruction of Tumor Cells. ACS NANO, 2012, vol. 6, nr. 2, p. 1065-1073.

41. Schewertman, U.; Cornell, R.M. Iron Oxides in the Laboratory Preparation and Characterization. Weinheim: Wiley-vch, 2000. ISBN 3-527-29669-7.

42. Liu H., Hou P., Zhang W.X., Wu J.H., Synthesis of monosized core-shell Fe_3O_4/Au multifunctional nanoparticles by PVP-assisted nanoemulsion process. Colloids & Surfaces A: Physicochem. Eng. Aspects 2010, 356, 21-27.

43. Cui Y.L., Xu D.D., Fang Y., Ma J.B., *Preparation and mechanism of Fe_3O_4/Au core/shell super-paramagnetic microspheres.* Science in China (Series B) 44, 404-410, 2001.

44. Jesus, M.; Grazu, V. *Nanobiotechnology: inorganic Nanoparticles vs Organic Nanoparticles in Great Britain* [interaktyvus]. Elsevier, 2012, vol. 4, p. 269-286. ISSN 1876-2778.

45. Braun K.J., Walter D.G., Natan M.J., Seeding of colloidal Au nanoparticle solutions. 2. Improved control of particle size and shape. Chem. Mater. 2000, 12, 306-313.

46. Lyon J.L., Fleming D.A., Stone M.B., Schiffer P., Williams M.E., *Synthesis of Fe oxide core/Au shell nanoparticles by iterative hydroxylamine seeding.* Nano Lett. 4, 719-723, 2004.

47. Yu Q., Shi M., Cheng Y., Wg M., Chen H.-z., Fe_3O_4@Au/polyaniline multifunctional nanocomposites: their preparation and optical, electrical and magnetic properties. Nanotechnology 19, 265702, 2008.

48. Ren J., Shen S., Pang Z., Lu X., Deng C., Jiang X., Facile synthesis of superparamagnetic Fe_3O_4@Au nanoparticles for photothermal destruction of cancer cells. Chem. Comm. 47, 11692-11694, 2011.

49. Cho S.J., Idrobo J.C., Olamit J., Liu K., Browning N.D., Kauzlarich S.M., *Growth mechanisms and oxidation resistance of gold-coated iron nanoparticles.* Chem. Mater. 17, 3181-3186, 2005.

50. Wang L., Luo J., Maye M.M., Fan Q., Rendeng Q., Engelhard M.H., Wang C., Lin Y., Zhong C.-J., *Core@shell nanomaterials: gold-coated magnetic oxide nanoparticles.* J. Mater. Chem. 15, 1821-1832, 2005.

51. Park J.N., An K.J., Hwang Y.S., Park J.G., Noh H.J., Kim J.Y., Park J.H., Hwang N.M., Hyeon T.W., *Ultra-large-scale syntheses of monodisperse nanocrystals.* Nat. Mater. 3, 891-895, 2004.

52. Stephen, Papell Solomon. Low viscosity magnetic fluid obtained by the colloidal suspension of magnetic particles. U.S. Patent No. 3,215,572. 2 Nov. 1965.

53. Jagminas ir A. Mikalauskaite. Functionalization of Iron Oxide-Based Magnetic Nanoparticles with Gold Shell. In: Xiao-Yu Yang & Nidhi Chauhan (Eds) Photoenergy and Thin Film Materials (Chapter 15, p. 617-660) 2019. Scrivener Publishing LLC.

54. Hembury M, Chiappini C, Bertazzo S, et al. *Gold–silica quantum rattles for multimodal imaging and therapy.* Proc Natl Acad Sci USA 2015; 112(7), 1959-1964.

55. Retnakumari A, Setua S, Menon D, et al. Molecular-receptor-specific, non-toxic, near-infrared-emitting Au cluster-protein nanoconjugates for targeted cancer imaging. Nanotechnol 2009; 21(5), 055103.

56. Zheng J., Zhang C.W., Dickson R.M., Highly Fluorescent, *Water-Soluble, Size-Tunable Gold Quantum Dots,* Physical Review Letters, 93, 077402, 2004.

57. Kumar S, Jin R. Water-soluble Au_{25}(Capt)18 nanoclusters: Synthesis, thermal stability and optical properties. Nanoscale 2012; 4(14), 4222-4227.

58. Shang L, Yang L, Stockmar F, et al. Microwave-assisted rapid synthesis of luminescent gold nanoclusters for sensing Hg2+ in living cells using fluorescence imaging. Nanoscale 2012; 4(14), 4155-4160.

59. Chaki NK, Singh P, Dharmadhikari CV, et al. Single-electron charging features of larger, dodecanethiol-protected gold nanoclusters: electrochemical and scanning tunneling microscopy studies. Langmuir 2004; 20(23), 10208-10217.

60. Shang L, Dörlich RM, Brandholt S, et al. Facile preparation of water-soluble fluorescent gold nanoclusters for cellular imaging application. Nanoscale 2010; 3(5), 2009-2014.

61. Nair LV, Nazeer SS, Jayasree RS, et al. Fluorescence imaging assisted photodynamic therapy using photosensitizer-linked gold quantum clusters. ACS Nano 2015; 9(6), 5825-5832.

62. Shiraishi Y, Arakawa D, Toshima N. pH-dependent color change of colloidal dispersions of gold nanoclusters: effect of stabilizer. Eur Phys J E 2002; 8(4), 377-383.

63. Lee D, Donkers RL, Wang G, et al. Electrochemistry and optical absorbance and luminescence of molecule-like Au_{38} nanoparticles. J Am Chem Soc 2004; 126(19), 6193-6199.

64. Paau MC, Lo CK, Yang X, et al. Synthesis of 1.4 nm α-cyclodextrin-protected gold nanoparticles for luminescence sensing of mercury (II) with picomolar detection limit. J Phys Chem C 2010; 114(38), 15995-16003.

65. Huang T, Murray RW. Visible luminescence of water-soluble monolayer-protected gold clusters. J Phys Chem B 2001; 105(50), 12498-12502.

66. Jiang DE. The expanding universe of thiolated gold nanoclusters and beyond. Nanoscale 2013; 5(16), 7149-7160.

67. Negishi Y, Nobusada K, Tsukuda T. Glutathione-protected gold clusters revisited: bridging the gap between gold (I)-thiolate complexes and thiolate-protected gold nanocrystals. J Am Chem Soc 2005; 127(14), 5261-5270.

68. Negishi Y, Takasugi Y, Sato S, et al. Magic-numbered Aun clusters protected by glutathione monolayers (n= 18, 21, 25, 28, 32, 39): isolation and spectroscopic characterization. J Am Chem Soc 2004; 126(21), 6518-6519

69. Jin R. Quantum sized, thiolate-protected gold nanoclusters. Nanoscale 2010; 2(3), 343-362.

70. Liu J, Duchesne PN, Yu M, et al. *Luminescent gold nanoparticles with size-independent emission.* Angew Chem Int Ed 2016; 128(31), 9040-9044.

71. Zheng J, Petty JT, Dickson RM. *High quantum yield blue emission from water-soluble Au8 nanodots.* J Am Chem Soc 2003; 125(26), 7780-7781.

72. Zheng J, Zhang C, Dickson RM. Highly fluorescent, water-soluble, size-tunable gold quantum dots. Phys Rev Lett 2004; 93(7), 077402.

73. Chen Y, Zheng X, Wang X, et al. Near-infrared emitting gold cluster-poly(acrylic acid) hybrid nanogels. ACS Macro Lett 2014; 3(1), 74-76.

74. Huang X, Luo Y, Li Z, et al. Biolabeling hematopoietic system cells using near-infrared fluorescent gold nanoclusters. J Phys Chem C 2011; 115(34), 16753-16763.

75. Schaeffer N, Tan B, Dickinson C, et al. Fluorescent or not Size-dependent fluorescence switching for polymer-stabilized gold clusters in the 1.1–1.7 nm size range. Chem Commun 2008; 34, 3986-3988.

76. Xie J, Zheng Y, Ying JY. Protein-directed synthesis of highly fluorescent gold nanoclusters. J Am Chem Soc 2009; 131(3), 888-889.

77. Chen TH, Tseng WL. (Lysozyme type VI)-stabilized Au8 clusters: synthesis mechanism and application for sensing of glutathione in a single drop of blood. Small 2012; 8(12), 1912-1919.

78. West AL, Griep MH, Cole DP, et al. DNase I retains endodeoxyribonuclease activity following gold nanocluster synthesis. Anal Chem 2014; 86(15), 7377-7382.

79. Yan X, Li H, Hu T, et al. A novel fluorimetric sensing platform for highly sensitive detection of organophosphorus pesticides by using egg white-encapsulated gold nanoclusters. Biosens Bioelectron 2017; 91, 232-237.

80. Wen F, Dong Y, Feng L, et al. Horseradish peroxidase functionalized fluorescent gold nanoclusters for hydrogen peroxide sensing. Anal Chem 2011; 83(4), 1193-1196.

81. Wang LL, Qiao J, Qi L, et al. Construction of OVA-stabilized fluorescent gold nanoclusters for sensing glucose. Sci China Chem 2015; 58(9), 1508-1514.

82. Liu CL, Wu HT, Hsiao YH, et al. Insulin-directed synthesis of fluorescent gold nanoclusters: preservation of insulin bioactivity and versatility in cell imaging. Angew Chem Int Ed 2011; 50(31), 7056-7060.

83. Kawasaki H, Hamaguchi K, Osaka I, et al. pH-dependent synthesis of pepsin - mediated gold nanoclusters with blue green and red fluorescent emission. Adv Funct Mater 2011; 21(18), 3508-3515.

84. Kong Y, Chen J, Gao F, et al. Near-infrared fluorescent ribonuclease-A-encapsulated gold nanoclusters: preparation, characterization, cancer targeting and imaging. Nanoscale 2013; 5(3), 1009-1017.

85. Le Guével X, Daum N, Schneider M. Synthesis and characterization of human transferrin-stabilized gold nanoclusters. Nanotechnol 2011; 22(27), 275103.

86. Wang Y, Chen JT, Yan XP. Fabrication of transferrin functionalized gold nanoclusters/graphene oxide nanocomposite for turn-on near-infrared fluorescent bioimaging of cancer cells and small animals. Anal Chem 2013; 85(4), 2529-2535.

87. Liu JM, Chen JT, Yan XP. Near infrared fluorescent trypsin stabilized gold nanoclusters as surface plasmon enhanced energy transfer biosensor and in vivo cancer imaging bioprobe. Anal Chem 2013; 85(6), 3238-3245.

88. Guo C, Irudayaraj J. Fluorescent Ag clusters via a protein-directed approach as a Hg (II) ion sensor. Anal Chem 2011; 83(8), 2883-2889.

89. Kennedy TAC, MacLean JL, Liu J. Blue emitting gold nanoclusters templated by poly-cytosine DNA at low pH and poly-adenine DNA at neutral pH. Chem Commun 2012; 48(54), 6845-6847.

90. Zhang H, Huang X, Li L, et al. Photoreductive synthesis of water-soluble fluorescent metal nanoclusters. Chem Commun 2012; 48(4), 567-569.

91. Li L, Li Z, Zhang H, et al. Effect of polymer ligand structures on fluorescence of gold clusters prepared by photoreduction. Nanoscale 2013; 5(5), 1986-1992.

92. Golinska P, Wypij M, Ingle AP, et al. Biogenic synthesis of metal nanoparticles from actinomycetes: biomedical application and cytotoxicity. Appl Microbiol Biotechnol 2014; 98(19), 8083-8097.

93. Salunke GR, Ghosh S, Kumar RS, et al. Rapid efficient synthesis and characterization of silver, gold, and bimetallic nanoparticles from the medicinal plant Plumbago zeylanica and their application in biofilm control. Int J Nanomedicine 2014; 9, 2635-2653.

94. Wang J, Zhang G, Li Q, et al. In vivo self-bio-imaging of tumors through in situ biosynthesized fluorescent gold nanoclusters. Sci Rep 2013; 3, 1157.

95. Gonzalez BS, Rodriguez MJ, Blanco C, et al. One step synthesis of the smallest photoluminescent and paramagnetic PVP-protected gold atomic clusters. Nano Lett 2010; 10(10), 4217-4221.

96. Xavier P.L., Chaudhari K., Verma P.K., Pal S.K., Pradeep T., Luminescent quantum clusters of gold in transferrin family protein, lactoferrin exhibiting FRET. Nanoscale 2, 2769-2776, 2010.

97. Garcia, A. R., Rahn, I., Johnson, S., Patel, R., Guo, J., Orbulescu, J., ... & Leblanc, R. M. (2013). *Human insulin fibril-assisted synthesis of fluorescent gold nanoclusters in alkaline media under physiological temperature*. Colloids and Surfaces B: Biointerfaces, 105, 167-172.

98. Durgadas C.V., Sharma Ch.P., Sreenivasan K., Fluorascent and superparamagnetic hybrid quantum clusters for magnetic separation and imaging of cancer cells from blood. Nanoscale 3, 4780-4787, 2011.

99. Nebu J., Anjali Devi J.S., Aparna R.S., Abha K., Sony G., Erlotinib conjungated gold nanocluster enveloped magnetic iron oxide nanoparticles-A targeted probe for imaging pankreatic cancer cells. Sensors and Actuators B: Chemical 257, 1035-1043, 2018.

100. Fan Z, Fu PP, Yu H, Ray PC. *Theranostic nanomedicine for cancer detection and treatment.* J Food Drug Anal. 2014;22(1):3-17. doi:10.1016/j.jfda.2014.01.001

101. El-Boubbou, Kheireddine. Magnetic iron oxide nanoparticles as drug carriers: clinical relevance. Nanomedicine 13.8 (2018): 953-971.

102. Shi X, Thomas TP, Myc LA, Kotlyar A, Baker JR Jr. Synthesis, characterization, and intracellular uptake of carboxyl-terminated poly(amidoamine) dendrimer-stabilized iron oxide nanoparticles. Phys Chem Chem Phys. 2007; 9(42):5712-20.

103. Corchero J., Villaverde A., Biomedical applications of distally controlled magnetic nanoparticles. Trends Biotechnol. 27, 468-476, 2009.

104. Habash R., Bansai R., Krewski D., Alhafid D., *Thermal therapy, Part 2: Hyperthermia techniques.* Crit. Rev. Biomed. Eng. 34, 491-542, 2006.

105. Kawai N., Futakuchi M., Youshida T., Ito A., Sato S., Naiki T., Honda H., Shirai T., Kohri K., *Effect of heat therapy using magnetic nanoparticles conjugated with cationic liposomes on prostate tumor in bone.* Prostate 68, 784-792, 2008.

106. Suto M., Hirota Y., Manuya H., Heat dissipation mechanism of magnetite nanoparticles in magnetic fluid hyperthermia. J. Magn. Magn. Mater. 321, 1493-1496, 2009.

107. Bao F., Yao J.-L., Gu R.-A., Synthesis of magnetic Fe_2O_3/Au core/shell nanoparticles for bioseparation and immunoassay based on surface-enhanced Raman spectroscopy. Langmuir 25, 10782-10787, 2009.

108. Pisanic T.R., Blackwell J.D., Shubayev V.I., Finones R.R., Jin S., *Nanotoxicity of iron oxide nanoparticle internalization in growing neurons.* Biomaterials 28, 257-2581, 2007.

109. Apopa P.L., Qian Y., Shao R., Guo N.L., Swhwegler-Berry D., Pacurari M., Porter D., Shi X., Vallyathan V., Flynn D.C., Iron oxide nanoparticles induce human microvascular endothelial cell permeability through reactive oxygen species production and microtubule remodeling. Part. Fibre Toxicol. 6, 1-14, 2009.

110. Azhdarzadeh M., Atyabi F., Saei A.A., Varnamkhasti B.S., Omidi Y., Fateh M., Ghavami M., Shanehsazzadeh S., Dinarvand R., Theranostic MUC-1 aptamer

targeted gold coated superparamagnetic iron oxide nanoparticles for magnetic resonance imaging and photothermal therapy of colon cancer. Colloids Surf. B: Biointerfaces 143, 224-232, 2016.

111. Li J., Hu Y., Yang J., Wei P., Sun W., Shen M., Zhang G., Shi X., Hyaluronic acid-modified Fe3O4@Au core/shell nanostars for multimodal imaging and photothermal therapy of tumors. Biomaterials 38, 10-21, 2015.

112. Ma M., Chen H., Chen Y., Wang X., Chen F., Cui X., Shi J., Au capped magnetic core/mesoporous silica shell nanoparticles for combined photothermo-/chemo-therapy and multimodal imaging. Biomaterials 33, 989-998, 2012.

113. Montazerabadi A.R., Oghabian M.A., Irajirad, R., Muhammadnejad, S., Admadvand, D., Delavari, H., Mahdavi, S.R., *Development of gold-coated magnetic nanoparticles as a potential MRI contrast agent.* Nano 10, 1550048, 2015.

114. Li J., Zheng L., Cai H., Sun M., Shen W., Zhang G., Shi X., *Facile one-pot synthesis of Fe3O4@Au composite nanoparticles for dual-mode MR/CT imaging applications.* ACS Appl. Mater. Interf. 5, 10357-10366, 2013.

115. Zhao H.Y., Liu S., He J., Pan C.C., Li H., Zhou Z.Y., Ding Y., Huo D., Hu Y., Synthesis and application of strawberry-like Fe3O4-Au nanoparticles as CT-MR dual-modality contrast agents in accurate detection of the progressive liver disease. Biomaterials 51, 194-207, 2015.

116. Cai H., Li K., Shen M., Wen S., Luo Y., Peng C., Zhang G., Shi X., Facile assembly of Fe_3O_4@Au nanocomposite particles for dual mode magnetic resonance and computed tomography imaging applications. J. Mater. Chem. 22, 15110-15120, 2012.

117. Purushotham S., Chang P., Rumpel H., Kee I.H.C., Ng R.T.H., Chow P.K.H., Tan C.K., Ramanujan R.V., *Thermoresponsive core–shell magnetic nanoparticles for combined modalities of cancer therapy.* Nanotechnology 20, 305101, 2009.

118. Wang J., Wu X., Wang C., Ding H., Li H., Li S., Shao N., Dong P., Xiao R., Wang S., *Facile synthesis of Au-coated magnetic nanoparticles and their application in bacteria detection via a SERS method.* ACS Appl. Mater. Interfaces 8, 19958-19967, 2016.

119. Jagadeeshan S., Parsanathan R. (2019) Nano-metal Oxides for Antibacterial Activity. *In: Naushad M., Rajendran S., Gracia F. (eds) Advanced Nanostructured Materials for Environmental Remediation.* Environmental Chemistry for a Sustainable World, vol 25. Springer, Cham

120. Tri, P.N.; Nguyen, T.A.; Nguyen, T.H.; Carriere, P. *Antibacterial Behavior of Hybrid Nanoparticles. In Noble Metal-Metal Oxide Hybrid Nanoparticles;* Elsevier: Amsterdam, The Netherlands, 2019; pp. 141–155.

121. Ngo, T.D.; Le, T.M.H.; Nguyen, T.H.; Nguyen, T.V.; Nguyen, T.A.; Le, T.L.; Nguyen, T.T.; Van Tran, T.T.; Le, T.B.T.; Doan, N.H. *Antibacterial Nanocomposites Based on Fe3O4-Ag Hybrid Nanoparticles and Natural Rubber-Polyethylene Blends.* Int. J. Polym. Sci. 2016, 2016, 7478161.

122. El-Liethy, M. A., Elwakeel, K. Z., Ahmed, M. S.:Comparison study of Ag (I) and Au (III) loaded on magnetic thiourea-formaldehyde as disinfectants for water pathogenic microorganism's deactivation, Journal of Environmental Chemical Engineering, 2018, 6, (4), pp. 4380-4390

123. Jagminas, A.; Kurtinaitienė, M.; Mažeika, K., Synthesis of cobalt ferrite nanoparticles by co-precipitation at ambient and hydrothermal conditions. Chemija 2013, nr. 24 (2), p. 103-110.

124.

125. Jurgis Kadzijauskas *Biochemijos pagrindai* Leidėjas: Vilniaus universiteto leidykla Išleidimo metai: 2012 Puslapių skaičius: 648 ISBN ar kodas: 9789955634874

126. Bewick, M. Kalaji, G. Larramona, In-situ infrared spectroscopic study of the anodic oxide film on iron in alkaline solutions, J. Electroanal. Chem.1991, nr. 318, p. 207-221.

127. Namduri, H.; Nasrazadani, S., Quantitative analysis of iron oxides using Fourier transform infrared spectrophotometry. Corrosion Science, 2008, nr. 50 (9), p. 2493-2497.

128. Kim, J.; Park, S.; Lee, J. E.; Jin, S. M.; Lee, J. H.; Lee, I. S.; Yang, I.; Kim, J. S.; Kim, S. K.; Cho, M. H., Designed fabrication of multifunctional magnetic gold nanoshells and their application to magnetic resonance imaging and photothermal therapy. Angewandte Chemie, 2006, nr. 118 (46), p. 7918-7922.

129. Navarro, J. R.; Lerouge, F.; Cepraga, C.; Micouin, G.; Favier, A.; Chateau, D.; Charreyre, M.-T.; Lanoë, P.-H.; Monnereau, C.; Chaput, F., *Nanocarriers with ultrahigh chromophore loading for fluorescence bio-imaging and photodynamic therapy.* Biomaterials, 2013, nr. 34 (33), p. 8344-8351.

130. Li, Y.-S.; Church, J. S.; Woodhead, A. L., *Infrared and Raman spectroscopic studies on iron oxide magnetic nano-particles and their surface modifications.* Journal of Magnetism and Magnetic Materials, 2012, nr. 324 (8), p. 1543-1550.

131. Mažeika, K.; Mikalauskaitė, A. Jagminas, A. *Influence of interactions to the properties of ultrasmall $CoFe_2O_4$ nanoparticles estimated by Mössbouer study.* Journal of Magnetism and Magnetic materials, 2015, nr. 389, p. 21-26.

132. Aigou, W.; Ping, U.; Leyong, Z. *Biomedical applications of magnetic nanparticles.* Nano, 2010, nr. 5, p. 245-270.

133. Gunasekaran, S.; Kumar, R.T.; Ponnusamy, S.Vibrational spectra and normal coordinate analysis of adrenaline and dopamine. Ind. J. Pure and Appl. Phys. 2007, nr. 45, p. 884-892., S.; Kumar, R.T.; Ponnusamy, S.*Vibrational spectra and normal coordinate analysis of adrenaline and dopamine.* Ind. J. Pure and Appl. Phys. 2007, nr. 45, p. 884-892.

134. Ojea-Jiménez, I.; Lorenzo, J.; Rebled, J. M.; Sendra, J.; Arbiol, J.; Puntes, V., *Synthesis of Co–Organosilane–Au Nanocomposites via a Controlled Interphasic Reduction. Chemistry of Materials,* 2012, nr. 24 (21), p. 4019-4027.

135. Rotomskis, R.; Karabanovas, V.; Poderys, V.; Bagdonas, S.; Didžiapetrinė, J., *Įvadas į nanomediciną.* VU Onkologijos institutas, 2008, p. 214-280.

136. Scognamiglio, V., Nanotechnology in glucose monitoring: advances and challenges in the last 10 years. Biosensors and Bioelectronics, 2013, nr. 47, p. 12-25.

137. Guinier, A.; Lorrain, P.; Lorrain, D. S.-M. *X-Ray Diffraction. Crystals, Imperfect Crystals and Amorphous Bodies; Freeman*, W. H. & Co.: San Francisco, CA, U.S.A., 1963; p 356.

138. Wang, Lingyan, et al. *Monodispersed core− shell Fe3O4@ Au nanoparticles.* The Journal of Physical Chemistry B 109.46 (2005): 21593-21601.

139. Haiss, Wolfgang, et al. Determination of size and concentration of gold nanoparticles from UV− Vis spectra. Analytical chemistry 79.11 (2007): 4215-4221.

140. Njoki, Peter N., et al. "*Size correlation of optical and spectroscopic properties for gold nanoparticles."* The Journal of Physical Chemistry C 111.40 (2007): 14664-14669.

141. King, R. C. J. "Physical Electronics: Eden Prairie." (1995).

142. Venezia, Anna Maria, et al. "*Relationship between structure and CO oxidation activity of ceria-supported gold catalysts.*" The Journal of Physical Chemistry B 109.7 (2005): 2821-2827.

143. Willyard, Cassandra. "The drug-resistant bacteria that pose the greatest health threats." Nature News 543.7643 (2017): 15.

144. Rozgonyi, F., Kocsis, E., Kristóf, K., & Nagy, K. *Is MRSA more virulent than MSSA?*." (2007): 843-845.

145. Zheng, Kaiyuan, et al. "*Antimicrobial gold nanoclusters*." ACS nano 11.7 (2017): 6904-6910.

146. Palencia, Manuel S., María E. Berrio, and Sixta L. Palencia. "*Effect of capping agent and diffusivity of different silver nanoparticles on their antibacterial properties.*" Journal of Nanoscience and Nanotechnology 17.8 (2017): 5197-5204.

147. Shang L., Stockmar F., Azadfar N., Nienhaus G.U., *Intracellular Thermometry by Using Fluorescent Gold Nanoclusters*, Angewandte Chemie International Edition, 52, 11154-11157,.

AUTORIAUS MOKSLINIŲ DARBŲ, APIBENDRINTŲ DAKTARO DISERTACIJOJE SĄRAŠAS

Monografija

A. Jagminas, **A. Mikalauskaitė,** Chapter 15 „Functionalization of iron oxide-based magnetic nanoparticles with gold shells.“ In: Xiao-Yu Yang and Nidhi Chauhan (eds.) Photoenergy and Thin Film Materials, (p. 617–660) Scrivener Publishing LLC, 2019.

Moksliniai straipsniai

1. Jagminas A, **Mikalauskaitė A**, Karabanovas V, Vaičiūnienė J. Methionine-mediated synthesis of magnetic nanoparticles and functionalization with gold quantum dots for theranostic applications. Sivakov V, ed. Beilstein Journal of Nanotechnology. 2017, 8, 1734-1741. DOI: 10.3762/bjnano.8.174 (**IF** 2,612).
2. **Mikalauskaitė A.,** Karabanovas V., Karpicz R., Rotomskis R. ir Jagminas A., Green synthesis of red-fluorescent gold nanoclusters. Characterization and application for breast cancer detection. Biointerface Research in Applied Chemistry, 2016, 6, 1702 – 1709. (**IF**-).
3. **Mikalauskaitė A.,** Kondrotas R., Niaura G. ir Jagminas A., Gold-Coated Cobalt Ferrite Nanoparticles via Methionine Induced Reduction. Journal of Physical Chemistry C, 2015, 119 (30), 17398–17407. DOI: 10.1021/acs.jpcc.5b03528. (**IF** 4,189).
4. Žalnėravičius R., **Mikalauskaite A**., Niaura G., Paškevičius A. ir Jagminas A. Ultra-small methionine-capped Au^0/Au^+ nanoparticles as efficient drug against the antibiotic-resistant bacteria, Materials Science and Engineering C-materials for biological applications, 2019, 102, 646-652. DOI: 10.1016/j.msec.2019.04.062, (**IF** 5,88).
5. Mažeika K, **Mikalauskaitė A** ir Jagminas A. Influence of interactions to the properties of ultrasmall $CoFe_2O_4$ nanoparticles estimated by Mössbauer study. Journal of Magnetism and Magnetic Materials, 2015, 389, 21-26. DOI: 10.1016/j.jmmm. 2015.04.044 (**IF** 2,717).

Konferencijų tezės

Žodiniai pranešimai:

1. **Mikalauskaitė A,** Jagminas A. Superparamagnetinių kobalto ferito nanodalelių paviršiaus funkcionalizavimo metioninu

tyrimas. 7-oji Doktorantų ir Jaunųjų mokslininkų konferencija. Vilnius, Lietuva, Spalio 24-25 d., 2017 m.

2. **Mikalauskaitė A,** BASF 133rd International Summer Course Tema: Gold Coated Cobalt Ferrite Nanoparticles via Methionine-Induced Reduction. Ludwigshafen, Vokietija, Rugpjūčio 21-26 d. 2017 m.
3. **Mikalauskaitė A**, Jagminas A. Gold Coated Cobalt Ferrite Nanoparticles via Methionine-Induced Reduction. Chemistry & Chemical Technology 2017 International Conference of Lithuanian Society of Chemistry, Kaunas, Lietuva, Balandžio 28 d. 2017 m.
4. **Mikalauskaitė A**, Karabanovas V., Karpicz R., Jagminas A. Green synthesis of red-luminescent gold nano-clusters. Characterization and application for breast cancer detection. 24-th Young Researcher Fellows' Meeting of the French Medicinal Chemistry Society" Châtenay-Malabry, Prancūzija, Vasario 8-10 d. 2017 m.
5. **Mikalauskaitė A**, Jagminas A. Gold Coated Cobalt Ferrite Nanoparticles via Methionine-Induced Reduction. 6-oji Doktorantų ir Jaunųjų mokslininkų konferencija. Vilnius, Lietuva, Spalio 26-27 d., 2016 m.
6. **Mikalauskaitė A**, Jagminas A. Gold Coated Cobalt Ferrite Nanoparticles via Methionine-Induced Reduction, 9-th Nano-conference "Advances in Bioelectrochemistry and Nanomaterials", Vilnius, 2016 m. Spalio 20-22 d.

Stendiniai pranešimai:

7. **Mikalauskaitė A,** Jagminas 3rd Global Summit and Expo on Nanotechnology and Nanomedicine, Functionalization of iron oxide-based magnetic nanoparticles with gold shells. Rugsėjo 23-29 d., 2019 (Barselona, Ispanija).
   (Finansuota © Lietuvos mokslo tarybos).
8. **Mikalauskaitė A,** Jagminas A. Gold Coated Cobalt Ferrite Nanoparticles via Methionine Inducted Reduction, 1st International conference on Nanotechnologies and Bionanoscience 2018 Rugsėjo 24-28 d., 2018 (Heraklion, Graikija)

(Finansuota © Lietuvos mokslo tarybos)

9. **Mikalauskaitė A**, Jagminas A. Magnetic Properties of Amino Acids-Mediated Cobalt Ferrite Nanoparticles. 20th International Conference-School "Advanced Materials and Technologies 2018,, Rugpjūčio 27-31 d., 2018 (Palanga, Lietuva) Gautas apdovanojimas su už geriausią stendinį pranešimą.
10. **Mikalauskaitė A**, Jagminas A. 19th International Conference-School "Advanced Materials and Technologies 2017,, Amino Acids-Mediated Synthesis of Superparamagnetic Cobalt Ferrite Nanoparticles. Palanga, Lietuva, Rugpjūčio 27-31 d., 2017 m.
11. **Mikalauskaitė A**, Jagminas A. 60 th International Conference for Students of Physics and Natural sciences. The Influence of Addition Pure Amino Acids on the Properties of Luminescent Gold Clusters. Vilnius, Lietuva, Kovo 14-17 d., 2017 m.
12. **Mikalauskaitė A**, Karpicz R., Jagminas A. The Influence of dialysis on the properties of red luminescent gold clusters, 2nd International Conference "Current Trends of Cancer Theranostics" (CTCT-2016), Druskininkai, 2016 m. Birželio 19-23 d.
13. **Mikalauskaite A**, Karpicz R., Karabanovas V., Jagminas A. Synthesis, characterization and application of red luminescent gold cluster, Tarptautinė konferencija "Chemija ir Cheminė Technologija 2016", Vilnius, 2016 m. balandžio 28-29 d.

Tarptautinės mokylos ir stažuotės

1. ES struktūrinių fondų bendrai finansuojamo projektas „Kompetencijos kėlimas mokslinėje stažuotėje „Superparamagnetinių kobalto ferito nanodalelių, magnetinių savybių slopimo priklausomybės tyrimas" Nr. 09.3.3-LMT-K-712-06-0085. Stažuotės vieta Italijoje, Modenos mieste, Modena e Reggio Emilia universiteto, Fizikos ir Nanomokslų fakultete, Prof. Marco Affronte laboratorijoje. Nuo Birželio 3 d. iki Liepos 31 d., 2017 m. trukmė (59 d.).(Finansuota © Lietuvos mokslo tarybos)
2. Stažuotės vieta Italijoje, Modenos mieste, Modena e Reggio Emilia universiteto, Fizikos ir Nanomokslų fakultete, Prof. Marco Affronte laboratorijoje. Spalio 4 – Birželio 3, 2017-2018 m.(Modena, Italija). (Finansuota © Ministero degli Affari Esteri e della Cooperazione Internazionale)

3. Stažuotės vieta Italijoje, Modenos mieste, Modena e Reggio Emilia universiteto, Fizikos ir Nanomokslų fakultete, Prof. Marco Affronte laboratorijoje. Nuo Rugsėjo 3 d. iki Spalio 4 d., 2017 m. trukmė (31 d.) (Finansuota © Lietuvos mokslo tarybos)
4. Ludwigshafen, Vokietija Vasaros mokykla: BASF 133rd International Summer Course Rugpjūčio 21-26 d., 2017 m. trukmė (savaitė). (Finansuota © BASF)
5. Caparica, Portugalija „VII Hands-on Course in Sample Preparation Using Nanoparticles for Proteomics“. Birželio 27-29 d., 2017 m. (4 dienos). (Finansuota © Lietuvos mokslo tarybos)

PADĖKA

Didžiausią padėką, norėčiau išreikšti disertacijos vadovui dr. **Arūnui Jagminui**, kuris mane nuo pat bakalauro studijų veda mokslo keliu. Dėkoju už jo tikėjimą manimi, pasitikėjimą atliekant darbus bei jų nuoseklų pavedimą. Suteiktą galimybę dirbti mokslinėje Nanostruktūrų laboratorijoje, už negęstantį pozityvumą, už įkvėpimą vykdant ir rašant baigiamąjį disertacijos darbą, o labiausią už žmogišką rūpestingumą ir supratingumą.

Dėkoju oponentams prof. habil. dr. **A. Ramanavičienei** ir prof. habil. dr. **R. Ramanauskui** už skirtą laiką bei vertingus patarimus. LMT už doktorantūros studijų metu skirtas stipendijas bei finansavimą mokslinėms konferencijoms ir stažuotėms. Italijos ambasadai už suteiktą finansavimą stažuotis Italijoje, Modenos Reggio de Emilia universitete, prof. **Marco Affronte** ir jo mokslinei grupei už nuoširdų priėmimą ir suteiktą galimybę darbuotis jų laboratorijoje. Dr. **Renatai Karpič** už skirtą laiką apmokant dirbti su jų turimais įrenginiais bei suteiktus patarimus studijų metu. Dr. **Kęstučiui Mažeikai** už pagalbą atliekant magnetinių nanodalelių tyrimus. FTMC, Medžiagų str. analizės ir Katalizės skyrių darbuotojams už pagalbą atliekant tyrimus charakterizuojant medžiagas. NVI dr. **Vitalijui Karabanovui** ir kt. prisidėjusiems atliekant teranostikos tyrimus.

Nuoširdi padėka kolegoms dr. Rokui Žalnėravičiui, Simonui Ramanavičiui, dr. Marijai Kurtinaitienei, dr. Aldonai Balčiūnaitei, dr. Vaclovui Klimui, Editai Sodaitienei už palaikymą doktorantūros studijų metu.

Ačiū šeimai: Tėvams Vytautui ir Ilonai, broliui Ramūnui, sesei Elvinai, kantriajam Viačeslavui, dar negimusiam vaikeliui ir visiems artimiesiems už tykėjimą, besąlyginį palaikymą, kantrybę ir būvimą šalia šiame gyvenimo etape.

Monografija / Monograph

„Functionalization of iron oxide-based magnetic nanoparticles with gold shells“

A. Jagminas, **A. Mikalauskaitė,**
Chapter 15
In: Xiao-Yu Yang and Nidhi Chauhan (eds.) Photoenergy and Thin Film Materials, (p. 617–660) Scrivener Publishing LLC, 2019.
Perspausdinama gavus *John Wiley and Sons* leidyklos leidimą.
Monografija galite rasti adresu:
https://doi.org/10.1002/9781119580546.ch15

15

Functionalization of Iron Oxide-Based Magnetic Nanoparticles with Gold Shells

Arūnas Jagminas* and Agnė Mikalauskaitė

Department of Electrochemical Materials Science, State Research Institute Center for Physical Sciences and Technology, Vilnius, Lithuania

Abstract

This chapter is aimed at reviewing the methods reported to date for covering of magnetic iron oxide-based nanoparticles (NPs) with gold species and shells have found numerous applications in the recent nanomedicine as biocompatible materials for magnetohyperthermia, photothermal therapy, fluorescent and computed tomography imaging. Furthermore, through coating of magnetic NPs with gold their chemical and colloidal stability can be significantly improved allowing constructing a versatile platform for further NPs functionalization with antibodies, drugs, aptamers, and fluorescent agents.

Various studies have established the fact that a direct coating of magnetic NPs *via* electroless deposition using typical reducers such as sodium borohydride or citric acid is frequently problematic due to formation of gold crystallites in the solution bulk. To overcome this drawback, several methods for deposition of gold directly or through the intermediate layer onto the surface of magnetic NPs have been proposed during past 15 years. However, the reported approaches are mainly devoted to covering of magnetite (Fe_3O_4) and hematite (γ-Fe_2O_3). Therefore, our recent findings dealt with these and other iron oxide-based, e.g., cobalt ferrite, NPs are presented in more detail. Contrary to the previous works reported the formation of continuous Au^0 nanoparticulate shells, we succeed in the decoration of magnetic NPs with numerous Au^0/Au^+ quantum dots (QDs) contributing to their prospective future applications. In addition to presentation of reported to date gold deposition techniques, an attempt was made to discuss shortly the possible application trends of these core-shelled NPs.

**Corresponding author:* arunas.jagminas@ftmc.lt

Xiao-Yu Yang and Nidhi Chauhan (eds.) Photoenergy and Thin Film Materials, (617–660) © 2019 Scrivener Publishing LLC

Keywords: Gold deposition, magnetic nanoparticles, quantum dots, clusters, TEM characterization

15.1 Introduction

Recently, gold-shelled iron oxide-based NPs are widely used for biological treatments and medical investigations because of their superparamagnetic behavior, nontoxicity, chemical stability in various fluids and biocompatibility as well as capability to interact with the specific ligands, such as proteins, antibodies, drugs, nucleic acids, etc. Taken together, uniformly sized gold-coated magnetic NPs possess a great potential for tumors detection, anticancer therapy, immunogenicity [1, 2] and analytical sensing [3–7]. Besides, the attached gold due to collective oscillation of free electrons in a continuous band structure can demonstrate crystallite size dependent plasmonic resonance band sensitive to the microenvironment [8]. As a matter of a collective magnetic and optical behavior, a variety of new applications of gold-coated magnetic NPs were reported during the past decade [8–11].

It should be noticed that in spite of numerous fabrication recipes of the gold-shelled magnetite (Fe_3O_4), maghemite (γ-Fe_2O_3), and ferrite ($MeFe_2O_4$, where Me: Ni, Co, Cu, Cr, Zn, Mn) NPs reported until now, different aspects related to the formation of the desired Au shell composition, uniformity, and thickness remain the challenging.

This study highlights the methods typically used for covering of iron oxide-based NPs with gold species and continuous shells imparting the magnetic core many intriguing functional properties. Besides, the recent synthesis routes for obtaining superparamagnetic iron oxide NPs are briefly presented because the selected route can certainly play a crucial role in the gold plating result.

15.2 Synthesis of Iron Oxide-Based Nanoparticles by Co-Precipitation Reaction

Currently, iron oxide-based NPs in average size of from several to several dozen's nanometers can be synthesized by co-precipitation reaction [12] conducted in the aqueous alkaline solutions containing Me^{2+} (Me^{2+}: Fe^{2+}, Co^{2+}, Ni^{2+}, Zn^{2+}, Mn^{2+}) and Fe^{3+} ions under environment or micro wave-assisted conditions [13, 14]. Except for the traditional NaOH and ammonia bases, other bases such as alkanolamines having properties of both as alkalis and complexing agents were suggested [15] emphasizing improved

magnetic properties and colloidal stability of the alkanolamine-stabilized NPs. According to Sugimoto and Matijevic [16], magnetite NPs can be also formed by oxidation of ferrous hydroxide suspensions [16, 17]. It is commonly accepted that by these co-precipitation ways, it is possible to fabricate NPs in predetermined shapes and size by adjusting the solution pH, concentration of precursors, as well as the nature and concentration of the capping agents [18].

The syntheses of iron oxide-based NPs under hydrothermal treatment conditions can be also attributed to a separate co-precipitation approach. In the case of Fe(II) and Fe(III) salts, a high pressure induced hydrolysis of these ions proceeded by reaction:

$$Fe^{2+} + Fe^{3+} + 8OH^{-} = Fe_3O_4 + 4H_2O \tag{15.1}$$

results in the facile one-pot formation of magnetite NPs [19]. The same result can be obtained by hydrolysis and oxidation in an aqueous solution containing Fe(II) salt and oxidizing additive under hydrothermal conditions [20–22] via reaction:

$$6Fe^{2+} + 12OH^{-} + O_2 = 2Fe_3O_4 + 6H_2O \tag{15.2}$$

High efficiency, crystallinity, and *in situ* functionalization of magnetite NPs with the desired linkers are typical advantages of these NPs. In many cases, however, these NPs are not monodisperse and prone agglomerate in aqueous solutions and physiological fluids. To prevent agglomeration, their surface are covered with positively charged polymers [23, 24]. As a matter of this fact, the attached molecules changed the surface charge and chemical properties of magnetic core. What's more, these capping layers may affect the capability to coat them with gold.

15.3 Synthesis of Iron Oxide-Based Nanoparticles by Thermal Decomposition

The second common synthesis approach of superparamagnetic iron oxide-based NPs is thermal decomposition of organic precursors in high temperature boiling solvents containing usually oleic acid and oleylamine ensuring the control of their size and stability via capping onto the NP surface. Although quite uniform in size, these NPs are highly soluble only in organic solvents. In order to make them water soluble, the subsequent modifications of their surface by substitution of the capping agents [25–29] or formation of a double layer from amphiphilic molecules [30] is required.

In the latter case, the amphiphilic drug molecules, such as phospholipids, reversibly bound to the surface of NPs can be easily released *in vivo*.

15.4 Less Popular Chemical Syntheses

A separate synthesis approach for iron oxide-based NPs fabrication at moderate temperatures is sol-gel [31]. By this way, spherical NPs possessing a high purity and narrow size distribution can be obtained [32, 33].

15.5 Gold Shell Formation Onto the Surface of Magnetite Nanoparticles

The general strategy to synthesize core-shelled hybrid nanomaterials: form NPs of iron oxide, then use them as seeds that should be coated with gold directly or through the intermediate shell. However, it is worth noticing that to combine materials with very different lattice parameters such as iron oxide (0.835 nm for Fe_3O_4) and gold (0.408 nm) still faces challenging. Therefore, to overcome this drawback the activation of magnetite NP surface with perchloric acid [34–37], sodium citrate [38], hydroxylamine [39], followed by iterative additions of chlorauric acid and a reducing agent to pre-treated NPs suspension have been proposed. In the most frequently used procedure, the reduction of Au^{3+}-containing ions directly onto the surface of magnetite NPs was conducted under a vigorous stirring of NPs in the $HAuCl_4$ boiling solution and sodium citrate [34, 40–45]. Besides, a variety of other water soluble reducing agents, such as hydroxylamine [29, 34, 46–50], glucose [51, 52], formaldehyde [53, 54], and sodium borohydridre [55], has been proposed. First report on the formation of magnetite NPs with gold shell via reduction of Au^{3+} ions with hydroxylamine was dated by Cui's group in 2001 [46]. Later, this approach with modifications was successfully used for coating of small Fe_3O_4 and γ-Fe_2O_3 NPs after their surface functionalization in a 0.1 M tetramethylammonium hydroxide solution for hydroxylamine seeding [56, 57], followed by NPs sonication in the solution of sodium citrate, to exchange adsorbed OH^- ions with citrate anions, and finally – in the gold deposition bath containing an excess of $NH_2OH \cdot HCl$ as reducer and 1% $HAuCl_4$ aliquots added several times with 10 min intervals. The resultant NPs shown in Figure 15.1 reveal a significant NP average size increase from the initial up to 60 nm becoming obviously less aggregating [57]. Later, to design multifunctional

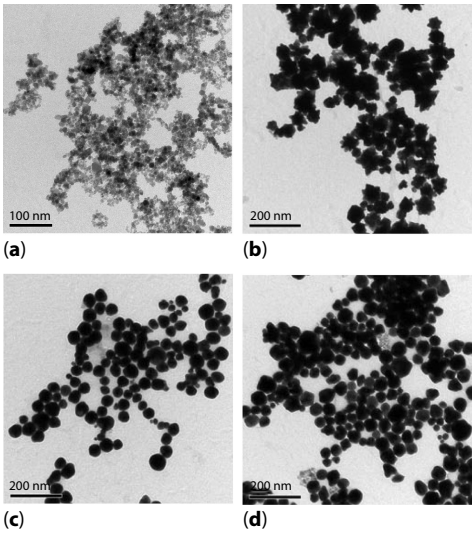

Figure 15.1 Representative TEM images of citrate-stabilized Fe_3O_4 NPs before (a) and after gold deposition by one (b), three (c), and five (d) incremental additions of Au^{3+} to an aqueous solution of Fe_3O_4 NPs. Reproduced in part from ref [57]. Copyright 2017 Am. Chem. Soc.

composites of magnetite NPs synthesized by the typical co-precipitation way from an alkaline Fe^{2+}/Fe^{3+} solution and sodium citrate, the reduction *in situ* of the $AuCl_4^-$ ions onto the surface of Fe_3O_4 NPs with the sodium citrate solution kept at the boiling temperature has been reported by Yu *et al.*, [42]. However, the yield and uniformity of depositions as well as the role of citrate ions linked tothe surface of Fe_3O_4 NPs during their synthesis on the reduction ofAu^{3+} and formation of gold shell have not been analyzed and discussed.Furthermore, by this way, it was impossible to prevent the aggregation of magnetite NPs and separation of the coated NPs from the uncoated ones.

The initial attempts to coat magnetite NPs with gold also involved the application of reverse micelles as the reactors for both NP synthesis and covering with a gold [3, 51, 58, 59]. In most cases, CTAB, octane and 1-butanol were used for magnetite NPs formation, whereas gold (III) chloride and sodium borohydride solution was used for initial nucleation of numerous gold seeds at the randomly selected sites of magnetite [60]. Following this, the further growth of the attached Au^0 seeds resulted in the formation of gold shell. By this way, however, it was difficult to reproduce Fe_3O_4@Au NPs of the same size and core shell thickness [61]. Besides, in the most cases the fabricated Fe_3O_4@Au NPs required separation from

the pure gold crystallites formed in the deposition solution bulk and were prone to agglomerate in the aqua media. Later, despite in the aqueous solutions the covering of magnetite and maghemite NPs with a thin gold shell has been proposed *via* prolonged by weeks processing in a two phase system composed of octane-based magnetic fluid, an aqueous $HAuCl_4$ solution, and N-(2-(didecylamino ethyl)-N,N-tridecyldecan-1-ammonium iodide as the phase-transfer reagent [62]. Besides, a number of hybrid NPs have been synthesized to date through a seed-mediated approach [62–64]. Similarly, gold coated magnetic NPs were prepared *via* attachment of 2–3 nm-sized Au NPs with 3-aminopropyl triethylsilane onto the 10 nm-sized Fe_3O_4 [65]. From the literature [23], polymer shells with the attached gold NPs prevent formation of large aggregates.

The third group of methods consists of both magnetic NPs synthesis and covering them with gold in organic solutions [66, 67]. Typically, the iron oxide NPs fabricated through the thermal decomposition of iron organic precursors such as carboniles, oleates, and acetylacetonates in the high temperature boiling solvents subsequently are coated *via* reduction of gold acetate in the chloroform media containing oleylamine as both a reducer and capping additive. For thicker gold shell formation, NPs should be pretreated in an aqueous solution of sodium citrate and cetyltrimethylammonium bromide (CTAB) and then in the room temperature aqueous solution containing gold ions, ascorbic acid and STAB. By this way, a complete gold shell with a desired thickness can be formed. To coat magnetite NPs capped with organic ligands, Wang *et al.,* [66] proposed the gold deposition from a hot (~190 °C) phenyl ether solution containing gold acetate and oleylamine. In this solution, the desorption of the capped ligands from the surface of NPs and an *in situ* gold deposition onto the cleaned magnetite surface was observed. By this way, however, only some part of NPs are covered with gold requiring separation from the uncoated and partially coated ones [67]. In 2007, Park *et al.,* reported the route for covering of the 10 nm-sized superparamagnetic Fe_3O_4 NPs fabricated by a typical thermal decomposition of iron (III) oleate way and the subsequent treatment in the chloroform solution containing $HAuCl_4$ and oleylamine as a reducing agent and surfactant [68]. To make these NPs water-soluble, Fe_3O_4@Au NPs were dried and dissolved *via* sonication in the solution containing 0.1 M CTAB and 0.1 M sodium citrate.

Poly(vinylpyrrolidone) (PVP) was an another polymer-surfactant employed for nanoemulsion synthesis of Fe_3O_4@PVP-Au NPs in two consecutive steps [69]. In this method, Fe_3O_4 NPs were also synthesized *via* a thermal decomposition of iron (III) acetylacetonate (Fe_{acac}) in octyl ether containing the reducing agent – 1,2-hexadecanediol and PVP. In the next

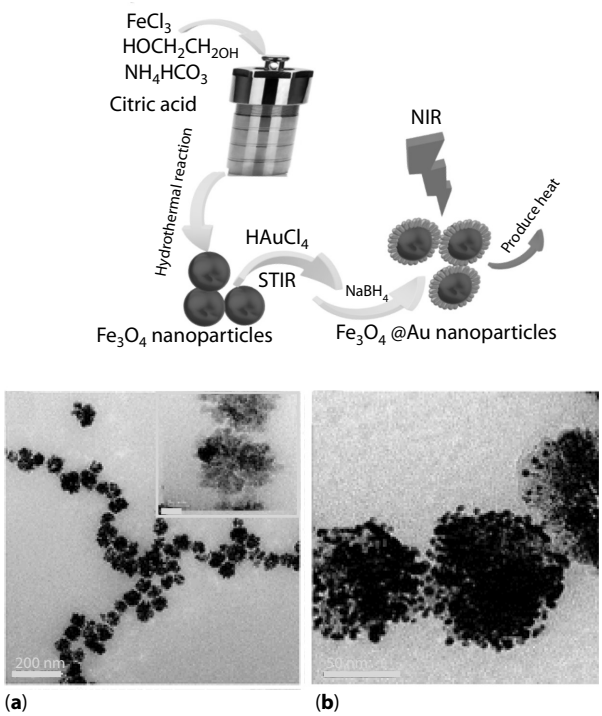

Figure 15.2 TEM images of Fe_3O_4 clustered NPs before (a) and after (b) gold coating for photothermal destruction of cancer cells. In the upper part the scheme of processing.

step, the as-grown Fe_3O_4 NPs were coated with gold using a same reducer and gold acetate dissolved in octyl ether at 80 °C and 215 °C under reflux for 2 hr in each. The method mentioned above, makes it possible to better control the size of quite monodisperse and long-time stable magnetite NPs as well as the thickness of their gold shells. However, these NPs tend to agglomerate quickly in the aqueous media.

In 2011 Ren *et al.,* reported a way for the synthesis of superparamagnetic Fe_3O_4@Au NPs by so-called a self-assembling approach [70]. This synthesis protocol involved the synthesis of positively charged Fe_3O_4 NPs by reduction of $FeCl_3$ with ethylene glycol (e.g.,) in the alkaline medium containing additionally ammonium bicarbonate and citric acid at 200 °C (see scheme in Figure 15.2). Then, the as- grown spherical Fe_3O_4 NPs in size of 60–200 nm were mixed with an aqueous $HAuCl_4$ solution. Upon the subsequent reduction of Au^{3+} with $NaBH_4$ solution under gentle stirring conditions, electrostatic adsorption of as-grown NPs onto the surface of Fe_3O_4 was obtained. It is worth noticing that thermal decomposition of

ammonium bicarbonate to NH_3 and CO_2 gases during growth of Fe_3O_4 NPunder solvothermal conditions results in the formation of mesoporous NP structure (Figure 15.2) possessing the NIR absorbance. Irradiation experiments indicated that these Fe_3O_4@Au NPs can rapidly convert laser beam energy into heat and can be used for photothermal destruction of cancer cells.

Similarly, to increase the size uniformity and viability of Fe_3O_4@Au NPs, their synthesis in organic solutions and the subsequent covering with gold shell in an aqueous solution have been proposed by Hu *et al.,* and Lim *et al.,* [71]. Note, that although NP size control has been well achieved by these syntheses, the aggregation of NPs even after formation of Au shell remained high in the aqua media. For example, for coating of the hydrophobic 10–13 nm-sized superparamagnetic Fe_3O_4 NPs with a gold shell in thickness of ca. 2–3 nm possessing saturation magnetization value of about 40 emu g^{-1} and rendering plasmonic properties, the following method has been reported by Chin *et al.,* [72]:

1. synthesis of 8 nm-sized Fe_3O_4 NPs in an aqueous alkaline solution by early reported way;
2. refluxing of the Fe_3O_4 NPs in an aqueous solution containing either (3-amino propyl)triethoxysilane or dopamine for the few hours resulting in the attachment of $-NH_2$ groups;
3. synthesis separately of gold seeds in an average size of ca. 2–3 nm from an aqueous solution containing tetrakis (hydroxymethyl) phosphonium chloride and $HAuCl_4$;
4. the sonication of imine-functionalized Fe_3O_4 NPs with gold seeds under stirring conditions overnight;
5. formation of Au shell onto the surface of NH_2-functionalized and gold-seeded Fe_3O_4 NPs in an aqueous glucose solution with $HAuCl_4$ added drop-wise.

As reported, by this way, superparamagnetic 12 ± 3 nm-sized Fe_3O_4@Au NPs with uniform Au shell in thickness of (2–3) nm can be fabricated. However, the size and shape of resulting Fe_3O_4@Au NPs typically are irregular.

The facile fabrication approach of the Fe_3O_4@Au NPs stabilized with polidopamine (PDA) molecules which in turn can attach the gold seeds, dissociate from the Fe_3O_4 surface and *in situ* reduce $AuCl_4^-$ ions by the catechol groups in PDA forming continuous gold shell, has been reported by An et all. in 2013 [73]. This procedure, however, was also multistep. To obtain magnetite NPs containing the gold shell, Au seeds should be

separately synthesized and attached to the Fe_3O_4@PDA NPs. Therefore, to form the dense gold shells onto the gold-seeded Fe_3O_4@PDA NPs, they must to be further sonicated in water under mechanical stirring adding several 1% $HAuCl_4$ small aliquots with 10 min intervals. From the TEM images, however, the size and shape of these NPs differ significantly.

To decorate the surface of hydrophobic Fe_3O_4 NPs with gold species, the amino-functionalized Fe_3O_4 NPs were prepared in the glycerol solution containing $FeCl_3$, anhydrous $Na(OOCCH_3)$ and 1,6-hexadiamine at 200 °C for 6 hr and then functionalized via keeping in a dimethylformamide solution containing Boc-L-cisteine,O-benzotriazole-N,N,N',N'-tetramethyluroniumhexafluoro phosphate and triethanolamine to react overnight [74]. Au NPs were synthesized separately in the $HAuCl_4$ solution containing cetyltrimethylammonium bromide and $NaBH_4$. The prepared Fe_3O_4 NPs were then dispersed in the ethanol and mixed with an aqueous solution of Au NPs under ultrasound agitation for 5 min. To remove unbounded Au NPs, Fe_3O_4@Au NPs were collected magnetically. As also reported, the conjugation of Au NPs with Fe_3O_4 surface should be ascribed to the strong interaction of gold with thiol groups in the capped layer of magnetite surface. Nevertheless, both TEM and SEM images of resultant Fe_3O_4@Au NPs revealed their agglomeration (Figure 15.3).

To date, most of the ferrite NPs were studied mainly for their magnetic properties with few having been implemented for biomedicine applications. However, the substitution of the Fe^{2+} ion in magnetite NPs with Co^{2+}, Zn^{2+}, Ni^{2+}, Cr^{2+} or Cu^{2+} allows to manage their magnetic and chemical properties, and biocompatibility that can be tuned to new applications. For example, cobalt ferrite ($CoFe_2O_4$) NPs have saturation magnetization of about 80 emu g^{-1}, good permeability, a high coercivity of more than 5 kOe, and Currie temperature as well as electromagnetic performance and excellent chemical stability [75, 76]. It is worth also noticing that copper-substituted $CoFe_2O_4$ NPs have the most effective contact biocidal property among all of the iron oxide NPs, whereas zinc-substituted ones – significantly improved antibacterial activity [77].

For attachment of gold to the surface of maghemite (γ-Fe_2O_3) NPs with a high yield, electron beam irradiation at a dose of 6 kGy of magnetic NPs probe spread in an aqueous solution of $HAuCl_4$, 2-propanol, and poly(vinyl alcohol) has been proposed [78, 79]. In this way, colloidal gold forms a strong Au-S bond with a thiol group without any catalysts or linker molecules.

The decoration of magnetite NP surface with the discrete gold species without formation of a complete Au shell has also been reported [65, 74, 80] via attaching of amine or thiol groups containing molecules directly to

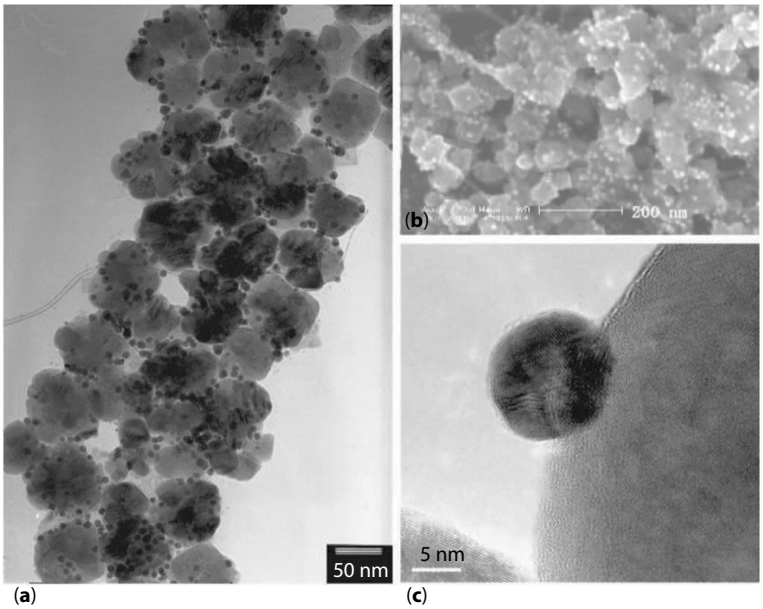

Figure 15.3 TEM (a), SEM (b), and HRTEM (c) images of Fe_3O_4 NPs covered with gold seeds upon functionalization the surface of magnetite NPs with -NH_2 and the subsequent attaching of Au^0 species (Reprinted from ref [74]. , with permission from the Am. Chem. Soc.).

the surface of as-grown bare Fe_3O_4 NP before Au^{3+} ions reduction. Note, that the capping molecules can also attach Au^0 species to the surface of magnetite NPs via a covalent binding [65, 74]. However, the decorated magnetic NPs with small Au NPs do not address NP stability and magnetite core leaching and degradation. To avoid this problem, the synthesis of Fe_3O_4@Au NPs through the formation of biocompatible intermediate shell composed of polyethyleneimine (PEI) and the subsequent attachment of 2 nm-sized Au NPs has been suggested by Goon *et al.,* [23]. Note, this way resulted in the formation of only some larger Fe_3O_4@PEI-Au NPs namely ~ 60 nm with respect to the size of magnetic core, ca. ~ 48 nm (Figure 15.3). Moreover, except for the possibility of controlling NP size through the control of PEI and Fe_3O_4 NPs amounts in the gold deposition solution this method allowed controlling the number of gold seeds attached to the Fe_3O_4 NP surface most likely via electrostatic and covalent bonding with amines on Fe_3O_4@PEI. Similarly, doubly-shelled microsheres with a magnetic core, decorated with Au^0 NPs, namely Fe_3O_4@ SiO_2@TiO_2-Au (Figure 15.4) have been recently designed as a smart and efficient photocatalytic system for environmental treatments [81]. To

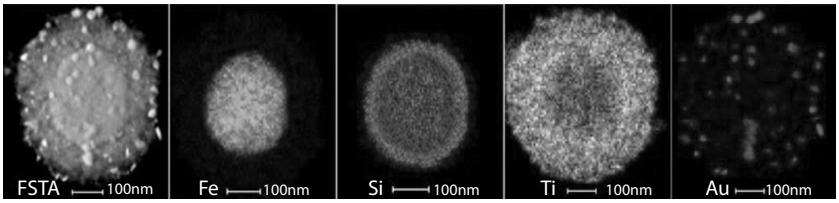

Figure 15.4 Dark-field TEM image and elemental mapping images of a single Fe_3O_4@SiO_2@TiO_2-Au NPs microsphere fabricated according to Wang and co-authors report. Reprinted from ref [81], with permission from the Springer.

increase photocatalytic efficiency, via separation of photogenerated carriers, the gold NPs were entrapped into the outer mesoporous TiO_2 shell by electroless deposition using sodium borohydride. Note that the outer shell which decreased the magnetic saturation value of the core from 44.7 to 18.5 emu g^{-1} still remained the possibility to separate them by recycling in a magnetic field.

The pioneering approach for attachment of red-fluorescent gold clusters to the surface of superparamagnetic Fe_3O_4 NP has been reported by Sreenivasan group [82]. According to their suggestion, fluorescent gold clusters separately prepared by well-known green synthesis way using Bovine serum albumin (BSA), can be well attached to the surface of Fe_3O_4 NPs through anchoring of dopamine molecules.

Several years ago, we have synthesized small ca ~ 5.0 nm sized (Figure 15.5) and ultra-small with a mean diameter of 1.85 nm (Figure 15.6) $CoFe_2O_4$ NPs by typical co-precipitation approach using $CoCl_2$, $Fe_2(SO_4)_3$ and citric acid at 80° for subsequent covering with gold shells [83]. In addition to EDX, compositional stoichiometry of both small and ultra-small NPs was estimated after their dissolution in HCl (1:1) by inductively coupled plasma mass spectrometry analysis on the emission peaks at 228.616 and 239.562 nm for Co and Fe, respectively, both revealing Co to Fe at% ratio close to 1:2 The XRD patterns of 5 nm-sized NPs (Figure 15.5.c) correlated well with the standard $CoFe_2O_4$ diffraction peaks attributable to polycrystalline inverse spinel structure. Our attempts to coat these small and pure $CoFe_2O_4$ NPs with gold in the aqueous $HAuCl_4$solutions with typical reducers such as sodium borohydride and citric acid were unsuccessfull, – in all these cases a significant fraction of gold crystallites were formed in the colloidal solution bulk instead of coating the surface of NPs.

Therefore, with the idea to reduce the gold ions at the NP surface, we checked the possibility to anchor initially some week reducer molecules to the surface of ferrite NP. Our choice drop on the attachment of Vitamin C

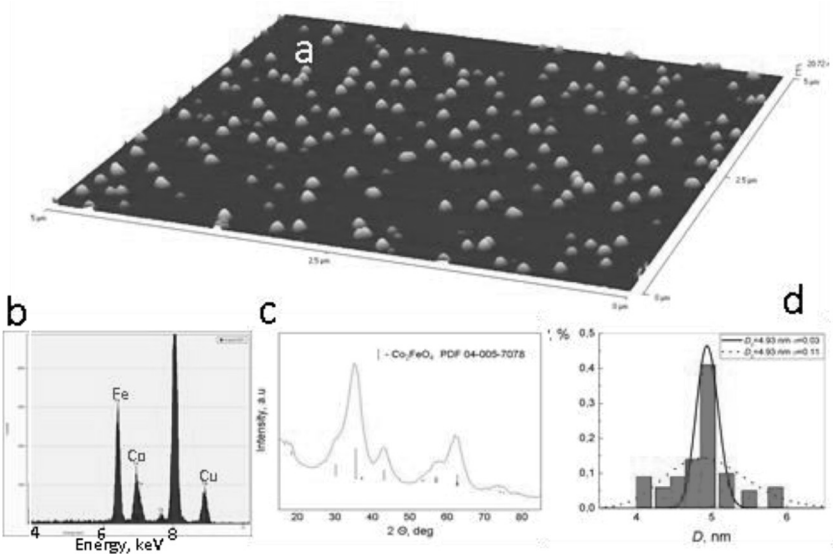

Figure 15.5 In (a): AFM view of $CoFe_2O_4$ NPs synthesized by co-precipitation reaction from an alkaline (pH = 12.1) de-aerated solution containing 100 mmol L^{-1} $CoCl_2$ + $Fe_2(SO_4)_3$ at the 1.1:1.0 ratio +100 mmol L^{-1} citric acid at 80 °C for 3 hr and collected by centrifugation at 8500 rpm for 3 min. In (b, c, and d) a typical EDX spectrum, XRD pattern, and histogram with lognormal (line) distribution of NP sizes, respectively, are shown.

(*VitC*) molecules because of a simple possibility to determine spectrophotometrically the concentration of ascorbic acid in the deposition solution (Figure 15.7) as well as biocompatibility and a weak reduction capability of *VitC*. The applied anchoring and covering scheme is depicted the histogram and log-normal distribution plot of the synthesized core-shelled NPs. Bellow, the scheme used for gold deposition and shell formation onto the surface of $CoFe_2O_4$ NPs. in Figure 15.8 together with the obtained TEM observation results indicated on the NP size increase to ca. 14 nm after two days NPs sonication in the initial 20 μmol L^{-1} $HAuCl_4$ solution (Figure 15.8c). The successful coatings of these NPs were obtained *via* several sequential additions of low concentrated $HAuCl_4$ and *VitC* solution probes to the deposition reactor under mild stirring conditions. The prolonged sonication of *VitC*-modified Co-ferrite NPs in the $HAuCl_4$ containing solution even at room temperature lead to decrease in the amount of adsorbed ascorbate ions down to zero (Figure 15.7B curve d). With further addition of *VitC* and Au(III) species, the color of ferrofluid changed to violet and pinkish tints visiable to the naked eye. The corresponding UV-vis spectra for these ferrofluids are also shown in Figure 15.7B (curves

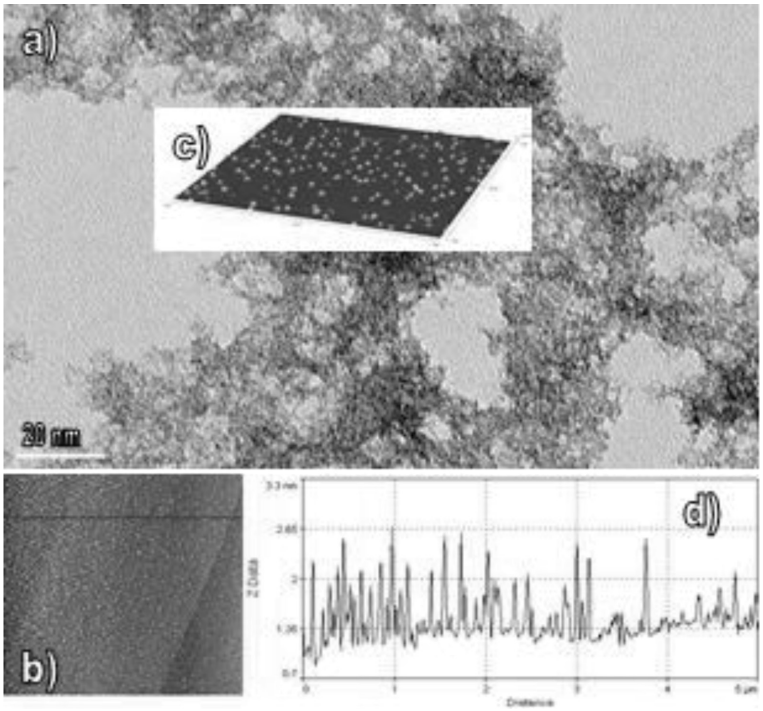

Figure 15.6 TEM (a) and AFM (b, c) images and size profiles (d) of ultra-small Co-ferrite NPs synthesized by co-precipitation reaction from an alkaline (pH = 12.1) de-aerated solution containing 100 mmol L^{-1} $CoCl_2$ + $Fe_2(SO_4)_3$ at the 1.1:1.0 ratio +100 mmol L^{-1} citric acid at 80 °C for 3 hr (supernatant fraction).

b and c) indicating the appearance and variation in a wide plasmonic absorption band peaked in a vicinity of 520–540 nm, characteristic of nm-scaled gold crystals [84]. With increased sonication time, this absorption band red-shifts towards a longer wavelengths and lower energies signaling on increase in the thickness of gold shell around the ferrite NP core as has been reported in [85].

According to the previous studies, the covering of magnetite NPs with a gold shell resulted in their saturation magnetization and blocking temperature (T_B) values decrease [66, 67]. Consequently, to preserve the magnetic properties of core, the gold shells ought to be uniform and as thin as possible. The influence of gold shell formed *via VitC*-assisted reduction on the magnetic properties of Co-ferrite core material we ascertained from the Mössbauer spectra and T_B variables with the recording temperature increase from cryogenic to 75 K for the case of ultra-small cobalt ferrite NPs in a mean size less than 2.0 nm (Figure 15.6). For

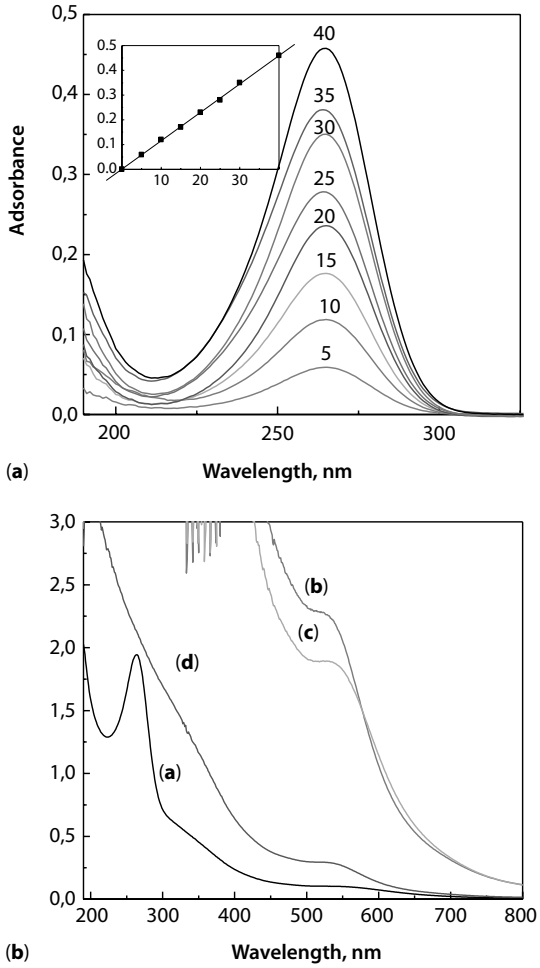

Figure 15.7A Light absorbance spectra *versus* concentration of ascorbic acid from 5 to 40 μmol L^{-1}. In the *Inset*: calibration plot of ascorbic acid at λ = 263 nm. **B:** Absorption spectra of ultra-small Co-ferrite NPs grown as in Figure 15.5 and neutralized by ascorbic acid to pH = 6.0 (a) at various stages of their subsequent sonication with 0.4 mmol L^{-1} $HAuCl_4$ at ambient temperature for one (b), two (c) and three (d) days. After the first and next day, 0.15 mL of ascorbic acid (0.05 mol L^{-1}) and 0.4 mL of $HAuCl_4$ (0.01 mol L^{-1}) was added for further gold reduction. For (a) and (d) spectra the ferrofluids were diluted 16 times.

this reason, dried NPs as well as their ferrofluid probes were cooled to 7–10 K and the Mössbauer spectra were recorded under transmission mode. Several Mössbauer spectra were recorded further as the sample temperature increased to 75 K. Note that T_B indicates the temperature

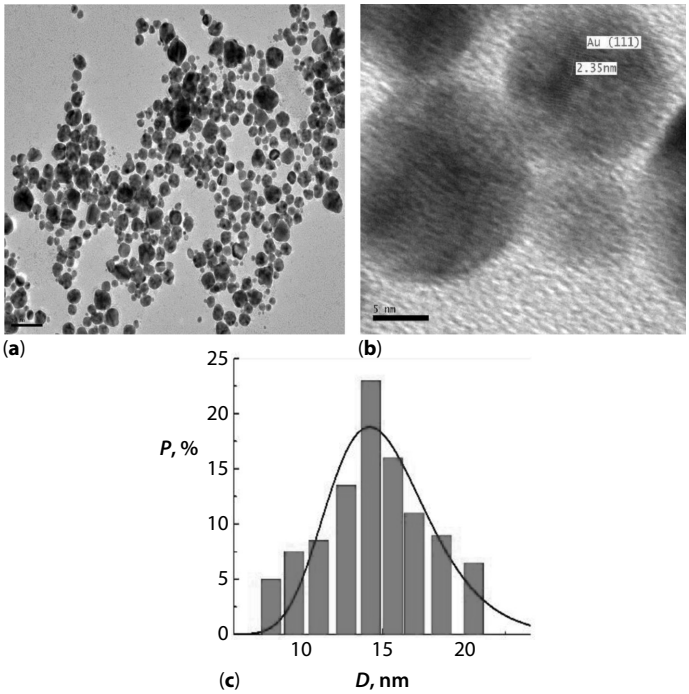

Figure 15.8 TEM (a) and HRTEM (b) views of $CoFe_2O_4$@Au NPs synthesized as in Figure 5 after surface functionalization with *VitC* and reduction of $[AuCl_4]^-$ ions through two days sonication in a 20 μmol L^{-1} $HAuCl_4$ solution containing the excess of *VitC*. In (c), the histogram and log-normal distribution plot of the synthesized core-shelled NPs. Bellow, the scheme used for gold deposition and shell formation onto the surface of $CoFe_2O_4$ NPs.

above which NPs are superparamagnetic. Typical Mössbauer spectra of ultra-small Co-ferrite NPs with $Ø_{mean} \approx 2.0$ nm in the aqueous ferrofluid at various recording temperatures are depicted in Figure 16.10a, while Having established the conditions of gold ions reduction with methionine amino acid through iterative addition of chlorauric acid and methionine to the suspension of $CoFe_2O_4$ NPs, similar as addition of *VitC*, hydroxylamine and glucose [86] we further succeed in the synthesis of cobalt ferrite and magnetite NPs using methionine amino acid as reducer variations in the hyperfine fields for the same gold-covered NPs with temperature are presented in Figure 15.10b. As seen, NPs covered with a gold shell in dry and ferrofluid states demonstrate a somewhat lower T_B than naked one; most likely due to a less effective coupling of the magnetic dipole moments in the lager $CoFe_2O_4$@Au NPs justifying the observations reported earlier for gold coutings of magnetite and maghemite [66, 67, 85].

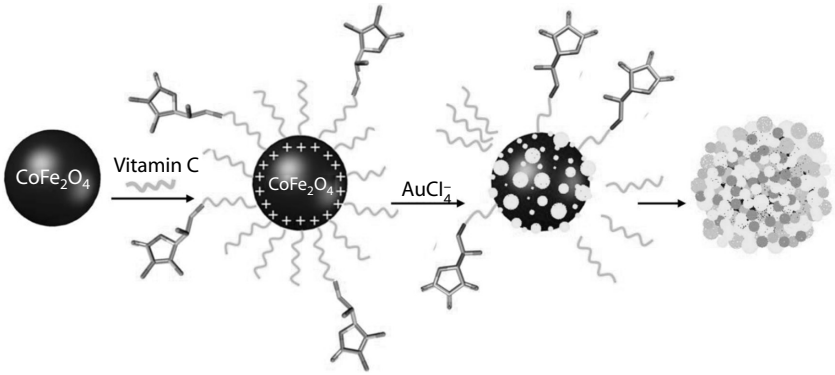

Figure 15.9 The scheme used for Vitamin-C assisted gold deposition and shell formation onto the surface of $CoFe_2O_4$ NPs.

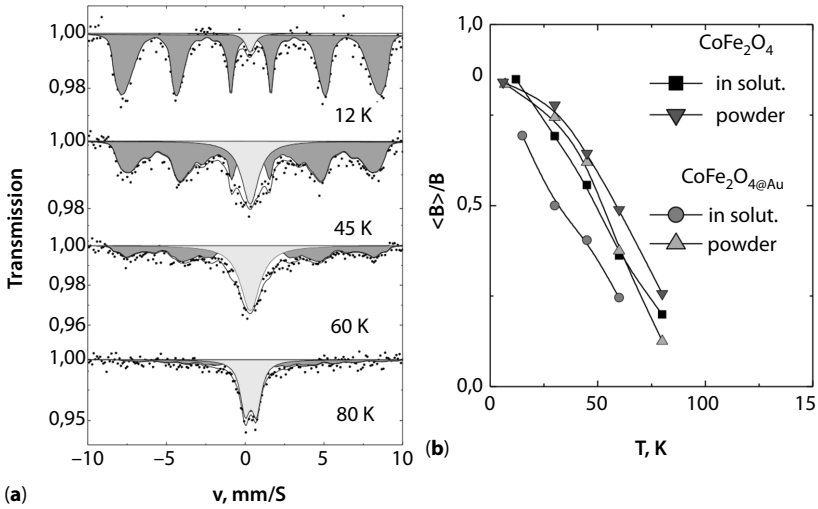

Figure 15.10 Mössbauer spectra of CoFe2O4 NPs (Ømean = 2.0 nm) dispersed in an aqueous solution before Au deposition at indicated temperatures and (b) the dependences of normalized average hyperfine field for the same CoFe2O4 NPs before and after Au deposition in the solution and powder state on temperature, as indicated.

It is noticing that *VitC*-assisted gold shell formation around Co ferrite NP method differs from the reported ones in such aspects as magnetic core material, small and ultra-small NP size, biodegradable reductant and simply controllable processing. In addition, we have found that high stability of ultra-small Co-ferrite *Nps*, fabricated by co-precipitation way under

conditions of this study, remains approximately the same after replacement of OH^- ions by *VitC* or ascorbic acid species.

15.6 Methionine-Induced Deposition of Au^0/Au^+ Species

Several years ago we have found that sequential addition of D,L-methionine and $HAuCl_4$ low concentrated aqua probes to the suspension of cobalt ferrite NPs allow coating them with gold shell [87]. To verify this finding, we have synthesized three groups of $CoFe_2O_4$ NPs different in size, namely from ultra-small to 15 nm-sized *via* a typical co-precipitation way (Figure 15.11). The deposition of gold was conducted later through sonication of cobalt ferrite NPs in the solution containing 0.9 mg mL^{-1} NPs, 0.3 $HAuCl_4$, 0.3 mmol L^{-1} methionine and NaOH (to adjust the pH to 12.0) at physiological temperature and stirring conditions for several hours. Figure 15.10 shows the TEM and STEM images of ultra-small cobalt ferrite NPs in average size of 1.85 nm after revealing the NP size increase to 2.45.

To determine the structure of gold as well as organic shell formation around the Co ferrite NP, gold-coated $CoFe_2O_4$@Au NP core was dissolved in 1:1 HCl solution and the remaining precipitates were collected by centrifugation for subsequent TEM investigations. Figure 15.12 shows the TEM images of gold-coated $CoFe_2O_4$ NPs before (a) and after (c, d) dissolution of magnetic core in HCl. The selected area electron diffraction (SAED) pattern of gold coated ferrite NPs presented in Figure 15.12b clearly demonstrated the diffraction from 0.238 nm and 0.282 nm gold lattices (111) with the atoms spacing 0.235 nm and (110) with atoms spacing 0.28 nm, respectively. In this way, it was found that in the case of one-step gold plating, the thin platelet gold corpuscles remained after dissolution of NPs core allowing us to conclude about their true nature: most probably they are the fragments formed from the shell of $CoFe_2O_4$@Au NPs. In the case of NPs coated with thicker shell by repeating the deposition process, the shape of gold bubbles remaining after core etching (Figure 15.14d) resembles the shape of $CoFe_2O_4$@Au NPs, pointing to the nice covering of ferrite NPs with gold by methionine-induced deposition approach reported herein. Note that application of amino acids such as L-lysine, D,L-methionine, L-arginine, etc. as the capping agents in the co-precipitation reaction of magnetic NPs have been suggested earlier by several authors [88–91].

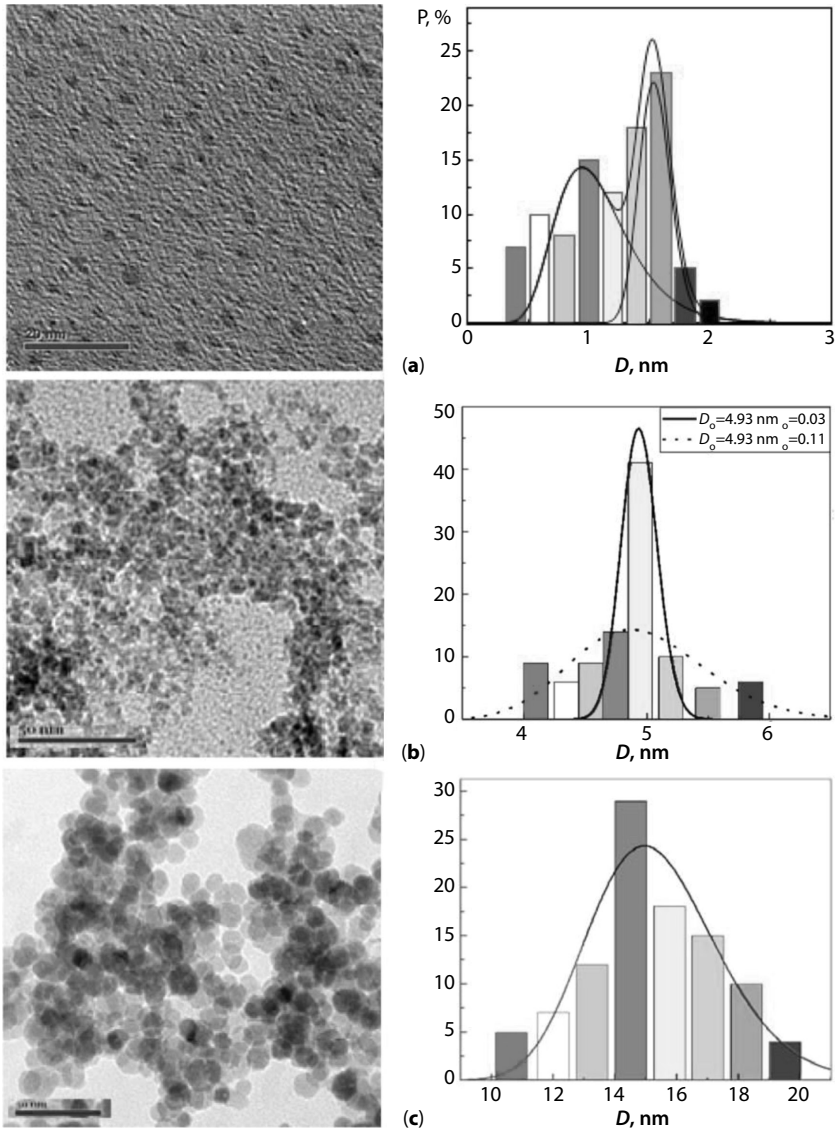

Figure 15.11 TEM images of nanoparticulated products synthesized in the deoxygenated solution containing 50 $CoCl_2$ +50 $Fe_2(SO_4)_3$ + 75 mmol L^{-1} diglycolic acid +NaOH up to pH = 12.4 at 80 °C for 3 hr (a, b) and by hydrothermal treatment at 130 °C for 10 hr (c). The size distribution histograms of corresponding NPs are shown on the right. nm after processing. Similar results were also obtained in the case of sonication $CoFe_2O_4$ NPs with average size of 4.93 nm (Figure 15.11b) and 14.6 nm (Figure 15.11c). In these cases, the average size of ferrite Nps increased to 6.6 and 17.1 nm, respectively.

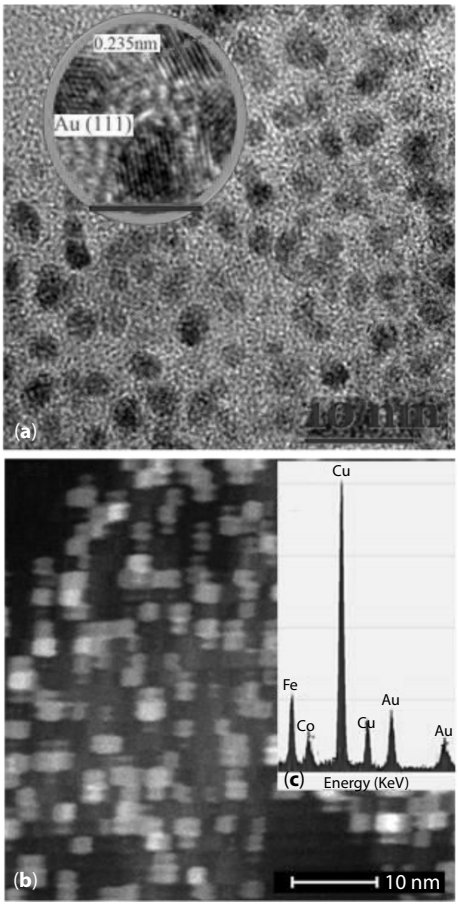

Figure 15.12 TEM (a) and STEM (b) images of $CoFe_2O_4$@Au NPs fabricated by methionine-directed gold deposition. In (c) EDX spectrum of gold-plated NPs. In the green circled Inset: HRTEM image of the products demonstrating the Au lattice spacing ca. 0.235 nm (scale bar 5 nm). Upon the plating, an average size of $CoFe_2O_4$ NPs increased from 1.85 to 2.45 nm.

It is commonly accepted that superparamagnetic magnetite NPs capped with amino acids are spherical, more uniform in size, more biocompatible, and possess stability for months. We have also determined that cobalt ferrite NPs hydrothermally synthesized in an alkaline solution containing $CoCl_2$, $FeCl_3$, and D,L-methionine at 130 °C for 10 hr are spherical and ~6.0 nm-sized (Figure 15.15). The stabilization of cobalt ferrite NPs with metnionine molecules confers them strong non-fouling properties not allowing aggregate. The XRD pattern of these NPs

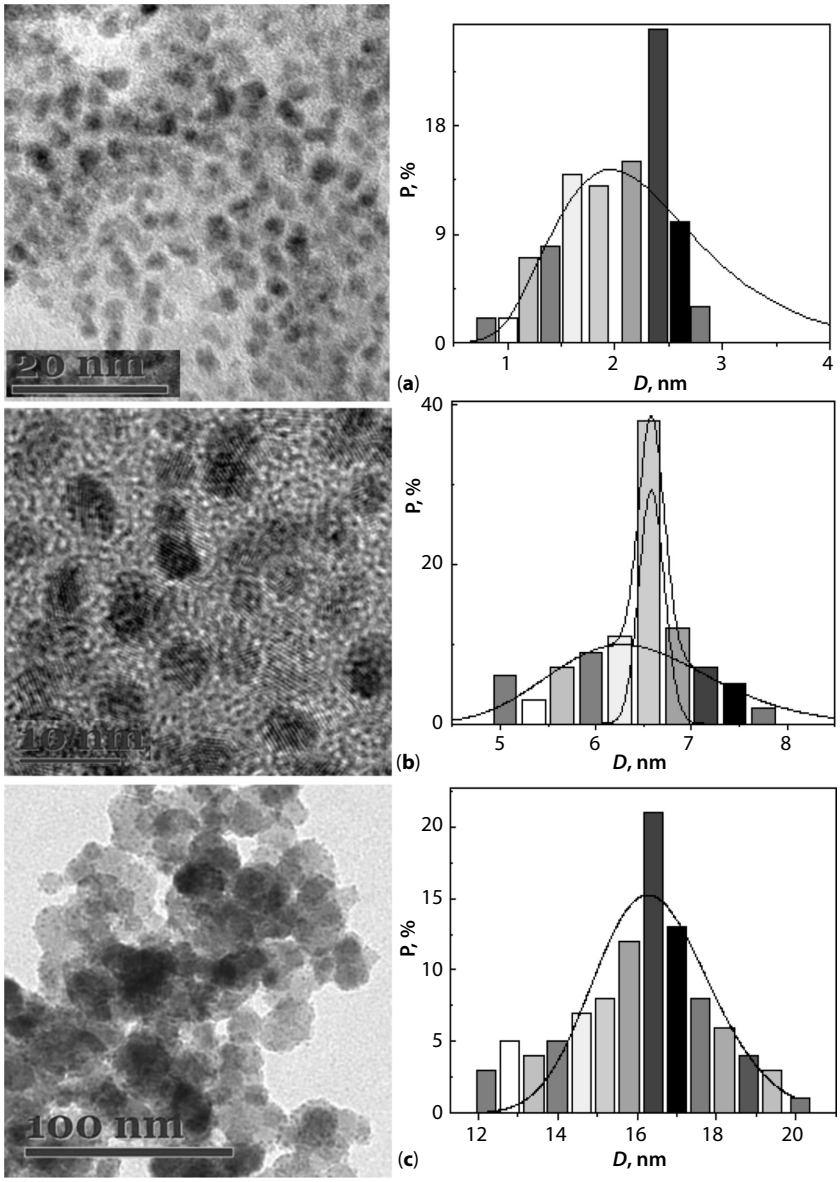

Figure 15.13 Size distribution histograms for cobalt ferrite NPs after gold deposition from the alkaline (pH = 12.2) solution containing 0.3 $HAuCl_4$ and 0.3 mmol L^{-1} D,L-Methionine at 37 °C for 4 hr. Lines are fits to lognormal distributions. On the left side TEM views of corresponding $CoFe_2O_4$@Au NPs.

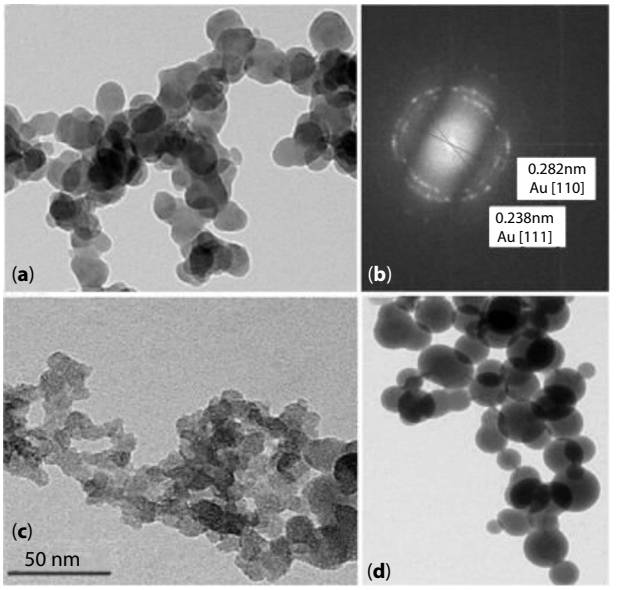

Figure 15.14 TEM images of the $CoFe_2O_4$@Au NPs (a) and gold products remaining after $CoFe_2O_4$@Au NPs etching in the HCl (1:1) solution for thinner (c) and thicker (d) shells. In (b) the SAED spectrum taken from the scope of gold-coated cobalt ferrite NPs.

(Figure 15.15c) implied the formation of pure, inverse spinel structure $CoFe_2O_4$, because all diffraction peaks observed at 2Θ positions matched well with the standard polycrystalline $CoFe_2O_4$ diffraction data summarized in the PDF Card No.: 00.022–1086. applied magnetic field before (1) and following their sonication in the gold acid solution (2) revealing the saturation magnetization value decrease from initial 27 emu g^{-1} to 21 emu g^{-1} at H_{max} = 4.4 kOe supporting the claim that gold species are deposited onto the magnetic core remaining superparamagnetic. The deposition of gold species at the surface of magnetite NPs was confirmed also by high-resolution TEM image of $CoFe_2O_4$@Met NPs after gold deposition and EDX investigations (see Figure 15.16). From these results, the formation of numerous gold species at the surface side of Met-stabilized ferrite NPs is obvious. Moreover, our investigations have shown that methionine molecules are capable reduce the gold ions at the NP surface side with more than 99% yield [92].

To determine the size of gold species tethered to the NP surface *via* Met-induced deposition, they were detached from ferrite NP surface, collected by centrifugation, spread on freshly cleaved mica substrate and imaged

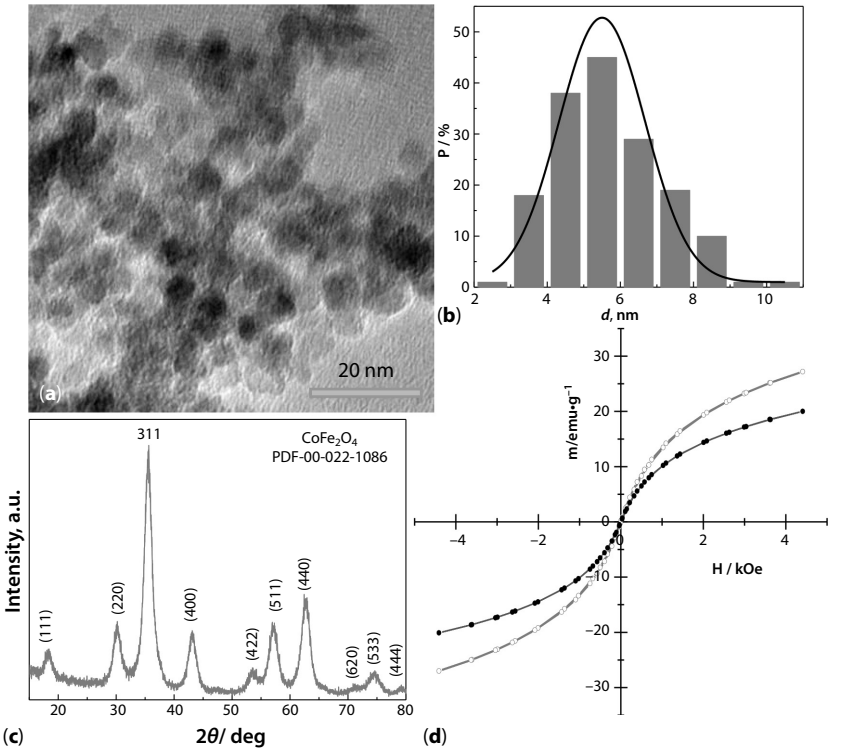

Figure 15.15 (a) TEM image of cobalt ferrite NPs synthesized hydrothermally in the solution containing 25.0 mmol L^{-1} $CoCl_2$, 50 mmol L^{-1} $FeCl_3$, 0.2 mol L^{-1} methionine, and NaOH to pH = 12.4 at 130 °C for 10 hr. The size distribution histogram and XRD pattern of the as-formed NPs are shown in (b) and (c), respectively, whereas in (d) the magnetic responses of as-formed (1) and sonicated NPs in a 10 mmol L^{-1} $HAuCl_4$ solution, kept at a pH = 12.2 °C and 37 °C temperature for 4 hr (2) are presented.

using AFM (Figure 15.17). From this observation, the vast majority of gold species tethered to ferrite NP surface was 1.85 nm-sized.

To determine the state of gold species, X-ray photoelectron spectroscopy (XPS) investigations were further conducted. Figure 15.18 depicts the characteristic XP spectrum of as-grown $CoFe_2O_4$@Au-Met NPs. The analysis of the Au $4f_{7/2}$ core-level spectrum revealed the binding energy (BE) value 83.94 eV typical for metallic Au^0 [93]. The fitting of the Au 4f core-level spectrum using two spin-orbit split Au $4f_{7/2}$ and Au $4f_{5/2}$ components, however, shows an additional shoulder peaked at 85.74 eV which could be ascribed to the presence of Au^+ [93]. The relative distribution areas of Au^0 and Au^+ BE reveals the ~13.7% fraction of Au^+ species from the total gold content attached to ferrite NP surface equaled to 1.39 at.% (Table 15.1). To

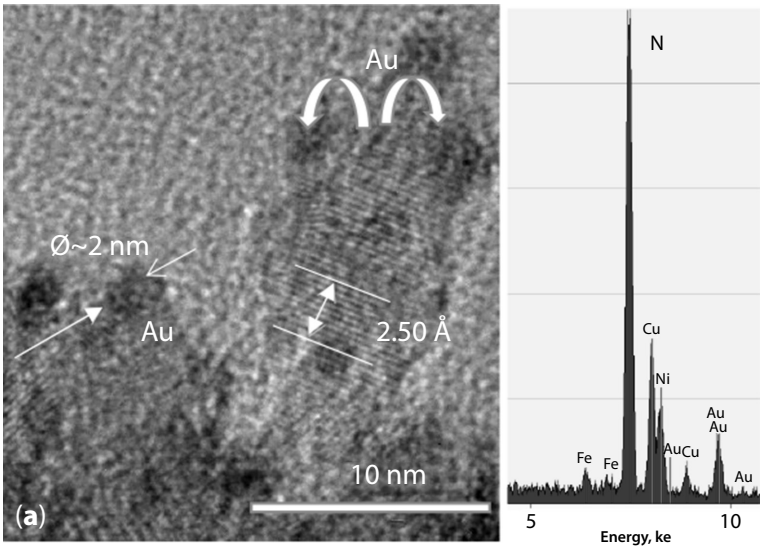

Figure 15.16 High resolution TEM image of $CoFe_2O_4$@Met NPs after sonication in 15 mmol L^{-1} $HAuCl_4$ solution at 37 °C for 4 hr (a) and the selected area EDX spectrum (b).

our best knowledge, there is only one Au^0/Au^+ anchoring method reported recently by us which uses the methionine amino acid both for control on the magnetic NP growth and the subsequent surface decoration with gold quantum dots [92]. Magnetic measurements showed that, compared with naked $CoFe_2O_4$ NPs, decorated with Au^0/Au^+ ones exhibited just some lower magnetic saturation and coercivity values (Figure 15.15d). To the end, we suspect that entrap of extremely active Au^+ species into the ferrite NP shell can have a dramatic effect on the nonspecific uptake of these hybrid NPs in the body.

15.7 Application Trends

15.7.1 Imagining

The advantages of iron oxide-based NPs relay on biocompatibility, biodegradability [94], easily injection into tumor cells [95, 96], and a controlled generation of heat in the oscillating magnetic field [97]. Of these, magnetic NPs have found successful applications as magnetic resonance imaging (MRI) contrast enhancing and hypothermia agents for cancer detection and therapy [98–101]. In addition, due to well-known gold

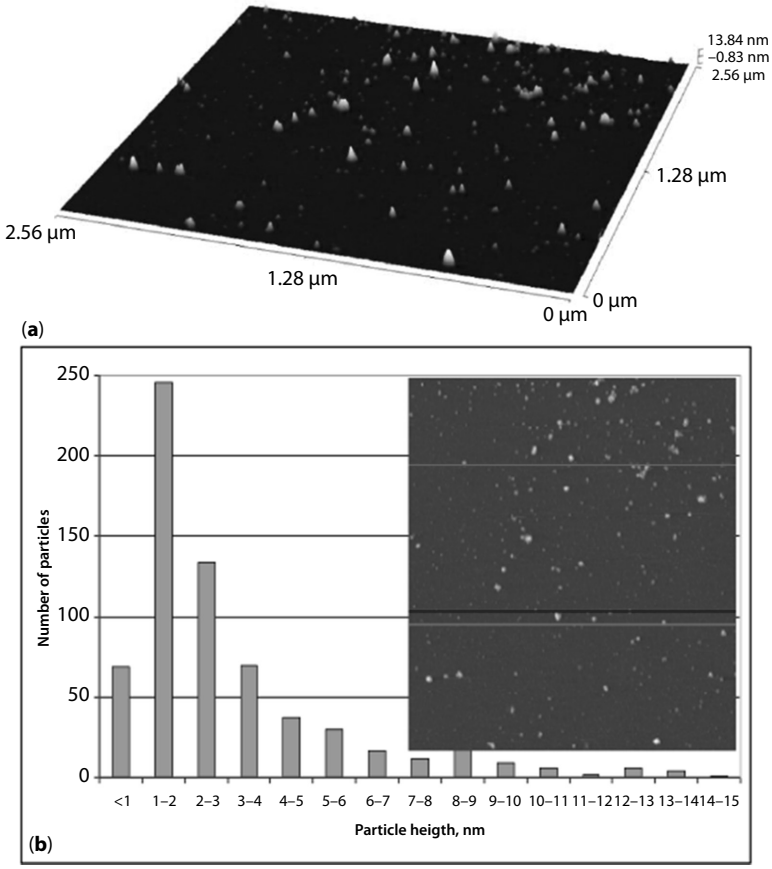

Figure 15.17 AFM 3D image (a) and size distribution histogram (b) of Au species removed from the surface of $CoFe_2O_4$@Met-Au NPs.

surface functionalization capability Fe_3O_4@Au NPs linked with various aptamer molecules. As reported in several papers [102–104] hyperthermia effect of superparamagnetic NPs depends on the thickness and structure of gold shell around them. Usually, the temperature rise and the time required to reach the therapeutic temperature, *i.e.* 42 °C, are faster for gold-coated NPs by a 4–5 fold difference at the same concentrations. This enhancement was linked with the ability of gold-coated NPs to retain superparamagnetic feature in the oscillating magnetic field much better as compared to the naked NPs. Besides, it has been established that maghemite (Fe_2O_3) NPs are cytotoxic to different cell types [105, 106]. Their coating with gold shells prevent the seepage of Fe into cellular milieu and Fe-induced intracellular formation of reactive oxygen species. Consequently, gold-coated

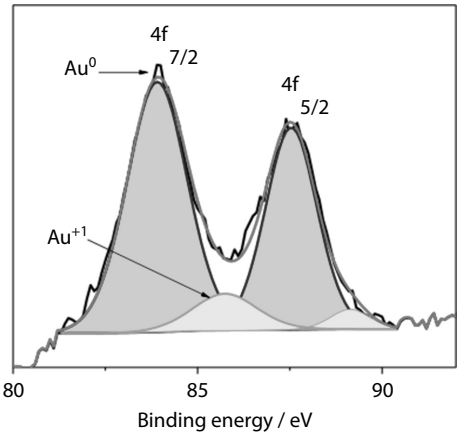

Figure 15.18 Deconvoluted X-rays photoelectron spectrum of Au 4f.

Table 15.1 Elemental ID and quantification of $CoFe_2O_4$@Met-Au NPs.

Name	Peak *BE*	*FWHM*, eV	Area (*P*) CPS	Atomic %
Au4f	83.94	1.96	12435.07	1.39
C1s	284.87	2.88	18041.56	36.02
N1s	399.98	2.24	2647.25	3.02
O1s	530.21	3.03	55974.26	40.37
Fe2p3	710.75	3.70	63210.72	12.68
Co2p3	780.67	3.29	36815.35	6.47

superparamagnetic NPs are attributed to a new generation of multifunctional NPs for diagnosis, therapy, and thermolysis of cancer cells [107].

In recent nanomedicine, uniformly sized superparamagnetic NPs covered with gold shell are successfully used as magnetic resonance imaging (MRI) T_2 contrast-enhancing agents. As reported, the formation of gold shell enhances MRI contrast. In addition, due to well-known gold surface functionalization capability of Fe_3O_4@Au NP linked with various aptamer molecules [108], organic species [109], silica shells [110], and polymers [111] are prospective multimodal contrast agents for bioimaging. *In vivo* tests performed by Li *et al.,* [109] for imaging of tumor HeLa cells in mice through injection of the Fe_3O_4@Au NPs revealed an obvious darkening of

tumor regions even after 10 min post-injection. Also, due to good X-ray absorption gold-coated magnetic NPs can be used as computed tomography contrast agents with dual modality [112, 113]. For example, Cai *et al.,* [114] developed poly(g-glutamic acid(PGA) and poly(L-lysine) (PLL) followed by entrap of gold NPs. The MRI tests have shown that Fe_3O_4@Au NP caped with PGA and PLL can be used both for MRI and for computed tomography.

For fluorescent imaging of integrin avβ3 mAb cancer cells Zhou and co-workers [115] developed contrast probes comprised of Fe_3O_4@Au NPs labeled with fluorescein isothiocyanate. Due to generation of photoacoustic and microwave-induced thermoacoustic signals these NPs can be applied for photoacoustic imaging and microwave-induced thermoacoustic tomography.

Red-photoluminescent gold clusters stabilized with proteins such as bovine serum albumin (BSA) [116], lactoferrin [117], human insulin [118], etc. possessing good photostability, long life time, and biocompatibility gained a great attention during last years. However, the conjugation of magnetic NPs with fluorescent gold clusters remains a great problem to date because of fluorescence quenching in hybrid nanostructures. The pioneering approach for the attachment of red-fluorescent gold clusters to the surface of superparamagnetic NP has been reported by Sreenivasan group [82]. According to this suggestion, gold clusters were prepared separately by well-known green synthesis way using BSA. As reported, this cluster tethered to the surface of magnetic NP through dopamine NPs. The analysis of the Au $4f_{7/2}$ core-level spectrum revealed the binding energy (BE) value 83.94 eV typical for metallic Au^0 [93]. The fitting of the Au 4f core-level spectrum using two spin-orbit split Au $4f_{7/2}$ and Au $4f_{5/2}$ components, however, shows an additional shoulder peaked at 85.74 eV which could be ascribed to the presence of Au^+ [93]. The relative distribution areas of Au^0 and Au^+ BE reveals the ~13.7% fraction of Au^+ species from the total gold content attached to ferrite NP surface equaled to 1.39 at.% (Table 15.1). To our best knowledge, there is only one Au^0/Au^+ anchoring method reported recently by us which uses the methionine amino acid both for control on the magnetic NP growth and the subsequent surface decoration with gold quantum dots [92]. link (see scheme 15.1) remains fluorescent. Such hybrid NPs were successfully used to remove C6 glioma cancer cells from blood and lymphatic fluids. Currently, Sony *et al.,* [119] reported the design of superparamagnetic NPs with the attached red-fluorescent gold nanocluster (NC) and a specific targeting agent erlotimib for *in vitro* imaging and killing of pancreatic cancer cells. This result was achieved *via* four steps:

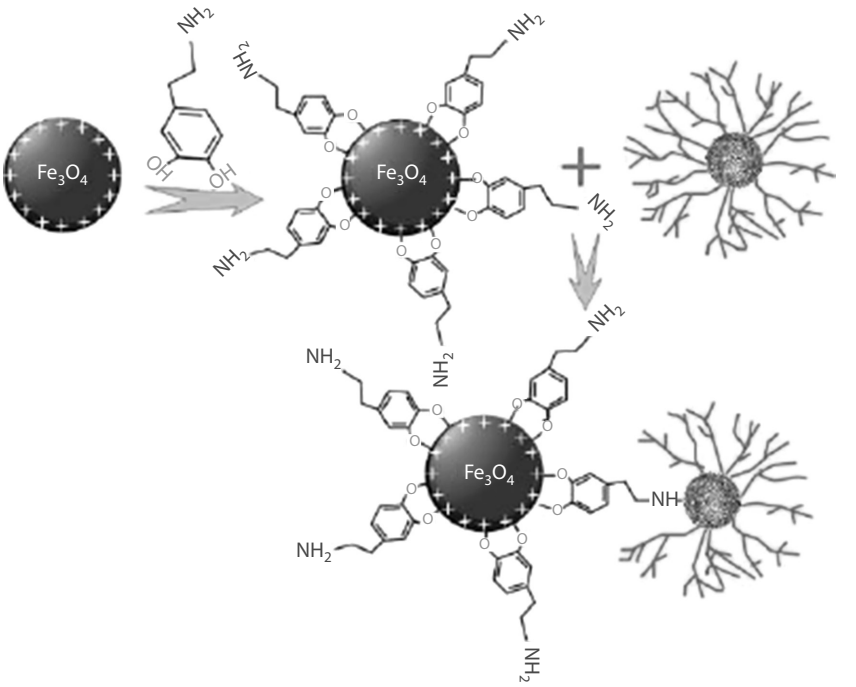

Scheme 15.1 The attachment of gold clusters to the surface of magnetite NP *via* dopamine anchors.

(i) synthesis of positively charged Fe_3O_4 NPs using Arginine amino acid as reducer, (ii) synthesis of bovine serum albumin (BSA) templated gold clusters under microwave heating, (iii) conjugation of Fe_3O_4 NPs with Au NCs *via* sonication together in the PBS buffer under vigorous stirring, (iV) the drug loading to Fe_3O_4@AuNCs surface *via* sonication at 25 °C for day according to presented Scheme 15.2.

15.7.2 Hyperthermia

Hyperthermia is based on the local heating of body tissues. This therapeutic phenomenon is based on the higher sensitivity of tumor cells to heat in comparison with the health ones since exposure of tumor cells at 42–46 °C results in opoptosis and at 46–49 °C to their killing whereas of health cells not. Superparamagnetic NPs inducing size-dependent heat in the oscillating magnetic fields, microwaves, and infrared radiation have been utilized successfully during past two decades for hyperthermia of cancer cells

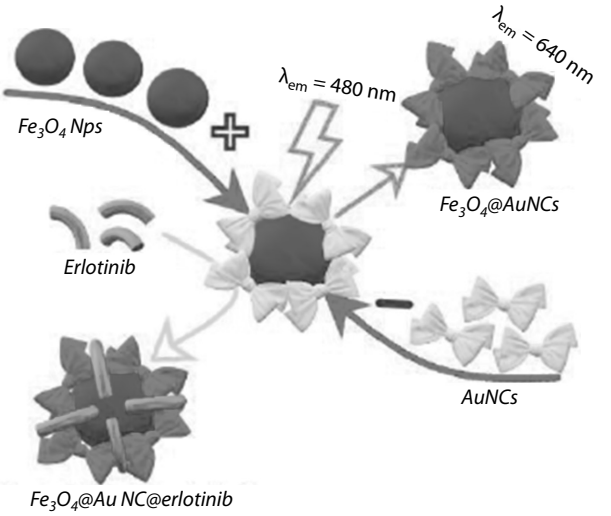

Scheme 15.2 Formation stages of red-fluorescent Fe_3O_4@Au NC@erlotinib nanoparticulate species.

[120–125]. It is worth noticing that gold shells improved in times the hyperthermic effect of magnetic NPs especially in a low frequency oscillating magnetic fields [126]. As also reported, the gold shells decreased cytotoxicity of magnetic NPs and induced biocompatibility [126]. Furthermore, the typical surface Plasmon resonance of gold from the visible light range in a vicinity of 520–530 cm^{-1} [127] can be simply shifted to the near infrared by the increase in the NP size and gold shell thickness [125]. Consequently, the irradiation of tissues with entrapped gold as well as gold-coated NPs with an infrared laser can also increase the temperature of surrounding tissues causing hyperthermia therapy [70, 128, 129]. For example, Ren *et al.,* reported destruction of cancer cells due to the Fe_3O_4@Au NPs photothermal heating just after 2 min of the NIR treatment with 3.5 W cm^{-2}power. Moreover, the combined light and magnetic field irradiations of Fe_3O_4@Au NPs injected in the HeLa cancer cells results in a quick rise of the medium temperature to 47 °C within 5 min and in the killing of tumor cells [130]. Similar multifunctional behavior of theranostic Fe_3O_4@Au-HA NPs were observed by Jingchao *et al.,* both *in vivo* and *in vitro* tests with HeLa cells allowing to conclude that just thin gold shell on the Fe_3O_4 NP displayed a huge role in hyperthermia treatments efficiency [109].

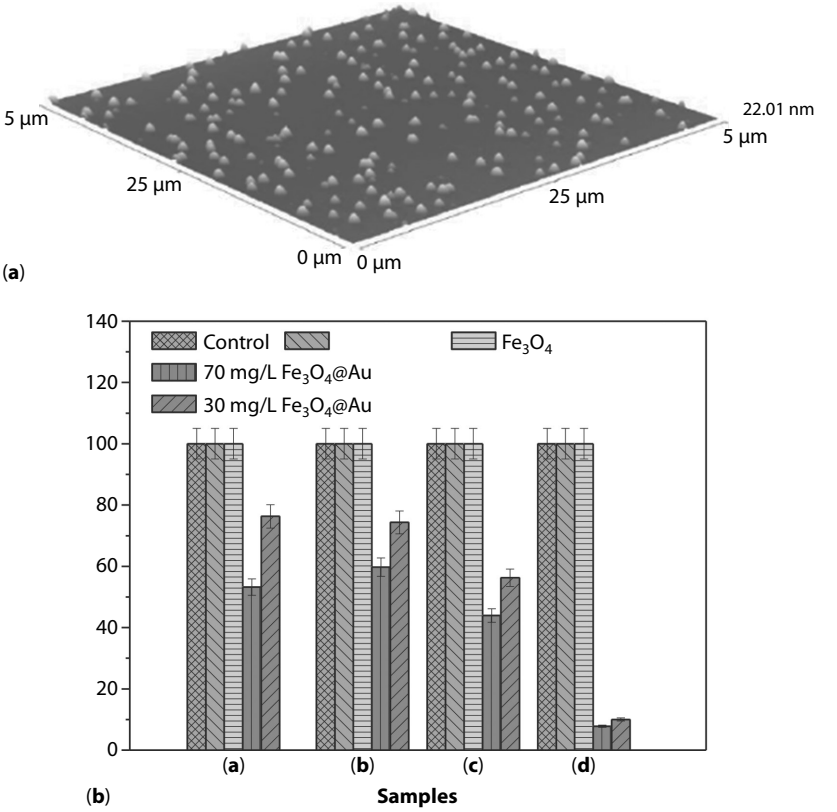

Figure 15.19 AFM image (a) and antimicrobial activities (b) of the synthesized Fe_3O_4@Au NPs after 24 hr their incubation with gram-negative *A. baumannii* (a), *S. enterica* (b) and gram-positive *S. aureus* (c), *M. luteus* (d). For comparison, the behavior of pure D,L-methionine and magnetite NPs is presented.

15.7.3 Antimicrobial Agents

It is commonly accepted that gold NPs are nontoxic and biocompatible. Currently, Xie and co-workers [131] reported that small-sized gold NPs possess cytotoxity against several cancel cells. To check this effect, we performed a set of antimicrobial tests with ultra small Au^0/Au^+ NPs attached to the surface of magnetite Nps *via* Methionine-templated growth and gold deposition way [132]. In these experiments, two multidrug resistant gram-negative microorganisms (*A. baumanni* and *S. enterica*) and two gram-positive ones (*S. aureus* and *M. luteus*) were tested. Bacterium survival data after 24 hr incubation with bare Fe_3O_4 and gold-decorated Fe_3O_4@Au NPs are shown in Figure 15.19. For comparison, the survival results of

all tested bacteria sonicated with methionine alone are also presented. As seen, any antimicrobial effects can be viewed for the nude Fe_3O_4 NPs and D,L-Methionine amino acid. Contrary, the incubation of Fe_3O_4@Au NPs with all bacteria tested in this study demonstrated more or less antimicrobial efficiency. Most significant, e.g., about 90%, reduce was obtained for *M. luteus* population whereas in the cases of *A. baumannii, S. enterica,* and *S. aureus* incubation with a same content of Fe_3O_4@Au NPs result in reduction of bacteria population survival to 55, 60% and 43%, respectively.

15.7.4 Bio-Separation

In previous studies [38, 74, 133, 134] Fe_3O_4@Au NPs have been considered as a material that is well suitable for separation of cells and proteins. For example, in 2007 Zhong group [133] reported the formation of functionalized Fe_3O_4@Au and Fe_2O_3 @Au NPs of controllable sizes from 5 to 100 nm *via* conjugation of magnetic NPs with gold NPs prepared separately for their application in thermally activated separation of biomolecules. To achieve this goal, gold NPs were capped with alkanethiolates whereas magnetic NPs – with oleic acid and oleylamine. These results have been reached owing to a simple capability of plasmonic gold shell attach highly specific aptameric and antibody species through the Au-S bond [19, 134–138] for detection, collection, and bio-separation of cancer targeting cells in blood and body liquids at the early stage of cancer [139, 140]. By this way, the separation capability of various cancer cells has been demonstrated even at 0.001% concentrations [141].

Gold-coated magnetic NPs can be also used to recognize and concentrate bacteria with external magnetic field. For example, Wang *et al.,* [81] synthesized $MnFe_2O_4$@Au NPs conjugated with *Staphylococcus aureus* antibody for recognition and separation of *S. aureus* with a detection limit 10 cells in mL. Although numerous other suggestions have been reported during last decade, protein-based separation and purification is still difficult in practice [142–145].

15.7.5 Targeted Drug Delivery

Chemotherapy treatments relay on the injection of the large amount of drug to the patient body thus affecting non-diseased tissues. Therefore, magnetic NPs targeted drug delivery to tumor sites are nice alternative to chemotherapy [140, 145–149]. The application of magnetic NPs functionalized with antibody, enzymes or nucleotide molecules for targeted drug delivery have been reported in several papers [150, 151]. Gold shells

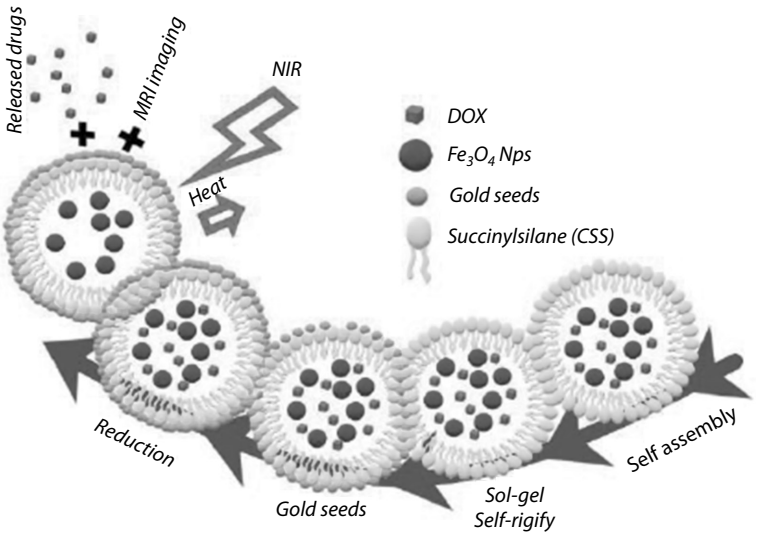

Scheme 15.3 Formation steps of multifunctional nanomicelles composed of DOX as therapeutic agent, Fe_3O_4, gold shell, and cholesteryl succinylsilane (CSS) template according to [150].

have proven to be desirable instrument not only for improving biocompatibility and stability of magnetic NPs but also for their surface functionalization with the linkers required to attach drug and antigen molecules [140, 149, 152]. To combine magnetic resonance imaging, targeted drug delivery, light-induced drug release and photothermal therapy, hybrid type nanomicelles composed of gold-coated Fe_3O_4 NPs, doxorubicin (DOX) drug molecules, and CSS-type silane nanomicelles have been synthesized using a Scheme 15.3 [153]. These nanomiceles possess surface Plasmon absorbance in the NIR region, NIR-induced hyperthermia, and controlled release of encapsulated drug during NIR illumination.

15.8 Outlooks

In summary, this review describes the recent progress on iron oxide-based nanoparticles coating with gold species and shells. The main issue is devoted to superparamagnetic NPs in size from a few to 20 nm can successfully be applied in nanomedicine. Also, this review not seeks to cover all aspects of the gold-coated superparamagnetic Au NPs fabrication recipes reported in the hundreds of papers and several reviews presenting jus more interesting and prospective recent findings. What's more, the biocompatible magnetic

NPs with attached gold QDs containing a significant amount of extremely active Au^+ ions can be a useful tool for biomedical investigations because these NPs except their own distinct functionalities offer a possibility to bind and carry various ligands and drugs into tumor cells allowing their intracellular movements to be controlled by magnetic field.

Looking at the future of this field, we envisage the main strategy for controllable decoration of magnetic NPs with gold species and subsequent formation of gold shells through the grafting of stabilizing molecules such as amino acid Methionine of Agninine capable to reduce later the gold-containing species directly at the surface. The interactions between $MeFe_2O_4@Au^0/Au^+$ NPs and DNA resulting in the damage of the DNA double helix chains by Au^+ ions and apoptosis of the HeLa cells has yet to be evidenced by further studies.

References

1. Connor, E.E., Mwamuka, J., Gole, A., Murphy, C.J., Wyatt, M.D., Gold nanoparticles are taken up by human cells but do not cause acute cytotoxicity. *Small*, 1(3), 325–327, 2005.
2. Duncan, B., Kim, C., Rotello, V.M., Gold nanoparticle platforms as drug and biomacromolecule delivery systems. *J. Control. Release*, 148(1), 122–127, 2010.
3. Lin, P.C., Chou, P.H., Chen, S.H., Liao, H.K., Wang, K.Y., Chen, Y.J., *et al.*, Ethylene glycol-protected magnetic nanoparticles for a multiplexed immunoassay in human plasma. *Small*, 2(4), 485–489, 2006.
4. Liu, Z., Liu, Y., Yang, H., Yang, Y., Shen, G., Yu, R., A phenol biosensor based on immobilizing tyrosinase to modified core-shell magnetic nanoparticles supported at a carbon paste electrode. *Anal. Chim. Acta*, 533(1), 3–9, 2005.
5. Liu, J.C., Tsai, P.J., Lee, Y.C., Chen, Y.C., Affinity capture of uropathogenic escherichia coli using pigeon Ovalbumin-bound $Fe_3O_4@Al_2O_3$ magnetic nanoparticles. *Anal. Chem.*, 80, 5425–5432, 2008.
6. Tsai, H.Y., Hsu, C.F., Chiu, I.W., Fuh, C.B., Detection of C-reactive protein based on immunoassay using antibody-conjugated magnetic nanoparticles. *Anal. Chem.*, 79(21), 8416–8419, 2007.
7. Gao, L.Z., Zhuang, J., Nie, L., Zhang, J.B., Zhang, Y., Gu, N., *et al.*, Intrinsic peroxidase-like activity of ferromagnetic nanoparticles *Nat. Nanotechnol*, 2, 577–583, 2007.
8. Hu, M., Chen, J., Li, Z.-Y., Au, L., Hartland, G.V., Li, X., *et al.*, Gold nanostructures: engineering their plasmonic properties for biomedical applications. *Chem. Soc. Rev.*, 35(11), 1084–1094, 2006.
9. Huang, X., Jain, P.K., El-Sayed, I.H., El-Sayed, M.A., Gold nanoparticles: interesting optical properties and recent applications in cancer diagnostics and therapy. *Nanomedicine*, 2(5), 681–693, 2007.

10. Jain, P.K., Huang, X., El-Sayed, I.H., El-Sayed, M.A., Review of some interesting surface plasmon resonance-enhanced properties of noble metal nanoparticles and their applications to biosystems. *Plasmonics*, 2(3), 107–118, 2007.
11. Grzelczak, M., Pérez-Juste, J., Mulvaney, P., Liz-Marzán, L.M., Shape control in gold nanoparticle synthesis. *Chem. Soc. Rev.*, 37(9), 1783–1791, 2008.
12. Massart, R., Inventor, Agence Nationale de Valorisation de la Recherche (ANVAR), assignee. Magnetic fluids and process for obtaining them. *US Patent*, 4329241, 1982.
13. Bensebaa, F., Zavaliche, F., L'Ecuyer, P., Cochrane, R.W., Veres, T., Microwave synthesis and characterization of Co-ferrite nanoparticles. *J. Colloid Interface Sci.*, 277(1), 104–110, 2004.
14. Tu, W., Liu, H., Rapid synthesis of nanoscale colloidal metal clusters by microwave irradiation. *J. Mater. Chem.*, 10(9), 2207–2211, 2000.
15. Pereira, C., Pereira, A.M., Fernandes, C., Rocha, M., Mendes, R., Fernández-García, M.P., *et al.*, Superparamagnetic MFe_2O_4 (M = Fe, Co, Mn) Nanoparticles: Tuning the Particle Size and Magnetic Properties through a Novel One-Step Coprecipitation Route. *Chem. Mater.*, 24(8), 1496–1504, 2012.
16. Sugimoto, T., Matijević, E., Formation of uniform spherical magnetite particles by crystallization from ferrous hydroxide gels. *J. Colloid Interface Sci.*, 74(1), 227–243, 1980.
17. Tartaj, P., Morales, MadelP., Veintemillas-Verdaguer, S., Gonz lez-Carre o, T., Serna, C.J., The preparation of magnetic nanoparticles for applications in biomedicine. *J. Phys. D Appl. Phys.*, 36(13), R182–R197, 2003.
18. Sabale, S., Kandesar, P., Jadhav, V., Komorek, R., Motkuri, R.K., Yu, X.Y., Recent developments in the synthesis, properties, and biomedical applications of core/shell superparamagnetic iron oxide nanoparticles with gold. *Biomater. Sci.*, 5(11), 2212–2225, 2017.
19. Gao, J., Gu, H., Xu, B., Multifunctional magnetic nanoparticles: design, synthesis, and biomedical applications. *Acc. Chem. Res.*, 42(8), 1097–1107, 2009.
20. Ge, S., Shi, X., Sun, K., Li, C., Uher, C., Baker, J.R, Jr, B., *et al.*, Facile hydrothermal synthesis of iron oxide nanoparticles with tunable magnetic properties. *J. Phys. Chem. C*, 113(31), 13593–13599, 2009.
21. Fan, R., Chen, X.H., Gui, Z., Liu, L., Chen, Z.Y., A new simple hydrothermal preparation of nanocrystalline magnetite Fe_3O_4. *Mater. Res. Bull.*, 36(3–4), 497–502, 2001.
22. Wang, J., Sun, J., Sun, Q., Chen, Q., One-step hydrothermal process to prepare highly crystalline Fe_3O_4 nanoparticles with improved magnetic properties. *Mater. Res. Bull.*, 38(7), 1113–1118, 2003.
23. Goon, I.Y., Lai, L.M.H., Lim, M., Munroe, P., Gooding, J.J., Amal, R., Fabrication and dispersion of gold-shell-protected magnetite nanoparticles: Systematic control using polyethyleneimine. *Chem. Mater.*, 21(4), 673–681, 2009.

24. Goon, I.Y., Zhang, C., Lim, M., Gooding, J.J., Amal, R., Controlled fabrication of polyethylenimine-functionalized magnetic nanoparticles for the sequestration and quantification of Free $Cu2^{+}$. *Langmuir*, 26(14), 12247–12252, 2010.
25. Li, Z., Sun, Q., Gao, M., Preparation of water-soluble magnetite nanocrystals from hydrated ferric salts in 2-pyrrolidone: mechanism leading to Fe_3O_4. *Angew. Chem. Int. Ed.*, 44(1), 123–126, 2005.
26. W.W, Y., Falkner, J.C., Yavuz, C.T., Colvin, V.L., Synthesis of monodisperse iron oxide nanocrystals by thermal decomposition of iron carboxylate salts. *Chem. Commun*, 2306–2307, 2004.
27. Peng, S., Wang, C., Xie, J., Sun, S., Synthesis and stabilization of monodisperse Fe nanoparticles. *J. Am. Chem. Soc.*, 128(33), 10676–10677, 2006.
28. Tran, P.H.-L., Tran, T.T.-D., Vo, T.V., Lee, B.-J., Promising iron oxide-based magnetic nanoparticles in biomedical engineering. *Arch. Pharm. Res.*, 35(12), 2045–2061, 2012.
29. Ling, D., Hyeon, T., Chemical design of biocompatible iron oxide nanoparticles for medical applications. *Small*, 9(9–10), 1450–1466, 2013.
30. Luchini, A., Vitiello, G., Rossi, F., Ruiz De Ballesteros, O., Radulescu, A., D'Errico, G., *et al.*, Developing functionalized Fe_3O_4-Au nanoparticles: A physico-chemical insight. *Phys. Chem. Chem. Phys.*, 15, 6087–6097, 2015.
31. Niederberger, M., Nonaqueous sol–gel routes to metal oxide nanoparticles. *Acc. Chem. Res.*, 40(9), 793–800, 2007.
32. Lemine, O.M., Omri, K., Zhang, B., El Mir, L., Sajieddine, M., Alyamani, A., *et al.*, Sol–gel synthesis of 8nm magnetite (Fe_3O_4) nanoparticles and their magnetic properties. *Superlattices and Microstructures*, 52(4), 793–799, 2012.
33. Xu, J., Yang, H., Fu, W., Du, K., Sui, Y., Chen, J., *et al.*, Preparation and magnetic properties of magnetite nanoparticles by sol–gel method. *J. Magn. Magn. Mater.*, 309(2), 307–311, 2007.
34. C.K, L., Xiao, D., Choi, M.M.F., Homocysteine-protected gold-coated magnetic nanoparticles: synthesis and characterization. *J. Mater. Chem.*, 17, 2418–2427, 2007.
35. Rudakovskaya, P.G., Beloglazkina, E.K., Majouga, A.G., Zyk, N.V., Synthesis and characterization of terpyridine-type ligand-protected gold-coated Fe_3O_4 nanoparticles. *Mendeleev Communications*, 20(3), 158–160, 2010.
36. Ahmad, T., Bae, H., Rhee, I., Chang, Y., Jin, S.U., Hong, S., Gold-coated iron oxide nanoparticles as a T_2 contrast agent in magnetic resonance imaging. *J. Nanosci. Nanotechnol.*, 12(7), 5132–5137, 2012.
37. Klyachko, N.L., Sokolsky-Papkov, M., Pothayee, N., Efremova, M.V., Gulin, D.A., Pothayee, N., *et al.*, Changing the enzyme reaction rate in magnetic nanosuspensions by a non-heating magnetic field. *Angew. Chem. Int. Ed.*, 51(48), 12016–12019, 2012.
38. Hien Pham, T.T., Cao, C., Sim, S.J, Pham, T.T.H, Cao, T., Application of citrate-stabilized gold-coated ferric oxide composite nanoparticles for biological separations. *J. Magn. Magn. Mater.*, 320(15), 2049–2055, 2008.

39. Liang, C.H., Wang, C.C., Lin, Y.C., Chen, C.H., Wong, C.H., Wu, C.Y., Iron oxide/gold core/shell nanoparticles for ultrasensitive detection of carbohydrate-protein interactions. *Anal. Chem.*, 81(18), 7750–7756, 2009.
40. Pang, L.-L., Li, J.-S., Jiang, J.-H., Le, Y., Shen, G.L., Yu, R.-Q, J.-S, L, R.-Q, Y., A novel detection method for DNA point mutation using QCM based on Fe_3O_4/Au core/shell nanoparticle and DNA ligase reaction. *Sens. Actuators*, 127(2), 311–316, 2007.
41. Zhao, X., Cai, Y., Wang, T., Shi, Y., Jiang, G., Preparation of Alkanethiolate-functionalized core/shell Fe_3O_4@Au nanoparticles and its interaction with several typical target molecules. *Anal. Chem.*, 80(23), 9091–9096, 2008.
42. Yu, Q., Shi, M., Cheng, Y., Wang, M., Chen, H.-zheng, Wg, M., H.-z, C., Fe_3O_4@Au/polyaniline multifunctional nanocomposites: their preparation and optical, electrical and magnetic properties. *Nanotechnology*, 19(26), 265702, 2008.
43. Ahmad, T., Bae, H., Rhee, I., Chang, Y., Jin, S.U., Hong, S., Gold-coated iron oxide nanoparticles as a T_2 contrast agent in magnetic resonance imaging. *J. Nanosci. Nanotechnol.*, 12(7), 5132–5137, 2012.
44. Chen, H., Qi, F., Zhou, H., Jia, S., Gao, Y., Koh, K., *et al.*, Fe_3O_4@Au nanoparticles as a means of signal enhancement in surface plasmon resonance spectroscopy for thrombin detection. *Sens. Actuators B*, 212, 505–511, 2015.
45. Ghorbani, M., Hamishehkar, H., Arsalani, N., Entezami, A.A., Preparation of thermo and pH-responsive polymer@Au/Fe_3O_4 core/shell nanoparticles as a carrier for delivery of anticancer agent. *J. Nanopart. Res.*, 17(7), 305, 2015.
46. Cui, Y., Hu, D., Fang, Y., Ma, J., Preparation and mechanism of Fe_3O_4/Au core/shell super-paramagnetic microspheres. *Sc. China Ser. B-Chem.*, 44(4), 404–410, 2001.
47. Cui, Y., Hui, W.L., Wang, H.R., D.D, X., Fang, Y., J.B, M., Preparation and characterization of Fe_3O_4 composite particles. *Sci. China Ser. B*, 47(2), 152–158, 2004.
48. Kinoshita, T., Seino, S., Okitsu, K., Nakayama, T., Nakagawa, T., Yamamoto, T.A., Magnetic evaluation of nanostructure of gold–iron composite particles synthesized by a reverse micelle method. *J. Alloys Compd.*, 359(1–2), 46–50, 2003.
49. Lim, J., Tilton, R.D., Eggeman, A., Majetich, S.A., Design and synthesis of plasmonic magnetic nanoparticles. *J. Magn. Magn. Mater.*, 311(1), 78–83, 2007.
50. Ma, Z., Han, H., Tu, S., Xue, J., Fabrication of shape-controlled hematite particles and growth of gold nanoshells. *Colloid. Surf. A*, 334(1–3), 142–146, 2009.
51. Mandal, M., Kundu, S., Ghosh, S.K., Panigrahi, S., Sau, T.K., Yusuf, S.M., *et al.*, Magnetite nanoparticles with tunable gold or silver shell. *J. Colloid Interface Sci.*, 286(1), 187–194, 2005.

52. Chin, S.F., Iyer, K.S., Raston, C.L., Facile and green approach to fabricate gold and silver coated superparamagnetic nanoparticles. *Cryst. Growth Des.*, 9(6), 2685–2689, 2009.
53. Stavka, I., Stoeva, F., HuoLee, J.-S., Mirkin, C.A., Three-Layer Composite Magnetic Nanoparticle Probes for DNA. *J. Am. Chem. Soc.*, 127, 15362–15363, 2005.
54. Huang, W.-C., Tsai, P.-J., Chen, Y.-C., Multifunctional Fe_3O_4@Au nanoeggs as photothermal agents for selective killing of nosocomial and antibiotic resistant bacteria. *Small*, 5(1), 51–56, 2009.
55. Coelho, B.C.P., Siqueira, E.R., Ombredane, A.S., Joanitti, G.A., Chaves, S.B., da Silva, S.W., *et al.*, Maghemite–gold core–shell nanostructures (γ-Fe_2O_3@Au) surface-functionalized with aluminium phthalocyanine for multi-task imaging and therapy. *RSC Adv.*, 7(19), 11223–11232, 2017.
56. Braun, K.J., Walter, D.G., Natan, M.J., Seeding of colloidal Au nanoparticle solutions. 2. Improved control of particle size and shape. *Chem. Mater.*, 12, 306–313, 2000.
57. Lyon, J.L., Fleming, D.A., Stone, M.B., Schiffer, P., Williams, M.E., Synthesis of Fe oxide core/Au shell nanoparticles by iterative hydroxylamine seeding. *Nano Lett.*, 4(4), 719–723, 2004.
58. Cho, S.-J., Kauzlarich, S.M., Olamit, J., Liu, K., Grandjean, F., Rebbouh, L., *et al.*, Characterization and magnetic properties of core/shell structured Fe/Au nanoparticles. *J. Appl. Phys.*, 95(11), 6804–6806, 2004.
59. Mikhaylova, M., Kim, D.K., Bobrysheva, N., Osmolowsky, M., Semenov, V., Tsakalakos, T., *et al.*, Superparamagnetism of Magnetite Nanoparticles: Dependence on Surface Modification. *Langmuir*, 20(6), 2472–2477, 2004.
60. Cho, S.-J., Idrobo, J.-C., Olamit, J., Liu, K., Browning, N.D., Kauzlarich, S.M., Growth mechanisms and oxidation resistance of gold-coated iron nanoparticles. *Chem. Mater.*, 17(12), 3181–3186, 2005.
61. Lee, Y., Lee, J., Bae, C.J., Park, J.-G., Noh, H.-J., Park, J.-H., *et al.*, Large-scale synthesis of uniform and crystalline magnetite nanoparticles using reverse micelles as nanoreactors under reflux conditions. *Adv. Funct. Mater.*, 15(3), 503–509, 2005.
62. Semenova, E.M., Vorobyova, S.A., Lesnikovich, A.I., Fedotova, J.A., Bayev, V.G., Fabrication and investigation of magnetite nanoparticles with gold shell. *J. Alloys Compd.*, 530, 97–101, 2012.
63. Wang, H., Brandl, D.W., Le, F., Nordlander, P., Halas, N.J., Nanorice: A hybrid plasmonic nanostructure. *Nano Lett.*, 6(4), 827–832, 2006.
64. Wu, Y., Zhang, T., Zheng, Z., Ding, X., Peng, Y., A facile approach to Fe_3O_4@Au nanoparticles with magnetic recyclable catalytic properties. *Mater. Res. Bull.*, 45(4), 513–517, 2010.
65. Caruntu, D., Cushing, B.L., Caruntu, G., O'Connor, C.J., Attachment of gold nanograins onto colloidal magnetite Nanocrystals. *Chem. Mater.*, 17(13), 3398–3402, 2005.

66. Wang, L., Luo, J., Maye, M.M., Fan, Q., Rendeng, Q., Engelhard, M.H., *et al.*, Core@shell nanomaterials: gold-coated magnetic oxide nanoparticles. *J. Mater. Chem.*, 15, 1821–1832, 2005.
67. Wang, L.W.L., Luo, J., Fan, Q., Suzuki, M., Suzuki, I.S., Engelhard, M.H., *et al.*, Monodispersed core-shell Fe_3O_4@Au nanoparticles. *J. Phys. Chem. B*, 109, 21593–21601, 2005.
68. Park, J., An, K., Hwang, Y., Park, J.-G., Noh, H.-J., Kim, J.-Y., *et al.*, Ultra-large-scale syntheses of monodisperse nanocrystals. *Nat. Mater.*, 3(12), 891–895, 2004.
69. Liu, H., Hou, P., Zhang, W.X., J.H, W., Synthesis of monosized core-shell Fe_3O_4/Au multifunctional nanoparticles by PVP-assisted nanoemulsion process. Colloids & Surfaces A: Physicochem. *Eng. Aspects*, 356, 21–27, 2010.
70. Ren, J., Shen, S., Pang, Z., Lu, X., Deng, C., Jiang, X., Facile synthesis of superparamagnetic Fe_3O_4@Au nanoparticles for photothermal destruction of cancer cells. *Chem. Commun.*, 47(42), 11692–11694, 2011.
71. Lim, J., Eggeman, A., Lanni, F., Tilton, R.D., Majetich, S.A., Synthesis and single-particle optical detection of low-polydispersity plasmonic-superparamagnetic nanoparticles. *Adv. Mater.*, 20(9), 1721–1726, 2008.
72. Chin, S.F., Iyer, K.S., Raston, C.L., Saunders, M., Size selective synthesis of superparamagnetic nanoparticles in thin fluids under continuous flow conditions. *Adv. Funct. Mater.*, 18(6), 922–927, 2008.
73. An, P., Zuo, F., Li, X., Wu, Y., Zhang, J., Ding, X., A bio-inspired polydopamine approach to preparation of gold-coated Fe_3O_4 core-shell nanoparticles: synthesis, characterization and mechanism. *Nano Brief Reports and Reviewers*, 8, 1350061, 2013.
74. Bao, J., Chen, W., Liu, T., Zhu, Y., Jin, P., Wang, L., *et al.*, Bifunctional Au-Fe_3O_4 nanoparticles for protein separation. *ACS Nano*, 1, 293–298, 2007.
75. Phua, L.X., Xu, F., Ma, Y.G., Ong, C.K., Structure and magnetic characterization of cobalt ferrite films prepared by spray pyrolysis. *Thin Solid Films*, 517(20), 5858–5861, 2009.
76. Meng, X., Li, H., Chen, J., Mei, L., Wang, K., Li, X., Mössbauer study of cobalt ferrite nanocrystals substituted with rare-earth Y^{3+} ions. *J. Magn. Magn. Mater.*, 321(9), 1155–1158, 2009.
77. Sanpo, N., Berndt, C.C., Wen, C., Wang, J., Transition metal-substituted cobalt ferrite nanoparticles for biomedical applications. *Acta Biomater.*, 9(3), 5830–5837, 2013.
78. Mizukoshi, Y., Seino, S., Okitsu, K., Kinoshita, T., Otome, Y., Nakagawa, T., Sonochemical preparation of composite nanoparticles of Au/gamma-Fe_2O_3 and magnetic separation of glutathione. *Ultrason. Sonochem.*, 12(3), 191–195, 2005.
79. Kojima, H., Mukai, Y., Yoshikawa, M., Kamei, K., Yoshikawa, T., Morita, M., *et al.*, Simple PEG conjugation of SPION via an Au-S bond improves its tumor targeting potency as a novel MR tumor imaging agent. *Bioconjug. Chem.*, 21(6), 1026–1031, 2010.

80. Seino, S., Kinoshita, T., Otome, Y., Nakagawa, T., Okitsu, K., Mizukoshi, Y., Nakayama, T., *et al.*, Gamma-ray synthesis of magnetic nanocarrier composed of gold and magnetic iron oxide. *J. Magn. Magn. Mater.*, 293(1), 144–150, 2005.
81. Wang, D., Yang, J., Li, X., Zhai, H., Lang, J., Song, H., Preparation of magnetic Fe_3O_4@SiO_2@mTiO_2-Au spheres with well-designed microstructure and superior photocatalytic activity. *J. Mater. Sci.*, 51(21), 9602–9612, 2016.
82. Durgadas, C.V., Sharma, C.P., Sreenivasan, K., Fluorescent and superparamagnetic hybrid quantum clusters for magnetic separation and imaging of cancer cells from blood. *Nanoscale*, 3(11), 4780–4787, 2011.
83. Jagminas, A., Mažeika, K., Kondrotas, R., Kurtinaitienė, M., Jagminienė, A., Mikalauskaitė, A., Functionalization of cobalt ferrite nanoparticles by a vitamin C-assisted covering with gold. *Nanomater. Nanotechn.*, 4(2), 11, 2014.
84. Taleb, A., Petit, C., Pileni, M.P., Synthesis of highly monodisperse silver nanoparticles from AOT reverse micelles: A Way to 2D and 3D self-organization. *Chem. Mater.*, 9(4), 950–959, 1997.
85. Xie, Y., Ye, R., Liu, H., Synthesis of silver nanoparticles in reverse micelles stabilized by natural biosurfactant. *Colloids Surf. A Physicochem. Eng. Asp.*, 279(1-3), 175–178, 2006.
86. Liang, C.-H., Wang, C.-C., Lin, Y.-C., Chen, C.-H., Wong, C.-H., Wu, C.-Y, ., Iron oxide/gold core/shell nanoparticles for ultrasensitive detection of carbohydrate–protein interactions. *Anal. Chem.*, 81(18), 7750–7756, 2009.
87. Mikalauskaitė, A., Kondrotas, R., Niaura, G., Jagminas, Arūnas, Jagminas, A., Gold-coated cobalt ferrite nanoparticles via methionine-induced reduction. *J. Phys. Chem. C*, 119(30), 17398–17407, 2015.
88. Bagherpour, A.R., Kashanian, F., Seyyed Ebrahimi, S.A., Habibi-Rezaei, M., L-arginine modified magnetic nanoparticles: green synthesis and characterization. *Nanotechnology*, 29(7), 075706, 2018.
89. Durmus, Z., Kavas, H., Toprak, M.S., Baykal, A., Altınçekiç, T.G., Aslan, A., *et al.*, l-lysine coated iron oxide nanoparticles: Synthesis, structural and conductivity characterization. *J. Alloys Compd.*, 484(1–2), 371–376, 2009.
90. Žalnėravičius, R., Paškevičius, A., Mažeika, K., Jagminas, A., Fe(II)-substituted cobalt ferrite nanoparticles against multidrug resistant microorganisms. *Appl. Surf. Sci.*, 435, 141–148, 2018.
91. Rehana, D., Haleel, A.K., Rahiman, A.K., Hydroxy, carboxylic and amino acid functionalized superparamagnetic iron oxide nanoparticles: synthesis, characterization and *in vitro* anti-cancer studies. *J. Chem. Sci.*, 127(7), 1155–1166, 2015.
92. Jagminas, A., Mikalauskaitė, A., Karabanovas, V., Vaičiūnienė, J., Methionine-mediated synthesis of magnetic nanoparticles and functionalization with gold quantum dots for theranostic applications. *Beilstein J. Nanotechnol.*, 8, 1734–1741, 2017.

93. Moulder, J.F., Stickle, W.F., Sobol, P.E., Bompen, P.E., Handbook of X-ray photoelectron spectroscopy. Chastain, J., King, R.C. Jr., (Eds.), *Physical Electronics. Eden Prairee, MN*, 1995.
94. Sanvicens, N., Marco, P., Multifunctional nanoparticles –properties and prospects for their use in human medicine *Trends Biotechn*, 26, 425–433, 2008.
95. Corchero, J.L., Villaverde, A., Biomedical applications of distally controlled magnetic nanoparticles. *Trends Biotechnol.*, 27(8), 468–476, 2009.
96. Purushotham, S., Chang, P.E., Rumpel, H., Kee, I.H., Ng, R.T., Chow, P.K.H., *et al.*, Thermoresponsive core-shell magnetic nanoparticles for combined modalities of cancer therapy. *Nanotechnology*, 20(30), 305101, 2009.
97. Thiesen, B., Jordan, A., Clinical applications of magnetic nanoparticles for hyperthermia. *Int. J. Hyperther.*, 24(6), 467–474, 2008.
98. Habash, R.W.Y., Bansal, R., Krewski, D., Alhafid, H.T., Thermal therapy, Part 2: Hyperthermia techniques. *Crit. Rev. Biomed. Eng.*, 34(6), 491–542, 2006.
99. Kawai, N., Futakuchi, M., Yoshida, T., Ito, A., Sato, S., Naiki, T., *et al.*, Effect of heat therapy using magnetic nanoparticles conjugated with cationic liposomes on prostate tumor in bone. *Prostate*, 68(7), 784–792, 2008.
100. Suto, M., Hirota, Y., Mamiya, H., Fujita, A., Kasuya, R., Tohji, K, Manuya, H., *et al.*, Heat dissipation mechanism of magnetite nanoparticles in magnetic fluid hyperthermia. *J. Magn. Magn. Mater.*, 321(10), 1493–1496, 2009.
101. Bao, F., Yao, J.L., Gu, R.A., Synthesis of magnetic Fe_2O_3/Au core/shell nanoparticles for bioseparation and immunoassay based on surface-enhanced Raman spectroscopy. *Langmuir*, 25(18), 10782–10787, 2009.
102. Wang, L., Park, H.-Y., Lim, S.I.-I., Schadt, M.J., Mott, D., Luo, J, Lim Stephanie, I.-I., *et al.*, Core@shell nanomaterials: gold-coated magnetic oxide nanoparticles. *J. Mater. Chem.*, 18(23), 2629–2635, 2008.
103. Lu, Z., Prouty, M.D., Guo, Z., Golub, V.O., Kumar, C.S.S.R., Lvov, Y.M, Gao, Z, Kumar, C., Magnetic switch of permeability for polyelectrolyte microcapsules embedded with Co@Au nanoparticles. *Langmuir*, 21(5), 2042–2050, 2005.
104. Mohammad, F., Balaji, G., Weber, A., Uppu, R.M., Kumar, C.S.S.R., Influence of gold nanoshanell on hydrothermia of superparamagnetic iron oxide nanoparticles. *J. Phys. Chem. C*, 114(45), 19194–19201, 2010.
105. Pisanic, T.R., Blackwell, J.D., Shubayev, V.I., Fiñones, R.R., Jin, S., Nanotoxicity of iron oxide nanoparticle internalization in growing neurons. *Biomaterials*, 28(16), 2572–2581, 2007.
106. Apopa, P.L., Qian, Y., Shao, R., Guo, N.L., Schwegler-Berry, D., Pacurari, M., *et al.*, Iron oxide nanoparticles induce human microvascular endothelial cell permeability through reactive oxygen species production and microtubule remodeling. *Part. Fibre Toxicol.*, 6, 1–14, 2009.
107. Xu, Y., Mahmood, M., Fejleh, A., Li, Z., Watanabe, F., Trigwell, S., *et al.*, Carbon-covered magnetic nanomaterials and their application for the thermolysis of cancer cells. *Int. J. Nanomedicine*, 5, 167–176, 2010.

108. Azhdarzadeh, M., Atyabi, F., Saei, A.A., Varnamkhasti, B.S., Omidi, Y., Fateh, M., *et al.*, Theranostic MUC-1 aptamer targeted gold coated superparamagnetic iron oxide nanoparticles for magnetic resonance imaging and photothermal therapy of colon cancer. *Colloids Surf. B Biointerfaces*, 143, 224–232, 2016.
109. Li, J., Hu, Y., Yang, J., Wei, P., Sun, W., Shen, M., *et al.*, Hyaluronic acid-modified Fe_3O_4@Au core/shell nanostars for multimodal imaging and photothermal therapy of tumors. *Biomaterials*, 38, 10–21, 2015.
110. Ma, M., Chen, H., Chen, Y., Wang, X., Chen, F., Cui, X., *et al.*, Au capped magnetic core/mesoporous silica shell nanoparticles for combined photothermo-/chemo-therapy and multimodal imaging. *Biomaterials*, 33(3), 989–998, 2012.
111. Montazerabadi, A.R., Oghabian, M.A., Irajirad, R., Muhammadnejad, S., Ahmadvand, D., Delavari H, H., *et al.*, Development of gold-coated magnetic nanoparticles as a potential MRI contrast agent. *Nano*, 10(04), 1550048, 2015.
112. Zhao, H.Y., Liu, S., He, J., Pan, C.C., Li, H., Zhou, Z.Y., *et al.*, Synthesis and application of strawberry-like Fe_3O_4-Au nanoparticles as CT-MR dual-modality contrast agents in accurate detection of the progressive liver disease. *Biomaterials*, 51, 194–207, 2015.
113. Li, J., Zheng, L., Cai, H., Sun, W., Shen, M., Zhang, G, Sun, M, Shen, W., *et al.*, Facile one-pot synthesis of Fe_3O_4@Au composite nanoparticles for dual-mode MR/CT imaging applications. *ACS Appl. Mater. Interfaces*, 5(20), 10357–10366, 2013.
114. Cai, H., Li, K., Shen, M., Wen, S., Luo, Y., Peng, C., *et al.*, Facile assembly of Fe_3O_4@Au nanocomposite particles for dual mode magnetic resonance and computed tomography imaging applications. *J. Mater. Chem.*, 22(30), 15110–15120, 2012.
115. Zhou, C., Yu, J., Qin, Y., Zheng, J., Grain size effects in polycrystalline gold nanoparticles. *Nanoscale*, 4(14), 4228–4233, 2012.
116. Xie, J., Zheng, Y., Ying, J.Y., Protein-directed synthesis of highly fluorescent gold nanoclusters. *J. Am. Chem. Soc.*, 131(3), 888–889, 2009.
117. Xavier, P.L., Chaudhari, K., Verma, P.K., Pal, S.K., Pradeep, T., Luminescent quantum clusters of gold in transferrin family protein, lactoferrin exhibiting FRET. *Nanoscale*, 2(12), 2769–2776, 2010.
118. Garcia, A.R., Rahn, I., Johnson, S., Patel, R., Guo, J., Orbulescu, J., *et al.*, Human insulin fibril-assisted synthesis of fluorescent gold nanoclusters in alkaline media under physiological temperature. *Colloids Surf. B Biointerfaces*, 105, 167–172, 2013.
119. Nebu, J., Anjali Devi, J.S., Aparna, R.S., Abha, K., Sony, G., Erlotinib conjungated gold nanocluster enveloped magnetic iron oxide nanoparticles–A targeted probe for imaging pankreatic cancer cells. *Sensors and Actuators B: Chemical*, 257, 1035–1043, 2018.

120. Pineiro, Y., Vargas, Z., Rivas, J., Lopez-Quintela, M.A., Iron oxide based nanoparticles for magnetic hyperthermia strategies in biological applications. *Eur. J. Inorg. Chem.*, 2015(27), 4495–4509, 2015.
121. Shete, P.B., Patil, R.M., Ningthoujam, R.S., Ghosh, S.J., Pawar, S.H., Magnetic core–shell structures for magnetic fluid hyperthermia therapy application. *New J. Chem.*, 37(11), 3784–3792, 2013.
122. Chatterjee, D.K., Diagaradjane, P., Krishnan, S., Nanoparticle-mediated hyperthermia in cancer therapy. *Ther. Deliv.*, 2(8), 1001–1014, 2011.
123. Salunkhe, A.B., Khot, V.M., Pawar, S.H., Magnetic hyperthermia with magnetic nanoparticles: a status review.. *Curr. Top. Med. Chem.*, 14(5), 572–594, 2014.
124. Bohara, R.A., Thorat, N.D., Pawar, S.H., Role of functionalization: strategies to explore potential nano-bio applications of magnetic nanoparticles. *RSC Adv.*, 6(50), 43989–44012, 2016.
125. Liu, B., Li, C., Cheng, Z., Hou, Z., Huang, S., Lin, J., Functional nanomaterials for near-infrared-triggered cancer therapy. *Biomater. Sci.*, 4(6), 890–909, 2016.
126. Mohammad, F., Balaji, G., Weber, A., Uppu, R.M., Kumar, C.S.S.R., Influence of gold nanoshell on hyperthermia of superparamagnetic iron oxide nanoparticles. *J. Phys. Chem. C*, 114(45), 19194–19201, 2010.
127. Kawasaki, H., Hamaguchi, K., Osaka, I., Arakawa, R., pH-dependent synthesis of pepsin-mediated gold nanoclusters with blue green and red fluorescent emission. *Adv. Funct. Mater.*, 21(18), 3508–3515, 2011.
128. Shanmugam, V., Selvakumar, S., Yeh, C.-S., Near-infrared light-responsive nanomaterials in cancer therapeutics. *Chem. Soc. Rev.*, 43(17), 6254–6287, 2014.
129. Jain, S., Hirst, D.G., O'Sullivan, J.M., Gold nanoparticles as novel agents for cancer therapy. *Br. J. Radiol.*, 85(1010), 101–113, 2012.
130. Abdula–Al-Mamun, M., Kusumoto, Y., Zannat, T., Horie, Y., Manaka, H., core–shell, A.-ultrathinfunctionalized., Fe_3O_4@Au) monodispersed nanocubes for a combination of magnetic/plasmonic photothermal cancer cell killing. *RSC Adv.*, 3, 7816–7827, 2013.
131. Zheng, K., Setyawati, M.I., Leong, D.T., Xie, J., Antimicrobial gold nanoclusters. *ACS Nano*, 11(7), 6904–6910, 2017.
132. Jagminas, A., Mikalauskaitė, A., Karabanovas, V., Vaičiūnienė, J., Methionine-mediated synthesis of magnetic nanoparticles and functionalization with gold quantum dots for theranostic applications. *Beilstein J. Nanotechnol.*, 8, 1734–1741, 2017.
133. Park, H.Y., Schadt, M.J., Wang, L., Lim, I.I., Njoki, P.N., Kim, S.H., *et al.*, Fabrication of magnetic core@shell Fe oxide@Au nanoparticles for interface bioactivity and bio-separation. *Langmuir*, 23(17), 9050–9056, 2007.
134. Liu, H.L., Sonn, C.H., Wu, J.H., Lee, K.M., Kim, Y.K., Synthesis of streptavidin-FITC-conjugated core-shell Fe_3O_4-Au nanocrystals and their application for the purification of CD4+ þlymphocytes. *Biomaterials*, 29(29), 4003–4011, 2008.

135. Famulok, M., Hartig, J.S., Mayer, G., Functional aptamers and aptazymes in biotechnology, diagnostics, and therapy. *Chem. Rev.*, 107(9), 3715–3743, 2007.
136. Lal, S., Clare, S.E., Halas, N.J., Nanoshell-enabled photothermal cancer therapy: Impending clinical impact. *Acc. Chem. Res.*, 41(12), 1842–1851, 2008.
137. Bardhan, R., Lal, S., Joshi, A., Halas, N.J., Theranostic nanoshells: from probe design to imaging and treatment of cancer. *Acc. Chem. Res.*, 44(10), 936–946, 2011.
138. Xie, J., Liu, G., Eden, H.S., Ai, H., Chen, X., Surface-engineered magnetic nanoparticle platforms for cancer imaging and therapy. *Acc. Chem. Res.*, 44(10), 883–892, 2011.
139. Xu, C., Sun, S., Superparamagnetic nanoparticles as targeted probes for diagnostic and therapeutic applications. *Dalton Trans.*, 37(29), 5583–5591, 2009.
140. Elbialy, N.S., Fathy, M.M., Khalil, W.M., Doxorubicin loaded magnetic gold nanoparticles for *in vivo* targeted drug delivery. *Int. J. Pharm.*, 490(1–2), 190–199, 2015.
141. Fan, Z., Shelton, M., Singh, A.K., Senapati, D., Khan, S.A., Ray, P.C., Multifunctional plasmonic shell-magnetic core nanoparticles for targeted diagnostics, isolation, and photothermal destruction of tumor cells. *ACS Nano*, 6(2), 1065–1073, 2012.
142. Xie, H.-Y., Zhen, R., Wang, B., Feng, Y.-J., Chen, P., Hao, J., Fe_3O_4/Au Core/Shell Nanoparticles Modified with Ni^{2+}–Nitrilotriacetic Acid Specific to Histidine-Tagged Proteins. *J. Phys. Chem. C*, 114(11), 4825–4830, 2010.
143. Cui, Y.R., Hong, C., Zhou, Y.L., Li, Y., Gao, X.M., Zhang, X.X., Synthesis of oriented bioconjugated core/shell Fe_3O_4@Au magnetic nanoparticles for cell separation. *Talanta*, 85(3), 1246–1252, 2011.
144. Quaresma, P., Osório, I., Dória, G., Carvalho, P.A., Pereira, A., Langer, J., *et al.*, Star-shaped magnetite@gold nanoparticles for protein magnetic separation and SERS detection. *RSC Adv.*, 4(8), 3690–3698, 2014.
145. Li, J., Hu, Y., Yang, J., Wei, P., Sun, W., Shen, M., *et al.*, Hyaluronic acid-modi field Fe_3O_4 @Au core/shell nanostars for multimodal imaging and photothermal therapy of tumors. *Biomaterials*, 38, 10–21, 2015.
146. Wang, D.-Y., Lin, C.-P., Yeh, M.K., The recent development of gold nanoparticles in the applicationn of anticancer therapies and immunogenecity. *Lett in Appl. NanoBioScience*, 5, 335–341, 2016.
147. Mohammad, F., Yusof, N.A., Doxorubicin-loaded magnetic gold nanoshells for a combination therapy of hyperthermia and drug delivery. *J. Colloid Interface Sci.*, 434, 89–97, 2014.
148. Mody, V.V., Cox, A., Shah, S., Singh, A., Bevins, W., Parihar, H., Magnetic nanoparticle drug delivery systems for targeting tumor. *Appl. Nanosci.*, 4(4), 385–392, 2014.
149. Karamipour, S., Sadjadi, M.S., Farhadyar, N., Fabrication and spectroscopic studies of folic acid-conjugated Fe_3O_4@Au core–shell for targeted drug delivery application, *Spectrochim Acta A Mol. Biol. Spectrosc.*, 148, 146–155, 2015.

150. Chomoucka, J., Drbohlavova, J., Huska, D., Adam, V., Kizek, R., Hubalek, J., Magnetic nanoparticles and targeted drug delivering. *Pharmacol. Res.*, 62(2), 144–149, 2010.
151. Sensenig, R., Sapir, Y., MacDonald, C., Cohen, S., Polyak, B., Magnetic nanoparticle-based approaches to locally target therapy and enhance tissue regeneration *in vivo*. *Nanomedicine*, 7(9), 1425–1442, 2012.
152. del Mar Ramos-Tejada, M., Viota, J.L., Rudzka, K., Delgado, A.V., Preparation of multi-functionalized Fe_3O_4/Au nanoparticles for medical purposes. *Colloids Surf. B Biointerfaces*, 128, 1–7, 2015.
153. Ma, Y., Liang, X., Tong, S., Bao, G., Ren, Q., Dai, Z., Gold nanoshell nanomicelles for potential magnetic resonance imaging, light-triggered drug release, and photothermal therapy. *Adv. Funct. Mater.*, 23(7), 815–822, 2013.

1 publikacija / 1st publication

Ultra-small methionine-capped Au^0/Au^+ nanoparticles as efficient drug against the antibiotic-resistant bacteria

Žalnėravičius R., **Mikalauskaite A**., Niaura G., Paškevičius A. ir Jagminas A.,
Materials Science and Engineering C-materials for biological applications, 2019, 102, 646-652.
Perspausdinama gavus *Elsevier* leidyklos leidimą.
Publikaciją galite rasti adresu:
https://doi.org/10.1016/j.msec.2019.04.062

Materials Science & Engineering C 102 (2019) 646–652

Contents lists available at ScienceDirect

Materials Science & Engineering C

journal homepage: www.elsevier.com/locate/msec

Ultra-small methionine-capped Au^0/Au^+ nanoparticles as efficient drug against the antibiotic-resistant bacteria

Rokas Žalnėravičius[a], Agnė Mikalauskaitė[a], Gediminas Niaura[a], Algimantas Paškevičius[b], Arūnas Jagminas[a,*]

[a] State Research Institute Centre for Physical Sciences and Technology, Sauletekio av. 3, LT-10257 Vilnius, Lithuania
[b] Laboratory of Biodeterioration Research, Nature Research Centre, Akademijos 2, LT-08412 Vilnius, Lithuania

ARTICLE INFO

Keywords:
Gold species
Antimicrobial behavior
Magnetite nanoparticles
Methionine

ABSTRACT

In this study we examined the influence of ultra-small gold and magnetite-gold nanoparticles (NPs) stabilized with D,L-methionine, Fe_3O_4@Au@Met, on their antibacterial efficacy against three of twelve the worst bacterial family members included in the World Health Organization (WHO) list. In particular, gram-negative *Acinetobacter baumannii*, *Salmonella enterica* and gram-positive methicillin-resistant *Staphylococcus aureus* and *Micrococcus luteus* were tested. Apart from the synthesis, gold species reduction and NP stabilization, an excess of methionine has been used herein to detach ultra-small gold NPs from the Fe_3O_4@Au@Met surface, collect them and investigate. The antimicrobial efficiency of the ultra-small (Ø ~ 1.8 nm) Au@Met NPs and Fe_3O_4@Au@Met NPs was evaluated through the quantitative analysis by comparing with that of naked magnetite NPs, D,L-Met and BSA. It has been determined that compared with the control sample, 70 mg L^{-1} probe of Au@Met NPs exhibited the killing efficiency of 84.4–58.5% against gram-negative bacteria and 89.1–75.7% against gram-positive bacteria. The composition, structure, and morphology of the synthesized and tested herein NPs were investigated by inductively coupled plasma optical emission spectrometry, magnetic measurements, FTIR, XRD, XPS, AFM and HRTEM.

1. Introduction

It is commonly accepted that contrary to silver, gold in the metallic state is highly stable, biocompatible, and not cytotoxic even in the nanoparticulated size [1]. Au^0 nanoparticle (NP) antimicrobials render the grafted drug molecules, such as ampicillin, peptides or zwitterionic ligands [2–6]. On the other hand, antimicrobial behavior of gold ions is well-known, has been widely investigated, and well-reviewed in Djuran and Glišic paper [7]. According to the some recent reports, Au^0 NPs reduced down to the nanocluster size, *e.g.* ≤2.0 nm in diameter, may also exhibit the antimicrobial activity against some fungi and bacteria strains. For example, Zheng et al. [8] synthesized and tested 6-nm sized Au^0 NPs and ≤2.0-sized gold nanoclusters both templated and protected with the 6-mercaptohexanoic acid. Although these NPs possessed quite similar surface *zeta*-potential, a remarkable antimicrobial efficacy has been established just for nanoclusters against *S. aureus* and *E. coli* killing roughly from 95 to 96% of their population. Besides, it was concluded that the antimicrobial effect is not derived from the surface ligand and its content. On the contrary, Zhang et al. [9] reported that cationic ligands of gold NPs contributed to their antimicrobial activity. This effect has been attributed to the strong ionic interaction with the bacteria indicating that positively charged ligand molecules of Au NPs are responsible for the bacteria membrane permeability increase. Eventually, Chen et al. have synthesized gold clusters in lysozyme template and demonstrated their significant antimicrobial efficacy against two strains of multidrug-resistant bacteria [10].

Inspired by these works, in this study, we synthesized and tested ultra-small gold and gold-functionalized magnetite NPs comprised of Au^0/Au^+ for possible inactivation of multi-drug resistant bacteria. To the best of our knowledge, the antimicrobial behavior of ultra-small gold NPs stabilized with the amino acid has not been investigated against the most dangerous microorganism such as methicillin-resistant *Staphylococcus aureus*, *Acinetobacter baumannii*, and *Salmonella enterica*. For comparison, the antimicrobial efficacy of the magnetite NPs decorated with Au^0/Au^+ species as well as typical red-luminescent gold clusters formed and templated in a bovine serum albumin (BSA) matrix was also tested herein. It should be noted that *Salmonella* serotypes are associated with three distinct human disease syndromes: bacteremia, typhoid fever, and enterocolitis, whereas enterocolitis is the second most frequently bacterial food-borne disease causing roughly 1.4

* Corresponding author.
E-mail address: arunas.jagminas@ftmc.lt (A. Jagminas).

https://doi.org/10.1016/j.msec.2019.04.062
Received 15 November 2018; Received in revised form 14 March 2019; Accepted 20 April 2019
Available online 22 April 2019

million illnesses [11] and approximately 550 annual deaths per year just in the United States [12]. Consequently, the interest in *Acinetobacter* serotypes has risen sharply over the recent years from both the scientific and public community since they cause a wide spectrum of infections that include pneumonia, bacteremia, meningitis, urinary tract infection, and wound infection [13,14].

2. Experimental

2.1. Chemical reagents and materials

All the reagents in this study were at least of the analytical grade and, except NaOH, were used as received. Iron(III) chloride hexahydrate ($FeCl_3{\cdot}6H_2O$, ≥99%), iron(II) chloride tetrahydrate ($FeCl_2{\cdot}4H_2O$, ≥99%), tetrachloroauric(III) acid tetrahydrate ($HAuCl_4{\cdot}4H_2O$, ≥99.9%) D,L-methionine (≥99%), M9 5× minimal microbial growth medium (33.9 g L^{-1} Na_2HPO_4, 15 g L^{-1} KH_2PO_4, 5 g L^{-1} NH_4Cl and 2.5 g L^{-1} NaCl, pH = 7) and bovine serum albumin (BSA, 96%) were supplied by Sigma-Aldrich Chemical Co. Nutrient agar (3 g L^{-1} beef extract, 15 g L^{-1} peptone and 15 g L^{-1} agar) and Nutrient Broth (1 g L^{-1} glucose, 5 g L^{-1} peptone, 6 g L^{-1} sodium chloride and 3 g L^{-1} yeast extract) were obtained from Liofilchem. Sodium hydroxide was purified by preparation of a saturate solution resulting in the crystallization of other sodium salts. Following the analysis, this solution was diluted to the 2.0 mol L^{-1} concentration and applied. Milli-Q grade water was used (18 MΩ) for preparation of all solutions.

Gram-positive methicillin-resistant *Staphylococcus aureus* (MRSA) (ATCC 433300), *Micrococcus luteus* (GTC-BTL, B-30S) and gram-negative *Acinetobacter baumannii* (ATCC BAA-747), *Salmonella enterica* (GTC-BTL, B-25) bacteria strains were obtained from the Nature Research Centre collection of microbial strains.

2.2. Synthesis of NPs

In this study, the synthesis of ultra-small gold NPs was carried out in the following way (Fig. 1). In the first step, magnetite NPs were synthesized from the alkaline solution containing 15 mmol L^{-1} $FeSO_4$, 30 mmol L^{-1} $FeCl_3$, and 0.2 mol L^{-1} D,L-methionine (Met) amino acid, as chelating agent, and NaOH up to pH ≅ 12.35 ± 0.1 at 130 °C for 10 h hydrothermally using the 10 °C min^{-1} ramp. Then, as-grown NPs were collected by centrifugation at 7500 rpm for 5 min, carefully rinsed several times with water and dried at 60 °C. In the second step, the surface of magnetite NPs was loaded with ultra-small gold nanocrystals *via* Met-induced chemical reduction of the chloroauric acid according to our previous work [15]. Briefly, Fe_3O_4@Met NP probe (3.5 mg) was dispersed in 5 mL of water under ultrasound agitation until the mixture became bright mustard-coloured. Then, 3.5 mL of this suspension was transferred into a glass reactor along with 5 mL of Met (10 mM) and $HAuCl_4$ (4 mM) solutions under stirring. The solution pH was adjusted to ≅12.4 with 2 M NaOH drop-wise and the synthesis was conducted at 37 °C for 4 h under mild stirring. The products identified as Fe_3O_4@Au@Met NPs were washed thoroughly with water and ethanol for further examination. In the third step, ultra-small gold NPs were detached from the surface of Fe_3O_4@Au@Met NPs by chemical means. To achieve this result, Fe_3O_4@Au@Met NPs were sonicated in the 0.3 M Met solution under ultra-sound agitation for 7 min resulting in Fe_3O_4 removal from the surface of magnetite NPs viewed from the suspension colour changes from bright brown to light pink. Finally, Au@Met NPs were separated from the magnetic ones using a permanent magnet, rinsed and stored at 4 °C for characterization and further experiments.

2.3. Measurements and equipment

The morphology of the as-growth NPs was investigated with the transmission electron microscope (TEM) FEI Tec-nai F20 X-TWIN operated at an accelerating voltage of 200 kV. TEM images were recorded using a Gatan Orius CCD camera. The nanoparticles subjected to TEM observations were dispersed in ethanol and drop-cast on a carbon-coated nickel grid. The size distribution histograms of Fe_3O_4@Met, Fe_3O_4@Au@Met and Au@Met NPs were estimated using the Image J software. The average diameter of particles was estimated by analyzing high resolution TEM images. For this purpose, at least one hundred of NPs were randomly selected and measured.

Phase analysis of magnetite and Fe_3O_4@Au@Met NPs was carried out using a diffractometer SmartLab (Rigaku) with rotating Cu anode. CuK_α radiation (α = 0.154183 nm) was separated with the multilayer bent graphite monochromator. The XRD patterns were performed in the Bragg-Brentano scan mode in the 2theta range from 10 o to 80° with the step size of 0.02° and a counting time of 8 s per step. Phase identification was performed using the powder diffraction database PDF4+ (2015). The size of NPs was determined by the Halder-Wagner (H-W) approximation.

X-ray photoelectron spectroscopy (XPS) experiments were carried out in order to obtain information about the chemical state of ultra-small gold NPs deposited as well as detached from the magnetite surface on the upgraded Vacuum Generator "VG ESCALAB MK II" (VG Scientific) spectrometer fitted with a new XR4 twin anode. The non-monochromatised MgKα X-ray source was operated at $h\nu$ = 1253.6 eV with the 300 W power (20 mA/15 kV). During the spectral acquisition, the pressure in the analysis chamber was lower than 5·107 Pa. The spectra were acquired with the electron analyzer pass energy of 20 eV and resolution of 0.05 eV.

Infrared spectra were recorded in the transmission mode on an ALPHA FTIR spectrometer (Bruker, Inc., Germany) equipped with a room temperature detector DLATGS. The spectral resolution was set at 4 cm^{-1}. Spectra were acquired from 64 scans. Samples were dispersed in the KBr tablets. Parameters of the bands were determined by fitting the experimental spectra with Gaussian-Lorentzian shape components using GRAMS/A1 8.0 (Thermo Scientific) software.

The amount of gold in the Fe_3O_4@Au@Met and ultra-small Au@Met NP probes was estimated using an inductively coupled plasma optical emission spectrometer ICP-OES OPTIMA 7000DV (Perkin Elmer). In this way, a small pinch of nanopowders was dissolved in the aqua regia solution. Then, a calibration curve was drawn using a series of calibration standard solutions in the HCl:HNO_3 (3:1 by volume) acidic matrix as the unknown solutions. All measurements were carried

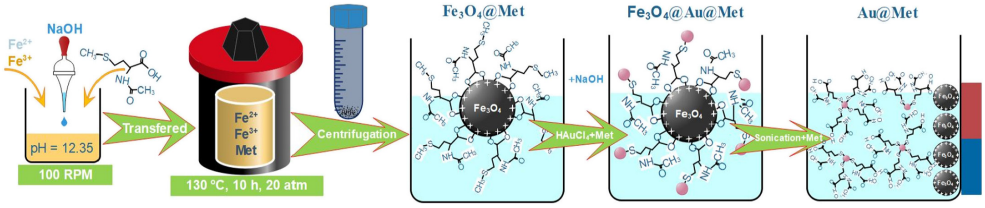

Fig. 1. The scheme illustrating fabrication of Fe_3O_4@Met, Fe_3O_4@Au@Met, and ultra-small Au@Met NPs.

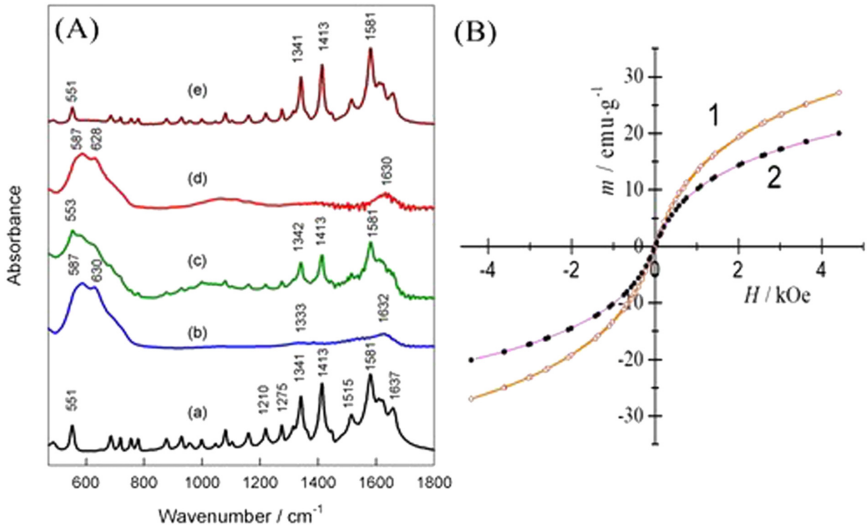

Fig. 2. (A): The FTIR spectra of pure Met (a) and as-synthesized NP samples "b, c, d and e" corresponding to Fe_3O_4, Met-caped Fe_3O_4, gold-capped Fe_3O_4 and gold species detached from the magnetite, respectively. In (B): the magnetic response plots of magnetite NPs before (1) and after (2) gold deposition.

out at emission peaks λ_{Au} = 267.595 nm and λ_{Au} = 242.795 nm.

The morphology of ultra-small gold NPs, spin coated onto the mica surface, was also investigated with the atomic force microscope (AFM) Veeco AFM diInnova (Veeco Instruments Inc.) in a tapping mode. TESPA-V2 cantilevers (Veeco Instruments Inc.) with a tip curvature of 8 nm were used. Images were acquired at the scan rate of 1 Hz per line with the 512 × 512 pixel image resolution. Image processing included flattening to remove the background slope caused by the irregularities of the piezoelectric scanner. The analysis was performed using the SpmLabAnalysis software (Veeco Instruments Inc.).

Magnetization measurements were accomplished using a vibrating-sample magnetometer calibrated by a Ni sample of similar dimensions as the studied sample. The magnetometer was composed of the vibrator, the lock-in amplifier, and the electromagnet. The magnetic field was measured with a test meter FH 54 (Magnet-Physics Dr. Steingrover GmbH).

2.4. Antimicrobial activity of as-grown nanoparticles

Antimicrobial assessments of the synthesized Fe_3O_4@Au@Met NPs and ultra-small gold nanocrystals were tested against gram-negative A. baumannii and *S. enterica* and gram-positive *S. aureus* (MRSA) and *M. luteus* bacteria strains using the serial dilution method. Following these investigations bacteria strains were propagated in the Nutrient agar medium at 37° ± 1 °C for 24 h. The fresh cultures were harvested and diluted in the sterile M9 minimal microbial growth medium to yield colony-forming units (CFU) inoculum of 6.4–8 × 108 for bacteria cells, based on the optical density at 600 nm (OD600). The range of OD600 was obtained to be between 0.08 and 0.1. Then, 100 μL probe of the diluted microorganism suspension was collected at the logarithmic stage of growth and transferred in a 96 well cell culture plate. Finally, 100 μL of water containing 140 mg L^{-1} or 60 mg L^{-1} of Fe_3O_4@Au@Met or ultra-small gold NPs was added to the liquid medium, resulting in their final concentration of 70 and 30 mg L^{-1}, respectively, and incubated further for 24 h with 150 rpm shaking. In these investigations, D,L-methionine and magnetite NPs were used as negative controls. During the cultivation, 100 μL of suspension was taken from each reaction mixture, diluted in the glass tube *via* the broth dilution method and spread on the Nutrient Broth agar media plate using a stainless steel spreader. The growth of microorganisms was tested after incubation at 37° ± 1 °C for one day. Each assay was performed in triplicate with three independent experiments.

3. Results and discussion

3.1. Synthesis and characterization of Fe_3O_4@Met nanoparticles

In this study, gold NPs, ultra-small, quite uniform in size, and containing zero-valent gold were synthesized on the surface of magnetite NPs by reducing the gold acid with Met molecules capped at the surface of Fe_3O_4. For this purpose, magnetite NPs were synthesized hydrothermally employing both Fe^{2+} and Fe^{3+} salts at the 2:1 molar ratio as precursors and Met amino acid as the stabilizing agent for control over the uniformity of the NPs growth. The adapted concentration of iron salts (45 mmol L^{-1}) and Met (0.2 mol L^{-1}), synthesis temperature (130 °C) and duration (10 h) allowed us to grow the spherical NPs (Fig. 1S). The morphology of NPs synthesized *via* this hydrothermal approach was investigated further by high-resolution TEM and is depicted in Fig. 1S, part B revealing that as-grown NPs possess mainly an average diameter of roughly 11 nm and quite narrow size distribution (Fig. 2S). Besides, from the HRTEM image inspection (Fig. 1S, part B) as-grown NPs are single crystalline as clearly indicated by atomic lattice fringes and most probably they grow preferentially along the (311) direction with a lattice interatomic distance of *ca.* 0.252 nm. It should be noted that the XRD pattern taken from the scope of these NPs (Fig. 3S) demonstrated a set of diffraction peaks clearly seen at 2Θ positions: 18.28, 30.08, 35.43, 43.06, 53.42, 56.94, 62.53, 70.94, 73.97, 74.97, and 78.93. These peaks matched well with the diffraction peaks characteristic of polycrystalline Fe_3O_4 planes (111), (220), (311), (400), (422), (511), (440), (620), (533), (622), and (444),

respectively, (PDF Card No. 04-005-4319), and confirmed the formation of a face-centered cubic (fcc) crystal structure (space group *Fd-3m*, $\alpha = \beta = \gamma = 8.396$ Å). It is also seen that the average size of Fe_3O_4 NPs estimated from the XRD pattern using Halder-Wagner approximation equaled to *ca.* 11.9 ± 0.15 nm was consistent with the data obtained from the HRTEM observations complementing the fact that our synthesized NPs are quite uniformly-sized.

To probe the Met adsorption on the NPs surface, the FTIR spectra of pure D,L-Met, as well as the synthesized and chemically modified Fe_3O_4 NPs were collected and are depicted in the part (A) of Fig. 2. The FTIR spectrum of pure Met (a) shows a set of numerous peaks most intense at the 1413 and 1581 cm^{-1} which according to the literature [16–19] are due to the symmetric and asymmetric stretching vibrations of $-COO^-$ group. The two peaks located at 1515 and 1637 cm^{-1} correspond to symmetric and asymmetric deformation vibrations of NH_3^+ group, respectively [16,17]. Thus, infrared spectrum confirms zwitterionic structure of studied compound. The intense band near 1341 cm^{-1} is associated with symmetric CH_3 deformation vibration with contribution from deformation vibration of CH group, δ(CH) [17]. The clearly defined band at 551 cm^{-1} belongs to out-of-plane deformation of carboxylate group, $\gamma(COO^-)$ [17].

According to the literature [20–22], the vibration band with the peaks at 628 and 587 cm^{-1} in the spectrum of as-grown Fe_3O_4 NPs should be assigned to the stretching modes of the Fe—O bond both at the tetrahedral sites and on the surface of magnetite NPs. Besides, the FTIR spectrum of as-grown Fe_3O_4 NPs has an additional broad shoulder peaked at 1630 cm^{-1} attributable to the asymmetric C=O stretching vibration of deprotonated carboxyl group $-(COO^-)$ [23] in the Met molecule bound to the surface of Fe_3O_4. The intense bands from both Fe_3O_4 and Met species are visible in the spectrum of Met-capped Fe_3O_4 (curve c of Fig. 2A) indicating presence of adsorbed Met in zwitterionic form.

3.2. Fe_3O_4@Met NPs decoration with ultra-small gold nanoparticles

Fig. 3 shows the formation of numerous gold species on the surface of methionine-stabilized Fe_3O_4 NPs after their sonication in the $HAuCl_4$ solution under adapted herein conditions. From the TEM inspection, however, it was difficult to determine the size distribution of attached gold species, although most of them seem to be spherical and ≤2.0 nm-sized (Fig. 3B). From the literature the attachment of gold seeds [24] and functionalization of magnetite Nps with gold-containing shells [25] resulted in the saturation magnetization (M_s) decrease although in the case of gold nanograins attachment onto magnetite nanocrystals with an amino-terminated silane [26] M_s decrease was insignificant. Therefore, the attachment of gold species to the magnetite surface was verified by EDX and FTIR spectra and magnetization investigations. Fig. 2A shows the room-temperature magnetization plots as a function of the applied magnetic field for Fe_3O_4@Met NPs before (1) and after (2) their sonication in the chloroauric acid solution. From these measurements, the saturation magnetization value of magnetite NPs decreased from 27 to 21 emu·g^{-1} (at H_{max} = 4.4 kOe) supporting the proposition that gold species were deposited although NPs remained superparamagnetic. The deposition of gold onto the surface of Fe_3O_4@Met NPs has also been certified by EDX spectra (see Fig. 4S). In addition, the FTIR spectrum of gold-decorated Fe_3O_4@Met NPs (Fig. 2B, sample d) clearly evidenced the bond with Met molecules even after the careful NP rinse.

3.3. Detachment and characterization of Au@Met NPs

To remove ultra-small gold NPs from the surface of magnetite NP for the first time we have used the same methionine amino acid as a detaching agent. This procedure was conducted *via* ultrasound agitation of gold-coated magnetite NPs in methionine solution attributing the detachment effect to the stronger interaction of the amino acid with gold nanocrystals compared to the Au-Fe_3O_4 bond. The obtained light-pink solution due to dispersion of ultra-small gold NPs was further investigated by sampling on the Lacey grid followed by AFM and TEM observations for the particle size inspection. As seen from Fig. 4 images, the detached ultra-small gold nanocrystals exhibit mainly the spherical particle morphology with an average diameter of 1.8 nm and a quite narrow size distribution. It is noteworthy, that they seems to be not aggregated.

3.4. Antimicrobial activity of Au@Met and Fe_3O_4@Au@Met NPs

For these investigations, we have chosen three the worst bacterial family members included in the World Health Organization (WHO) list of the drug-resistant bacteria that pose the greatest threat to human health and for which new antibiotics are desperately needed [27]. Therefore, the antimicrobial activity of ultra-small gold and Fe_3O_4@Au@Met NPs was investigated against gram-negative *A. baumannii* (ATCC BAA-747), *S. enterica* (GTC-BTL, B-25) and gram-positive methicillin-resistant *S. aureus* (ATCC 433300), and *M. luteus* (GTC-BTL,

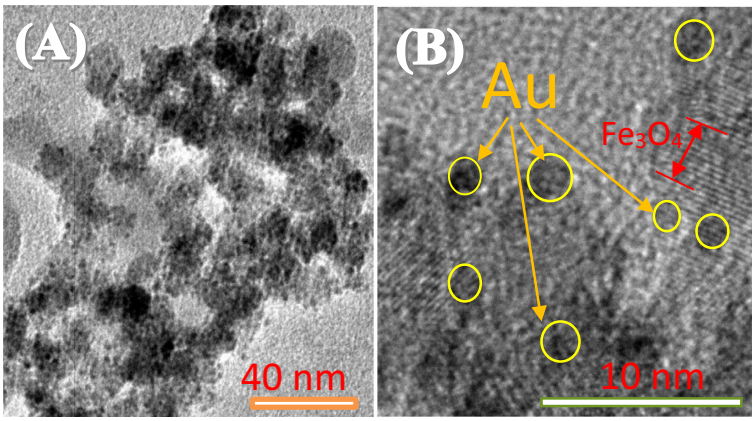

Fig. 3. TEM (A) and HRTEM (B) images of magnetite NPs after decoration with gold nanocrystals *via* methionine-induced $HAuCl_4$ reduction.

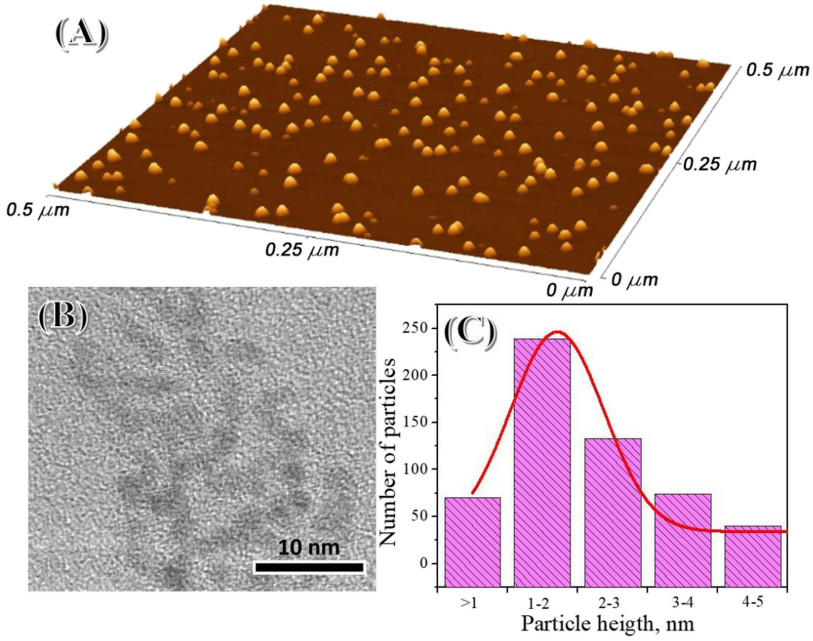

Fig. 4. AFM 3D view of magnetite Nps (A), whereas TEM image and size distribution histogram of gold NPs detached from magnetite nanoparticles are shown in the (B) and (C) parts, respectively.

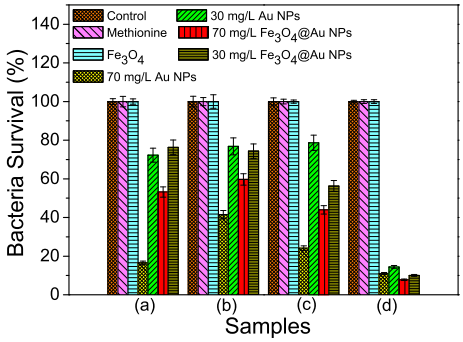

Fig. 5. Antimicrobial activities of the synthesized Au@Met and Fe_3O_4@Au NPs after 24 h incubation with gram-negative *A. baumannii* (a), *S. enterica* (b), and gram-positive *S. aureus* (MRSA) (c), *M. luteus* (d). For comparison, the behavior of pure D,L-methionine and magnetite NPs is presented.

B-30S) by assessing the colony forming units (CFU). During this investigation, the microorganisms were incubated in the M9 liquid medium together with 70 or 30 mg L^{-1} of Au@Met either Fe_3O_4@Au@Met NP probes, respectively, under shaking for 24. The percentage ratios of bacteria survival obtained from these assays are shown in Fig. 5. Moreover, 100 mg $L^{-1}$of D,L-methionine and 1 g L^{-1} of Fe_3O_4@Met NP probes were also investigated as the negative control samples. It can be easily seen that Au@Met and Fe_3O_4@Au@Met NPs show the highest killing efficiency against the *M. luteus* bacteria strain. These results further support the idea that human pathogenic microorganisms are more virulent and resistant than antibiotic-susceptible microbes such as *M. luteus* [28]. A positive correlation was also found between the concentration of Au in NPs and bacteria survival. In comparison with the control sample, 70 mg L^{-1} of Au@Met NP probe exhibits the killing efficiency of 84.4–58.5% against gram-negative bacteria and 89.1–75.7% against gram-positive bacteria. In addition, Fig. 6 shows the quantity of gram-negative and gram-positive microorganisms grown on the Nutrient agar plates demonstrating a significant reduction of the colonies count. From these tests, one unanticipated finding was that the decreasing of the concentration of gold NPs approximately in the 2.3 times results in the weakening of bacteria assessment by 3.05, 2.52, 1.35, and 1.04 fold against *A. baumannii*, *S. enterica*, *S. aureus* (MRSA), and *M. luteus* bacteria, respectively. These results seem to be consistent with other investigation which determined that 6 nm-sized AuNPs showed no concentration dependent antibacterial effect against *B. subtilis* and *E. coli* microorganisms [8]. It should be noted that *S. enterica* demonstrated the strongest resistance against the ultra-small gold and Fe_3O_4@Au@Met NPs.

It is noteworthy, however, that in the case of Fe_3O_4@Met NPs, as well as D,L-methionine amino acid, the same amount of colony forming units as for the control sample was grown. From the antimicrobial activity tests of methionine, this stabilizing agent of gold species and magnetite Nps is nontoxic because this is an amino acid and can be easily metabolized by bacteria [29]. Having in mind the biocompatibility and non-toxicity of gold materials even in the nm-scaled dimensions, the established antimicrobial behavior of the synthesized Au@Met nanocrystals as well tethered to the surface of Fe_3O_4 NPs

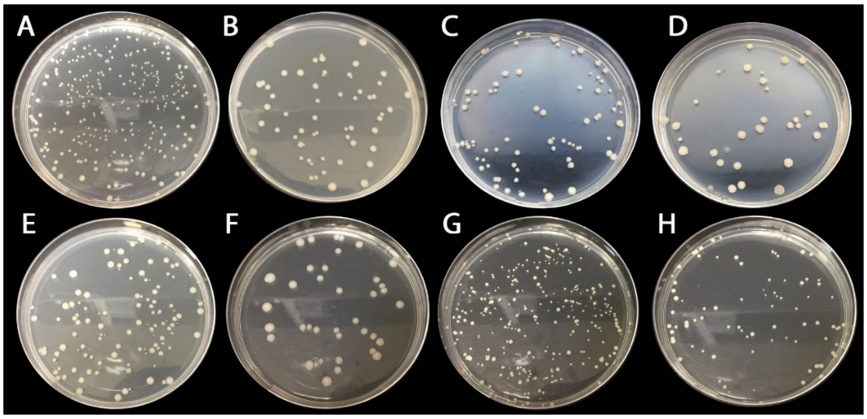

Fig. 6. Photographs showing the antimicrobial activity of Au@Met nanocrystals for growth inhibition of gram-negative (a–b) *A. baumannii*, (c–d) *S. enterica* (top row) and gram-positive (e–f) methicillin-resistant *S. aureus*, (g–h) *M. luteus* (bottom row) microorganisms incubated in the Nutrient agar plates. All the microorganisms were cultivated in liquid M9 medium without (a, c, e, g) and with (b, d, f, h) 70 mg L^{-1} Au@Met species for 24 h.

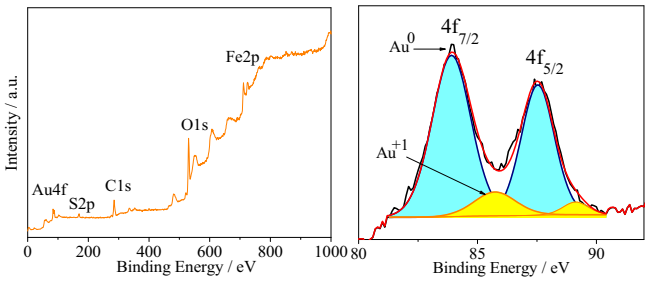

Fig. 7. XPS survey of gold-coated magnetite NPs (A) and high-resolution deconvoluted XP spectrum of Au 4f (B).

required explanation. We hypothesized that one possible explanation of such behavior should be ascribed to the composition and structure of ultra-small gold species because the methionine shell showed no cytotoxicity and antimicrobial efficacy. In an attempt to shed light on the reasons for the strong bactericidal effect of Au@Met nanocrystals and Fe_3O_4@Au@Met NPs, X-ray photoelectron spectroscopy (XPS) investigations of these species were further performed. Fig. 7A displays the XPS survey spectrum of the tested Fe_3O_4@Au@Met NP sample revealing the clear signals from Fe, O, C, S, and Au. The carbon and sulfur peaks were tentatively assigned mainly to the methionine molecules attached to the magnetite and gold NPs. The deconvoluted

Au 4f XP spectrum taken from the scope of Fe_3O_4@Au@Met NPs is presented in Fig. 7B. It is clear that the main Au $4f_{7/2}$ photoelectron peak is located at a binding energy (BE) 83.94 eV characteristic of the pure metallic Au^0 [30]. The fitting of this spectrum was further performed using the two spin-orbit split Au $4f_{7/2}$ and Au $4f_{5/2}$ components, separated by 3.56 eV. In addition, the Au 4f plot fitting revealed an additional shoulder peaked at 85.74 eV indicating the presence of Au^+ [23,31]. Based on the relative contents of Fe, O, N, C, S, and Au measured by high-resolution XPS, the average content of the deposited gold was estimated roughly to be 1.67 at.% of the total NP mass. We suggest that the main reason for the antimicrobial activity of our Fe_3O_4@Au@Met NPs as well as Au@Met nanocrystals should be ascribed to the presence of Au^+ ions on the surface of gold species. Therefore, we attributed this effect to the small gold species size coupled to their composition, particularly Au^0/Au^+, capable to interact with bacteria cell walls and membranes. The interaction between ultra-small gold Nps containing Au^+ and bacteria is expected induce a metabolic imbalance in bacterial cells and protein denaturation that kills bacteria. Note that metallic gold (Au^0) is inert, highly stable, and not easily dissociate into ions [32] remaining highly biocompatible even in the few-nm size [33].

4. Conclusions

Antimicrobial properties of ultra-small gold species as well as tethered to the surface of magnetite NPs have been studied against multidrug-resistant gram-negative A. baumannii, *S. enterica* and gram-positive *S. aureus* (MRSA), *M. luteus* bacteria strains using the serial dilution method. Uniformly sized gold species were formed by reduction of the gold acid with the Met capped to the surface of superparamagnetic magnetite NPs of the average size of 11.9 ± 0.15 nm. Both the attached to magnetite surface (Fe_3O_4@Au@Met) and alone (Au@Met) gold species were tested. It was determined that 70 mg L^{-1} Au@Met NPs probe exhibited the killing efficiency of 84.4–58.5% against gram-negative bacteria and 89.1–75.7% against gram-positive

bacteria. Numerous methods have been applied for characterization of the synthesized gold species shown to be spherical, average sized (≤ 1.8 nm) and composed of $Au^0 + Au^+$. The strong antimicrobial efficiency of Met-capped gold species against several most dangerous bacteria was related to the presence of single-valent gold on the surface side.

Acknowledgements

We appreciate Drs. V. Pakštas for powder XRD collection, J. Vaičiūniene for chemical analysis, and V. Jasulaitiene for XPS spectra collection.

Appendix A. Supplementary data

Supplementary data to this article can be found online at https://doi.org/10.1016/j.msec.2019.04.062.

References

[1] N. Lewinski, V. Colvin, R. Drezek, Small 4 (2008) 426–449.
[2] T. Pellegrino, S. Kureda, T. Liedl, A.M. Javier, L. Manna, W.J. Parak, Small 1 (2005) 48–63.
[3] P. Juzenas, W. Chen, Y.P. Sun, M.A.N. Coelho, R. Generalov, N. Generalova, I.L. Chistensen, Adv. Drug Deliv. Rev. 60 (2008) 1600–1614.
[4] M.A. Walling, J.A. Novak, J.R.E. Shepard, Int. J. Mol. Sci. 10 (2009) 441–491.
[5] G.L. Burygin, B.N. Khlebtsov, A.N. Shantrokha, L.A. Dykman, V.A. Bogatyrev, N.G. Khlebtsov, Nanoscale Res. Lett. 4 (2009) 794–801.
[6] A.M. Allahverdiyev, K.V. Kon, E.S. Abamor, M. Bagirova, M. Rafailovich, Expert Rev. Anti-Infect. Ther. 9 (2011) 1035–1052.
[7] B.D. Glišic, M.I. Djuran, Dalton Trans. 43 (2014) 5950–5969.
[8] K. Zheng, M.I. Setyawati, D.T. Leong, J. Xie, ACS Nano 11 (2017) 6904–6910.
[9] Y. Zhang, H. Peng, W. Huang, Y. Zhou, D. Yan, J. Colloid Interface Sci. 325 (2008) 371–376.
[10] W.Y. Chen, J.Y. Lin, W.J. Chen, L. Luo, E.W.G. Diau, Y.C. Chen, Nanomedicine 5 (2010) 755–764.
[11] P.S.L. Mead Slutsker, V. Dietz, L.F. McCaig, J.S. Bresee, C. Shapiro, P.M. Griffin, R.V. Tauxe, Emerg. Infect. Dis. 5 (1999) 607–625.
[12] F.C. Fang, J. Fierer, Medicine (Baltimore) 70 (1991) 198–207.
[13] A.T. Bernards, H.I. Harinck, L. Dijkshoorn, T.J. van der Reijden, P.J. van den Broek, Infect. Control Hosp. Epidemiol. 25 (2004) 1002–1004.
[14] P.E. Fournier, H. Richet, Clin. Infect. Dis. 42 (2006) 692–699.
[15] A. Jagminas, A. Mikalauskaitė, V. Karabanovas, J. Vaičiūnienė, Beilstein J. Nanotechnol. 8 (2017) 1734–1741.
[16] E. Cooper, F. Krebs, McD. Smith, R. Raval, J. Electron Spectrosc. Relat. Phenom. 64/65 (1993) 469 – 475.
[17] M. Wolpert, P. Hellwig, Spectrochim. Acta A 64 (2006) 987 – 1001.
[18] N.B. Colthup, L.H. Daly, S.E. Wiberley, Introduction to Infrared and Raman Spectroscopy, Academic Press, New York, 1990.
[19] Z. Wang, H. Zhu, F. Wang, X. Yang, Nanotechnology 20 (2009) 465606.
[20] A. Barth, Prog. Biophys. Mol. Biol. 74 (2000) 141–173.
[21] K. Basavaiah, P.Y. Kumar, A.V. Prasada Rao, Appl. Nanosci. 3 (2013) 409–415.
[22] N. Belachew, D. Rama Devi, K. Basavaiah, J. Mol. Liq. 224 (2016) 713–720.
[23] R.M. Cornell, S. Chwertmann, The Iron Oxides: Structures, Properties, Reactions, Occurrences and Uses, Willey-VCH, Weinheim, 2003.
[24] S. Sabale, P. Kandesar, V. Jadhav, R. Komorek, R.K. Motkuri, X.-Y. Yu, Biomater. Sci. 5 (2017) 2212–2225.
[25] S. Karamipour, M.S. Sadjadi, N. Farhadyar, Spectrochim. Acta A Mol. Biomol. Spectrosc. 148 (2015) 146–155.
[26] D. Caruntu, B.L. Cushing, G. Caruntu, C.J. O'Connor, Chem. Mater. 17 (2005) 3398–3402.
[27] C. Willyard, Nature 543 (2018) 15–16.
[28] F. Rozgonyi, E. Kocsis, K. Kristof, K. Nagy, Clin. Microbiol. Infect. 13 (2007) 843–845.
[29] M.S. Palencia, M.E. Berrio, S.L. Palencia, J. Nanosci. Nanotechnol. 17 (2017) 5197–5204.
[30] J.F. Moulder, W.F. Sticker, P.E. Sobol, K.D. Bomben, R.C. King (Eds.), Physical Electronics, Eden Prairee, MN, U.S.A., 1995.
[31] A.M. Venezia, G. Pantaleo, A. Longo, G. Di Carlo, M.P. Casaletto, L. Liotta, G. Deganello, J. Phys. Chem. B 109 (2005) 2821–2827.
[32] B. Hammer, J. Norskov, Nature 376 (1995) 238.
[33] N. Lewinski, V. Colvin, R. Drezek, Small 4 (2008) 26–49.

2 publikacija / 2nd publication

Methionine-mediated synthesis of magnetic nanoparticles and functionalization with gold quantum dots for theranostic applications.

Jagminas A, **Mikalauskaitė A**, Karabanovas V, Vaičiūnienė J.

Sivakov V, ed. Beilstein Journal of Nanotechnology. 2017, 8, 1734-1741.

Perspausdinama gavus *Beilstein Journal of Nanotechnology* leidyklos leidimą.

Publikaciją galite rasti adresu: https://doi.org/10.3762/bjnano.8.174

BEILSTEIN JOURNAL OF NANOTECHNOLOGY

Methionine-mediated synthesis of magnetic nanoparticles and functionalization with gold quantum dots for theranostic applications

Arūnas Jagminas[*1,§], Agnė Mikalauskaitė[1], Vitalijus Karabanovas[2] and Jūrate Vaičiūnienė[1]

Full Research Paper

Open Access

Address:
[1]State Research Institute Center for Physical Sciences and Technology, Sauletekio Ave. 3, LT- 10222, Vilnius, Lithuania and
[2]National Cancer Institute, Baublio 3b, LT- 08406, Vilnius, Lithuania

Email:
Arūnas Jagminas[*] - arunas.jagminas@ftmc.lt

* Corresponding author
§ Tel: +370 5648891

Keywords:
functionalization; gold; magnetic nanoparticles; quantum dots; theranostics

Beilstein J. Nanotechnol. **2017,** *8,* 1734–1741.
doi:10.3762/bjnano.8.174

Received: 24 March 2017
Accepted: 02 August 2017
Published: 22 August 2017

This article is part of the Thematic Series "Nanomaterial-based cancer theranostics".

Guest Editor: V. Sivakov

Abstract

Biocompatible superparamagnetic iron oxide nanoparticles (NPs) through smart chemical functionalization of their surface with fluorescent species, therapeutic proteins, antibiotics, and aptamers offer remarkable potential for diagnosis and therapy of disease sites at their initial stage of growth. Such NPs can be obtained by the creation of proper linkers between magnetic NP and fluorescent or drug probes. One of these linkers is gold, because it is chemically stable, nontoxic and capable to link various biomolecules. In this study, we present a way for a simple and reliable decoration the surface of magnetic NPs with gold quantum dots (QDs) containing more than 13.5% of Au^{+}. Emphasis is put on the synthesis of magnetic NPs by co-precipitation using the amino acid methionine as NP growth-stabilizing agent capable to later reduce and attach gold species. The surface of these NPs can be further conjugated with targeting and chemotherapy agents, such as cancer stem cell-related antibodies and the anticancer drug doxorubicin, for early detection and improved treatment. In order to verify our findings, high-resolution transmission electron microscopy (HRTEM), atomic force microscopy (AFM), FTIR spectroscopy, inductively coupled plasma mass spectroscopy (ICP-MS), and X-ray photoelectron spectroscopy (XPS) of as-formed $CoFe_2O_4$ NPs before and after decoration with gold QDs were applied.

Introduction

In current nanomedicine, biocompatible iron oxide-based NPs have attracted particular interest due to their size-dependent magnetic, optical and chemical properties that allow for the design of NPs for multimodal imaging and photothermal therapy of cancer cells [1]. Dual-imaging probes, capable to perform simultaneously magnetic resonance and fluorescent imaging, allow for a more rapid and precise screening of the oncological disease sites. This is frequently achieved by covering magnetic NPs with shells containing luminescent quantum dots (QDs) [2-6]. The target molecules can be attached to the surface of magnetic NPs through biocompatible links such as Au–S– [7]. Iron oxide NPs can be coated with polymeric or silica shells containing incorporated gold NPs [8-10]. However, in this case the size of the magnetic NPs increases up to ten times [9], resulting in a significant decrease in the saturation magnetization value of the magnetic core. To eliminate this drawback, several methods for the deposition of the gold directly onto the surface of magnetic NPs have been proposed that are based on the reduction of Au(III) species by the typical reducing agents such as borohydride, ascorbic acid and citric acid [11-14]. However, the direct-deposition protocols are mainly suitable for covering γ-Fe_2O_3 NPs. The formation of a gold shell on magnetite (Fe_3O_4) or ferrite surfaces through reduction of chloroauric acid by citrates or borohydride is usually problematic due to the formation of pure gold crystallites in the solution [5,15]. The deposition of gold onto the surface of magnetic iron oxide-based NPs can also be achieved via their impregnation with hydroxylamine [16], vitamin C [17] or methionine [18,19], which are capable to reduce the gold ions at the surface of NPs. However, in this case, uniform coating of magnetic NPs can only be obtained via precise control of the precursor content and all steps of the multistep process [17,18]. As a result, this way is time-consuming and it does not fully prevent the formation of gold crystallites in the plating solution. Moreover, to avoid the aggregation of magnetic NPs during or at the end of the synthesis they must be covered with capping materials such as acid anions [20,21], surfactants [22] or proteins [23]. Besides, for in vivo and in vitro applications of magnetic NPs their capping materials should be biocompatible and allow for the attachment of gold species. In recent publications amino acids such as methionine [19] and lysine [24] have been reported to be effective capping agents to control the size of magnetite [19] and Co ferrite [24] NPs during co-precipitation synthesis [25]. The main goal of the methionine capping was the application of Fe_3O_4@Met NPs for the adsorption of water pollutants.

In this study, we report a novel synthesis protocol for superparamagnetic cobalt ferrite NPs capped with a biocompatible methionine shell ($CoFe_2O_4$@Met), which in turn is capable to reduce and attach the gold species. In this way, hybrid magnetoplasmonic cobalt ferrite NPs decorated with Au^0/Au^{1+} quantum dots (QDs) were formed for the first time. The formation of plasmonic gold QDs at the surface of iron oxide-based NPs was confirmed by HRTEM, AFM, FTIR, XPS and chemical analysis.

Results and Discussion

Synthesis and characterization of methionine-functionalized cobalt ferrite nanoparticles

A hydrothermal approach was applied to synthesize the superparamagnetic cobalt ferrite NPs stabilized with methionine. The proposed approach differs from the reported one [19] in the nature of magnetic NPs, the composition of the aqueous solution applied, synthesis atmosphere and modes. It involves the preparation of an alkaline aqueous solution containing $CoCl_2$, $FeCl_3$, methionine, and NaOH up to pH 12.4, followed by autoclaving at 130 °C for 10 h. To the best of our knowledge, methionine has not been applied before for hydrothermal synthesis and stabilization of cobalt ferrite NPs as the capping ligand and reducing agent of gold ions. The interest in NPs capped with methionine was based on the current understanding that methionine can reduce chloroauric acid from alkaline solutions anchoring Au^0 at the surface of the NPs [18]. As-synthesized NPs were characterized by TEM, XRD, FTIR and magnetic measurements. Figure 1a depicts the TEM image of the as-grown NPs that have been carefully rinsed and reveals their spherical shape and a size distribution in the range of (3.0 – 8.5) nm with a mean value of 5.7 nm (Figure 1b). Furthermore, the stabilization of cobalt ferrite NPs with metionine molecules confers them strong non-fouling properties not allowing aggregate. The XRD pattern of these NPs (Figure 1c) implied the formation of pure, inverse spinel structure $CoFe_2O_4$, as all diffraction peaks at 2Θ positions: 18.29 (111), 30.08 (220), 35.44 (311), 43.06 (400), 53.45 (422), 56.97 (511) 62.59 (440), and 74.01 (533) match well with the standard polycrystalline $CoFe_2O_4$ diffraction data summarized in the PDF Card No. 00.022-1086. The average size of as-grown Nps, calculated by the Scherrer formula [26] from the (311) XRD line broadening ~ 6.0 nm, it is a close proximity to the one calculated from the TEM data (5.8 nm, Figure 1b).

Magnetization measurements were further performed to evaluate the gold deposition onto the surface of cobalt ferrite NPs. Figure 1d shows the room-temperature magnetization plots as a function of applied magnetic field for $CoFe_2O_4$@Met NPs before (1) and after (2) their sonication in the chloroauric acid solution. It was found that the saturation magnetization value of

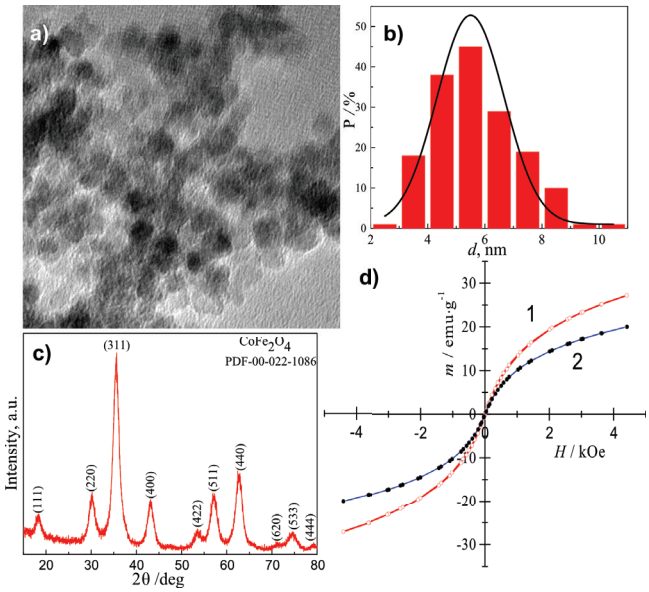

Figure 1: a) TEM image of cobalt ferrite NPs synthesized hydrothermally in a solution containing 25.0 mmol·L^{-1} $CoCl_2$, 50 mmol·L^{-1} $FeCl_3$, 0.2 mol·L^{-1} methionine, and NaOH to pH 12.4 at 130 °C for 10 h. The size distribution histogram and XRD pattern of the as-formed NPs are shown in panels b) and c), respectively. In panel d) the magnetic responses of as-formed (1) and sonicated NPs in a 10 mmol·L^{-1} $HAuCl_4$ solution, kept at a pH 12.2, at 37 °C for 4 h (2) are presented.

$CoFe_2O_4$@Met NPs decreases from 27 to 21 emu·g^{-1} (at H_{max} = 4.4 kOe) upon sonication supporting the claim that gold species are deposited but the NPs remain superparamagnetic. The high-resolution TEM image of the $CoFe_2O_4$@Met NPs after gold deposition with methionine and the EDX spectrum of these NPs are shown in Figure 2.

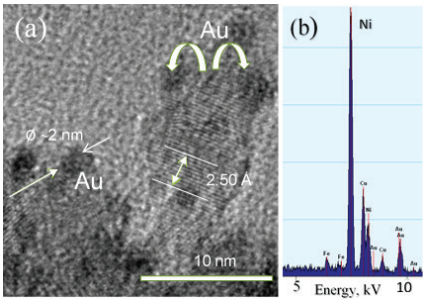

Figure 2: HRTEM image of $CoFe_2O_4$@Met NPs after sonication in 15 mmol·L^{-1} $HAuCl_4$ solution at 37 °C for 4 h (a) and their EDX spectrum (b).

The HRTEM image shows the formation of numerous gold species at the surface of methionine-stabilized $CoFe_2O_4$@Met NPs. In accordance with HRTEM image and EDX spectrum, the ICP-MS analysis of the gold plating solution performed before and after 30 min of sonication of the NPs indicated the reduction of ca. 99.3% of gold ions. From the HRTEM inspection, however, it was difficult to determine the size distribution of the attached gold species, although some of them seemed to be spherical with a diameter of ca. 2.0 nm. More precise results were obtained by the determination of the size of gold species that were removed from the NP surface by the ultrasonic agitation of 10 mg $CoFe_2O_4$@Met/Au NPs probe in 10 mmol·L^{-1} methionine solution. As a result a reddish-pink solution was obtained after 20 min processing (see inset in Figure 3). This process is most likely due to the stronger capping of Au NPs with methionine molecules than with $CoFe_2O_4$@Met/Au NPs. Note that no fluorescence was seen under UV and blue-light excitation of this solution. Typical UV–vis absorption spectra of aqueous methionine, tetrachlorauric acid and gold species solution are shown in Figure 3.

The pure methionine solution does not exhibit any absorption peaks in the measured spectral range. For the chloroauric acid

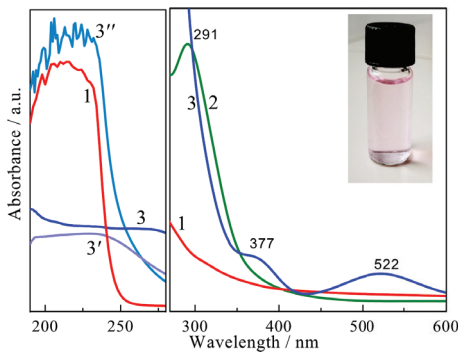

Figure 3: Absorption spectra of methionine (1), tetrachlorauric acid (2) and reddish-pink colored solution of gold species (inset) collected from the $CoFe_2O_4$@Met–Au nanoparticles initially (3) and after dilution to one half (3′) and to on quarter (3″).

solution, however, a clearly resolved absorption peak at 291 nm is observed. The UV–vis absorption spectrum of the solution containing the gold species collected from the surface of the cobalt ferrite NPs (Figure 3, plot 3) exhibits two absorption shoulders at 522 and 377 nm. The former seems to be originated from the surface plasmon absorption of metallic Au [27-29]. The position of this band mainly depends on the size of Au species [30]. So the absorption position of this peak indicates that the size of the methionine-stabilized gold species is extremely small. This assumption was further verified by AFM of gold species spread on a freshly cleaved mica substrate (Figure 4a).

According to these investigations, the shape and size of gold species attached to the surface of magnetic NPs were estimated. The vast majority of species are 1–2 nm sized gold quantum dots (QDs) (Figure 4b). Control experiments demonstrated that the gold species detached from the surface of magnetic NPs coalesced upon dilution of the analyzed Au@Met solution. Consequently, it can be assumed that a significant part of the NPs larger than 2–3 nm are coalesced ultra-small gold QDs.

The state of gold species formed and attached to the surface of methionine-stabilized cobalt ferrite NPs was also investigated using X-ray photoelectron spectroscopy (XPS). The surface chemical composition of the $CoFe_2O_4$@Met–Au NPs is presented in Table 1, whereas the typical core-level spectrum of the deposited gold is presented in Figure 5. As shown, the main Au $4f_{7/2}$ photoelectron peak is located at a binding energy (BE)

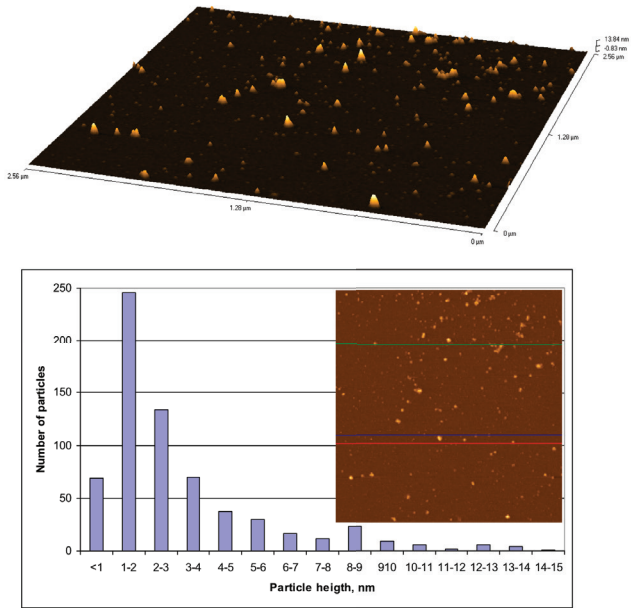

Figure 4: a) AFM 3D image and b) size distribution histogram b) of Au species removed from the surface of $CoFe_2O_4$@Met–Au NPs.

Table 1: Elemental composition of $CoFe_2O_4$@Met–Au NPs.

name	peak BE (eV)	FWHM (eV)	peak area (arb. un.)	atom %
Au 4f	83.94	1.96	12435.07	1.39
C 1s	284.87	2.88	18041.56	36.02
N 1s	399.98	2.24	2647.25	3.02
O 1s	530.21	3.03	55974.26	40.37
Fe 2p	710.75	3.70	63210.72	12.68
Co 2p	780.67	3.29	36815.35	6.47

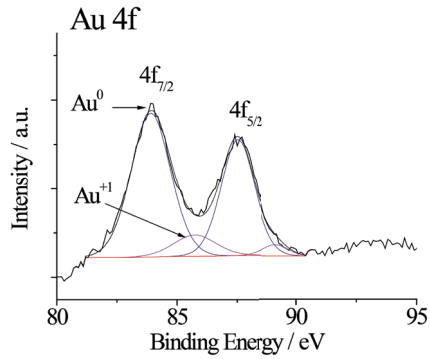

Figure 5: Deconvoluted X-ray photoelectron spectrum (XPS) of Au 4f.

value of 83.94 eV, typical of pure metallic Au^0 species [31]. The fitting of the Au 4f core-level spectrum is performed further by using two spin–orbit split Au $4f_{7/2}$ and Au $4f_{5/2}$ components, separated by 3.56 eV. Surprisingly, the Au 4f curve fitting shows an additional shoulder peaked at 85.74 eV indicating the presence of Au^+ species [31,32]. Their relative distribution reveals a fraction of about 13.7% of Au^+ on the NPs surface of the total deposited gold content of 1.39% (Table 1). It is noticeable that plasmonic gold NPs upon excitation with nanosecond laser light the wavelength of which corresponds to the maximum absorption peak can create hot electrons in the conductive band of gold and, as a result, generate especially active singlet oxygen ($^1O_2$), $^{\cdot}OH$ and O_2^- [33,34].

FTIR spectra

Figure 6 compares the infrared spectra of cobalt ferrite NPs grown via the methionine-assisted hydrothermal approach, and methionine as well as methionine sulfoxide. The FTIR spectrum of the same NPs sonicated in an aqueous solution of chloroauric acid at 37 °C for 4 h is presented. The characteristic peaks of methionine are at 1582 cm^{-1}, assigned to antisymmetric ν_{as}(COO) and symmetric ν_s(COO) stretching vibrations of the COO^- group, whereas the bands in the spectral region of 1277–1341 cm^{-1} are due to the coupled vibration of CH_2 antisymmetric deformation and CH deformation modes [35,36]. According to the literature data [27], the band at 1516 cm^{-1} is

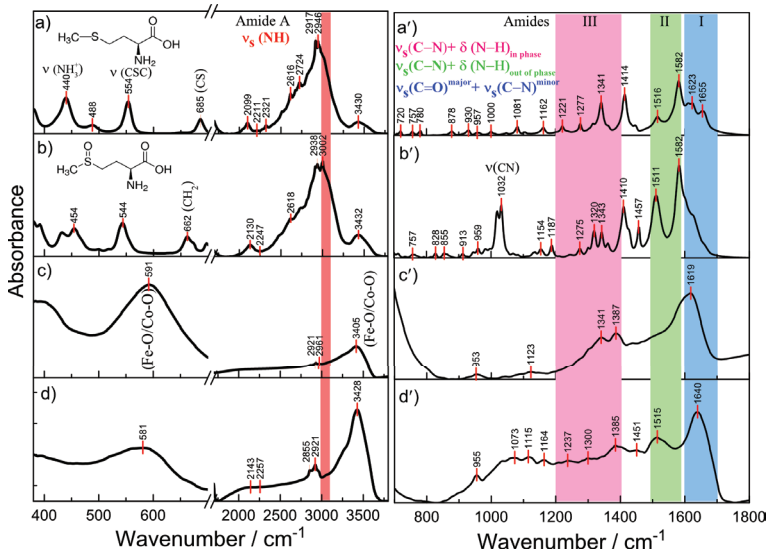

Figure 6: FTIR spectra of methionine (a, a′), methionine sulfoxide (b, b′), cobalt ferrite NPs stabilized with methionine (c, c′), and the same NPs after decoration with gold (d, d′) within the indicated wavenumbers.

associated with the symmetric deformation vibration of NH_3^+, $\delta_s(NH_3)$. Besides, the typical methionine S–C stretching mode at 685 cm^{-1} [37,38] and a clear resolved C–S–C stretching mode, ν(CSC), peaked at 554 cm^{-1} [39] are present in the spectrum. In the FTIR spectra of methionine and methionine sulfoxide a broad and strong band peaked at 2950–3002 cm^{-1} belongs to the symmetric stretching of NH_3^+ ions [40]. In the spectrum of Co ferrite NPs, presented in Figure 6c, the intense and broad band peaked at 591 cm^{-1} belongs to Fe–O/Co–O stretching vibrations in the tetrahedral metal complex [41]. The broad band, peaked near 1515 cm^{-1}, belongs to $\delta_s(NH_3)$ mode and is indicative of the presence of charged amino groups [35,37]. The symmetric C–H deformation mode is also observed at 1341 cm^{-1} in the FTIR spectra of both pure methionine and $CoFe_2O_4$@Met. The attachment of methionine molecules during the synthesis of NPs can also be proven by the presence of the vibration modes in the frequency range of 2961–2855 cm^{-1}, attributable to the symmetric stretching of NH_3^+ ions [42]. The frequency of $\nu_s(COO)$ downshifts from 1414 to 1387 cm^{-1} upon stabilization of ferrite NPs with methionine molecules. The band near 1515 cm^{-1}, however, can only be seen in the $CoFe_2O_4$@Met FTIR spectrum after sonication of NPs in the chloroauric acid-containing solution. The well-resolved band peaked at 1385 cm^{-1} is also characteristic for the FTIR spectrum of NPs after their sonication in the chloroauric acid solution (Figure 6d). As has been previously reported, such frequency downshift is due to the direct interaction of the carboxylate group of the amino acid with the NP surface [43]. We also suspect that the appearance of the significantly stronger symmetric vibration mode in the FTIR spectrum of gold decorated NPs at 1515 cm^{-1} due to cooperative vibrations of $–CH_3$ and $–NH_2$ groups is indicative of the oxidation of methionine to methionine sulfoxide. However, this mechanism requires more specific evidence and needs to be studied.

Conclusion

Superparamagnetic methionine-coated cobalt ferrite nanoparticles with an average size of ca. 6 nm were hydrothermally synthesized via co-precipitation. Then the stabilizing shell of methionine molecules attached to Np surface was successfully applied for the reduction of the chloroauric acid. The formation of ultra-small Au^0/Au^+ QDs with a mean size of ca. 1.5 nm at the surface of magnetic NPs, which retains their magnetic, binding and conjugation properties, has been confirmed by HRTEM, AFM, XPS and magnetic investigations. Contrary to the previous works reported on the formation of Au^0 nanoparticulate shells with thicknesses above 10 nm, we obtained numerous Au^0/Au^+ QDs at the surface of magnetic NPs stabilized with a biocompatible methionine shell. In this way, the initial saturation magnetization of the $CoFe_2O_4$@Met NPs (ca. 27 emu·g^{-1}) decreased by ca. 22%. Besides, the formation of more than 13.5% of extremely active Au^+ species of the total gold content at the surface can have a dramatic effect on the formation of the surface protein corona in the bloodstream that affects $CoFe_2O_4$@Met–Au NPs passive targeting and uptake into tumor cells.

The elaborated functionalization of magnetic NPs with gold QDs represents a promising multi-task platform for linking magnetic NPs with specific targeting ligands, such as aptamers and antibodies. This synthesis way may also be explored in future to design superparamagnetic, methionine-stabilized plasmonic magnetite NPs decorated with Au^0/Au^{+1} QDs.

Experimental

Chemicals: All chemicals, including Co(II) and Fe(III) chlorides, and $HAuCl_4·4H_2O$ were of analytical grade, purchased from Aldrich and used without further purification. NaOH was purchased from Poch SA (Poland) and purified by preparation of a saturated solution, which lead to crystallization of other sodium salts. D,L-methionine (99% purity) and D,L-methionine sulfoxide (≥99.0% purity) were purchased from Sigma-Aldrich Co. Distilled water was used throughout the experiments.

Synthesis of Co-ferrite nanoparticles: Superparamagnetic cobalt ferrite nanoparticles were synthesized by a hydrothermal approach in an alkaline solution (40 mL) of Co(II) and Fe(III) chlorides, at a molar ratio 1:2, at 130 °C for 10 h using a 10 K·min^{-1} ramp. The total metal salt concentration was 75 mmol·L^{-1}. Methionine (0.2 mol·L^{-1}) was used as the reducing and capping additive. The pH value of the solution was kept at 12.4 by addition of 2.0 mol·L^{-1} NaOH solution. The required quantity of NaOH solution was determined by an additional blank experiment. In the subsequent experiment, this quantity was placed in the reactor, and mixed with the other components, during several seconds under vigorous stirring. The as-grown products were collected by centrifugation at 8500 rpm for 3 min and carefully rinsed 5 times using fresh portions (10 mL) of H_2O. Afterwards, the NPs were dried at 60 °C. The collected NPs were studied and subjected to further processing within the following two days.

Gold deposition: The deposition of gold onto the Co ferrite surface was carried out through the methionine-induced chemical reduction of $HAuCl_4$. Briefly, 3.5 mL of NP solution was diluted to 5 mL under ultrasonic agitation for 10 min and 2.0 mL of $HAuCl_4$ (10 mmol·L^{-1}) was introduced into the reaction medium under ultrasound agitation. The solution was alkalized to the required pH value by addition of 2.0 mol·L^{-1} NaOH under vigorous stirring. The deposition process was performed at 37 °C for 4 h under mild mixing conditions. The products ob-

tained were collected by magnetic separation, carefully rinsed several times with deionized water and re-dispersed in ethanol for further examinations. For TEM observations, a drop of NPs suspension was placed onto a lacey grid, whereas for FTIR and magnetic investigations the suspension was dried at 60 °C.

Analysis: The concentration of gold remaining in the deposition solution was determined by inductively coupled plasma mass spectrometry. Measurements were made on emission peaks at λ_{Au} = 267.595 nm, λ_{Au} = 242.795 nm, λ_{Co} = 228.616 nm and λ_{Fe} = 238.204 nm using an OPTIMA 7000DV (Perkin Elmer, USA) spectrometer. Calibration curves were made using dissolved standards (1 to 50 ppm) in the same acid matrix as the unknown samples.

Characterization: The morphology of as-grown products was investigated using a transmission electron microscope (TEM, model MORGAGNI 268) operated at an accelerating voltage of 72 keV. The average size of nanoparticles was estimated from at least 150 species observed in the TEM images. High-resolution transmission electron microscopy (HRTEM) studies of as-synthesized products were performed using a LIBRA 200 FE at an accelerating voltage of 200 keV. X-ray powder diffraction experiments were performed on a D8 diffractometer (Bruker AXS, Germany), equipped with a Göbel mirror as a primary beam monochromator for Cu Kα radiation. Upgraded vacuum generator (VG) ESCALAB MKII spectrometer, fitted with a new XR4 twin anode, was used for XPS investigations. The non-monochromatised Mg Kα X-ray source was operated at $h\nu$ = 1253.6 eV with 300 W power (20 mA/15 kV) and the pressure in the analysis chamber was lower than 5×10^{-7} Pa during spectral acquisition. The spectra were acquired with an electron analyzer pass energy of 20 eV and resolution of 0.05 eV and with a pass energy of 100 eV. All spectra were recorded at a 90° take-off angle and the binding energies (BE) scale was calibrated by measuring of the C 1s peak at 284.6 eV. The spectra calibration, processing and fitting routines were done using Avantage software (5.918) provided by Thermo VG Scientific. Core-level peaks of Fe 2p, Co 2p, Au 4f, C 1s and O 1s were analyzed using a nonlinear Shirley-type background and the calculation of the elemental composition was performed on the basis of Scofield's relative sensitivity factors. The FTIR spectra were recorded in transmission mode with a Bruker Vertex 70v vacuum FTIR spectrometer over the wavenumber range of 4000–400 cm^{-1}. A 7 mm thick KBr discs were prepared under high pressure by mixing the powdered samples with KBr powder. Samples for AFM measurements were prepared by casting a drop (20 µL) of gold NP solution on freshly cleaved V-1 grade muscovite mica (SPI supplies, USA). The drop of solution was removed after 60s by spinning the sample at 1000 rpm. The commercially available atomic force microscope (AFM) diInnova (Veeco instruments inc., USA) was used to take three-dimensional (3D) images of gold nanoparticles. TESPA-V2 cantilevers (Veeco Instruments Inc., USA) with a tip curvature of 8 nm were used. Measurements were performed in the tapping mode in air. Images were acquired at the scan rate of 1 Hz per line with the 512 × 512 pixel image resolution. Image processing included flattening (2nd order) to remove the background slope caused by the irregularities of the piezoelectric scanner. The analysis was performed using the SpmLabAnalysis software (Veeco Instruments Inc., USA).

Magnetization measurements were accomplished using a vibrating-sample magnetometer calibrated by a Ni sample of similar dimensions as the studied sample. The magnetometer was composed of the vibrator, the lock-in amplifier, and the electromagnet. The magnetic field was measured by a testameter FH 54 (Magnet-Physics Dr. Steingrover GmbH).

Acknowledgements

The authors are thankful to Drs. Saulius Tumėnas, Vitalija Jasulaitiene, Kęstutis Mažeika, and Vilius Poderys for FTIR and XPS spectra, magnetic measurements and AFM tests, respectively.

References

1. Demirer, G. S.; Okur, A. C.; Kizilela, S. *J. Mater. Chem. B* **2015,** *3,* 7831–7849. doi:10.1039/C5TB00931F
2. Acharaya, A. J. *Nano Sci. Nano Technol.* **2013,** *13,* 3753–3768. doi:10.1166/jnn.2013.7460
3. Mashhadizadeh, M. H.; Amoli-Diva, M. *J. Nanomed. Nanotechnol.* **2012,** *3,* 2–8. doi:10.4172/2157-7439.1000139
4. Viswanathan, K. *Colloids Surf., A* **2011,** *386,* 11–15. doi:10.1016/j.colsurfa.2011.06.017
5. Lu, H.; Yi, G.; Zhao, S.; Chen, D.; Guo, L.-H.; Chen, J. *J. Mater. Chem.* **2004,** *14,* 1336–1341. doi:10.1039/b315103d
6. Salgueiriño-Maceira, V.; Correa-Duarte, M. A.; Spasova, M.; Liz-Marzán, L. M.; Farle, M. *Adv. Funct. Mater.* **2006,** *16,* 509–514. doi:10.1002/adfm.200500565
7. Cai, H.; Li, K.; Shen, M.; Wen, S.; Luo, Y.; Peng, C.; Zhang, G.; Shi, X. *J. Mater. Chem.* **2012,** *22,* 15110. doi:10.1039/c2jm16851k
8. An, P.; Zuo, F.; Li, X.; Wu, Y.; Zhang, J.; Zheng, Z.; Ding, X.; Peng, Y. *Nano* **2013,** *8,* 1350061. doi:10.1142/S1793292013500616
9. Wu, A.; Ou, P.; Zeng, L. *Nano* **2010,** *05,* 245–270. doi:10.1142/S1793292010002165
10. Deng, Y.-H.; Wang, C.-C.; Hu, J.-H.; Yang, W.-L.; Fu, S.-K. *Colloids Surf., A* **2005,** *262,* 87–93. doi:10.1016/j.colsurfa.2005.04.009
11. Larsen, B. A.; Haag, M. A.; Serkova, N. J.; Shroyer, K. R.; Stoldt, C. R. *Nanotechnology* **2008,** *19,* 265102. doi:10.1088/0957-4484/19/26/265102
12. Cui, Y.; Wang, Y.; Hui, W.; Zhang, Z.; Xin, X.; Chen, C. *Biomed. Microdevices* **2005,** *7,* 153–156. doi:10.1007/s10544-005-1596-x
13. Tamer, U.; Gündoğlu, Y.; Boyacı, İ. H.; Pekmez, K. *J. Nanopart. Res.* **2010,** *12,* 1187–1196. doi:10.1007/s11051-009-9749-0

14. Fan, Z.; Shelton, M.; Singh, A. K.; Senapati, D.; Khan, S. A.; Ray, P. C. *ACS Nano* **2012,** *6,* 1065–1073. doi:10.1021/nn2045246
15. Chen, M.; Yamamuro, S.; Farrell, D.; Majetich, S. A. *J. Appl. Phys.* **2003,** *93,* 7551–7553. doi:10.1063/1.1555312
16. Brown, K. R.; Walter, D. G.; Natan, M. J. *Chem. Mater.* **2000,** *12,* 306–313. doi:10.1021/cm980065p
17. Jagminas, A.; Mažeika, K.; Kondrotas, R.; Kurtinaitienė, M.; Jagminienė, A.; Mikalauskaitė, A. *Nanomater. Nanotechnol.* **2014,** *4,* 11. doi:10.5772/58453
18. Mikalauskaitė, A.; Kondrotas, R.; Niaura, G.; Jagminas, A. *J. Phys. Chem. C* **2015,** *119,* 17398–17407. doi:10.1021/acs.jpcc.5b03528
19. Belachew, N.; Rama Devi, D.; Basavaiah, K. *J. Mol. Liq.* **2016,** *224,* 713–720. doi:10.1016/j.molliq.2016.10.089
20. Sun, C.; Zhou, R.; Jianan, E.; Sun, J.; Su, Y.; Ren, H. *RSC Adv.* **2016,** *6,* 10633–10640. doi:10.1039/C5RA22491H
21. Coelgo, B. C. P.; Siqueira, E. R.; Ombredane, A. S.; Joanitti, G. A.; Chaves, S. B.; da Silva, S. W.; Chaker, J. A.; Longo, J. P. F.; Azevedo, R. B.; Morais, P. C.; Sousa, M. H. *RSC Adv.* **2017,** *7,* 11223–11232. doi:10.1039/C6RA27539G
22. Kim, D. K.; Zhang, Y.; Voit, W.; Rao, K. V.; Muhammed, M. *J. Magn. Magn. Mater.* **2001,** *225,* 30–36. doi:10.1016/S0304-8853(00)01224-5
23. Berry, C. C.; Wells, S.; Charles, S.; Curtis, A. S. G. *Biomaterials* **2003,** *24,* 4551–4557. doi:10.1016/S0142-9612(03)00237-0
24. Žalnėravičius, R.; Paškevičius, A.; Mažeika, K.; Jagminas, A. *Appl. Surf. Sci.* **2017,** submitted.
25. Massart, R. *IEEE Trans. Magn.* **1981,** *17,* 1247–1248. doi:10.1109/TMAG.1981.1061188
26. Guinier, A.; Lorrain, P.; Lorrain, D. S.-M. X-Ray Diffraction. *Crystals, Imperfect Crystals and Amorphous Bodies;* Freeman, W. H. & Co.: San Francisco, CA, U.S.A., 1963; p 356.
27. Hains, W.; Thanh, N. T. K.; Aveyard, J.; Fernig, D. G. *Anal. Chem.* **2007,** *79,* 4215–4221. doi:10.1021/ac0702084
28. Amendola, V.; Meneghetti, M. *J. Phys. Chem. C* **2009,** *113,* 4277–4285. doi:10.1021/jp8082425
29. Njoki, P. N.; Lim, I-I. S.; Mott, D.; Park, H. Y.; Khan, B.; Mishra, S.; Sujakumar, R.; Luo, J.; Zhong, C.-J. *J. Phys. Chem. C* **2007,** *111,* 14664–14669. doi:10.1021/jp074902z
30. Wang, L.; Luo, J.; Fan, Q.; Suzuki, M.; Suzuki, I. S.; Engerlhard, M. H.; Lin, Y.; Kim, N.; Wang, J. Q.; Zhong, C.-J. *J. Phys. Chem. B* **2005,** *109,* 21593–21601. doi:10.1021/jp0543429
31. Moulder, J. F.; Stickle, W. F.; Sobol, P. E.; Bomben, K. D. In *Handbook of X-Ray Photoelectron Spectroscopy;* Chastain, J.; King, R. C., Eds.; Physical Electronics: Eden Prairee, MN, U.S.A., 1995.
32. Venezia, A. M.; Pantaleo, G.; Longo, A.; Di Carlo, G.; Casaletto, M. P.; Liotta, L.; Deganello, G. *J. Phys. Chem. B* **2005,** *109,* 2821–2827. doi:10.1021/jp045928i
33. Misawa, M.; Takahashi, J. *Nanomedicine* **2011,** *7,* 604–614. doi:10.1016/j.nano.2011.01.014
34. Zhang, W.; Li, Y.; Niu, J.; Chen, Y. *Langmuir* **2013,** *29,* 4647–4651. doi:10.1021/la400500t
35. Ito, A.; Honda, H.; Kobayashi, T. *Cancer Immunol. Immunother.* **2006,** *55,* 320–328. doi:10.1007/s00262-005-0049-y
36. Saha, K.; Agasti, S. S.; Kim, C.; Li, X.; Rotello, V. M. *Chem. Rev.* **2012,** *112,* 2739–2779. doi:10.1021/cr2001178
37. Abadeer, N. S.; Murphy, C. J. *J. Phys. Chem. C* **2016,** *120,* 4691–4716. doi:10.1021/acs.jpcc.5b11232
38. Paiva, F. M.; Batista, J. C.; Rego, F. S. C.; Lima, J. A., Jr.; Freire, P. T. C.; Melo, F. E. A.; Mendes Filho, J.; de Menezes, A. S.; Nogueira, C. E. S. *J. Mol. Struct.* **2017,** *1127,* 419–426. doi:10.1016/j.molstruc.2016.07.067
39. Wolpert, M.; Hellwig, P. *Spectrochim. Acta, Part A* **2006,** *64,* 987–1001. doi:10.1016/j.saa.2005.08.025
40. Pandiarajan, S.; Umadevi, M.; Briget Mary, M.; Rajaram, R. K.; Ramakrishnan, V. *J. Raman Spectrosc.* **2004,** *35,* 907–913. doi:10.1002/jrs.1224
41. Safi, R.; Ghasemi, A.; Shoja-Razavi, R.; Tavousi, M. *J. Magn. Magn. Mater.* **2015,** *396,* 288–294. doi:10.1016/j.jmmm.2015.08.022
42. Zor, S.; Kandemirli, F.; Bingul, M. *Prot. Met. Phys. Chem. Surf.* **2009,** *45,* 46–53. doi:10.1134/S2070205109010079
43. Dagys, M.; Lamberg, P.; Shleev, S.; Niaura, G.; Bachmatova, I.; Marcinkeviciene, L.; Meskys, R.; Kulys, J.; Arnebrant, T.; Ruzgas, T. *Electrochim. Acta* **2014,** *130,* 141–147. doi:10.1016/j.electacta.2014.03.014

License and Terms

The definitive version of this article is the electronic one which can be found at:
doi:10.3762/bjnano.8.174

3 publikacija / 3th publication

Green synthesis of red-fluorescent gold nanoclusters. Characterization and application for breast cancer detection.

Mikalauskaitė A., Karabanovas V., Karpicz R., Rotomskis R. ir Jagminas A.,

Biointerface Research in Applied Chemistry, 2016, 6, 1702 – 1709

Perspausdinama *OPEN ACCESS JOURNALS* priegą.
Publikaciją galite rasti adresu:
https://biointerfaceresearch.com/?page_id=1657

d-fluorescent gold nanoclusters: characterization and cancer detection

gy

Vitalijus Karabanovas
National Cancer Institute

gy

Ricardas Rotomskis
Vilnius University

Volume 6, Issue 6, 2016, 1702 - 1709 **ISSN 2069-5837**

Biointerface Research in Applied Chemistry

www.BiointerfaceResearch.com

Original Research Article **Open Access Journal**

Received: 20.10.2016 / Revised: 07.11.2016 / Accepted: 08.11.2016 / Published on-line: 09.11.2016

Green synthesis of red-fluorescent gold nanoclusters: characterization and application for breast cancer detection

Agnė Mikalauskaitė [1], Vitalijus Karabanovas [2], Renata Karpicz [3], Ričardas Rotomskis [2], Arūnas Jagminas[1,]*

[1] Department of Electrochemical Material Science, Center for Physical Sciences and Technology, Vilnius, Lithuania
[2] Biomedical Physics Laboratory, National Cancer Institute, Vilnius, Lithuania
[3] Department of Molecular Compound Physics, Center for Physical Sciences and Technology, Vilnius, Lithuania

*corresponding author e-mail address: ***arunas.jagminas@ftmc.lt***

ABSTRACT

The use of biocompatible precursors for the synthesis and stabilization of fluorescent gold nanoclusters (NCs) with strong red photoluminescence creates an important link between natural sciences and nanotechnology. Herein, we report for the first time the cost-effective synthesis of Au nanoclusters by templating and reduction of chloroauric acid with the cheap amino acid food supplements. This synthesis under the optimized conditions leads to formation of biocompatible Au NCs having good stability and intense red photoluminescence, peaked at 680 to 705 nm, with a quantum yield (QY) of ≈7% and average lifetime of up to several µs. The composition and luminescent properties of the obtained NCs were compared with ones formed via well-known bovine serum albumin reduction approach. Our findings implied that synthesized Au NCs tend to accumulate in more tumorigenic breast cancer cells (line MDA-MB-213) and after dialysis can be prospective for bio imagining.

Keywords: *gold nanoclusters, proteins, materials chemistry, red-photoluminescence, bio imaging.*

1. INTRODUCTION

In the past decade, ultra-small gold nanoparticles (USNps) [1], 1 to 3 nm in size, and nanoclusters (NCs) [2], ≤ 1.5 nm in size, have received a great deal of attention because they can exhibit strong photoluminescence and, in contrast to semiconducting fluorescent quantum dots, comprised mainly of cadmium selenides and tellurides [3-5], are nontoxic in vivo and biocompatible. It should be noted, however, that to achieve strong photoluminescence of gold NCs and USNps nearly monodisperse size distribution is required because the addition of even one atom can induce significant changes in their properties [5]. Moreover, stable and high purity products free from $AuCl_4^-$ ion inclusions are required for the application of gold USNps and NCs in in vivo bio imaging tests. On the other hand, purification by dialysis and rinsing/centrifugation procedures frequently leads to destruction of surroundings, which stabilize NCs.

To produce Au NCs, the method which involves ablating the material with plasma under high pressure has been reported by Smalley et al. three decades ago [6]. Later, this method has been successfully applied to synthesize close-shell Au_{13}, Au_{55} (n=3) and Au_{147} (n=4) USNps [7]. Schmidt et al. [8] have prepared Au USNps with quite uniform size of 1.4 nm by the reduction of Ph_3PAuCl with highly toxic diborane in benzene. Similarly, 1.5 nm sized gold particles have been obtained by reduction of $AuCl_4^-$ with $NaBH_4$ in aqueous solution containing triphenylphosphine [9]. Numerous syntheses have been also reported for thiol-stabilized gold USNps, namely Au_{25} [10], Au_{38} [11,12], Au_{40} [13], Au_{68} [14], Au_{102} [15,16], Au_{144} [17], Au_{333} [18], and others [19]. To obtain nearly monodisperse Au USNps of 1.3 and 1.6 nm size, Kim et al. suggested the encapsulation in dendrimers by capping the cysteine as a bound ligand around USNps and examined the process in terms of size, composition and environment [20]. The synthesis of biocompatible, red-luminescent gold NCs with emission peak at 640 nm and QY≈6% has been first reported by Ying et al. [21]. The authors used encapsulation of Au(III) ions by thiol groups, present in cysteine residues, in alkaline solution of bovine serum albumin (BSA) and the subsequent reduction. Similarly, for cells bio imagining, Liu et al. [22] successfully prepared water-soluble fluorescent Au NCs capped with dihidrolipoic acid and modified with polyethylene glycol, BSA and streptavidin, demonstrating that these proteins are advantageous as reducing and stabilizing agents. During past several years, Au NCs have been also successfully synthesized using other proteins such as lysozyme [23,24], trypsin [25], pepsin [26], bovine [27] and human insulin [28] and horseradish peroxidase [29]. The formation of fluorescent Au NCs in protein-containing solutions was attributed to complexation of $AuCl_4^-$ ions to Au(I) and the subsequent reduction to Au^0 by tyrosine or tryptophan residues [30] and stabilization with cysteine residues, although exact formation and stabilization mechanisms are still an open question. Recently, the effects of size and amino acid contents in the several suitable proteins, namely bovine serum albumin, lysozyme, trypsin and pepsin, on the fluorescent properties of fabricated Au NCs have been investigated in detail demonstrating that photoluminescence spectrum, emission lifetime and photo stability depended on the concentration ratio of amine and tyrosine/tryptophan-containing residues [31]. It was also presumed that application of multiple proteins containing amine and thiol groups is a prerequisite to obtain stable, well fluorescent product [31]. However, it seems likely that fluorescent properties (intensity and wavelength of emitted light) of Au NCs, fabricated by protein-templating approach, depend also on the source, size and purity of protein, pH of solution applied and concentration

ratio of all reaction counterparts. In addition, due to large molecular weight of proteins, the overall size of fluorescent Au NCs formed and stabilized in protein solutions can attain several tens of nanometres, which makes it difficult to preserve the composition and properties of the shells in in vivo environments. To avoid this problem, Bao et al. [32] reported the formation of blue-fluorescent Au NCs by templating $AuCl_4^-$ ions in the biological small-sized buffer MES and L-ascorbic acid solution. However, in this case the yield of Au NCs was poor due to the concomitant formation of Au Nps.

Herein, we report for the first time the cost-effective synthesis of Au NCs by reduction of chloroauric acid with amino acid food supplement (AAFS) resulting in the formation of stable and biocompatible NCs, with characteristic intense red photoluminescence (PL), peaked at 660 to 705 nm, and average lifetime of up to several μs. We note that application of cheap amino acid cocktails, instead of earlier proposed pure and significantly expensive BSA [21], insulin [27,28] and others, makes this synthesis very attractive. We also found that synthesized Au NCs after dialysis are non-toxic and covered with protein-based shells quite similar with Au@BSA NCs. To assess viability and versatility of synthesized products, in vitro experiments were performed by incubation with two breast cancer cell lines differing in malignancy.

2. EXPERIMENTAL SECTION

2.1. Materials. All tested amino acids (purity ≥ 99.0%) in powder form, glucose and $HAuCl_4$ were purchased from Sigma-Aldrich Co. High quality amino acids food supplement INTRA BCAA'S was purchased from Stockton-on-Tees. Analytical grade NaOH was purchased from Reachem (Slovakia). Ultra-pure water (18 MΩ cm) was obtained using Water purification system and used in all experiments. The pH of the resulting solutions was adjusted by addition of 1.0 M NaOH solution under continuous stirring.

2.2. Synthesis of amino acid-encapsulated gold nanoclusters. In this study, the red-fluorescent gold nanoclusters (AuNCs) were synthesized through the amino acids food supplement (AAFS) templating and reduction of $AuCl_4^-$ in alkaline medium at a physiological temperature of 37 °C. In a typical synthesis, 7 mL of an aqueous solution were prepared by dissolving 0.140 g of AAFS together with $HAuCl_4$ and NaOH to make pH within 10.0 to 13.5. Resulting concentrations of amino acids and $HAuCl_4$ were 5 mg/mL and 3 μM/mL, respectively. After the addition of base, the synthesis reaction was conducted at 37 °C for up to 20 h. Similarly, various mixed compositions of pure amino acids with the total amount of 5 mg/mL with and without various additives, such as glucose, starch and citric acid, were tested. For comparison, bovine serum albumin-encapsulated gold clusters were also synthesized under the same conditions. The resultant clear yellow-coloured Au NCs solutions were examined using high resolution transmission electron microscopy, AFM, UV-vis and fluorescence spectroscopy.

2.3. Spectroscopic characterization of Au NCs. Absorption spectra of investigated Au NCs solutions were measured using the Jasco V670 spectrophotometer. Hellma Optik (Jena, Germany) quartz cuvette with 1 cm length optical path was used for all optical measurements. Photoluminescence spectra and photoluminescence decay kinetics were measured with a time-correlated single photon counting spectrometer Edinburgh-F900 (Edinburg instruments, United Kingdom). A picosecond pulsed diode lasers EPL-375, EPL-405, EPL-470 emitting picosecond duration pulses were used for the excitation. "FAST" software package for the advanced analysis of Au NC FL multi-exponential decay kinetics was used. The stationary photoluminescence properties of the synthesized Au NCs solutions were registered on Cary Eclipse spectrophotometer (Varian Inc., USA). All photoluminescence spectra were corrected for the instrument sensitivity.

The quantum yield (QY) of gold nanoclusters formation was calculated by comparing the fluorescence intensities of the sample to that of a standard laser dye 2-[2-[2-(4-Dimethylamino-phenyl)-vinyl]-6-isopropyl-pyran-4-ylidene]-malononitrile (DCM) in methanol, which QY was 33-34%.

2.4. Live cell imaging and confocal laser scanning microscopy. Human breast cancer cell lines MCF-7 (ECCC No. 86012803) and MDA-MB-231 (ATCC No. HTB-26TM) were purchased from European Collection of Cell Cultures and American Type Culture Collection, respectively. The cells were cultured in Dulbecco's Modified Eagle Medium (DMEM), which was supplemented with 10% fatal bovine serum, 100 U/ml penicillin and 100 mg/ml streptomycin. All media and supplements were purchased from Gibco (UK). Cells were cultured in 25 cm^2 culture dishes in a humidified 37 °C, 5% CO^2 atmosphere and sub cultured twice a week. To evaluate Au NCs accumulation, MCF-7 and MDA-MB-231 cells were plated in 8-well chambered cover-slips (Nunc, USA) at an appropriate density (5 x 104 cells per well) and cultured in a CO_2 incubator for 24 hours. Next day cells were washed three times with phosphate-buffered saline (pH 7.4) (PBS) and treated with 3 mM/L Au NCs for 24 hours. After treatment, MCF-7 and MDA-MB- cells were routinely rinsed 3 times with DME medium and then were analysed by the confocal Nikon Eclipse TE2000 C1 Plus laser scanning microscope equipped with CO2 Microscope Stage Incubation System (OkoLab, Italy). Measurements were done using 60×/1.4 NA oil immersion objective (Plan Apo VC, Nikon, Japan) and 488 nm argon-ion laser. To visualize Au NCs photoluminescence, the 621-755 nm band pass filter was applied. The images were further processed using the EZ-C1 Bronze version 3.80 (Nikon, Japan) and ImageJ 1.41 software (NIH, USA). An Atomic force microscope (Dimension 3100a Nanoscope, Veeco Instruments Inc.) was used to image the fabricated films.

3. RESULTS SECTION

In the first setup, several currently popular amino acid food supplements, namely Anabolic Whey protein (AWP), Natural Whey protein (NWP), 100% Milk Complex (MC), 100% Whey protein professional (WPP), and Branched Amino Acids

supplement (BCAA'S), can be purchased in the market, were tested as reducers of chloroauric acid in an alkaline medium and physiological temperature (37 ºC). It is of note that after 20 h synthesis, the red-fluorescent Au NCs were obtained only in the case of BCAA'S. In all other cases, to obtain even light reddish excitation, the synthesis ought to be continued by week (Fig. 1). Therefore, further investigations were carried out with BCAA'S food supplement.

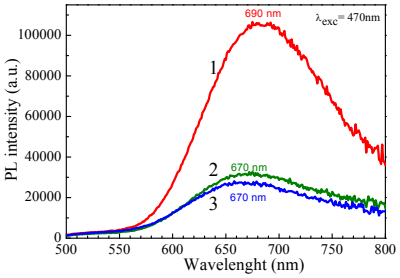

Figure 1. Fluorescence spectra of Au NCs formed from the alkaline (pH=12.0) solutions containing 3 μM/mL $HAuCl_4$ and 20 mg/mL amino acid food supplements: (1) BCAA'S, (2) 100% Milk complex and (3) 100% Whey protein professional after 20 (1) and 200 h (2,3) synthesis at 37 ºC.

In order to find the optimal conditions for the synthesis of Au NCs in the solution of BCAA'S food supplement and $HAuCl_4$ at physiological temperature of 37 ºC, the dependence of PL properties such as intensity and wavelength range of the obtained products on the variation of the content of all precursors and pH was investigated. Figs. 2a and 2b depict the absorption and PL spectra of light yellow coloured solutions obtained after reduction of 3.0 mM/L $HAuCl_4$ with different contents of BCAA'S and pH value, respectively, after 20 h synthesis. Judging from the intensity of red PL it seems that AuNCs with the maximum fluorescence emission in the range between 670 and 690 nm are synthesized in the solution containing 16-20 mg/mL of BCAA'S (Fig. 2a, curves 3 and 4) at pH≈12.0 (Figure 2b, curve 3). If concentration of BCAA'S exceeds 20 mg/mL, the PL intensity of Au NCs decreases and the peak shifts by 10 nm towards higher wavelengths region (Fig. 2a, curve 5). When concentration of BCAA'S was lower than 8 mg/mL, formation of stable Au NCs band was not observed et all. Besides, in contrast to the synthesis of Au NCs from the other reported protein solutions [22-31], only weak red PL in the 660 to 770 nm spectral region was determined for the BCAA'S synthesis products formed in the solutions with pH 10.0 and 11.0 (Fig. 2b, PL spectrum 1). Note that increase of pH to 12.0, resulted in an obvious increase of UV light absorption in the longer wavelengths region (Fig. 2b). However, further increase of pH, resulted in the significant absorption decrease perhaps due to conformational changes of BCAA'S proteins resulting in the spatial redistribution of fluorophores.

Fig. 3a shows photoluminescence excitation spectrum and PL spectra of BCAA'S-mediated Au NCs formed in the optimized solution under various excitation wavelengths. As seen, the PL intensity of the obtained Au@BCAA'S NCs and emission light peak strongly depend on the excitation light decreasing with λ_{exc}. Again, the photoluminescence excitation spectrum of Au NCs solution (λ_{em}=690 nm) has a band at 510 nm and a gradual slope towards the longer wavelength region. In addition, photoluminescence excitation spectrum does not coincide with absorption spectrum of Au@BCAA'S NCs.

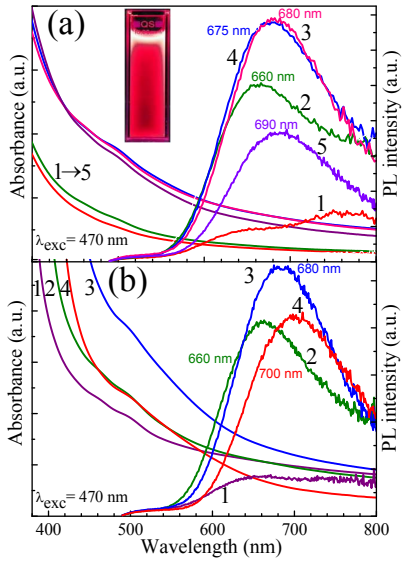

Figure 2. (a) Absorption and PL spectra of Au NCs formed via BCAA'S food supplement-mediated synthesis in the 3.0 μM/mL $HAuCl_4$ solution containing: 8 (1); 12 (2); 16 (3); 20 (4) and 24 (5) mg/mL BCAA'S; all kept at a pH = 12.2 and 37 ºC for 20 h. (b) Absorption and PL spectra of Au clusters fabricated in 3.0 μM/mL $HAuCl_4$ solution containing 20 mg/mL BCAA'S at pH: 11.0 (1); 11.5 (2) 12.0 (3) and 12.5 (4) at 37 ºC for 20 h. λ_{exc}= 470 nm. In the Inset, the colour of fabricated Au NCs under UV irradiation is shown.

The lifetime of red PL of Au@BCAA'S NCs with non-exponential decay typically exceeds several μs (Fig. 3b). Such long lifetimes are not typical for Au NCs fabricated via templating of $AuCl_4^-$ in the similar alkaline solutions using proteins such as BSA [22,24] and others [31] but are close to lifetimes of lipoic acid-protected Au NCs, synthesized recently [33].

It was found that the PL spectrum of BCAA'S-mediated Au NCs solution shifted slightly from the peak position of 705 nm to 680 nm upon dilution and after six fold dilution integral intensity decreased about 14 times (Fig. 4a). It is worth noticing that neutralizing of as-formed Au@BCAA'S NCs solutions by addition of citric acid, blue-shifted the PL peak position only insignificantly, namely about 4.0 nm/pH. At the same time, the PL intensity and lifetime of Au NCs changed only slightly (Fig. 4b and 4c), allowing to expect such photoluminescence lifetimes also after insertion of Au NCs into bio entities for cells imaging.

The quantum yield (QY) of ~7.0% was obtained for red-luminescent Au@BCAA'S NCs fabricated under the optimized conditions. Note that such QY is higher than reported for red-luminescent Au NCs synthesized by BSA protein-directed reduction of chloroauric acid [21]. Furthermore, the obtained in this study Au@BCAA'S NCs typically have photoemission peak position at from 670 to 705 nm, indicating on the inclusion of

Au27-Au29 atoms in each nanocluster, based on the spherical Jellium model [34].

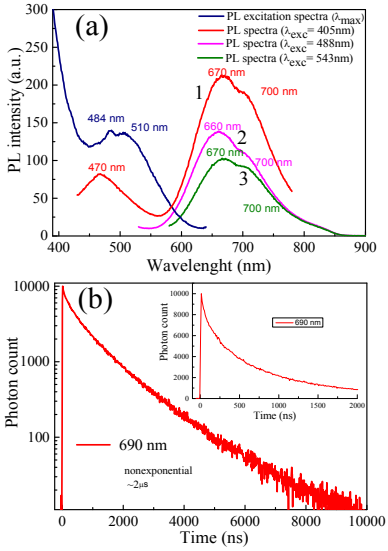

Figure 3. (a) Variation of the PL spectra of BCAA'S-mediated Au NCs formed in the optimized solution with the excitation light wavelength (nm): 405 (1); 488 (2) and 543 (3). (b): Typical photoluminescence intensity decay for BCAA'S-mediated Au NCs at PL band peak position 690 nm.

Fig. 5 depicts variation of absorbance and PL spectra of Au@BCAA'S NCs solution upon dialysis for 24 and 48 hours. As seen, the dialysis results in the significant increase of PL intensity, light absorption decrease and blue-shift of PL spectra peak from 700 nm to 680 nm. The analysis of solutions before and after dialysis have showed that only 42.5% of chloroauric acid was consumed for Au@BCAA'S NCs formation under the optimized synthesis conditions determining a lower PL intensity of these NCs with respect to Au@BSA NCs. However, we found in this study that addition of some amino acids to the synthesis solution of BCAA'S and chloroauric acid can significantly increase or decrease the PL intensity of the synthesized NCs (Fig. 6) and the yield of red-luminescent gold clusters. The most effective influence was obtained using leucine, serine and glutamic acid whereas the addition of cysteine hindered the formation of red luminescent gold NCs. On the other hand, the addition of cysteine resulted in the formation of blue fluorescent gold clusters possessing emission peak at 495 nm (spectrum 5 in Fig. 6).

The AFM topography images of dialyzed Au@BCAA'S NCs and Au@BSA NCs synthesized according to [21], for comparison, are shown in Fig. 7. From these observations, the average size of gold clusters stabilized with BCAA'S is quite similar to ones formed via BSA reduction of chloroauric acid under a same conditions, while the calculated size distribution histograms demonstrated some larger Au@BCAA'S NCs with a main size of 2.7 nm instead of ~2.0 nm [21].

The FTIR spectra of the BCAA'S, BSA and corresponding gold nanoclusters Au@BCAA'S and Au@BSA before and after dialysis were also studied to compare the composition of shells stabilized these NCs. As seen (Fig. 8), the FTIR spectra of Au@BCAA'S and Au@BSA NCs after the complete purification by dialysis for 48 h are quite similar implying on the compositional similarity of shells stabilizing these NCs. The bands corresponding to amide I (CO stretch) in a vicinity of 1658-1643 cm^{-1} and amide II (CN stretch and NH in-plane) band in a vicinity of 1515-1544 cm^{-1} [33] are clearly seen in the spectra of both clustered products.

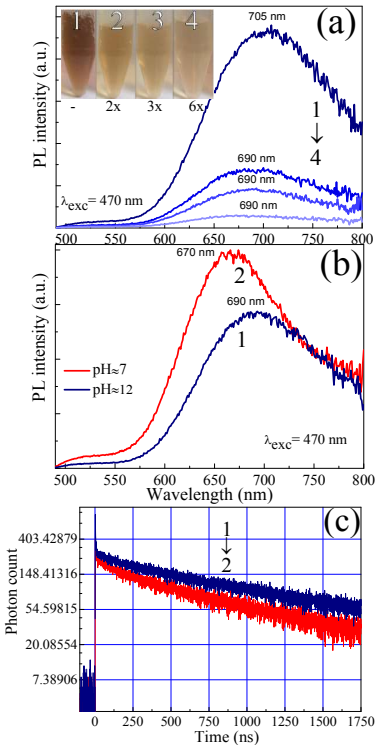

Figure 4. Variation of the PL spectra of 3.0 μM/mL Au NCs solution mediated with 20 mg/mL BCAA'S upon dilution (a) and neutralization (b). The Inset in (a) shows the colour of Au NCs solutions before and after dilution by the extent indicated under solar light illumination. In (c): the emission light intensity decay of corresponding Au NCs (b) solutions under excitation with λ_{exc} of their peak positions.

Besides, in the both cases, the dialysis of NCs results in the more prominent and stronger vibrations of these bands. The exact reasons of this phenomenon is not clear and probably can be linked with more ordering distribution of the corresponding protein residues around gold nanocrystal after dialysis. To the end, the wide vibration band appearing at ~700 cm^{-1} in all samples was assigned to $-NH_2$ and –NH wagging and that of 1398 ± 1 cm^{-1} to C=O stretching of COO-.

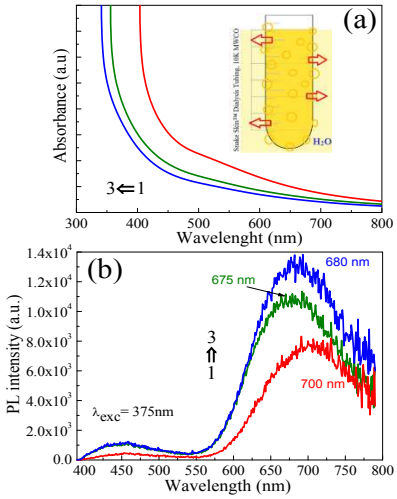

Figure 5. Typical absorption (a) and PL (b) spectra of Au@ BCAA'S clusters before (1) and following the dialysis for 24 h (2) and 48 h (3). λ_{exc}= 470 nm. In the Inset, the scheme of dialysis is shown.

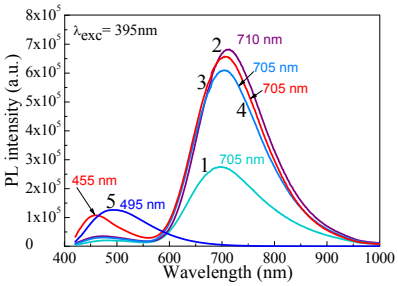

Figure 6. PL spectra of gold clusters fabricated at 37 °C for 20 h in the solution containing 15 mg mL^{-1} BCAA'S and 3.0 μM/mL $HAuCl_4$ without (1) and with addition of 15 mM Leu (2), Ser (3), Glutamic acid (4) and Cis (5).

The data presented in Table 1 revealed a significantly lower concentration of most amino acids (AA), except Ala, Glu and Val, in the BCAA'S additive with respect to ones in other tested herein food supplements can be used for red-photoluminescent Au NCs formation from alkaline medium at physiological temperature of 37 ºC. However, the percentage of branched AA (Leu, Ileu and Val) in the BCAA'S approximated to 30% from the total contamination of all AA, what is about 50% more than in the 100% MC and 100% MPP food supplements.

Again, based on the recent discussion [31], the lower concentration of –S- and –SH containing entities in BCAA'S, as well as Thr and Trp, not allow us to explain the significantly higher efficiency of BCAA'S, with respect to 100% MC and 100% MPP usage.

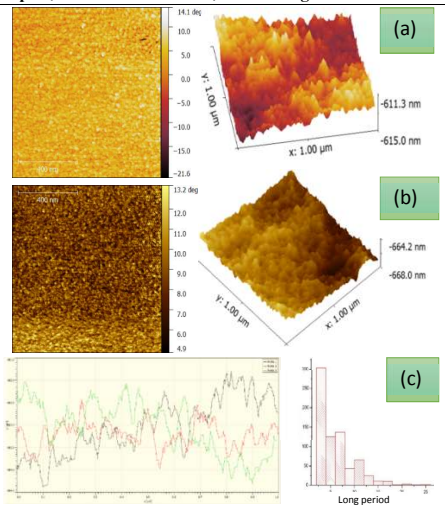

Figure 7. The AFM and 3D deflection images of gold clusters fabricated using food supplement BCAA'S (a) and BSA reducers (b) under a same synthesis and dialysis conditions. In (c) the size distribution histogram calculated from the corresponding profile-grams for Au@BCAA'S NCs (left side) is presented.

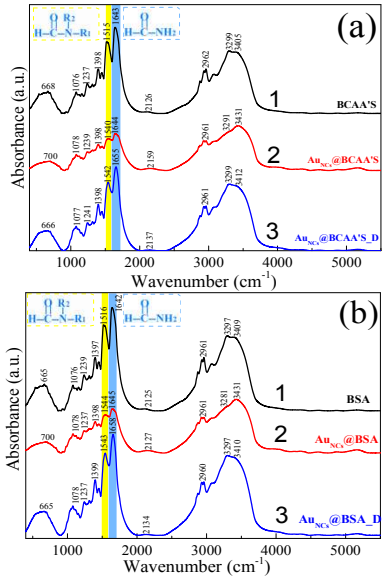

Figure 8. (a) FTIR spectra of pure BCAA'S (1), and BCAA'S-encapsulated Au NCs before (2) and after (3) dialysis. (b) a same for pure BSA protein (1) and Au NCs generated by BSA-encapsulated Au NCs before (2) and after (3) dialysis.

Thence, it can be inferred that other BCAA'S components, such as carbohydrates, could be responsible for the higher reduction

capability of BCAA'S. At a same time, it can be deduced that except –S- and –SH containing AA, others can also stabilize Au NCs bonding via amino groups to gold, as predicted in [31].

To assess which amino acid favoured the formation of red-fluorescent Au NCs, twenty individual amino acids in 0.15 mol/L concentration were incubated each with 3.0 μM/mL $AuCl_4^-$ alkaline solution at pH = 12 and 37^{0}C for 20 hours. The results obtained in these experiments indicated that only in the solution containing histidine amino acid, bluish-green fluorescent Au NCs without larger Au nanoparticles were formed (Fig. 9a, plots 1and 1'). However, the photoluminescence intensity of the obtained Au@histidine NCs solution was exceptionally poor and decayed rapidly (Fig. 9b). Note that similar results were obtained recently by creating fluorescent Au@His NCs capped with molecules of organic fluorescent dye MPA in the acidic solution, emphasizing the crucial role of histidine imidazole group [35].

No red-fluorescent Au NCs were formed by the templating of $AuCl_4^-$ in the alkaline solutions containing single amino acid. On the other hand, the reduction of $AuCl_4^-$ ions to the metallic state was observed in the solutions containing methionine, isoleucine, leucine, alanine, threonine, asparagine, lysine, aspartate and phenylalanine, forming plasmonic Au nanoparticles (Fig. 10 a). The excitation of resulting solutions with UV light resulted mainly in the blue or bluish-green luminescence (Fig. 10b). As from early report [24], this effect could be explained by the formation of exceptionally small Au clusters composed of only several gold atoms.

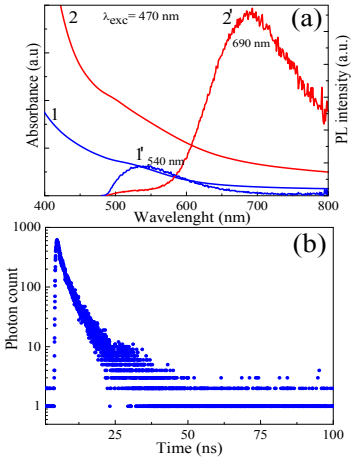

Figure 9. (a) Typical absorption (1, 2) and photoluminescence (1', 2') spectra of gold clusters produced by reduction of 3.0 μmol/mL $HAuCl_4$ in the alkaline medium (pH = 12.0) with 20 mg/mL histidine (1) and 20 mg/mL BCAA'S (2) at 37 ^{0}C for 20 h. (b) Photoluminescence decay plot for Au@histidine NCs under excitation with λ_{exc} = 375 nm light.

Table 1. The contents of indicated amino acids in a 100 g of tested food supplements.

Food supplement	Amino acid																		
	Ala	Arg	Asp	Cys	Glu	Gln	Gly	His	Ileu	Leu	Lys	Met	Phe	Pro	Ser	Thr	Trp	Tyr	Val
100% MC	3.34	1.47	7.63	1.54	-	12.67	0.98	1.19	4.48	7.42	6.72	1.54	2.17	3.92	3.22	4.62	0.98	1.86	4.13
100% WPP	3.37	1.78	7.6	2.06	-	14.7	1.28	1.24	4.7	8.28	7.46	1.6	2.23	4.23	3.73	4.8	1.27	2.36	4.34
BCAA'S	3.99	0.39	2.1	0.49	3.4	-	0.3	0.7	1.34	3.96	2.97	0.38	0.58	1.21	0.96	1.36	0.42	0.52	3.08

In the subsequent experiments, solutions of several mixed amino acids were prepared with 3.0 μM/mL $HAuCl_4$ and NaOH up to pH = 12.0 and left at 37 ºC for 5, 10, 15, 20, 25 and 30 h. The cocktails of amino acids (AA) with the total content of 30.0 mg/mL were composed from the following groups: (A) branched AA (leucine, isoleucine, valine); (B): -S- and –SH groups containing AA (methionine, cysteine), (C): =NH and =N- groups containing AA (histidine, arginine, tryptophan, proline) and (D): two COO- groups containing AA (aspartic, glutamic) at various concentration ratios. In this way, it was found that formation of fluorescent Au NCs in the solutions containing dominant amount of branched AA, e.g. 30%, like in the tested BSAA'S case, proceeds very slowly. The resultant products, even after 30 h long synthesis, demonstrated quite weak photoluminescence in comparison with Au NCs formed in the BCAA'S-containing solution at the same pH and other conditions. Variations in the composition of AA cocktail by increasing the content of sulphur- as well as nitrogen-containing AAs up to 30% resulted mainly in the formation of non-red-fluorescent solutions, implying that other reductants could be responsible for the formation of red-fluorescent Au NCs in the AAFS-templated solutions. With this in mind, the influence of typical carbohydrates such as glucose and sucrose, which are the constituents of food supplement, was also tested herein. From these experiments, it was found that addition of up to 10% of carbohydrates to the synthesis solution composed of histidine and $HAuCl_4$ as well as AA mixture cocktails and $HAuCl_4$ results in the formation of 5 to 6 times more intense bluish-green fluorescence. Further increase in the concentration of glucose and sucrose up to 25% from the total content of AA, with other conditions being the same, led to the formation of more intense blue-fluorescent Au NCs under UV illumination. In these experiments, however, no red-photoluminescent Au NCs were formed. These experimental findings revealed the crucial role of amino acids and carbohydrates in the formation and encapsulation of red-photoluminescent Au NCs. Further investigations are in progress.

Cellular internalization behaviours of our red-luminescent BCAA'S-Au NCs were further visualized by fluorescence confocal microscope imaging in two human breast cancer cell lines with different degree of malignancy. After 24 h, MCF-7 and MDA-MB-231 cells internalized different amounts of Au NCs (Fig. 11).

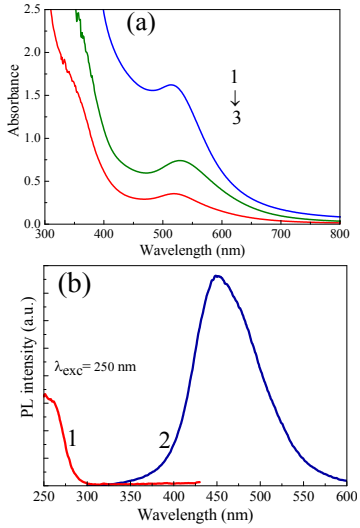

Figure 10. (a): UV-vis absorption spectra of 3.0 µmol/mL $HAuCl_4$ alkaline solutions (pH = 12.0) after 20 h of incubation with 0.15 mM/L alanine (1), threonine (2) and phenylalanine (3) at 37 °C. In (b) excitation (1) and photoluminescence (2) spectra of methionine templated 3.0 µmol/mL $AuCl_4^-$ solution kept at 37 ^{0}C for 20 h. In the Inset (b) the PL colour of as-formed Au NCs under UV illumination is shown.

No detectable intracellular uptake of Au NCs was observed in MCF-7 cells, however numerous bright red luminescent spots illuminating the cell cytoplasm were clearly observed in MDA-MB-231 cells after 1 h of incubation (data not shown) and their amount increased with incubation time (Fig. 11b). The granulated pattern of red photoluminescence of

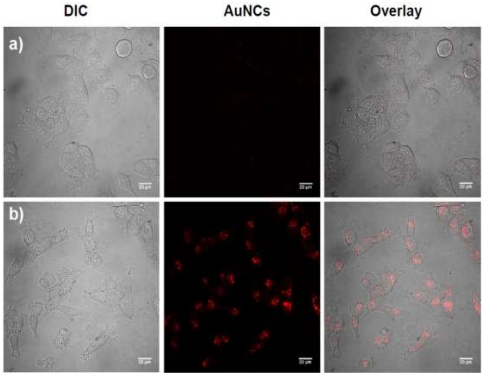

Figure 11. Confocal fluorescence microscopy images of MCF-7 (a) and MDA-MB-231 (b) cells incubated with Au NCs for 24 h. Images were captured in DIC mode and Au NCs channel. Scale bar: 20 µm.

Au NCs present inside MDA-MB-231 cells indicates that Au NCs were trapped in vesicular structures. Our previous studies with negatively charged nanoparticles demonstrated similar intracellular distribution pattern, which means that Au NCs were entrapped in intracellular vesicles and internalized into cells by endocytosis [36,37]. Note, that our recent results well satisfied with ones obtained investigating the accumulation of red-luminescent Au @BSA NCs in tumours MDA-MB-45 and Hela into the nude mice [38] showing the higher fluorescence intensity in the tumour areas after several hours post injection due to enhanced permeability and retention effect [39].

4. CONCLUSIONS

In this study, the formation of red-photoluminescent gold nanoclusters (Au NCs) were studied by the templating of $AuCl_4^-$ alkaline solutions with several food supplements composed of amino acids cocktails. We found that in the case of branched amino acids food supplement, BCAA'S, application the obtained Au NCs are characterized by good stability, intense red photoluminescence, peaked in the vicinity of 690 nm with surprisingly long lifetime attaining several microseconds and high quantum yield. In vitro investigations also implied that fabricated Au NCs tend to accumulate in more tumorigenic breast cancer cells (line MDA-MB-213) and are promising candidates for bio imagining.

The formation of red-photoluminescent Au NCs in the alkaline solutions of $AuCl_4^-$ containing individual amino acid as well as various amino acid cocktails with and without carbohydrates such as sucrose and glucose was also tested herein. In all cases, however, only blue- or bluish-green-emitting Au NCs, if at all, were formed.

We suspect that this study opens new direction for research in the green synthesis of biocompatible Au NCs using cost-effective amino acid food supplements instead of pure proteins and can be useful for future fluorescent nanoclusters technologies.

5. REFERENCES

[1]. Kim B.H., Hackett M.J., Park, J., Hyeon T. Synthesis, Characterization, and Application of Ultra small Nanoparticles, *Chemistry of Materials*, 26, 59-71, **2014**.

[2]. Li Y., Liu S., Yao T., Sun Z., Jiang Z., Huang Y., Cheng H., Huang Y., Jiang Y., Xie Z., Pan G., Yan W., Wei S. Controllable synthesis of gold nanoparticles with ultra-small size and high monodispersed via continuous supplement of precursor, *Dalton Transactions*, 41, 11725-11730, **2012.**

[3]. Zheng Y., Gao S., Jing J. Y. Synthesis and Cell-Imaging Applications of Glutathione-Capped CdTe Quantum Dots, *Advanced Materials*, 19, 376-380, **2007**.

[4]. Hardman R.A Toxicological Review of Quantum Dots: Toxicity Depends on Physicochemical and Environmental Factors, *Environmental Health Perspectives*, 114, 165-172, **2006**.

[5] Gilb S., Weis P., Furche F., Ahlrichs R., Kappes M.M. Structures of small gold cluster cations Ion mobility measurements versus density functional calculations, *The Journal of Chemical Physics*, 116, 4094-4101, **2002.**

[6] Kroto H.W., Heath J.R., O'Brien G.C., Curl R.F., Smalley R.E., C60: Buckminsterfullerene, *Nature*, 318, 162-163, **1985**.

[7] Schmid G. Metal clusters and cluster metals, *Polyhedron*, 7, 2321-2329, **1988.**

[8] Schmid G., Pfeir R., Boese R., Bandermann F., Meyer S., Calis G.H. M., van der Velder, J. W. A. $Au_{55}[P(C_6H_5)_3]_{12}CI_6$ — ein Gold cluster un gewöhnlicher Größe, *Chemische Berichte*, 114, 3634-3642, **1981**.
[9] Weare W.W., Reed S.M., Warner M.G., Hutchison J.E. Improved Synthesis of Small (dCORE ≈ 1.5 nm) Phosphine-Stabilized Gold Nanoparticles, *Journal of the American Chemical Society,* 122, 12890-12891, **2000**.
[10] Schaaff T.G., Whetten R.L. Giant, Gold−Glutathione Cluster Compounds: Intense Optical Activity in Metal-Based Transitions, *The Journal of Physical Chemistry B,* 104, 2630-2641, **2000**.
[11] Pei Y., Gao Y., Zeng X.C. Structural Prediction of Thiolate-Protected Au38: A Face-Fused Bi-icosahedral Au Core, *Journal of the American Chemical Society*, 130, 7830-7832, **2008**.
[12] Toikkanen O., Ruiz V., Ronnholm G., Kalkkinen N., Liljeroth P., Quinn B.M., Synthesis and Stability of Monolayer-Protected Au_{38} Clusters, *Journal of the American Chemical Society,* 130, 11049-11055, **2008.**
[13] Qian H., Zhu Y., Jin R., Isolation of Ubiquitous $Au_{40}(SR)_{24}$ Clusters from the 8 kDa Gold Clusters, *Journal of the American Chemical Society*, 132, 4583-4585, **201.**
[14] Dass A. Mass Spectrometric Identification of $Au_{68}(SR)_{34}$ Molecular Gold Nanoclusters with 34-Electron Shell Closing, *Journal of the American Chemical Society,* 131, 11666-11667, **2009.**
[15] Jadzinsky P.D., Calero G., Ackerson C.J., Bushnell D.A., Kornberg R.D., Structure of a Thiol Monolayer-Protected Gold Nanoparticle at 1.1 Å Resolution, *Science*, 318, 430-433, **2007**.
[16] Levi-Kalisman Y., Jadzinsky P.D., Kalisman N., Tsunoyama H., Tsukuda T., Bushnell, D.A., Kornberg R.D., Synthesis and Characterization of $Au_{102}(p\text{-}MBA)_{44}$ Nanoparticles, *Journal of the American Chemical Society,* 133, 2976-2982, **2011**.
[17] Qian H., Jin R., Controlling Nanoparticles with Atomic Precision: The Case of $Au_{144}(SCH_2CH_2Ph)_{60}$, *Nano Letters*, 9, 4083-4087, **2009.**
[18] Qian H., Zhu Y., Jin R., Atomically precise gold nanocrystal molecules with surface plasmon resonance, *Proceedings of the National Academy of Sciences,* 109, 696-700, **2012.**
[19] Shichibu Y., Negishi Y., Tsunoyama H., Kanehara M., Teranishi T., Tsukada T., Extremely High Stability of Glutathione-Protected Au_{25} Clusters Against Core Etching, *Small*, 3, 835-839, **2007.**
[20] Kim Y.-G., Oh S.-K., Crooks R.M., Preparation and Characterization of 1−2 nm Dendrimer-Encapsulated Gold Nanoparticles Having Very Narrow Size Distributions, *Chemistry of Materials,* 16, 167-172, **2004**.
[21] Xie J., Zheng Y., Ying J.Y., Protein-Directed Synthesis of Highly Fluorescent Gold Nanoclusters, *Journal of the American Chemical Society,* 131, 888-889, **2009.**
[22] Lin,C.-A. J., Yang T.-Y., Lee C.-H., Huang S.H., et al., Synthesis, Characterization, and Bio conjugation of Fluorescent Gold Nanoclusters towards Biological Labelling Applications, *American Chemical Society NANO*, 3, 395-401, **2009.**
[23] Wei H., Wang Z., Yang L., Tian S., Hou C., Lu Y., Lysozyme-stabilized gold fluorescent cluster: Synthesis and application as Hg^{2+} sensor, *Analyst*, 135, 1406-1410, **2010**.
[24] Chen T.-H., Tseng W.-L. (Lysozyme Type VI)-Stabilized Au 8 Clusters: Synthesis Mechanism and Application for Sensing of Glutathione in a Single Drop of Blood, *Small*, 8, 1912-1919, **2012.**
[25] Kawasaki H., Yoshimura K., Hamaguchi H., Arakawa R., *Analytical Sciences*, 27, 591-596, **2011**.
[26] Kawasaki H., Hamaguchi K., Osaka I., Arakawa R., pH-Dependent Synthesis of Pepsin-Mediated Gold Nanoclusters with Blue Green and Red Fluorescent Emission, *Advanced Functional Materials*, 21, 3508-3515, **2011**.
[27] Liu C., Wa H., Hsiao Y., Lai C., Cheng J.-T., Chou P.-T., et al.; Insulin-Directed Synthesis of Fluorescent Gold Nanoclusters: Preservation of Insulin Bioactivity and Versatility in Cell Imaging. *Angewandte Chemie International Edition,* 50, 7056-7060, **2011**.
[28] Garcia A.R., Rahn I., Johnson S., Patel R., Guo J., Orbulescu J., Micic M., Whyte J.D., Blackwelder P., Leblanc R.M., Human Insulin fibril-assisted synthesis of fluorescent gold nanoclusters in alkaline media under physiological temperature, *Colloids and Surfaces B: Biointerfaces*, 105, 167-172, **2013.**
[29] Wen F., Dong Y., Feng L., Wang S., Wang S., Zhang S., Horseradish Peroxidase Functionalized Fluorescent Gold Nanoclusters for Hydrogen Peroxide Sensing, *Analytical Chemistry*, 83, 1193-1196, **2011**.
[30] Xu Y., Pal Choudhury S., Qin Y., Macher T., Bao Y., Make Conjugation Simple: A Facile Approach to Integrated Nanostructures *Langmuir*, 28, 8767-8772, **2012.**
[31] Xu Y., Sherwood J., Gin Y., Crowley D., Bonizzoni M., Bao Y., The role of protein characteristics in the formation and fluorescence of Au nanoclusters, *Nanoscale,* 6, 1515-1524, **2014.**
[32] Wintzinger L., An W., Turner C.H., Bao Y., Synthesis and Modelling of Fluorescent Gold Nanoclusters, *Joshua*, 7, 24-27, **2010**.
[33] Shang L., Stockmar F., Azadfar N., Nienhaus G.U., Intracellular Thermometry by Using Fluorescent Gold Nanoclusters, *Angewandte Chemie International Edition,* 52, 11154-11157, **2013.**
[34] Zheng J., Zhang C.W., Dickson R.M., Highly Fluorescent, Water-Soluble, Size-Tunable Gold Quantum Dots, *Physical Review Letters*, 93, 077402, **2004.**
[35] Chen H., Li B., Wang C., Zhang X., Cheng Z., Dai X., Zhu R., Gu Y. Characterization of a fluorescence probe based on gold nanoclusters for cell and animal imaging, *Nanotechnology,* 24, 055704, **2013**
[36] Karabanovas, V., Zitkus, Z., Kuciauskas, D., Rotomskis, R., Valius, M. Surface Properties of Quantum Dots Define Their Cellular Endocytic Routes, Mitogenic Stimulation and Suppression of Cell Migration, *Journal of Biomedical Nanotechnology*, 10, 775-786, **2014**.
[37] Damalakiene L., Karabanovas V., Bagdonas S., Valius M.,R. Rotomskis R. Intracellular distribution of nontargeted quantum dots after natural uptake and microinjection, *Journal of International Journal of Nanomedicine*, 8, 555-568, **2013.**
[38] Wu X., He X., Wang K., Xie C., Zhou B., Qing Z., Ultrasmall near-infrared gold nanoclusters for tumour fluorescence imaging in vivo, *Nanoscale*, 2244-2249, **2010.**
[39] Choi H.S., Liu W.H., Misra P., Tanaka E., Zimmer J.P., Ipe MG, Bawendi M.G., Frangioni J.V., *Biotechnology,* 25, 1165-1170, **2007**.

4 publikacija / 4th publication

Gold-Coated Cobalt Ferrite Nanoparticles via Methionine Induced Reduction.

Mikalauskaitė A., Kondrotas R., Niaura G. ir Jagminas A.,

Journal of Physical Chemistry C, 2015, 119 (30), 17398–17407.

Publikaciją galite rasti adresu: https://doi.org/10.1021/acs.jpcc.5b03528

THE JOURNAL OF PHYSICAL CHEMISTRY C

Article

pubs.acs.org/JPCC

Gold-Coated Cobalt Ferrite Nanoparticles via Methionine-Induced Reduction

Agnė Mikalauskaitė, Rokas Kondrotas, Gediminas Niaura, and Arūnas Jagminas*

State Research Institute Center of Physical Sciences and Technology, Savanoriu 231, LT-02300 Vilnius, Lithuania

Supporting Information

ABSTRACT: Functionalized superparamagnetic nanoparticles (Nps) are among the most investigated research topics. In this study, we present an efficient protocol for gold deposition onto the surface of cobalt ferrite ($CoFe_2O_4$) Nps by a simple one-pot reduction of $AuCl_4^-$ ions with amino acid methionine, which, in turn, produces the biocompatible stabilizing shell. In contrast to previously reported gold deposition recipes, the one suggested herein is distinguished by the simplicity and prevention of monogold crystallite nucleation and growth in the deposition solution bulk. To demonstrate the preferential deposition of gold onto the surface of ferrite Nps, high-resolution transmission electron microscopy (HRTEM), energy-dispersive X-ray spectroscopy (EDX), inductively coupled plasma mass spectrometry, and Fourrier-transformed infrared spectroscopy (FTIR) investigations have been performed. The innovative gold deposition method is expected to open new horizons for the design of biocompatible water dispersible gold/methionine-functionalized ferrite nanoparticles by a simply controllable way.

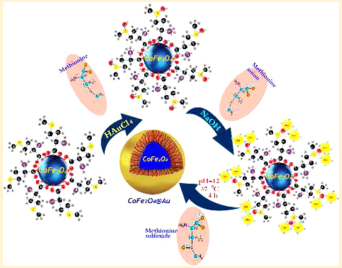

1. INTRODUCTION

Among various functional nanostructures, gold-coated and decorated magnetic nanoparticles (Nps) have attracted huge attention because of their biological compatibility and recently demonstrated potential applications in nanomedicine, biosensing, drug delivery, cells separation, etc. In fact, surface coating of superparamagnetic Nps with a biocompatible polymeric, organic, or precious metal shell is a well-known tool to tune the interactions between Nps, their saturation magnetization, surface energy, and other properties.[1−3] A number of protocols for attachment of gold species to the surface of magnetite (Fe_3O_4) and maghemite (γ-Fe_2O_3) Nps, such as sonochemical treatment, galvanic replacement, reverse micelles, laser ablation, and chemical reduction, among others, have been suggested during the past decade.[4−13] The reported gold tethering strategies can be grouped into a few well-defined approaches. According to the first of them, gold seeds prepared separately can be attached to the surface of magnetic Nps by coprecipitation together with or after formation of a polymeric shell.[14,15] As a result, the true and hydrodynamic size of Nps increases drastically, frequently becoming not suitable for many biomedical applications. For example, it has been reported that the initial size of Fe_3O_4 Nps (∼10 nm) and Co Nps (∼12 nm) increased up to 100 nm.[15] Another approach is direct coating of iron oxide Nps in the aqueous solutions by reduction of Au(III) species.[16−19] In fact, direct deposition methods are suitable for the covering or decoration of metallic or γ-Fe_2O_3 nanoparticles because the formation of gold shell on the magnetite (Fe_3O_4) or ferrite surfaces by a common approach involving citrate or borohydride reduction is problematic due to preferable formation of pure gold crystallites.[5,20] The direct coating of hydrophilic magnetite Nps, fabricated by thermal decomposition of organometallic precursors such as acetylacetonates and $Me(CO)_x$, by high-temperature-induced reduction of gold species has been also reported.[21,22] In this case, however, additional coating of gold-covered Nps with amphiphilic molecules such as lypopolysaccharides is required in order to obtain hydrophobic Nps suitable for biomedical as well as bioanalytical applications.[23,24] Lastly, the deposition of gold onto the surface of magnetic nanoparticles can be achieved via strong adsorption of some organic molecules, such as hydroxylamine[25] or Vitamin C,[26] capable of reducing subsequently the gold-containing ions and bind as-formed crystallites. To prevent gold crystallite formation in the plating solution bulk, this method, however, requires the precise control of the concentration of $AuCl_4^-$ ions as well as Vitamin C in the crystallochemical environment.

This work was based on our observation that, in contrast to other amino acids, methionine in alkaline medium is prone to reduce $AuCl_4^-$ species at the walls of the glass vessel instead of nucleation and growth of Au^0 particles in the solution bulk. In the presence of $CoFe_2O_4$ Nps, however, the covering of magnetic Nps instead of glass vessel walls was observed. The advantage of our functionalization method consists of its high yield, simplicity, and prevention of gold crystal formation. In addition to TEM observations of an increase in the Np size

Received: April 13, 2015
Revised: July 3, 2015

DOI: 10.1021/acs.jpcc.5b03528
J. Phys. Chem. C XXXX, XXX, XXX−XXX

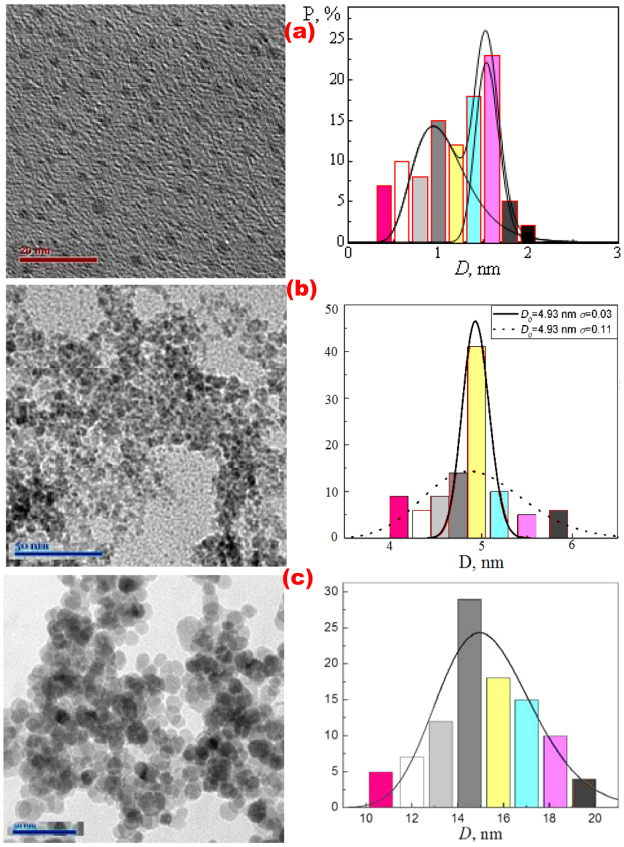

Figure 1. TEM images of nanoparticulated products synthesized in the deoxygenated solution containing $50CoCl_2 + 50Fe_2(SO_4)_3$ + 75 mmol L^{-1} diglycolic acid + NaOH up to pH = 12.4 at 80 °C for 3 h (a, b) and by hydrothermal treatment at 130 °C for 10 h (c). The size distribution histograms of corresponding Nps are shown in the right.

upon the deposition procedure, the formation of core/shell morphology was further confirmed by HRTEM, FTIR, SAED, XRD, and EDX analysis.

2. EXPERIMENTAL SECTION

Chemicals. The chemicals used in this study, including Co(II) and Fe(III) salts, $HAuCl_4{\cdot}4H_2O$, and diglycolic and citric acids were of analytical grade, purchased from Aldrich and used without further purification. NaOH was purchased from Poch SA (Poland) and purified by preparation of saturated solution, which led to the crystallization of other sodium salts. All tested amino acids, including D,L-methionine (99% purity) as well as dopamine hydrochloride and D,L-methionine sulfoxide (≥99.0%), were purchased from Sigma-Aldrich Co. Deionized distilled water was used throughout the experiments.

Synthesis of Co Ferrite Nanoparticles. In this study, ultrasmall (≤2.0 nm) and small (~5.0 nm) cobalt ferrite nanoparticles were synthesized from the complex-assisted alkaline solutions of Co(II) and Fe(III) salts by the coprecipitation method in a thermostated glass reactor at 80 °C and ambient pressure for 3 h under continuous argon gas bubbling, as reported earlier.[27] Briefly, the working solution was prepared from $CoCl_2$ and $Fe_2(SO_4)_3$ salts and 75 mmol L^{-1} diglycolic acid; the total metal salt concentration was 100 mmol L^{-1}. All solutions were deoxygenated with argon before mixing. The pH of solutions was kept at the level of 12.4 by addition of 5.0 mol L^{-1} NaOH solution. The required quantity of NaOH solution was determined by an additional blank experiment. In the subsequent experiment, this quantity was placed in the reactor and mixed with the other components, during several seconds under vigorous stirring. To obtain ultrasmall $CoFe_2O_4$ Nps, the as-grown products were centrifuged at 8500 rpm for 3 min and carefully rinsed 5 times using fresh portions (10 mL) of H_2O. The supernatants of the last three centrifugations were combined, rinsed again with ethanol, and collected by centrifugation. Afterward, ultrasmall Nps were dried at 60 °C. Small Nps, collected by centrifugation, were also carefully rinsed with water and dried. To obtain larger cobalt ferrite Nps,

DOI: 10.1021/acs.jpcc.5b03528
J. Phys. Chem. C XXXX, XXX, XXX−XXX

the hydrothermal synthesis from the similar solution at 130 °C for 10 h was performed followed by several rinsing/centrifugation procedures and drying at 60 °C. The collected Nps were studied and subjected to further processing within the following week.

Gold Shell Formation. The deposition of gold shell onto the Co ferrite surface was conducted via amino acid methionine-induced chemical reduction of $HAuCl_4$ in the suspension of $CoFe_2O_4$ Nps. Briefly, 25 mg of Nps was dispersed in 20 mL of aqueous 30 mmol L^{-1} D,L-methionine by ultrasonic agitation for 30 min. Afterward, the equimolar content of chlorauric acid was introduced into the reaction medium, and the solution was alkalized to the required pH by addition of 1.0 mol L^{-1} NaOH under vigorous stirring. The deposition process was performed at 37 °C for 4 h under mild mixing conditions. The products obtained was collected by centrifugation at 8500 rpm for 6 min, carefully rinsed several times with pure water, and redispersed in ethanol for further examinations. For TEM observations, a drop of Np suspension was placed onto the Lacey grid, whereas for FTIR investigations the suspension was dried at 60 °C. To obtain a thicker gold shell, the deposition procedure was repeated using the same Np probe.

Analysis. Infrared spectra were recorded in the transmission mode on an ALPHA FTIR spectrometer (Bruker, Inc., Germany) equipped with a room-temperature detector DLATGS. The spectral resolution was set at 4 cm^{-1}. Spectra were acquired from 100 scans. Nanoparticulated samples were dispersed in KBr tablets. Parameters of the bands were determined by fitting the experimental spectra with Gaussian−Lorentzian shape components using GRAMS/A1 8.0 (Thermo Scientific) software.

The concentration of gold remaining in the deposition solution was determined by inductively coupled plasma mass spectrometry analysis. Measurements were made on emission peaks at λ_{Au} = 267.595 nm and λ_{Au} = 242.795 nm using a OPTIMA 7000DV (PerkinElmer, USA) spectrometer. Calibration curves were made using dissolved standard within the 1−50 ppm concentration range in the same acid matrix as the unknown samples. In some experiments, the magnetic core of $CoFe_2O_4$@Au Nps was dissolved in HCl (1:1) by sonication at ambient temperature for 50 h.

Characterization. The morphology of as-grown products was investigated using a transmission electron microscope (TEM, model MORGAGNI 268) operated at an accelerating voltage of 72 keV. The average size of nanoparticles was estimated from at least 200 species observed in their TEM images. High-resolution transmission electron microscopy (HRTEM) studies of as-synthesized products were performed using a LIBRA 200 FE at an accelerating voltage of 200 keV.

X-ray powder diffraction experiments were performed on a D8 diffractometer (Bruker AXS, Germany), equipped with a Göbel mirror as a primary beam monochromator for Cu K_α radiation.

XPS measurements were carried out to obtain information about the elemental chemical states and surface composition of the $CoFe_2O_4$ and $CoFe_2O_4$@Au nanoparticles. Upgraded Vacuum Generator (VG) ESCALAB MKII spectrometer fitted with a new XR4 twin anode was used. The nonmonochromatized Mg K_α X-ray source was operated at $h\nu$ = 1253.6 eV with 300 W power (20 mA/15 kV), and the pressure in the analysis chamber was lower than 5×10^{-7} Pa during spectral acquisition. The spectra were acquired with an electron analyzer pass energy of 20 eV for narrow scans and resolution of 0.05 eV and with a pass energy of 100 eV for survey spectra. All spectra were recorded at a 90° takeoff angle and calibrated using the C 1s peak at 284.6 eV. The spectra calibration, processing, and fitting routines were done using Avantage software (5.918) provided by Thermo VG Scientific. Core level peaks of Fe 2p, Co 2p, Au 4f, C 1s, and O 1s were analyzed using a nonlinear Shirley-type background, and the calculation of the elemental composition was performed on the basis of Scofield's relative sensitivity factors.

3. RESULTS AND DISCUSSION

Fabrication and Characterization of Co Ferrite Nps. In this study ultrasmall and small cobalt ferrite, $CoFe_2O_4$, Nps were synthesized by diglycolic acid-assisted coprecipitation reaction of Co(II) and Fe(III) salts in the degassed alkaline (pH 12.4) solution at 80 °C for 3 h followed by several rinsing and centrifugation procedures, as reported earlier.[27] TEM investigations revealed that the resulting Co ferrite Nps, which remained in supernatant after washings and centrifugations at 8500 rpm for 3 min, are fairly spherical particles, 1.85 nm in average diameter, whereas those collected at the bottom of the test tube are also spherical with a mean diameter of 4.93 nm (Figure 1a,b). Larger $CoFe_2O_4$ Nps, e.g., with $Ø_{mean}$ = 14.6 nm (Figure 1c), were synthesized in a similar solution containing $CoCl_2$ and $FeCl_3$ (1:2 at the total concentration of 100 mmol L^{-1}) and 75 mmol L^{-1} diglycolic acid under hydrothermal conditions at 130 °C for 10 h. In all the cases, EDX and chemical analysis of Nps dissolved in the HCl solution (1:1) by inductively coupled plasma mass spectrometry indicated the $CoFe_2O_4$ composition close to stoichiometric. The crystalline nature of cobalt ferrite Nps was verified by X-ray diffraction investigations. The representative XRD patterns of the tested ultrasmall and small Nps are shown in Figures 2a and 2b, respecively. It should be emphasized that the position and relative intensity of all diffraction peaks match well with standard $CoFe_2O_4$ diffraction data, implying the polycrystalline inverse spinel structure of all tested Nps. The optimization of

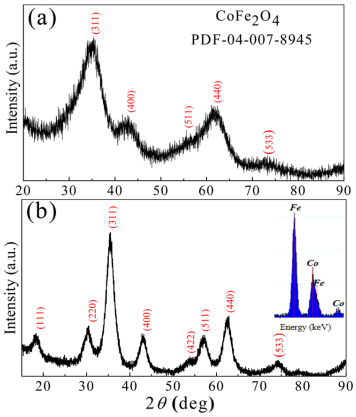

Figure 2. XRD patterns of Nps synthesized under conditions indicated in Figure 1 for ultrasmall (a) and larger (D_0 = 4.93 nm) (b) Nps. In the inset, the typical EDX spectrum of tested cobalt ferrite Nps.

DOI: 10.1021/acs.jpcc.5b03528
J. Phys. Chem. C XXXX, XXX, XXX−XXX

gold deposition conditions proved that reduction of gold species on the surface of ferrite Nps takes place at a physiological temperature of 37 °C in the alkaline to slightly acidic solutions within a pH window from 12.5 to 5.0. It should be noted, however, that only in the solutions containing equimolar contents of chlorauric acid and methionine the yield of reduction of gold-containing ions attained 99.3–99.9% without formation of separate Au^0 crystals. Surprisingly, the addition of methionine in excess resulted in the decrease of reduction yield. With a decrease in reaction medium pH down to 9.0 and further to 5.0, more than 23% and 29% of chlorauric acid, respectively, remained in the solution after reaction at 37 °C for 4 h. In both cases, the formation of numerous finely grained gold crystallites in the reaction solution as well as onto the surface of Np was also observed. Therefore, in the typical deposition conditions, an aqueous solution containing 0.9 mg mL^{-1} $CoFe_2O_4$, 0.3 mmol L^{-1} methionine, and 0.3 mmol L^{-1} $HAuCl_4$ adjusted to pH = 12.0 by addition of 1 M NaOH was used. Figure 3 shows the TEM images of the cobalt ferrite Nps in average size of 1.85 nm after incubation in the gold deposition solution at 37 °C for 4 h. The chemical analysis of solution used for deposition confirmed the reduction of more than 99% of gold-containing ions without any deposition onto the glass reactor surface. At the same time, ultrasmall cobalt ferrite Nps, being stable in water for months, after incubation in the gold plating solution with methionine are prone to deposit fully at the bottom of the reactor overnight. Furthermore, EDX analyses of carefully rinsed Nps confirmed the presence of a metallic gold phase in the tested range of magnetically collected Nps (Figure 3c), although from the TEM and STEM observations (Figure 3a and 3b) no formation of pure gold crystals was seen. Also, in the HRTEM image (inset in Figure 3a), the observed lattice fringes at the surface side have a characteristic spacing of 0.235 nm, which can be assigned to the (111) planes of Au^0. To determine the size variation of cobalt ferrite Nps upon the gold deposition, 200 Nps were inspected, and the results obtained are presented by size distribution histograms of gold-coated Nps in Figure 4. One can see that after 4 h sonication in the alkaline equimolar solution of methionine and chlorauric acid the average size of ultrasmall Nps increased from 1.85 nm (Figure 1a) to 2.45 nm (Figure 4a). Similar results were also obtained in the case of covering $CoFe_2O_4$ Nps with average size of 4.93 nm (Figure 1b) and 14.6 nm (Figure 1c). In these cases, the average size of ferrite Nps increased up to 6.6 and 17.1 nm, respectively (Figure 4b and c). These observations confirmed the conclusion regarding covering of $CoFe_2O_4$ Nps with a gold shell.

Further in-depth physicochemical characterization of cobalt ferrite nanoparticles, functionalized with gold by methionine-induced reduction, was performed applying several techniques. The object was to determine the structure of gold as well as the organic shell formed around the Co ferrite Np during the above-described treatment. To this purpose, the $CoFe_2O_4$@Au Np core was dissolved in 1:1 HCl solution, and the remaining precipitates were collected by centrifugation for subsequent TEM investigations. Figure 5 shows the TEM images of gold-coated $CoFe_2O_4$ Nps before (a) and after (c, d) dissolution of the magnetic core in HCl. The selected area electron diffraction (SAED) pattern of gold-coated ferrite Nps presented in Figure 5b clearly demonstrated the diffraction from 0.238 and 0.282 nm gold lattices (111) with the atom spacing 0.235 nm and (110) with atom spacing 0.28 nm, respectively. As also seen from Figure 5c, in the case of one-step gold plating, the thin

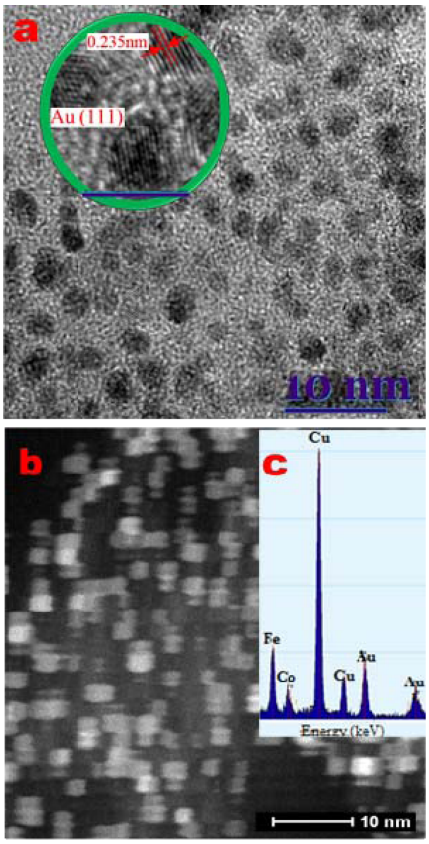

Figure 3. TEM (a) and STEM (b) images of $CoFe_2O_4$@Au nanoparticles fabricated by methionine-directed gold deposition. In (c) EDX spectrum of gold-plated nanoparticles. In the green circled inset, HRTEM image of the products demonstrating the Au lattice spacing at about 0.235 nm (scale bar 5 nm). Upon the plating the average size of $CoFe_2O_4$ Nps increased from 1.85 to 2.45 nm.

platelet gold corpuscles remained after dissolution of the Np core, allowing us to conclude about their true nature: most probably they are the fragments formed from the shell of $CoFe_2O_4$@Au Nps. In the case of Nps, coated thicker by repeating the deposition process, the shape of gold bubbles remaining after core etching (Figure 5d) resembles the shape of $CoFe_2O_4$@Au Nps, pointing to the nice covering of ferrite Nps with gold by the methionine-induced deposition approach reported herein. Next, to investigate variation in the elemental chemical states and surface composition of ferrite Nps before and after the gold plating procedure, they were rinsed carefully, spread onto the silica surface, and analyzed with XPS.

The characteristic XP spectra are presented in Figure 6a–f, and their analysis results are listed in Tables S1 and S2 of the Supporting Information. As seen, the contents of iron and cobalt at the surface side of ferrite Nps gold-coated under

DOI: 10.1021/acs.jpcc.5b03528
J. Phys. Chem. C XXXX, XXX, XXX–XXX

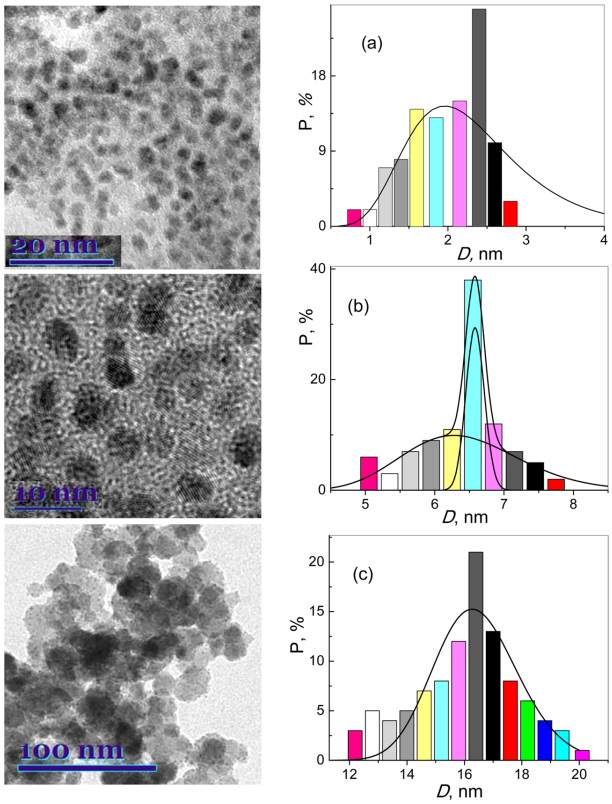

Figure 4. Size distribution histograms for cobalt ferrite Nps after gold deposition from the alkaline (pH = 12.2) solution containing 0.3 mmol/mL $HAuCl_4$ and 0.3 mmol L^{-1} methionine at 37 °C for 4 h. Lines are fits to log-normal distributions. In the left side, TEM views of corresponding $CoFe_2O_4$@Au Nps.

conditions of Figure 4 are approximately 5 to 5.6 times lower than that for bare $CoFe_2O_4$ ones. Furthermore, a well-resolved Au 4f peak with the binding energy (BE) centered at 84.06 eV, characteristic to metallic gold (6.74 at %; full width at half-maximum, fwhm = 1.71 eV), appeared to be pointing to the covering of about 80% of the $CoFe_2O_4$ Np surface. Finally, obvious changes in the shape of the O 1s spectrum were detected after gold plating. Instead of a single O 1s peak at BE = 530.06 eV, attributable to the Me−O bond, a well-resolved additional O 1s peak at BE = 532.83 eV, attributable to C═O, appeared, clearly implying the tethering of organic molecules to the surface of $CoFe_2O_4$@Au Nps.

To investigate the variation of the surface chemical properties of $CoFe_2O_4$ Nps upon the covering with a gold shell, the bare as well as gold-coated Nps were dispersed ultrasonically in the solution of 13 mmol L^{-1} dopamine hydrochloride and kept at ambient temperature overnight. Following careful rinsing and drying they were further investigated by Fourier transformed infrared (FTIR) spectroscopy. Figure 7 compares the infrared spectra of tested magnetic $CoFe_2O_4$ and $CoFe_2O_4$@Au Nps before and after adsorption of dopamine. The infrared spectrum of dopamine hydrochloride is also shown. Note that the intense and broad absorption band near 580 cm^{-1} observed for $CoFe_2O_4$@Au Nps (Figure 7a) corresponds to Fe−O and Co−O vibrational modes.[28−31] Thus, the infrared spectrum of Fe_3O_4 exhibits a characteristic band near 570−580 cm^{-1},[29,30] while the cobalt oxide (Co_3O_4) infrared spectrum shows a doublet at 570/670 cm^{-1}.[28] Several lower intensity broad bands located near 1380 and 1570 cm^{-1} are visible in the fingerprint spectral region of bare $CoFe_2O_4$@Au Nps (Figure 7a). These bands might be associated with vibrations of carboxylate and/or amino groups of adsorbed amino acid methionine used for the formation of nanoparticles or adsorbed oxidation product of methionine, presumably methionine sulfoxide.[32,33] Figure 8 shows the infrared spectrum of the possible oxidation product methionine sulfoxide. The strong band near 1032 cm^{-1} belongs to the stretching vibration of the S═O group, while the feature near 1510 cm^{-1} was assigned to bending vibration of the NH_2 group.[34] The intense bands at 1586 and 1411 cm^{-1} correspond to carboxylate group asymmetric and symmetric stretching vibrations, respectively.[34] The spectrum of $CoFe_2O_4$@Au nanoparticles (Figure 6a)

DOI: 10.1021/acs.jpcc.5b03528
J. Phys. Chem. C XXXX, XXX, XXX−XXX

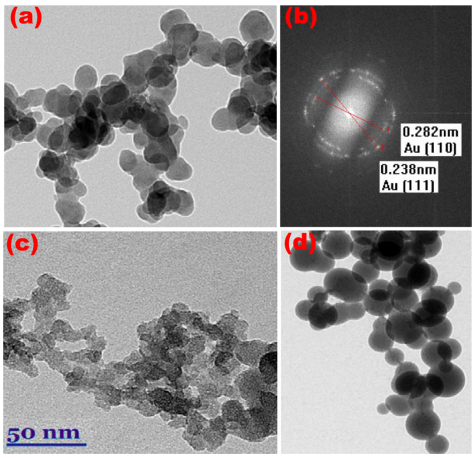

Figure 5. TEM images of the $CoFe_2O_4$@Au Nps (a) and gold products remaining after $CoFe_2O_4$@Au Nps etching in the HCl (1:1) solution for Nps coated with a thin (c) and thicker (d) shell. In (b) the selected area electron diffraction spectrum taken from the gold-coated cobalt ferrite Nps shown in the part (a).

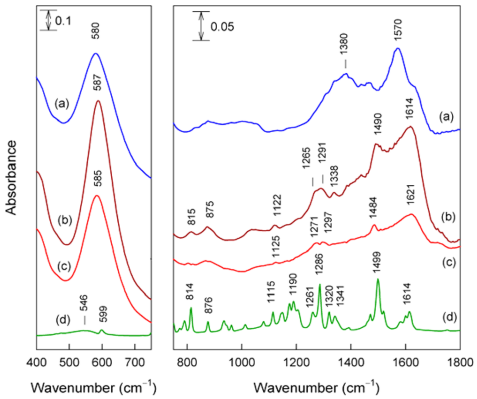

Figure 7. FTIR absorbance spectra of (a) $CoFe_2O_4$@Au nanoparticles, (b) dopamine-modified $CoFe_2O_4$@Au nanoparticles, (c) dopamine-modified $CoFe_2O_4$ nanoparticles, and (d) crystalline dopamine in the spectral regions of 400−750 (left panel) and 750−1800 cm^{-1} (right panel).

exhibits similar COO^- bands, however, at lower frequencies. It is of note that the low intensity broad feature near 1000 cm^{-1} might be associated with the S═O stretching vibration (Figure S1, Supporting Information). Analysis of complexation of methionine sulfoxide with nickel(II) ions has revealed a substantial downshift of the symmetric stretching vibration of the carboxylate group (down to 1390 cm^{-1}) and decrease in relative intensities of bands corresponding to bending vibration of the NH_2 group and stretching vibration of the S═O group. Similar changes are visible in our spectra, suggesting adsorption of methionine sulfoxide on the surface of Co−Fe−Au nanoparticles. The adsorption of dopamine results in partial displacement of surface-bound methionine sulfoxide (integrated intensity of the S═O band decreases by a factor of 1.7 (Figure S1, Supporting Information)).

Incubation of $CoFe_2O_4$@Au Nps in aqueous solution containing dopamine results in the appearance of several new bands located at 815, 875, 1122, 1265/1291, 1338, and 1490 cm^{-1} (Figure 7b). Comparison with the dopamine infrared spectrum (Figure 7d) immediately confirms the presence of adsorbed dopamine on the surface of nanoparticles. The most intense dopamine bands at 814, 1286, and 1499 cm^{-1} had equivalent features at 815, 1265/1291, and 1490 cm^{-1} in the

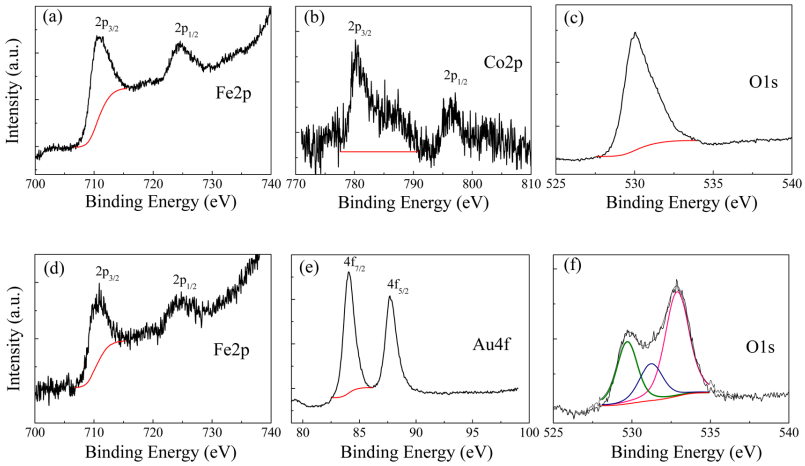

Figure 6. XPS spectra of the Fe 2p, Co 2p, O 1s, and Au 4f photoelectron for the bare (a−c) and gold-coated (d−f) cobalt ferrite nanoparticles.

DOI: 10.1021/acs.jpcc.5b03528
J. Phys. Chem. C XXXX, XXX, XXX−XXX

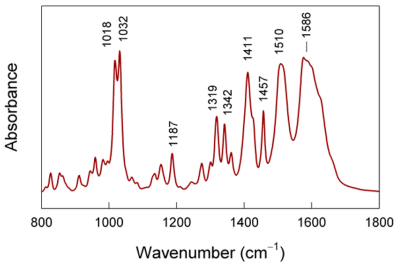

Figure 8. FTIR absorption spectrum of methionine sulfoxide in KBr tablet.

infrared spectrum of modified nanoparticles. The assignments of the bands based on previous studies of dopamine and catechol molecules[35−40] are provided in Table S3 (Supporting Information). The well-defined band near 1499 cm^{-1} in the solid state spectrum of dopamine belongs to aromatic ring CC stretching vibration coupled with in-plane CH bending mode, while the intense band near 1286 cm^{-1} is associated with ring CC stretching vibration coupled with C−OH stretching motion, although isotopic $^{18}O/^{16}O$ substitution experiments confirmed that in-plane ring stretching vibration has the major contribution for this mode.[41] The deformation vibration of catechol OH groups is mainly associated with a broad band near 1341 cm^{-1}. A similar band of dopamine in aqueous solution disappeared when water was exchanged with D_2O.[42] The discussed three modes are useful in analysis of interaction of dopamine with various surfaces.[39,40,43−46] Figure 9 compares the experimental infrared spectra with fitted Gaussian−Lorentzian form components of adsorbed dopamine on $CoFe_2O_4$ and $CoFe_2O_4$@Au nanoparticles and the spectrum of a crystalline compound in the spectral ranges of diagnostic bands. It was demonstrated[39] that chemical bonding with metal

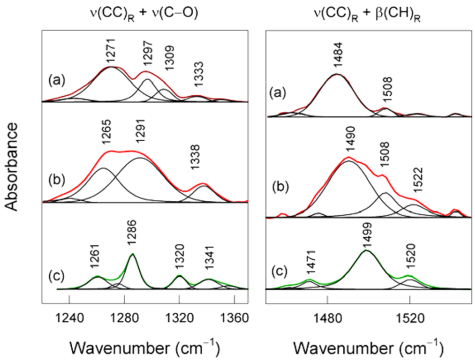

Figure 9. FTIR absorbance spectra of (a) dopamine-modified $CoFe_2O_4$, (b) dopamine-modified $CoFe_2O_4$@Au nanoparticles, and (c) crystalline dopamine in the spectral region of CC ring stretching coupled with C−OH stretching (left panel) and CC ring stretching coupled with CH in-plane deformation (right panel) modes. The fitted Gaussian−Lorentzian form components are also shown. Spectra are background corrected by using a polynomial function and normalized to the most intense band in the frequency region of 1220−1365 cm^{-1}.

oxides through the deprotonated catechol −OH groups results in broadening and downshift of a characteristic $\nu(CC)_R$ + $\nu(C-O)$ band near 1286 cm^{-1} (in the case of dopamine) by ∼10−20 cm^{-1}. In contrast, molecular adsorption through the intact −OH groups (without deprotonation) causes a slight increase in the corresponding frequency.[39] The higher frequency ring CC stretching vibration coupled with in-plane CH deformation also broadens and shifts to lower wavenumbers upon chemisorption of the catechol group; however, molecular adsorption induces a slight shift of this mode to lower wavenumbers as well.[39] In the case of $CoFe_2O_4$ nanoparticles, our spectral data show the appearance of a broad (fwhm = 24 cm^{-1}) and intense $\nu(CC)_R$ + $\nu(C-O)$ band at 1271 cm^{-1} (Figure 9a, left panel). The fwhm value of the corresponding 1286 cm^{-1} band of crystalline dopamine was found to be 11 cm^{-1}. Such spectral changes suggest chemical bonding of the catechol group with the $CoFe_2O_4$ oxide surface through the deprotonated −OH groups. Considerable downshift (15 cm^{-1}) and broadening (fwhm increases from 16 to 19 cm^{-1} upon adsorption) of the $\nu(CC)_R$ + $\beta(CH)_R$ band supports this conclusion (Figure 9a, right panel). The lower intensity higher frequency component near 1297 cm^{-1} probably belongs to molecularly adsorbed species. Coating of $CoFe_2O_4$ nanoparticles by Au results in a considerable increase in relative intensity of molecularly adsorbed species (1291 cm^{-1} band) and a decrease in relative intensity of the band associated with chemisorbed dopamine molecules (1265 cm^{-1} band). Dominant molecular adsorption in this case is consistent with the observed downshift of the $\nu(CC)_R$ + $\beta(CH)_R$ band at a lesser extent. Finally, the well-defined band near 1341 cm^{-1} for crystalline dopamine is assigned to deformation OH vibration, $\delta(OH)$.[40,42] It was demonstrated that this band disappears upon water exchange to D_2O[42] or due to deprotonation of catechol −OH groups.[39] Thus, observation of the relatively intense $\delta(OH)$ band in the case of $CoFe_2O_4$@Au nanoparticles (1338 cm^{-1} band) and a considerably lower intensity peak near 1333 cm^{-1} in the case of bare $CoFe_2O_4$ provides an additional support for the dominant chemisorption state for the latter system, compared with preferential molecular adsorption at nanoparticles coated by gold. It should be noted that we do not have any direct spectroscopic evidence on participation of the NH_2 group in the interaction with the studied surfaces; this might be the case for the $CoFe_2O_4$@Au nanoparticles.

The oxidation of amino acid methionine to methionine sulfoxide by an equimolar amount of chlorauric acid in slightly acidic aqueous medium has been reported four decades ago.[32] According to the aforementioned report, the oxidation of methionine proceeds through the formation of the protonated dihalide−*S*-methionine complex which in turn hydrolyzes to methionine sulfoxide and HCl. Upon this reaction, the intermediate Au(I)−methionine complex is formed reducing later to Au^0 but still remaining in the coordination sphere of sulfur. The role of the protonated amino acid group in further Au(I) reduction, however, was not envisaged. In our case, the participation of an unprotonated amino group of amino acid (due to alkaline medium) in the reduction reaction is highly expected. However, the exact mechanism of chlorauric acid reduction reactions with amino acid methionine in alkaline medium on the surface of cobalt ferrite remains unclear. To better understand the role of participating water, OH^- ions, and the intermediate complex of methionine anion attached to the surface of $CoFe_2O_4$ Np in the redox process, a set of additional

DOI: 10.1021/acs.jpcc.5b03528
J. Phys. Chem. C XXXX, XXX, XXX−XXX

investigations is further required. Nevertheless, some conclusive remarks made from this study can be outlined.

According to Vujačić et al.,[47] the reaction of $[AuCl_4]^-$ with Met proceeds through the binding of methionine sulfur to the gold atom via exchange of ligands and the formation of intermediate complexes and later—polymeric $[Au^IMet(Cl)]_n$ and methionine sulfoxide, Met-SO-CH_3. According to ion chromatograms presented by Wang et al.[48] aqueous $HAuCl_4$ due to hydrolysis reaction consists of $[AuCl_x(OH)_{4-x}]^-$ with $x \geq 2$ at low pH and with $x < 2$ at high pH. In the case of pHs $\geq$10.35, $x = 0$ and 1.0 corresponding to the average formula of $[AuCl_{0.1}(OH)_{3.90}]^-$. Different Au species exhibit different chemical reactivity in the reduction reaction in acidic and alkaline media.[49] For example, application of ascorbic acid, the reduction ability of which strengthens with increasing pH, results in the formation of gold colloids exhibiting a strong red-shift of the surface plasmon resonance (SPR) from typical 525−545 to 787 nm at pH = 10.35 due to formation of Au colloid assemblages consisting of fine crystallites.[49] Panda and Chatttopadhyay[50] also studied the synthesis of Au colloids by H_2O_2 reduction of chlorauric acid at pH ranging from 2.9 to 12.0 and obtained Au Nps with different morphologies. Therefore, it can be presumed that in the alkaline solution with L-methionine, similarly to the case of ascorbic acid, the assemblages of finely grained Au colloids are formed at the surface of ferrite Nps. Furthermore, according to ref 51 these positively charged species exhibit much higher Au 4f binding energy with the S element. We hypothesize that this could be the reason for gold deposition onto the surface of ferrite Nps, functionalized with the L-methionine anion through the $-COO^-$ unit, instead of formation of the bulk crystals. In accordance with the above discussion and similarly as in ref 49, we may suggest that the alkaline medium deposition of gold onto the ferrite Np surface, stabilized with methionine anion, proceeds via formation of intermediate $Au(III)(OH^-)_n$ complexes with n = 3, 2, 1, the further slow reduction of which leads to formation of the two-coordinated $[Au(I)-Met(OH)_2]^-$ complex. In the presence of water this complex disproportionates, giving Au^0, Au(III)hydroxide, and methionine sulfoxide.

Furthermore, in accordance with the Pearson theory[42] and the softness of all three functional groups of methionine, the S-donor atom-containing group has the highest affinity for Au(III) and Au(I) ions. Therefore, it can be supposed that even after reduction reaction the methionine sulfur still remains in the coordination sphere of metallic gold stabilizing Np (Scheme 1). These data provide an indication on the possible mechanism but are not sufficient to explain the exact picture of reactions resulting in the core−shell structure formation.

4. CONCLUSIONS

This study describes a novel and efficient pathway for covering of various cobalt ferrite nanoparticles with gold shell without nucleation and growth of the separate gold crystals using amino acid methionine as a reducer of gold species and stabilizing agent for Nps. It is supposed that upon initial dispersion of ferrite Nps in the methionine solution amino acid interacts with the surface of cobalt ferrite Nps through the carboxyl bond. From what is known in the acidic and slightly acidic media,[15] it is envisaged that further addition of chlorauric acid and alkalization of the reaction medium lead to reduction of gold-containing ions through the formation of an intermediate complex from methionine sulfur dihalide, OH^-, and Au(I) species. The reduced gold atoms still remain in the coordination sphere of methionine sulfur attached to the surface of ferrite Np and stabilize it. However, more detailed studies must be conducted to understand the exact mechanism of reactions taking place during methionine-induced reduction and functionalization of magnetic nanoparticles.

It is believed that the strategy developed here can easily be extended to coat nanoparticles composed of other iron oxides with a gold shell. It was also demonstrated that dopamine molecules adsorb differently on the surface of bare and gold-coated $CoFe_2O_4$ Nps suggesting the prospective application of this effect as gold shell formation criterion.

Scheme 1. Illustration of Methionine-Induced Chlorauric Acid Reduction at the Surface of the Cobalt Ferrite Nanoparticle

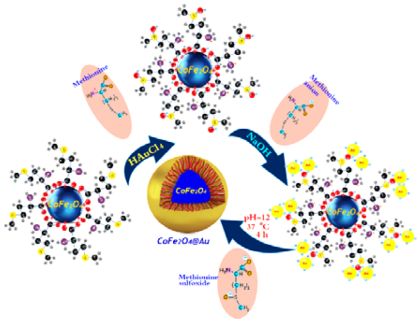

■ ASSOCIATED CONTENT

Supporting Information

XPS and FTIR spectra and corresponding data in tables. The Supporting Information is available free of charge on the ACS Publications website at DOI: 10.1021/acs.jpcc.5b03528.

■ AUTHOR INFORMATION

Corresponding Author

*E-mail: jagmin@ktl.mii.lt. Phone: +370 5 2648891.

Notes

The authors declare no competing financial interest.

■ ACKNOWLEDGMENTS

Dr. J. Vaičiūnienė is gratefully acknowledged for performing the analysis of reaction solutions. Authors also are grateful to Dr. V. Pakštas and Dr. V. Jasulaitiene for obtaining XRD and XPS spectra, respectively.

■ REFERENCES

(1) Luchini, A.; Vitiello, G.; Rossi, F.; Ruiz De Ballesteros, O.; Radulescu, A.; D'Errico, G.; Montesarchio, D.; de Julian Fernandez, C.; Paduano, L. Developing Functionalized Fe_3O_4-Au Nanoparticles: A Physico-Chemical Insight. *Phys. Chem. Chem. Phys.* **2015**, *17*, 6087−6097.

(2) Bao, J.; Chen, W.; Liu, T.; Zhu, Y.; Jin, P.; Wang, L.; Liu, J.; Wei, Y.; Li, Y. Bifunctional Au-Fe_3O_4 Nanoparticles for Protein Separation. *ACS Nano* **2007**, *1*, 293−298.

(3) Meledandri, C. J.; Stolarczyk, J. K.; Brougham, D. F. Hierarchical Gold-Decorated Magnetic Nanoparticle Clusters with Controlled Size. *ACS Nano* **2011**, *5*, 1747−1755.

DOI: 10.1021/acs.jpcc.5b03528
J. Phys. Chem. C XXXX, XXX, XXX−XXX

(4) Liu, Y.; Han, T.; Chen, C.; Bao, N.; Yu, C.-M.; Gu, H.-Y. A Novel Platform of Hemoglobin on Core−Shell Structurally Fe_3O_4@Au Nanoparticles and its Direct Electrochemistry. *Electrochim. Acta* **2011**, *56*, 3238−3247.
(5) Lyon, J. L.; Fleming, D. A.; Stone, M. B.; Schiffer, P.; Williams, M. E. Synthesis of Fe Oxide Core/Au Shell Nanoparticles by Iterative Hydroxylamine Seeding. *Nano Lett.* **2004**, *4*, 719−723.
(6) Kim, J.; Park, S.; Lee, J. E.; Jin, S. M.; Lee, J. H.; Lee, I. S.; Yang, I.; Kim, J.-S.; Kim, S. K.; Cho, M.-H.; et al. Designed Fabrication of Multifunctional Magnetic Gold Nanoshells and Their Application to Magnetic Resonance Imaging and Photothermal Therapy. *Angew. Chem., Int. Ed.* **2006**, *45*, 7754−7758.
(7) Caruntu, D.; Cushing, B. L.; Caruntu, G.; O'Connor, C. J. Attachment of Gold Nanograins onto Colloidal Magnetite Nanocrystals. *Chem. Mater.* **2005**, *17*, 3398−3402.
(8) Ojea-Jiménez, I.; Lorenzo, J.; Rebled, J. M.; Sendra, J.; Arbiol, J.; Puntes, V. Synthesis of Co-Organosilane-Au Nanocomposites via a Controlled Iterphasic Reduction. *Chem. Mater.* **2012**, *24*, 4019−4027.
(9) Zhang, J.; Post, M.; Veres, T.; Jakubek, Z. J.; Guan, J.; Wang, D.; Normandin, F.; Deslandes, Y.; Simard, B. Laser-Assisted Synthesis of Superparamagnetic Fe@Au Core−Shell Nanoparticles. *J. Phys. Chem. B* **2006**, *110*, 7122−7126.
(10) Xu, Z.; Hou, Y.; Sun, S. Magnetic Core/Shell Fe_3O_4/Au and Fe_3O_4/Au/Ag Nanoparticles with Tunable Plasmonic Properties. *J. Am. Chem. Soc.* **2007**, *129*, 8698−8699.
(11) Ban, Z.; Barnakov, Y. A.; Li, F.; Golub, V. O.; O'Connor, C. J. The Synthesis of Core−Shell Iron@gold Nanoparticles and Their Characterization. *J. Mater. Chem.* **2005**, *15*, 4660−4662.
(12) Spasova, M.; Salgueirino-Maceira, V.; Schlachter, A.; Hilgendorff, M.; Giersig, M.; Liz-Marzan, L. M.; Farle, M. Magnetic and Optical Tunable Microspheres with a Magnetite/Gold Nanoparticle Shell. *J. Mater. Chem.* **2005**, *15*, 2095−2098.
(13) Wu, W.; He, Q.; Chen, H.; Tang, J.; Nie, J. Sonochemical Synthesis, Structure and Magnetic Properties of Air-Stable Fe_3O_4/Au Nanoparticles. *Nanotechnology* **2007**, *18*, 145609.
(14) An, P.; Zuo, F.; Li, X.; Wu, Y.; Zhang, J.; Zheng, Z.; Ding, X.; Peng, L. A Bio-Inspired Polydopamine Approach to Preparation of Gold-Coated Fe_3O_4 Core−Shell Nanoparticles: Synthesis, Characterization and Mechanism. *Nano* **2013**, *08*, 1350061.
(15) Wu, A.; Ou, P.; Zeng, L. Biomedical Applications of Magnetic Nanoparticles. *Nano* **2010**, *05*, 245−270.
(16) Fan, Z.; Shelton, M.; Singh, A. K.; Senapati, D.; Khan, S. A.; Ray, P. C. Multifunctional Plasmonic Shell−Magnetic Core Nanoparticles for Targeted Diagnostics, Isolation, and Photothermal Destruction of Tumor Cells. *ACS Nano* **2012**, *6*, 1065−1073.
(17) Larsen, B. A.; Haag, M. A.; Serkova, N. J.; Shroyer, K. R.; Stoldt, C. R. Controlled Aggregation of Superparamagnetic Iron Oxide Nanoparticles for the Development of Molecular Magnetic Resonance Imaging Probes. *Nanotechnology* **2008**, *19*, 265102.
(18) Cui, Y.; Wang, Y.; Hui, W.; Zhang, Z.; Xin, X.; Chen, C. The Synthesis of Gold Mag Nano-Particles and their Application for Antibody Immobilization. *Biomed. Microdevices* **2005**, *7*, 153−156.
(19) Tamer, U.; Gündoğdu, Y.; Boyacı, İ.; Pekmez, K. Synthesis of Magnetic Core-Shell Fe_3O_4-Au Nanoparticle for Biomolecule Immobilization and Detection. *J. Nanopart. Res.* **2010**, *12*, 1187−1196.
(20) Chen, M.; Yamamuro, S.; Farrell, D.; Majetich, S. A. Gold Coated Iron Nanoparticles for Biomedical Applications. *J. Appl. Phys.* **2003**, *93*, 7551−7553.
(21) Wang, L.; Wang, L.; Luo, J.; Fan, Q.; Suzuki, M.; Suzuki, I. S.; Engelhard, M. H.; Lin, Y.; Kim, N.; Wang, J. Q.; et al. Monodispersed Core-Shell Fe_3O_4@Au Nanoparticles. *J. Phys. Chem. B* **2005**, *109*, 21593−21601.
(22) Smolensky, E. D.; Neary, M. C.; Zhou, Y.; Berquo, T. S.; Pierre, V. C. Fe_3O_4@organic@Au: Core−Shell Nanocomposites With High Saturation Magnetisation as Magnetoplasmonic MRI Contrast Agents. *Chem. Commun. (Cambridge, U. K.)* **2011**, *47*, 2149−2151.
(23) Hao, R.; Xing, R.; Xu, Z.; Hou, Y.; Gao, S.; Sun, S. Synthesis, Functionalization, and Biomedical Applications of Multifunctional Magnetic Nanoparticles. *Adv. Mater.* **2010**, *22*, 2729−2742.
(24) Piazza, M.; Colombo, M.; Zanoni, I.; Granucci, F.; Tortora, P.; Weiss, J.; Gioannini, T.; Prosperi, D.; Peri, F. Uniform Lipopolysaccharide (LPS)-Loaded Magnetic Nanoparticles for the Investigation of LPS−TLR4 Signaling. *Angew. Chem., Int. Ed.* **2011**, *50*, 622−626.
(25) Brown, K. R.; Walter, D. G.; Natan, M. J. Seeding of Colloidal Au Nanoparticle Solutions. 2. Improved Control of Particle Size and Shape. *Chem. Mater.* **2000**, *12*, 306−313.
(26) Jagminas, A.; Mažeika, K.; Kondrotas, R.; Kurtinaitienė, M.; Jagminienė, A.; Mikalauskaitė, A. Functionalization of Cobalt Ferrite Nanoparticles by a Vitamin C-assisted Covering with Gold. *Nanomater. Nanotechnol.* **2014**, *4*, 11.
(27) Jagminas, A.; Kurtinaitienė, M.; Mažeika, K.; Rotomskis, R.; Niaura, G.; Selskis, A. Fabrication and Characterization of Magnetic Ferrofluidsby the Co-precipitation Way Using Diglycolic Acid. *J. Nanopart. Res.* **2011**, *13*, 4133−4142.
(28) Ortega-Zarzosa, G.; Araujo-Andrade, C.; Compeán-Jasso, M. E.; Martínez, J. R.; Ruiz, F. Cobalt Oxide/Silica Xerogels Powders: X-Ray Diffraction, Infrared and Visible Absorption Studies. *J. Sol-Gel Sci. Technol.* **2002**, *24*, 23−29.
(29) Bewick, A.; Kalaji, M.; Larramona, G. In-situ Infrared Spectroscopic Study of the Anodic Oxide Film on Iron in Alkaline Solutions. *J. Electroanal. Chem. Interfacial Electrochem.* **1991**, *318*, 207−221.
(30) Li, Y.-S.; Church, J. S.; Woodhead, A. L. Infrared and Raman Spectroscopic Studies on Iron Oxide Magnetic Nano-Particles and Their Surface Modifications. *J. Magn. Magn. Mater.* **2012**, *324*, 1543−1550.
(31) Namduri, H.; Nasrazadani, S. Quantitative Analysis of Iron Oxides using Fourier Transform Infrared Spectrophotometry. *Corros. Sci.* **2008**, *50*, 2493−2497.
(32) Natile, G.; Bordignon, E.; Cattalini, L. Chlorauric Acid as Oxidant. Stereospecific Oxidation of Methionine to Methionine Sulfoxide. *Inorg. Chem.* **1976**, *15*, 246−248.
(33) Vujačić, A.; Savič, J. Z.; Sovilj, S. P.; Meszaros Szecsenyi, K.; Todorovič, N.; Petković, M. Ž.; Vasić, V. M. Mechanism of Complex Formation Between $[AuCl_4]$ and L-methionine. *Polyhedron* **2009**, *28*, 593−599.
(34) Corbi, P. P.; Melnikov, P.; Massabni, A. C. A Solid Nickel(II) Complex with Methionine Sulfoxide. *J. Alloys Compd.* **2000**, *308*, 153−157.
(35) Siddiqui, S. A.; Dwivedi, A.; Singh, P. K.; Hasan; Jain, S.; Sundaraganesan, N.; Saleem, H.; Misra, N. Vibrational Dynamics and Potential Energy Distribution of Two Well-Known Neurotransmitter Receptors: Tyramine and Dopamine Hydrochloride. *J. Theor. Comput. Chem.* **2009**, *08*, 433.
(36) Gunasekaran, S.; Kumar, R. T.; Ponnusamy, S. Vibrational Spectra and Normal Coordinate Analysis of Adrenaline and Dopamine. *Indian J. Pure Appl. Phys.* **2007**, *45*, 884−892.
(37) Park, S.-K.; Lee, N.-S.; Lee, S.-H. Vibrational Analysis of Dopamine Neutral Base based on Density Functional Force Field. *Bull. Korean Chem. Soc.* **2000**, *21*, 959−968.
(38) Wang, X.; Jin, B.; Lin, X. FTIR Spectroelectrochemical Study of Dopamine at a Glass Carbon Electrode in Neutral Solution. *Anal. Sci.* **2002**, *18*, 931−933.
(39) Lana-Villarreal, T.; Rodes, A.; Pérez, J. M.; Gómez, A. Spectroscopic and Electrochemical Approach to the Study of the Interactions and Photoinduced Electron Transfer Between Catechol and Anatase Nanoparticles in Aqueous Solution. *J. Am. Chem. Soc.* **2005**, *127*, 12601−12611.
(40) Araujo, P. Z.; Morando, P. J.; Blesa, M. A. Interactions of Catechol and Gallic Acid with Titanium Dioxide in Aqueous Suspensions. 1. Equilibrium Studies. *Langmuir* **2005**, *21*, 3470−3474.
(41) Michaud-Soret, I.; Andersson, K. K.; Que, L., Jr.; Haavik, J. Resonance Raman Studies of Catecholate and Phenolate Complexes of Recombinant Human Tyrosine Hydroxylase. *Biochemistry* **1995**, *34*, 5504−5510.

DOI: 10.1021/acs.jpcc.5b03528
J. Phys. Chem. C XXXX, XXX, XXX−XXX

(42) Chumillas, S.; Figueiredo, M. C.; Climent, V.; Feliu, J. M. Study of Dopamine Reactivity on Platinum Single Crystal Electrode Surfaces. *Electrochim. Acta* **2013**, *109*, 577−586.
(43) Öhrström, L.; Michaud-Soret, I. Fe-catecholate and Fe-oxalate Vibrations and Isotopic Substitution Shifts from DFT Quantum Chemistry. *J. Phys. Chem. A* **1999**, *103*, 256−264.
(44) Martin, S. T.; Kesselman, J. M.; Park, D. S.; Lewis, N. S.; Hoffmann, M. R. Surface Structures of 4-Chlorocatechol Adsorbed on Titanium Dioxide. *Environ. Sci. Technol.* **1996**, *30*, 2535−2542.
(45) Woodill, L. A.; O'Neill, E. M.; Hinrichs, R. Z. Impacts of Surface Adsorbed Catechol on Tropospheric Aerosol Surrogates: Heterogeneous Ozonolysis and its Effects on Water Uptake. *J. Phys. Chem. A* **2013**, *117*, 5620−5631.
(46) Gulley-Stahl, H.; Hogan, P. A., II; Schmidt, W. L.; Wall, S. J.; Buhrlage, A.; Bullen, H. A. Surface Complexation of Catechol to Metal Oxides: an ATR-FTIR Adsorption, and Dissolution Study. *Environ. Sci. Technol.* **2010**, *44*, 4116−4121.
(47) Vujačić, A. V.; Savić, J. Z.; Sovilj, S. P.; Szecsenyi, K. M.; Todorović, N.; Petković, M.Ž.; Vasić, V. M. Mechanism of Complex Formation Between $[AuCl_4]^-$ and L-methionine. *Polyhedron* **2009**, *28*, 593−599.
(48) Wang, S.; Qian, K.; Bi, X. Z.; Huang, W. Influence of Speciation of Aqueous $HAuCl_4$ on the Synthesis, Structure and Property of Au Colloids. *J. Phys. Chem. C* **2009**, *113*, 6505−6510.
(49) Al-Maythalony, B. A.; Wazeer, M. I. M.; Isab, A. A.; Ahmad, S. A Study of $[Au(ethylenediamine)Cl_2]Cl$ Interaction With L-methionine and D,L-Se-Met by ^1H and ^{13}C NMR Spectroscopy. *Spectroscopy* **2010**, *24*, 567−575.
(50) Murugadoss, A.; Chatttopadhyay, A. Stabilising Agent Specific Synthesis of Multi-Branched and Spherical Au Nanoparticles by Reduction of $AuCl^-_4$ by Fe^{2+} Ions. *J. Nanosci. Nanotechnol.* **2007**, *7*, 1730−1735.
(51) Meyer, R.; Lemire, C.; Shaikhutdinov, Sh.K.; Freund, H.-J. Surface Chemistry of Catalysis by Gold. *Gold Bull.* **2004**, *37*, 72−124.

DOI: 10.1021/acs.jpcc.5b03528
J. Phys. Chem. C XXXX, XXX, XXX−XXX

5 publikacija / 5th publication

Influence of interactions to the properties of ultrasmall $CoFe_2O_4$ nanoparticles estimated by Mössbauer study.

Mažeika K, **Mikalauskaitė A** ir Jagminas A.

Journal of Magnetism and Magnetic Materials, 2015, 389, 21-26.

Publikaciją galite rasti adresu:
https://doi.org/10.1016/j.jmmm.2015.04.044

Journal of Magnetism and Magnetic Materials 389 (2015) 21–26

Contents lists available at ScienceDirect

Journal of Magnetism and Magnetic Materials

journal homepage: www.elsevier.com/locate/jmmm

Influence of interactions to the properties of ultrasmall $CoFe_2O_4$ nanoparticles estimated by Mössbauer study

Kęstutis Mažeika *, Agnė Mikalauskaitė, Arūnas Jagminas

State Research Institute Center for Physical Sciences and Technology, Savanoriu ave. 231, 02300 Vilnius, Lithuania

ARTICLE INFO

Article history:
Received 31 May 2013
Received in revised form
2 April 2015
Accepted 9 April 2015
Available online 11 April 2015

Keywords:
Superferromagnetic nanoparticles
Dipolar interactions
Mössbauer spectrometry

ABSTRACT

Superparamagnetic properties of ultrasmall $CoFe_2O_4$ (1–3 nm) nanoparticles before and after gold plating were studied by Mössbauer spectrometry. The nanoparticles in the suspension in water were compared with same dried nanoparticles. Blocking temperature increases by 10–20 K after drying of the suspension. Strong dipolar and indirect exchange interactions between nanoparticles in the dried state were used to explain observed differences. The strength of interactions was estimated by the application of the multilevel model for the description of Mössbauer spectra. The strength of interactions between nanoparticles in the dried state, as it was observed, decreased with temperature. Moreover, the multilevel model allowed us to determine the superparamagnetic relaxation time and the barrier height. The results indicate that magnetic anisotropy of $CoFe_2O_4$ nanoparticles should be similar to the anisotropy of bulk $CoFe_2O_4$.

1. Introduction

The properties of materials in nanostructures may markedly change [1]. Particularly, magnetic properties also alter due to nanoscale effects [2], for example, the superparamagnetism of single domain nanoparticles [3]. Superparamagnetic nanoparticles as the main constituent are used in ferrofluids applicable in nanotechnology [4–6]. Moreover, magnetic nanoparticles can be used for a separation of cells, the hyperthermia treatment, as carriers of drugs in medicine [7–11]. $CoFe_2O_4$ nanoparticles in comparison with iron oxide nanoparticles have higher magnetic anisotropy and can be beneficial, for example, in hyperthermia applications [12,13]. Furthermore, the size effects on properties can be particularly interesting to study, especially in the case of ultrasmall $CoFe_2O_4$ (1–3 nm) nanoparticles. Enhanced magnetization [14] and the reduction in Curie temperature [15] were reported for $CoFe_2O_4$ nanoparticles. A dependence of magnetic anisotropy on the size of $CoFe_2O_4$ particles was also observed [16]. However, the studies of nanoparticles are complicated due to the influence of size distribution and interactions between the nanoparticles [17–19]. Strong interactions between superparamagnetic nanoparticles can lead to the magnetic (superferromagnetic) ordering above a blocking temperature characteristic of not interacting nanoparticles [3,19]. The superferromagnetic state of nanocrystalline antiferromagnetic goethite was explained by a partial exchange coupling between the surface atoms of neighboring nanoparticles [18,20]. It was shown that dipolar interactions can also be responsible for the superferromagnetic state in ordered 1D and 2D assemblies of superspins [3,21]. However, the weak exchange interactions may have an important role stabilizing the superferromagnetic ordering observed for the assemblies of dipolar interacting Fe nanostripes, isolated Fe, FeCo and Co nanoparticles in a nonmagnetic matrix [22–27].

The superparamagnetic nanoparticles are frequently characterized by blocking temperature which can be determined by means of different methods including Mössbauer spectrometry [28]. However, blocking temperature depends on both superparamagnetic properties of nanoparticles and characteristic measurement time of the applied method. The superparamagnetic dynamics of the magnetic moment of a nanoparticle can be described by the application of a multilevel model which allows obtaining the temperature dependent shape of Mössbauer spectra of superparamagnetic nanoparticles [29–31]. Herein, the multilevel method is used to evaluate properties of ultrasmall $CoFe_2O_4$ nanoparticles prepared by co-precipitation way using Mössbauer spectroscopy data at temperatures near superparamagnetic blocking temperature. The influence of interactions is investigated using a comparison of same nanoparticles in the frozen suspension in water with them in a dry state.

* Corresponding author.

http://dx.doi.org/10.1016/j.jmmm.2015.04.044
0304-8853/

2. Experimental

$CoFe_2O_4$ nanoparticles are synthesized by co-precipitation method using $CoCl_2$, $Fe_2(SO_4)_3$ and NaOH at 80 °C temperature and 12.0 pH [32]. The citric acid which acts as an electrostatic stabilizer [11] is added to make stable suspensions of nanoparticles in water. The size of nanoparticles (2–3 nm) is evaluated by means of AFM and TEM (Fig. 1). Previously prepared $CoFe_2O_4$ nanoparticles are covered with Au with an assistance of Vitamin C at 6.0 pH by an addition of HAuCl during two days as described in Ref. [33].

Mössbauer transmission spectra were collected using the Mössbauer spectrometer with a source of ^{57}Co(Rh) and the closed cycle helium cryostat (Advanced Research Systems, Inc.). 2 ml of suspensions either of $CoFe_2O_4$ or $CoFe_2O_4$@Au nanoparticles in water (the concentration of $CoFe_2O_4$ was 0.1% of volume) were placed in the special cell for low temperature measurements. After the measurements the suspensions were dried on a filter paper and measured again at same temperature region.

Superparamagnetic blocking temperature T_B of ultrasmall $CoFe_2O_4$ nanoparticles is determined using the dependence of average hyperfine field $\langle B\rangle$ on temperature (Fig. 2a) at $\langle B\rangle \approx 0.5B_0$. Average hyperfine field is evaluated by fitting of a hyperfine field distribution and a superparamagnetic singlet/doublet to Mössbauer spectrum using Normos Dist software. Average hyperfine field is obtained by the expression $\langle B\rangle = \frac{\sum P_i B_i}{\sum P_i + P_s}$, where P_i is the relative area of sextet having the hyperfine field B_i in the hyperfine field distribution. The hyperfine field $B_0 \approx 53.4$ T is the average hyperfine field of a bulk $CoFe_2O_4$ when $T \to 0$ [34,35]. Blocking temperature is also frequently determined at temperature when the area of paramagnetic part P_s is equal to the area of magnetically split part of Mössbauer spectra P_m (Fig. 2b). In this case blocking temperature (T'_B), as it is obtained, is larger by 11–18 K than T_B (Table 1). It is because $\langle B\rangle$ is affected by a change in both the area and hyperfine field distribution.

In addition, the multilevel model is used. It allows us to determine superparamagnetic relaxation time τ as well as other parameters. A line shape of Mössbauer spectrum in the multilevel model is given by the expression [29]:

$$I(\omega) = 2\,\mathrm{Re}(\mathrm{WM}^{-1}\mathbf{1}) \tag{1}$$

where elements of the matrix **W** are the occupation probabilities of the levels. The levels are associated with the projections S_z of the spin S to the easy magnetic axis and are used to describe dynamics of a magnetic moment of a nanoparticle. The diagonal matrix $\mathbf{\Omega}$ in the matrix $\mathrm{M}=i(\omega+\Gamma)\,\mathrm{I}+\mathbf{\Omega}+\mathbf{\Pi}$ describes the static positions of Mössbauer spectrum associated with the levels. The matrix **I** is a diagonal unit matrix and the matrix $\mathbf{\Pi}$ describes a relaxation rate which is determined by the diffusion parameter R and the energy difference between levels. The probability of a jump to the level having higher energy is $R\cdot\exp(-\Delta E/k_B T)$ where k_B is the Boltzmann constant, T is temperature and ΔE is the energy difference between the adjacent levels. When magnetic field H acting on magnetic moment of a nanoparticle m is collinear to easy magnetic axis magnetic energy of a nanoparticle:

$$E = KV\sin^2\theta - \mu_0 mH\cos\theta \tag{2}$$

depends only on one angle θ. KV (K is the magnetic anisotropy constant and V is a volume of a nanoparticle) is uniaxial magnetic anisotropy energy, θ is the angle between magnetic moment of the particle and the easy magnetic axis and μ_0 is the vacuum permeability. The magnetic moment of a nanoparticle $m = M_s V$ where M_s is volume magnetization. The Eq. (2) defines the energy of the levels because of $\cos\theta = S_z/S$. In the case of strong dipolar interactions between nanoparticles when nanoparticles order in chains or in assemblies of interacting nanoparticles (superferromagnetism) magnetic moments arrange mostly in parallel [18,19].

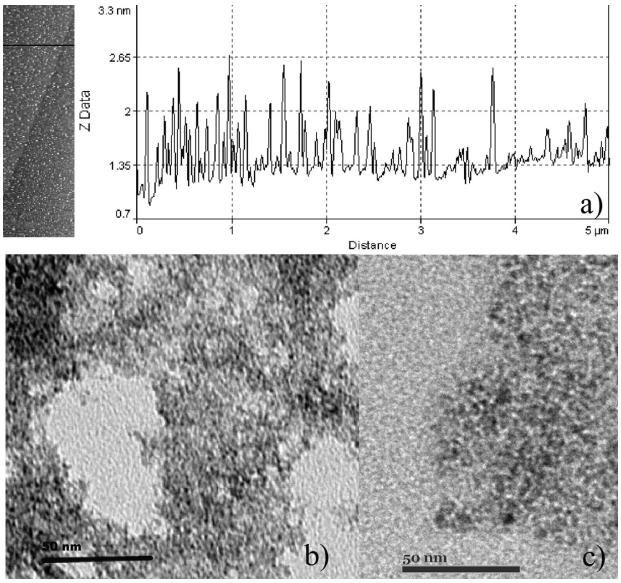

Fig.1. AFM data (a) and TEM images of $CoFe_2O_4$ (b) and $CoFe_2O_4$@Au (c) nanoparticles.

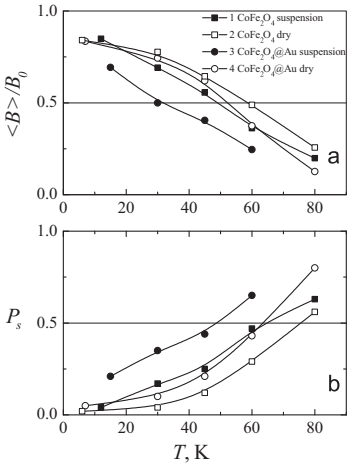

Fig. 2. Dependence of normalized average hyperfine field (a) and the relative area of superparamagnetic part of spectrum (b) of ultrasmall $CoFe_2O_4$ and $CoFe_2O_4$&@Au nanoparticles on temperature.

Table 1
Blocking temperature of $CoFe_2O_4$ and $CoFe_2O_4$@Au nanoparticles in the suspension and a dry state. T_B is found at $\langle B\rangle \approx 0.5B_0$, and T'_B is determined at equal areas.

Sample	T_B (K)	T'_B (K)
$CoFe_2O_4$		
In liquid	49	64
Dry	59	75
$CoFe_2O_4$@Au		
In liquid	31	49
Dry	52	63

The strength of interactions between nanoparticles is expressed by the parameter $h=\mu_0 M_s H/2K$. The multilevel model is fitted to two Mössbauer spectra of same nanoparticles, in the frozen suspension and the dried state, simultaneously. Only the parameter h is used to describe the difference in the Mössbauer spectra measured at same temperature applying one set of parameters for both spectra together. It is assumed that the interactions between nanoparticles are negligible, $h \approx 0$, in the frozen suspension and strong, $h > 0$, in a dry state. The superparamagnetic relaxation rate is determined applying the energy dependence of Eq. (2) and the parameters $\alpha=KV/k_BT$ and h.

The distribution of the parameter α follows the lognormal law:

$$P(\alpha) = \frac{1}{\sqrt{2\pi}\sigma_\alpha \alpha} \exp\left(-\frac{\ln^2(\alpha/\alpha_0)}{2\sigma_\alpha^2}\right) \tag{3}$$

because of the lognormal distribution of the nanoparticle size D. α_0 is median and σ_α is standard deviation of α. Herein, standard deviation of size $\sigma_D=\sigma_\alpha/3$ is used as the fitting parameter. The isomer shift δ is the additional fitting parameter which determines the center position of Mössbauer spectra. The other parameters of Mössbauer spectra – the static hyperfine field $B_0(T)$, the line width Γ – are fixed. The accuracy of these parameters has a little effect on the evaluation of a superparamagnetic relaxation rate. Therefore, instead of two sextets having slightly different Mössbauer parameters, which are used to fit to Mössbauer spectra of a bulk $CoFe_2O_4$ [34,35], only one line the shape of which is given by Eq. (1) is applied in our model.

Because a change in the parameters R, α and σ_α can have similar effects on the line shape the parameters can be not always reliably estimated. However, the variation in the parameters α and R can be restricted by means of additional relation. Given [21]

$$R = \frac{k_B T\gamma_0}{2M_s V} = \frac{\gamma_0 K}{2M_s \alpha} \tag{4}$$

where γ_0 is the gyromagnetic ratio it follows that $R\alpha = \gamma_0 K/2M_s$. Accordingly, the constraint $R\alpha = const$ is introduced in the fitting procedure. The results has shown that the dependences of α and h on temperature become more stable. Because R mainly depends on magnetic anisotropy and volume magnetization which are not exactly known, different values of the product $R\alpha$ are applied to evaluate possible uncertainties of results (Table 2).

3. Results and discussion

Blocking temperature of the same nanoparticles in a dry state is higher that in the frozen suspension (Fig. 2, Table 1). Considering that $CoFe_2O_4$ nanoparticles are coated with the surfactant layer (citric acid) and $CoFe_2O_4$@Au nanoparticles are coated with Au direct exchange interactions between nanoparticles in a dry state are unlikely. Therefore, dipolar as well as indirect exchange interactions (tunnel exchange [27] or RKYY coupling [36]) should to be used to explain observed differences. The relative contribution of interactions to the barrier height for superparamagnetic relaxation depends on both the strength of interactions and the state (superparamagnetic, spin-glass like or superferromagnetic [3]) of the nanoparticle system. For example, it is found that the weak dipolar interactions may not lead to an increase but to a decrease in blocking temperature T_B and the barrier height [28]. The arrangement of magnetic moments of nanoparticles is interrelated with the strength of the interactions. It can be shown that the dipolar interactions cause increase in the barrier height when the effective magnetic field due to the interactions acts mostly along the easy magnetic axis of a nanoparticle, for example, when the

Table 2
Parameters of the multilevel model used in the description of Mössbauer spectra: α_0 is median of the relative barrier height, σ_D is size dispersion, τ_0 is exponential prefactor, and τ_l and τ_d are superparamagnetic relaxation time for nanoparticles in the suspension and a in dry state, accordingly. First number in range corresponds to $R\alpha=25$ mm/s; the second number – $R\alpha=100$ mm/s.

Sample	T (K)	α_0	σ_D	τ_0, 10^{-10} s	τ_l, 10^{-9} s	τ_d, 10^{-9} s	h
$CoFe_2O_4$	30	4.6–5.9	0.33–0.18	2.3–0.5	23–18	24–18	0.2–0.11
	45	3.0–4.7	0.3–0.15	2.8–0.6	5.7–6.0	5.4–5.8	0.15–0.09
	60	1.8–3.7	0.34–0.17	3.6–0.6	2.2–2.5	2.1–2.4	0.11–0.07
$CoFe_2O_4$@Au	30	3.0–4.6	0.41–0.24	2.8–0.6	5.6–5.7	5.5–5.7	0.22–0.17
	45	2.1–3.9	0.36–0.2	3.3–0.6	2.8–3.0	2.9–2.6	0.14–0.09
	60	0.9–2.9	0.58–0.25	5.0–0.7	1.3–1.3	1.2–1.3	0.07–0.06

magnetic moments arrange in parallel and nanoparticles order in chains. In our case when the suspension is dried on a filter paper the assembly of nanoparticles can be in the state between "superferromagnetism", "spin-glass order" and superparamagnetism [3,19]. For example, the magnetic moments may be frozen at low temperature in lowest energy "superferromagnetic" state but when temperature increase and the magnetic moments are unblocked the average strength of interactions decreases due to the fluctuations of the direction of magnetic moments.

Blocking temperature (T_B) of $CoFe_2O_4$@Au nanoparticles in the frozen suspension which is determined at $\langle B \rangle \approx 0.5B_0$ (Fig. 2a) is lower by 18 K than that of $CoFe_2O_4$ nanoparticles. In the case of the dry nanoparticles, this difference is smaller (Table 1). It is evident that Au deposition leads to a change in the properties of $CoFe_2O_4$ nanoparticles similar to that reported for magnetite nanoparticles [37]. It is noteworthy that $CoFe_2O_4$@Au nanoparticles are slightly larger because of Au shell (Fig. 1c) but the decrease in blocking temperature can be due to the decrease in the size of a magnetic core by $\approx$ 0.2–0.4 nm.

The ordering temperature (Curie temperature) of superferromagnet which arises only due to dipolar interactions is given by [19]

$$T_c \approx \frac{\mu_0}{4\pi}\frac{\rho m^2}{k_B} \tag{5}$$

where ρ is the number of nanoparticles per unit volume. T_c is of order of 4–12 K for 2–3 nm $CoFe_2O_4$ nanoparticles. It is comparable with the difference in blocking temperature for $CoFe_2O_4$ nanoparticles in the frozen suspension and the dried state. However, for $CoFe_2O_4$@Au nanoparticles, the difference in blocking temperatures between the frozen suspension and the dried states was similar despite the plating with gold. For nanoparticles separated by a nonmagnetic shell the indirect exchange coupling such as a tunnel exchange [27] and RKKY interaction [36] was considered. RKKY (Ruderman–Kittel–Kasuya–Yosida) exchange interactions through conducting electrons was used to explain the enhancement of remanence of $CoFe_2O_4$ nanoparticles in a poly(aniline) matrix [38] as well as a spin-glass type behavior of transition metal ions diluted in a noble metal matrix [39]. In the case of antiferromagnetic nanocrystalline materials the partial direct exchange interactions between the nanoparticles were found to be responsible for the "superferromagnetic" state [18,20]. The method of effective mean field was applied to take such interactions into consideration. In the case of exchange interactions Eq. (2) can be replaced by

$$E = KV\sin^2\theta - J_{eff}M_s^2 b(T)\cos\theta \tag{6}$$

J_{eff} is an effective exchange coupling and $b(T) = \left\langle \vec{M}_s \right\rangle / M_s$ is the order parameter. In the case of Eq. (6) the parameter $h = J_{eff}M_s^2 b(T)/2KV$.

The multilevel model is applied to evaluate superparamagnetic relaxation time τ, median of the relative barrier height $\alpha = KV/k_BT$ and the strength of interactions h (Table 2) using Mössbauer spectra measured near blocking temperature. Superparamagnetic relaxation time for the dried nanoparticles is evaluated according to

$$\tau_d = \frac{\tau_0}{(1-h^2)(1+h)}\exp\left(\alpha(1+h)^2\right) \tag{7}$$

where τ_0 is the exponential prefactor [29]. It is assumed that in the frozen suspension nanoparticles do not interact significantly. In this case $h \approx 0$ and superparamagnetic relaxation time for nanoparticles in suspension is $\tau = \tau_0 \exp(\alpha)$.

As mentioned in the previous section, the fitting results are obtained using the constraint of the parameters: $R\alpha_0 = const$. The results when *const* is within 25–100 mm/s region (Table 2) corresponds to value of the magnetic anisotropy constant $K \approx (1.3–5)\cdot 10^5$ J/m^3 (Eq. (4)). The change in $R\alpha$ is used to evaluate possible uncertainties of parameters. The value of $R\alpha$ has small influence to the shape of the line obtained by fitting the multilevel model to experimental spectra (Fig. 3). Its influence to superparamagnetic relaxation time τ is also small in comparison with the total range of τ variation. The other parameters: the prefactor

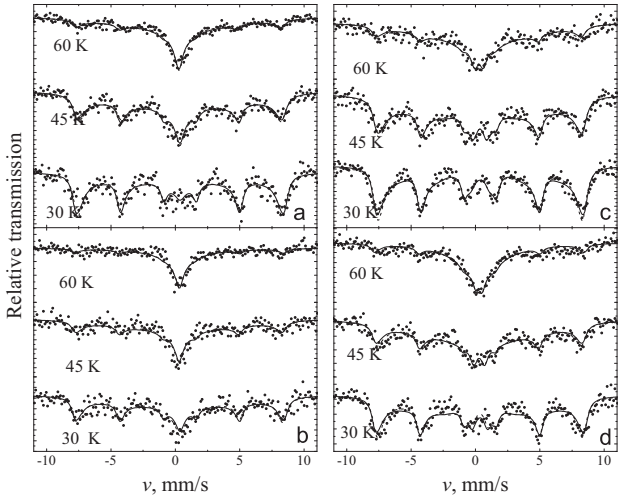

Fig. 3. Mössbauer spectra of ultrasmall $CoFe_2O_4$ nanoparticles before (a,c) and after gold plating (b,d) when nanoparticles are dispersed in water (a,b) and dried on the filter paper (c,d).

τ_0, median of the relative barrier height α_0, and dispersion of a size σ_D considerably depend on the $R\alpha$ value. The prefactor τ_0 is calculated according to the relation $\tau_0 = \sqrt{\pi}/\left(2R\alpha_0^{3/2}\right)$ [29] and is found to be $5\cdot10^{-11}$–$5\cdot10^{-10}$ s. The parameters α_0, σ_D and h, as presented in Table 2, can change approximately up to 2 times. It is noteworthy that an increase in $R\alpha$ over 100 mm/s leads to unlikely, too small values of τ_0 and σ_D.

The parameter h is used to evaluate the approximate value of effective field acting on nanoparticles either due dipolar or indirect exchange interactions. Considering the dependences of h on $R\alpha$ (Table 2) and $R\alpha$ on K (Eq. (4)) the maximum value of H is $\approx(0.9–1.7)\cdot10^5$ A/m for $CoFe_2O_4$ nanoparticles. It is little larger for $CoFe_2O_4$@Au. The parameter h decreases with temperature approximately two times within 30–60 K temperature region (Table 2). The strength of dipolar interactions should decrease when magnetic moments unblock and the system of nanoparticles becomes more superparamagnetic. The exchange energy contribution (Eq. (6)) decreases with the order parameter as here $\left\langle \vec{M_s} \right\rangle \propto \langle B \rangle$ (Fig. 2a).

The data on median of the barrier height α_0 (Table 2) are compatible with the magnetic anisotropy constant $K=(1.3–5)\cdot10^5$ J/m^3 for 2–3 nm-sized $CoFe_2O_4$ nanoparticles. On the contrary, the larger value of $K \approx 10^7$ J/m^3, as are reported in Ref. [16], would lead to the size of the magnetic core of a nanoparticle of less than 1 nm. τ_0 depends on temperature because of $R\sim T$ [29]. α_0 dependence on temperature is rather close to $\sim T^{-1}$ indicating the validity of our approximations. However, according to ref. [40], the temperature dependence of τ_0 may be more complicated and magnetic anisotropy can also be temperature dependent.

The experimental evidence of dependence of Curie temperature on the size of nanoparticles is interesting task where the application of Mössbauer spectroscopy is valuable [41]. For $\approx$ 3 nm size $CoFe_2O_4$ nanoparticles magnetic ordering/Curie temperature $T_c \approx 10$ K has been obtained by magnetization and ac susceptibility methods [15]. The blocking temperatures obtained by different methods are related according to the expression:

$$\frac{T_B^1}{T_B^2} = \frac{\ln\left(\tau_m^2/\tau_0\right)}{\ln\left(\tau_m^1/\tau_0\right)} \tag{8}$$

where τ_m is the characteristic measurement time which is 10^{-7}–10^{-9} s for Mössbauer spectroscopy. According to our data (Table 2) blocking temperature T_B determined at $\langle B \rangle \approx 0.5B_0$ is related with $\tau_m \approx 5.6\cdot10^{-9}$ s for non-interacting nanoparticles, $\tau_0 \approx (0.5\text{-}3)\cdot10^{-10}$ s and $\ln(\tau_m/\tau_0)$ is 3–4.5. The factor $\ln(\tau_m/\tau_0)$ is 27–28 for $\tau_m \approx 100$ s which is characteristic of the magnetization method. Accordingly, T_B=60–90 K obtained from Mössbauer spectroscopy data would correspond to $T_B \approx 10$ K from magnetization studies.

4. Conclusions

In the study it is obtained that blocking temperature of ultrasmall 2–3 nm size $CoFe_2O_4$ and $CoFe_2O_4$@Au nanoparticles in the dry state is larger by 10–20 K in comparison with them in the suspension. As it is known superparamagnetic blocking temperature of $CoFe_2O_4$ nanoparticles depends on a number of properties: the size, the composition, magnetic anisotropy and interactions between the nanoparticles. Herein, the difference in blocking temperature of same nanoparticles is explained by taking dipolar or indirect exchange interactions into consideration. These interactions should be strong enough to ensure the order of magnetic moments of nanoparticles at low temperature similar to "superferromagnetism". The strength of interactions, as it is observed, considerably decreases with the transition of system of nanoparticles to superparamagnetic state. Mössbauer spectroscopy data for ultrasmall 2–3 nm size $CoFe_2O_4$ and $CoFe_2O_4$@Au nanoparticles are consistent with the magnetic anisotropy ($K \approx (1.3–5)\cdot10^5$ J/m^3) which is rather similar to anisotropy of bulk $CoFe_2O_4$. The gold plating of $CoFe_2O_4$ nanoparticles cause a decrease in blocking temperature which could be due to the reduced (by $\approx$ 0.2–0.4 nm) size of the magnetic core of nanoparticles.

Acknowledgements

This work was supported by the Lithuanian Science Council under Grant no. MIP-088/2011. Authors thank Rokas Kondrotas for TEM images.

References

[1] P. Moriarty, Nanostructered materials, Rep. Prog. Phys. 64 (2001) 297–381.
[2] R. Skomski, Nanomagnetics, J. Phys.: Condens. Matter 15 (2003) R841–R896.
[3] S. Bedanta, W. Kleemann, Supermagnetism, J. Phys. D: Appl. Phys. 42 (2009) 013001.
[4] J. Popplewell, Technological applications of ferrofluids, Phys. Technol. 15 (1984) 150–156.
[5] M. Zahn, Magnetic fluid and nanoparticle applications to nanotechnology, J. Nanopart. Res. 3 (2001) 73–78.
[6] L.L. Vatta, R.D. Sanderson, K.R. Koch, Magnetic nanoparticles: properties and potential applications, Pure Appl. Chem. 78 (2006) 1793–1801.
[7] S. Laurent, S. Dutz, U.O. Häfeli, M. Mahmoudi, Magnetic fluid hyperthermia: focus on superparamagnetic iron oxide nanoparticles, Adv. Colloid Interface Sci. 166 (2011) 8–23.
[8] R. Hergt, S. Dutz, R. Müller, M. Zeisberger, Magnetic particle hyperthermia: nanoparticle magnetism and materials development for cancer therapy, J. Phys.: Condens. Matter 18 (2006) S2919–S2934.
[9] Monty Liong, Jie Lu, M. Kovochich, Tian Xia, S.G. Ruehm, A.E. Nel, Fuyuhiko Tamanoi, J.I. Zink, Multifunctional inorganic nanoparticles for imaging, targeting, and drug delivery, ACS Nano 2 (2008) 889–896.
[10] Wei Wu, Quanguo He, Changzhong Jiang, Magnetic iron oxide nanoparticles: synthesis and surface functionalization strategies, Nanoscale Res. Lett. 3 (2008) 397–415.
[11] M.E. de Sousa, M.B. Fernández van Raap, P.C. Rivas, P.M. Zélis, P. Girardin, G. A. Pasquevich, J.L. Alessandrini, D. Muraca, F.H. Sánchez, Stability and relaxation mechanisms of citric acid coated magnetite nanoparticles for magnetic hyperthermia, J. Phys. Chem. C 117 (2013) 5436–5445.
[12] R.E. Rosensweig, Heating magnetic fluid with alternating magnetic field, J. Magn. Magn. Mater. 252 (2002) 370–374.
[13] Dong-Hyun Kim, D.E. Nikles, D.T. Johnson, C.S. Brazel, Heat generation of aqueously dispersed $CoFe_2O_4$ nanoparticles as heating agents for magnetically activated drug delivery and hyperthermia, J. Magn. Magn. Mater. 320 (2008) 2390–2396.
[14] D. Peddis, C. Cannas, G. Piccaluga, E. Agostinelli, D. Fiorani, Spin-glass-like freezing and enhanced magnetization in ultra-small $CoFe_2O_4$ nanoparticles, Nanotechnology 21 (2010) 125705.
[15] V. Lopez-Dominguez, J.M. Hernàndez, J. Tejada, R.F. Ziolo, Colossal reduction in Curie temperature due to finite-size effects in $CoFe_2O_4$ nanoparticles, Chem. Mater. 25 (2013) 6–11.
[16] Sunghyun Yoon, Temperature dependence of magnetic anisotropy constant in cobalt ferrite nanoparticles, J. Magn. Magn. Mater. 324 (2012) 2620–2624.
[17] B. Huke, M. Lucke, Magnetic properties of colloidal suspensions of interacting magnetic particles, Rep. Prog. Phys. 67 (2004) 1731–1768.
[18] S. Mørup, M.F. Hansen, C. Frandsen, Magnetic interactions between nanoparticles, Beilstein J. Nanotechnol. 1 (2010) 182–190.
[19] S.A. Majetich, M. Sachan, Magnetostatic interactions in magnetic nanoparticle assemblies: energy, time and length scales, J. Phys. D: Appl. Phys. 39 (2006) R407–R422.
[20] S. Mørup, M.B. Madsen, J. Franck, J. Villadsen, C.J.W. Koch, A new interpretation of Mössbauer spectra of microcrystalline goethite: "super-ferromagnetism" or "super-spin-glass" behaviour? J. Magn. Magn. Mater. 40 (1983) 163–174.
[21] P. Politi, M.G. Pini, Dipolar interaction between two-dimensional magnetic particles, Phys. Rev. B 66 (2002) 214414.
[22] J. Hauschild, H.J. Elmers, U. Gradmann, Dipolar superferromagnetism in monolayer nanostripes of Fe(110) on vicinal W(110) surfaces, Phys. Rev. B 57 (1998) R677–R680.
[23] W. Kleemann, O. Petracic, Ch Binek, G.N. Kakazei, Yu.G. Pogorelov, J.B. Sousa, S. Cardoso, P.P. Freitas, Interacting ferromagnetic nanoparticles in discontinuous $Co_{80}Fe_{20}/Al_2O_3$ multilayers: from superspin glass to reentrant

superferromagnetism, Phys. Rev. B 63 (2001) 134423.
[24] S. Bedanta, T. Eimüller, W. Kleemann, J. Rhensius, F. Stromberg, E. Amaladass, S. Cardoso, P.P. Freitas, Overcoming the dipolar disorder in dense CoFe nanoparticle ensembles: superferromagnetism, Phys. Rev. Lett. 98 (2007) 176601.
[25] M.R. Scheinfein, K.E. Schmidt, K.R. Heim, G.G. Hembree, Magnetic order in two-dimensional arrays of nanometer-sized superparamagnets, Phys. Rev. Lett. 76 (1996) 1541–1544.
[26] P. Bruno, Theory of intrinsic and thermally induced interlayer magnetic coupling between ferromagnetic films separated by an insulating layer, Phys. Rev. B 49 (1994) 13231.
[27] V.N. Kondratyev, H.O. Lutz, Shell effect in exchange coupling of transition metal dots and their arrays, Phys. Rev. Lett. 81 (1998) 4508–4511.
[28] S. Mørup, E. Tronc, Superparamagnetic relaxation of weakly interacting particles, Phys. Rev. Lett. 72 (1994) 3278–3281.
[29] D.H. Jones, K.K.P. Srivastava, Many-state relaxation model for the Mössbauer spectra of superparamagnets, Phys. Rev. B 34 (1986) 7542–7548.
[30] J. van Lierop, D.H. Ryan, Mössbauer spectra of single-domain fine systems described using a multiple-level relaxation model for superparamagnets, Phys. Rev. B 63 (2001) 064406.
[31] M.A. Chuev, Multi-level relaxation model for describing the Mössbauer spectra of single-domain particles in the presence of quadrupolar hyperfine interaction, J. Phys.: Condens. Matter 23 (2011) 426003.
[32] A. Jagminas, M. Kurtinaitienė, K. Mažeika, Synthesis of cobalt ferrite nanoparticles by complex-assisted co-precipitation and hydrothermal approaches, Chemija 24 (2013) 103–110.
[33] A. Jagminas, K. Mažeika, R. Kondrotas, M. Kurtinaitienė, A. Jagminienė, A. Mikalauskaitė, Functionalization of cobalt ferritte nanoparticles by vitamin C-assisted covering with gold, Nanomater. Nanotechnol. 4 (2014) 11.
[34] Sam Jin Kim, Seung Wha Lee, Chul Sung Kim, Mössbauer studies on exchange interactions in $CoFe_2O_4$, Jpn. J. Appl. Phys. 40 (2001) 4897–4902.
[35] V. Rusanov, V. Gushterov, S. Nikolo, A.X. Trautwein, Detailed Mössbauer of the cation distribution in $CoFe_2O_4$ ferrites, Hyperfine Interact. 191 (2009) 67–74.
[36] C. Kittel, Quantum Theory of Solids, Second revised ed., Wiley, New York, 1987.
[37] L.W. Lingyan Wang, Jin Luo, Quan Fan, Masatsugu Suzuki, Itsuko S. Suzuki, Mark H. Engelhard, Yuehe Lin, Nam Kim, Jian Q. Wang, Chuan-Jian Zhong, Monodispersed core–shell Fe_3O_4@Au nanoparticles, J. Phys. Chem. B 109 (2005) 21593–21601.
[38] P.S. Antonel, F.M. Berhó, G. Jorge, F.V. Molina, Magnetic composites of $CoFe_2O_4$ nanoparticles in a poly(aniline) matrix: enhancement of remanence ratio and coercivity, Synth. Met. 199 (2015) 292–302.
[39] K. Binder, A.P. Young, Spin glasses: experimental and open questions, Rev. Mod. Phys. 58 (1986) 801–976.
[40] K.K.P. Srivastava, The theory of superparamagnetic relaxation: Mossbauer study, J. Phys.: Condens. Matter 15 (2003) 549–560.
[41] E. Skoropata, R.D. Desautels, B.W. Southern, J. van Lierop, Comment on "Colossal Reduction in Curie Temperature Due to Finite-Size Effects in $CoFe_2O_4$ Nanoparticles", Chem. Mater. 25 (2013) 1998–2000.

NOTES

NOTES

Vilniaus universiteto leidykla
Saulėtekio al. 9, III rūmai, LT-10222 Vilnius
El. p.: info@leidykla.vu.lt, www.leidykla.vu.lt
Tiražas 15 egz.